MICROSTRUCTURE-SENSITIVE EXTREME VALUE PROBABILITIES OF FATIGUE IN ADVANCED ENGINEERING ALLOYS

A Dissertation
Presented to
The Academic Faculty

by

Craig P. Przybyla

In Partial Fulfillment
of the Requirements for the Degree
Doctor of Philosophy in
Materials Science and Engineering

Materials Science and Engineering
Georgia Institute of Technology
August 2010

MICROSTRUCTURE-SENSITIVE EXTREME VALUE PROBABILITIES OF FATIGUE IN ADVANCED ENGINEERING ALLOYS

Approved by:

Professor David L. McDowell, Advisor
Materials Science and Engineering
Georgia Institute of Technology

Professor Richard W. Neu
The George W. Woodruff School of
Mechanical Engineering
Georgia Institute of Technology

Professor Hamid Garmestani
Materials Science and Engineering
Georgia Institute of Technology

Dr. Michael J. Caton
Materials and Manufacturing Directorate
Air Force Research Laboratory

Professor Arun M. Gokhale
Materials Science and Engineering
Georgia Institute of Technology

Dr. Michael D. Uchic
Materials and Manufacturing Directorate
Air Force Research Laboratory

Date Approved: June 28, 2010

To my wife Laura and my children Elizabeth, Dallin, and William.

ACKNOWLEDGEMENTS

It has been my honor and privilege to work under the advisement of Dr. David L. McDowell. I sincerely thank him for the many selfless hours of his time that he has given on my behalf without which this work would not have materialized. The support of my graduate committee is acknowledged including Dr. Hamid Garmestani, Dr. Arun Gokhale and Dr. Richard Neu, and my external committee members Dr. Michael Caton, and Dr. Michael Uchic of the Materials and Manufacturing Directorate at the Air Force Research Laboratory, Wright-Patterson AFB, Ohio. The diverse perspectives and technical expertise of the various committee members have collectively helped to shape many of the important contributions of this work.

For financial support, I am very grateful to Dr. Stephan Russ and Dr. Michael Shepard at the Air Force Research Laboratory for the internship and coop opportunities which supported me for the last several years of this effort. Earlier financial support from the Carter N. Paden, Jr. Distinguished Chair in Metals Processing held by Dr. David L. McDowell and support from the NSF Center for Computational Materials Design, a joint Penn State-Georgia Tech I/UCRC, is also gratefully acknowledged.

Throughout the course of my graduate studies, the support of my fellow graduate students and friends has been substantial. As such, I thank Ryan Austin, Sam Britt, Dr. DJ Luscher, Jason Mayeur, Dr. Rahesh Prasannavenkatesan, Nima Salajeheh, Dr. Mahesh Shenoy, Jin Song, Garrett Tucker, Dr. Mark Tschopp, and Dr. Ming Zhang. In particular, Jason Mayeur's assistance in helping me to develop some understanding of crystal plasticity theory has been invaluable. My friends and associates at the Air Force Research Laboratory have also provided much technical and non-technical support including Dr. Robert Brockman, Dr. Christopher Crouse, Brian Gockel, Dr. Patrick Golden, Dr. Michael

Groeber, Dr. Reji John, Dr. Christopher Szczepanski, Dr. Sushant Jha, Dr. Jeff Simmons and Dr. Garth Wilks.

This endeavor really began when I took a undergraduate research position under Dr. Brent L. Adams at Brigham Young University during my sophomore year. If it was not for Dr. Adams' contagious passion for research and his encouragement during my time at BYU, I would not have pursued this PhD. I am most grateful for his influence and continued support.

It goes without saying that without the sacrifices of and values instilled in me by my parents, I could not have accomplished this work. Most importantly, I must also thank my wife Laura for her patience, love and devotion during this difficult process. The support of her and my children Elizabeth, Dallin, and William have kept me coming back each day to complete this work even during the most discouraging of times.

TABLE OF CONTENTS

LIST OF TABLES

LIST OF FIGURES

LIST OF SYMBOLS OR ABBREVIATIONS

bcc	Base-centered cubic.
σ	Cauchy stress.
BOR	Burgers Orientation Relation.
ΔCTD	Cyclic crack tip displacement range.
$\dot{\gamma}^{\alpha}$	Slip rate for slip system α.
EPFM	Elastic-plastic fracture mechanics.
EVMCF	Extreme value marked correlation function.
FE	Finite element.
FEA	Finite element analysis.
FEM	Finite element method.
FIP	Fatigue indicator parameter.
FS	Fatemi-Socie fatigue indicator parameter.
$\hat{\mathbf{e}}$	Base vectors in the sample reference coordinate system.
$\hat{\mathbf{e}}^{c}$	Base vectors in the crystal coordinate system.
HCF	High cycle fatigue.
hcp	Hexagonal close-packed.
ISV	Internal state variable.
ΔJ	Elastic-plastic fracture mechanics parameter.
ΔK	Stress intensity factor.
LCF	Low cycle fatigue.
LEFM	Linear elastic fracture mechanics.
$\mathbb{C}$	Forth-order elastic stiffness in the intermediate configuration.
$\mathbb{C}^{c}$	Forth-order elastic stiffness in the crystal coordinate system.
$\mathbf{C}^{e}$	Right elastic Cauchy-Green tensor.
$\mathbf{D}$	Rate of deformation tensor.

$\mathbf{E}^e$	Elastic Green strain tensor in the intermediate configuration.
$\mathbf{F}$	Deformation gradient.
$\mathbf{F}^e$	Elastic part of the deformation gradient.
$\mathbf{F}^p$	Plastic part of the deformation gradient.
$\mathbf{I}$	Second rank identity tensor.
$\mathbf{L}$	Velocity gradient in the current configuration.
$\mathbf{L}^e$	Elastic velocity gradient in the current configuration.
$\mathbf{L}_o^p$	Plastic velocity gradient in the reference configuration.
$\mathbf{L}^p$	Plastic velocity gradient in the current configuration.
$\mathbf{n}^\alpha$	Vector normal to slip plane α in the current configuration.
$\mathbf{n}_o^\alpha$	Vector normal to slip plane α in the reference configuration.
$\mathbf{P}^\alpha$	Schmid tensor in the reference configuration.
$\mathbf{R}$	Rotation from the crystal coordinate system to the sample reference coordinate system.
$\mathbf{R}'$	Rotation from the crystal coordinate system to the sample current coordinate system.
$\mathbf{s}^\alpha$	Slip direction for slip system α in the current configuration.
$\mathbf{s}_o^\alpha$	Slip direction for slip system α in the reference configuration.
$\mathbf{T}$	Second Piola-Kirchhoff stress tensor in the intermediate configuration.
$\mathbf{T}_o$	Second Piola-Kirchhoff stress tensor in the reference configuration.
$\mathbf{W}$	Spin tensor.
MC	Mohr-Coulomb parameter.
MCF	Marked correlation function.
MLC	Mechanically long crack.
MPSS	Maximum plastic shear strain range fatigue indicator parameter.
MSC	Microstructurally small crack.
N_α	Total number of active slip systems.

N_{FOR}	Portion of fatigue life due to fatigue crack formation (nucleation and microstructurally small crack growth).
N_{MLC}	Portion of fatigue life due to mechanically long crack growth.
N_{PSC}	Portion of fatigue life due to physically small crack growth.
PSB	Persistent slip band.
PSC	Physically small crack.
ψ	Helmholtz free energy.
R	Stress/strain ratio of maximum to minimum load.
RVE	Representative volume element.
SVE	Statistical volume element.
T	Temperature.
τ^{α}	Resolved shear stress for slip system α.
UMAT	User Material Subroutine.
VHCF	Very high cycle fatigue life.

SUMMARY

A novel microstructure-sensitive extreme value probabilistic framework is introduced to evaluate material performance/variability for damage evolution processes (*e.g.*, fatigue, fracture, creep). This framework employs newly developed extreme value marked correlation functions (EVMCF) to identify the coupled microstructure attributes (*e.g.*, phase/grain size, grain orientation, grain misorientation) that have the greatest statistical relevance to the extreme value response variables (*e.g.*, stress, elastic/plastic strain) that describe the damage evolution processes of interest. This is an improvement on previous approaches that account for distributed extreme value response variables that describe the damage evolution process of interest based only on the extreme value distributions of a single microstructure attribute; previous approaches have given no consideration of how coupled microstructure attributes affect the distributions of extreme value response. This framework also utilizes computational modeling techniques to identify correlations between microstructure attributes that significantly raise or lower the magnitudes of the damage response variables of interest through the simulation of multiple statistical volume elements (SVE). Each SVE for a given response is constructed to be a statistical sample of the entire microstructure ensemble (*i.e.*, bulk material); therefore, the response of interest in each SVE is not expected to be the same. This is in contrast to computational simulation of a single representative volume element (RVE), which often is untenably large for response variables dependent on the extreme value microstructure attributes.

This framework has been demonstrated in the context of characterizing microstructure-sensitive high cycle fatigue (HCF) variability due to the processes of fatigue crack formation (nucleation and microstructurally small crack growth) in polycrystalline metallic

alloys. Specifically, the framework is exercised to estimate the local driving forces for fatigue crack formation, to validate these with limited existing experiments, and to explore how the extreme value probabilities of certain fatigue indicator parameters (FIPs) affect overall variability in fatigue life in the HCF regime. Various FIPs have been introduced and used previously as a means to quantify the potential for fatigue crack formation based on experimentally observed mechanisms. Distributions of the extreme value FIPs are calculated for multiple SVEs simulated via the FEM with crystal plasticity constitutive relations. By using crystal plasticity relations, the FIPs can be computed based on the cyclic plastic strain on the scale of the individual grains. These simulated SVEs are instantiated such that they are statistically similar to real microstructures in terms of the crystallographic microstructure attributes that are hypothesized to have the most influence on the extreme value HCF response. The polycrystalline alloys considered here include the Ni-base superalloy IN100 and the $\alpha + \beta$ Ti alloy Ti-6Al-4V. In applying this framework to study the microstructure dependent variability of HCF in these alloys, the extreme value distributions of the FIPs and associated extreme value marked correlations of crystallographic microstructure attributes are characterized. This information can then be used to rank order multiple variants of the microstructure for a specific material system for relative HCF performance or to design new microstructures hypothesized to exhibit improved performance. This framework enables limiting the (presently) large number of experiments required to characterize scatter in HCF and lends quantitative support to designing improved, fatigue-resistant materials and accelerating insertion of modified and new materials into service.

CHAPTER I

INTRODUCTION

1.1 Motivation

Failure of engineered components due to repeating or random cycles of applied loading and unloading (*i.e.*, fatigue) can be catastrophic and associated with the loss of life. Moreover, fatigue failure of components is costly in terms of loss in productivity and equipment. As such, extensive resources have been devoted to increase the understanding and mitigation of such failures. In particular, much effort has been devoted to characterizing the fatigue response and the scatter in fatigue life for specific material systems. Understanding the scatter in the number and magnitude of applied stress cycles before component failure (*i.e.*, fatigue life) is essential to ensure that inspection and/or replacement intervals can be confidently specified.

Despite the resources expended yearly to prevent fatigue failures, they still occur regularly. For example, on July 2, 2006 a high pressure turbine disk (HPT) failed in a General Electric CF6-80C2 engine mounted on an American Airlines Boeing 767-223 that was sitting on the ground in Los Angeles, California during a routine engine test [1]. As shown in Figure 1.1 the HPT turbine split into four pieces due to a rim-to-bore fracture that originated from an intergranular fatigue crack.

Current methods and models that characterize variability of fatigue response are predominantly empirical in nature. Such empirical approaches are material-specific and require extensive experimentation. In addition, little is understood regarding the effects of randomness of the underlying microstructure on the overall variability in the fatigue response. The ability to estimate variability of fatigue response using physically-based computational models to augment traditional experimental approaches has great potential for

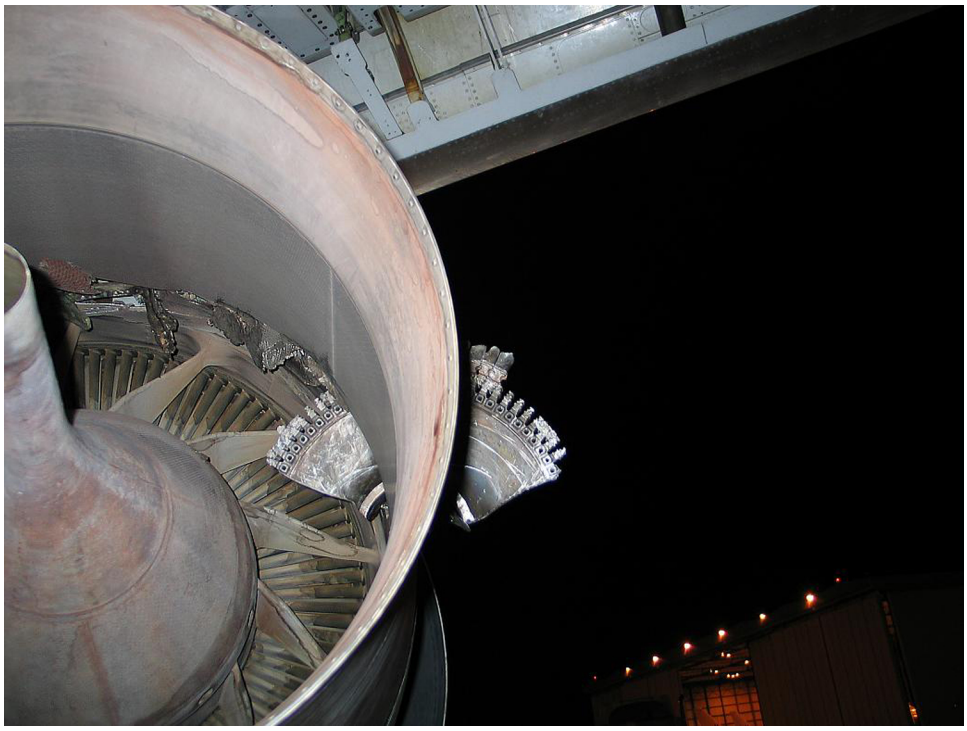

(a)

(b)

Figure 1.1: Failure of high pressure turbine (HPT) disk in an American Airlines Boeing 767-223. (a) Piece of HPT disk lodged in left engine's exhaust duct on opposite side of aircraft from failed engine. (b) Failed engine cut in two at the HPT module with front and rear sections of the engine hanging from the respective engine mounts [2].

accelerating insertion of materials and assisting in design of minimum life. In addition, such tools can aid in the development of materials with improved fatigue resistance and better determine inspection and replacement intervals to prevent failures.

1.2 Problem statement

In high cycle fatigue (HCF) where stress amplitudes remain below the effective yield point, fatigue crack formation (*i.e.*, nucleation and early growth) depends on certain extremal attributes of the microstructure. For example, both second phase inclusions with the highest stress concentration or largest size or the largest grains favorably oriented for slip can serve as likely nucleation sites for fatigue cracks. The probability of finding these attributes near the free surface or in a highly stressed volume also influences the variability in fatigue crack formation [3]. Hence, variability in fatigue life is related largely to the probabilities of finding extremal attributes that are relevant to the operant mechanisms of fatigue crack formation in a given material system. Moreover, the critical life limiting microstructure attributes can consist of multiple interacting attributes that together increase the local driving forces for fatigue crack formation more than any single independent attribute for a given volume. Therefore, in certain material systems the interactions between microstructure attributes are more important to the processes of fatigue crack formation then is the existence of any single attribute. This phenomena can also be dependent upon loading/operating conditions.

The dependence of fatigue crack formation on various microstructure attributes has been investigated extensively. In many cases, this dependence cannot merely be deduced from direct quantitative image analysis of various microstructure attributes. Assessment of the coupling of microstructure attributes with the driving forces for fatigue crack formation requires a combination of experiments and computational simulation, along with a connective framework based on extreme value statistics. Such a framework presently exists only in rudimentary form (*e.g.*, Weibull statistics [4] of fatigue strength and/or microstructure

attributes). Owing to microstructural stochasticity, HCF is a statistical problem for which the probability of fatigue crack formation in a particular volume of material is established by the extreme value (*i.e.*, rare event) probability of a particular existing combination of microstructure attributes that conspire with applied stress state in such a way to form and propagate cracks. Coupling of attributes with loading conditions and the resulting fatigue response is the main source of both scatter and size effects in fatigue. Moreover, multiple specimens or components will exhibit a significant scatter in the fatigue response even when they are manufactured from identically processed material. Much progress has been made in understanding the mechanisms of fatigue crack formation in various material systems in the last few decades [5, 6]; however, much remains to be understood concerning both the short and long range correlations between microstructure attributes and cyclic inelastic stress-strain response in the microstructure and how such correlations play a role in affecting the variability of fatigue life.

For most applications, large numbers of experiments are necessary to quantify variability in fatigue life and to identify any change in the mechanism of fatigue crack formation as a function of applied loading conditions for a given specimen size. Often, insufficient experimental data are available to support this quantification. Moreover, the mathematical form of the tails of the probability distributions for the driving forces for fatigue crack formation, such as the local distributions of stress/strain, are not well characterized, nor is the dependence of the character of those tails on single and/or interacting microstructure attributes well understood.

1.3 Research objective

This dissertation introduces and demonstrates a novel extreme value probabilistic framework to characterize the microstructure-dependent variability for damage evolution processes (*e.g.*, fatigue), and identify the important microstructure attributes or coupled microstructure attributes that drive the variability of damage evolution processes. Specifically,

the objectives of the developed probabilistic framework as depicted in Figure 1.2 are to:

1. Identify the shape and character of the tails (*i.e.*, extreme value) of the distribution of damage response (for a given damage evolution process) for given loading and boundary conditions.

2. Link extreme value distributions of damage response to the local microstructure attributes that most influence the distribution of that response. Moreover, it is desired to determine how the shape and character of the extreme value response distributions change depending on microstructure.

3. Account for the coupling between multiple microstructure attributes relative to their combined influence on the distributions of extreme value damage response. In other words, quantify the statistical influence of the interactions between certain key microstructure attributes on the extreme value response distributions.

By satisfying these objectives, the developed framework provides a probabilistic description of the microstructure-sensitive extreme value damage evolution processes that can then be used to estimate microstructure-dependent variability, identify microstructure attributes that are important to the considered damage evolution process, and compare or rank different materials or variants of the same material for a given loading condition or application. Additionally, this framework is designed to provide a better understanding of the tails of the probability distributions for various damage evolution processes, including the shape of the tails of these distributions and the sensitivity to variations in loading history, microstructure, and specimen size (critically stressed volume).

The development of this microstructure-sensitive extreme value framework has required the consideration of several secondary research objectives including:

- The development of new statistical functions that link correlated microstructure attributes to extreme value response.

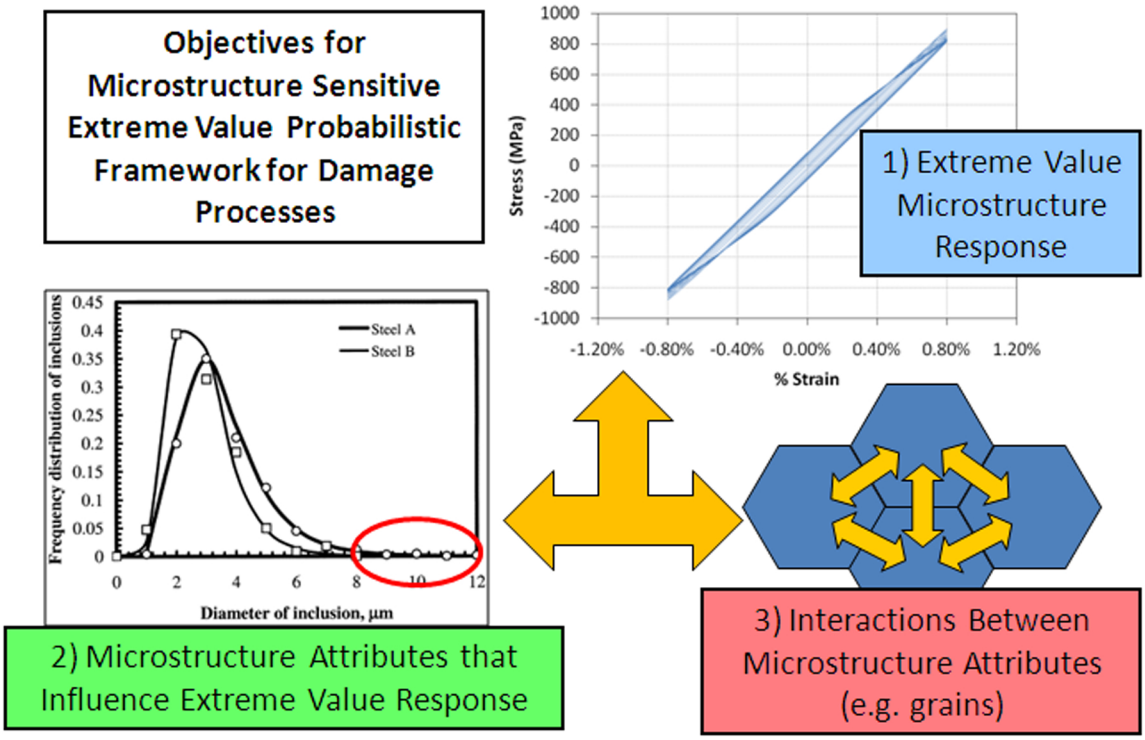

Figure 1.2: Schematic of the objectives of the developed microstructure-sensitive extreme value probabilistic framework for damage evolution processes. Note that the plot of the inclusion size was reproduced from Atkinson and Shi [3] (Reprinted from [3], with permission, copyright Elsevier).

- The development of algorithms for the instantiation and simulation of microstructure volume elements representative of real materials that can be utilized to computationally estimate the distributions of extreme value response via simulation.
- The development of robust and efficient algorithms to exercise constitutive models to predict material behavior on the scale of the microstructure attributes most important to the damage response.

Here each one of these secondary research objectives will be outlined in more detail.

1.3.1 Development of statistical functions that link microstructure to extreme value response

To link the extreme value microstructure-dependent response for damage evolution processes to stochastic microstructure, new statistical functions are required. Although various statistical functions have been used extensively to quantify and describe random heterogeneous materials (*e.g.*, [7]) or extreme value distributions of response, they have rarely been used to link the two. A primary objective here has been to develop new statistical measures and correlation functions that are able to quantify the coupling between extreme value response and the associated microstructure attributes that most influence that response.

1.3.2 Instantiation and simulation of microstructure volume elements

To understand and quantify the influence of various microstructure attributes on the damage response, a knowledge of the stress and strain fields around the microstructure attributes important to the considered damage evolution processes is required; however, such information is not typically available experimentally, especially in three dimensions. Thus, the developed framework incorporates a strategy where damage response is estimated computationally using experimentally calibrated constitutive models. Simulation of material microstructure is not trivial and there is much ongoing research on this topic (*cf.* [8, 9]). In this work, some of the challenges associated with simulating the microstructure-dependent response are considered including:

- The development of simple efficient algorithms for generation of statistically representative microstructure volume elements for simulation.

- The evaluation of how boundary conditions and meshing influence the predicted extreme value response of simulated microstructure volume elements.

- The determination of how many simulated microstructure volume elements of a given size are required to characterize the tails of the distributions of extreme value response for a given loading condition.

1.3.3 Robust and efficient constitutive models

Although the developed microstructure-sensitive extreme value probabilistic framework is broadly applicable for a myriad of material systems and damage evolution processes, here it is used to characterize the extreme value high cycle fatigue (HCF) response in polycrystalline metals. As such, polycrystalline plasticity models implemented in a FEM package are used to estimate the elastic-plastic response at the scale of the grains for material volumes subjected to cyclic loads. As exercising the developed microstructure-sensitive extreme value probabilistic framework requires the simulation of hundreds of microstructure volume elements, it is a primary objective to improve the efficiency of these algorithms and the implementation of these algorithms in an automated fashion. Thus, the computational efficiency and stability of polycrystal plasticity codes is considered as well as the development of pre and post processing algorithms to automate consecutive simulation runs.

1.4 Significance of this research

It is envisioned that the development of this microstructure-sensitive extreme value probabilistic framework will have several primary consequences, namely:

- A first of its kind methodology will be available that links coupled microstructure attributes to the distributions of extreme value response.

- A procedure will be identified by which variability of microstructure-dependent damage evolution processes like fatigue can be evaluated computationally and ranked for different materials and different variants of the same material.

- This methodology will aid in the evaluation of critical damage evolution processes in complex material systems and be able to quantify the key correlated microstructure attributes that have the greatest influence on the variability of material response.

- Computational tools and algorithms will be available to generate and simulate volumes of material microstructure. Additional tools will be available to aid in characterizing complex microstructural statistics and correlation functions and automate the pre and post-processing of hundreds of simulated microstructure volume elements.

- Application of this framework to evaluate the microstructure-sensitive extreme value fatigue response of the Ni-base superalloy IN100 and the Ti alloy Ti-6Al-4V offers new insight to the influence that the local microstructure in these material systems has on the variability of HCF response. In particular, the combinations of crystallographic attributes that have the most influence on the driving forces for fatigue crack formation in these material systems are identified.

- An alternative to traditional empirical modeling will be available to evaluate microstructure-dependent variability for various damage evolution processes like fatigue. However, unlike the empirical models, this framework will offer insight about the coupled microstructure attributes that most influence the variability of damage response and direct materials design of new microstructures more resistant to variability. Additionally, information will be available to help better understand the microstructure-dependence of the mechanisms of fatigue crack formation and propagation.

1.5 Dissertation structure

Following this introduction, this dissertation will be laid out as follows. Chapter two will discuss the current understanding of fatigue crack formation in metals with particular emphasis the use of certain fatigue indicator parameters to estimate the driving forces for fatigue crack formation. Chapter three will discuss the current models available to estimate the influence of extreme value (*i.e.*, rare event) microstructure attributes on the fatigue response. Additionally, a novel extreme value marked correlation function will be introduced that quantifies the coupling between correlated microstructure attributes and the extreme value response. Chapter four will review large strain based crystal plasticity theory. Several continuum scale internal state variable (ISV) models formulated to simulate cyclic plasticity in polycrystalline aggregates will be considered including the Ni-base superalloy IN100 and the Ti alloy Ti-6Al-4V. Implementation of these types of ISV models in typical commercially available finite element codes along with the integration of the constitutive relations at a material point will be considered. Chapter four will discuss the challenges addressed in this work regarding the simulation of fatigue response at the microscale including the instantiation and simulation of microstructure volume elements including meshing and applying appropriate boundary conditions. Also of interest are the issues concerned with the simulation of representative versus statistical volume elements. Chapters six and seven will discuss the application of the developed microstructure-sensitive extreme value probabilistic framework in IN100 and Ti-6Al-4V, respectively. In particular, the relationships between the extreme value distributions of the driving forces for fatigue crack formation and newly introduced extreme value marked correlation functions will be considered for the respective material systems. In Chapter eight, the applicability of the microstructure-sensitive extreme value probabilistic framework to computational materials design will be discussed. This dissertation will then end with the conclusions and recommendations for future work that will be given in chapter nine.

CHAPTER II

METAL FATIGUE

2.1 Introduction

Chapter 2 reviews the mechanisms of fatigue crack nucleation and growth in metals. Of particular interest is how microstructure influences the processes of crack formation (*i.e.*, nucleation and early growth). The different mechanisms of nucleation and growth will be classified based on the scales of the microstructure attributes (*i.e.*, phase, grain orientation/misorientation, *etc.*) pertinent to these damage evolution processes. The mechanics of fatigue crack formation will also be addressed including the use of fatigue indicator parameters (FIP) to estimate the nonlocal driving forces of fatigue crack formation.

2.2 Fatigue Damage Mechanisms in Metals

Different damage processes govern the changing regimes of fatigue crack nucleation and growth in polycrystals and various classifications have been used to describe them. Forsyth [10] classified two regimes of crack nucleation and growth. The first, Stage I, describes the processes of shear-dominated fatigue crack growth, which is typically characterized by cracks whose size is on the scale of the dominant microstructural barriers (*e.g.*, grain/phase boundaries); accordingly, cracks form and propagate along the directions of the maximum shear planes. Subsequent Stage II growth is normal stress-dominated such that cracks propagate normal to the direction of the maximum principal cyclic stress [11, 12]. Stage II cracks are typically much larger than the dominant microstructural barriers and are minimally affected by these barriers. Various alloys differ according to the extent to which they exhibit these two stages, with some transitioning to Stage II growth almost immediately [13, 14].

Another proposed classification of the various mechanisms of fatigue crack nucleation and growth defines distinct regimes based on the change of mechanisms as the fatigue cracks and cyclic plastic zones increase in size relative to the scale of the dominant microstructure attributes [11, 12, 15, 16]. Using this microstructure-scale dependent decomposition, the regimes of nucleation and growth can be categorized as follows:

1. Fatigue crack formation, which includes the processes of fatigue crack nucleation and microstructurally small crack (MSC) growth for cracks up to the size of one to three microstructural barrier spacings

2. Physically small crack (PSC) growth for cracks up to the size of three to ten microstructural barrier spacings

3. PSC and mechanically long crack (MLC) growth with size greater than about ten microstructural barrier spacings

Accordingly, the total fatigue life N_T can be expressed as

$$N_T = N_{FOR} + N_{PSC} + N_{MLC} \tag{2.1}$$

where N_{FOR}, N_{PSC}, and N_{MLC} correspond to the number of cycles required for formation, PSC growth, and MLC growth, respectively. Although this classification distinguishes between distinct mechanisms of fatigue crack nucleation and growth, it is somewhat difficult to unambiguously define transitions between the various mechanisms and regimes. However, describing the processes based on the spacing of the dominant microstructural barriers is logical as the modes of nucleation and growth change based on the size of the developing cracks relative to these barrier spacings. This classification scheme will be used throughout the remainder of this dissertation.

2.2.1 Fatigue Crack Formation

Fatigue crack formation describes the processes of crack nucleation and MSC growth. Fatigue crack nucleation encompasses classical slip band nucleation or other decohesion or micro-fracture processes. Cracks form within the microstructure as a result of damage accumulation associated with irreversible dislocation migration under cyclic loading. Such conditions exist even when the stresses are well below the macroscopic yield strength of the material due to strain localization. Strain localization might occur, for example, in grains that are favorably oriented for plastic flow, in grains neighboring harder oriented grains, or near inhomogeneities such as harder second phase particles or inclusions. Additionally, many materials have pre-existing microvoids or aggregated vacancies/voids as artifacts from processing, which become sites of strain localization.

In metals subjected to cyclic plastic straining, the formation of distinct dislocation structures like persistent slip bands (PSBs) are associated with fatigue crack nucleation, which occurs either within PSBs or at interfaces such as grain or phase boundaries [5]. Surface grains are particularly vulnerable to formation of PSBs or the development of extrusions and intrusions because of more localized slip activity near the surface, assisted kinematically by the lack of constraint of the free surface. These extrusions and intrusions are one mechanism for crack nucleation, particularly in pure metals as can be seen in Figure 2.1. Once sufficiently developed, these extrusions and intrusions lead to the nucleation of cracks that will propagate and eventually lead to fracture during subsequent cycling.

Internal damage due to cyclic plastic strain accumulation can also form cracks. In Figures 2.2-2.3, intragranular slip bands are observed. Cracks form at the boundaries, as indicated in these figures by the arrows, due to the damage caused by heterogeneous plastic flow. Figure 2.4 shows the nucleation of a crack at the site of a debonded inclusion. These and other mechanisms are manifested in various material systems due to differing phases, impurities, texture, *etc.* In practical alloy systems, cracks can form at grain/phase boundaries due to impingement of slip. Often, nonmetallic particles introduced during

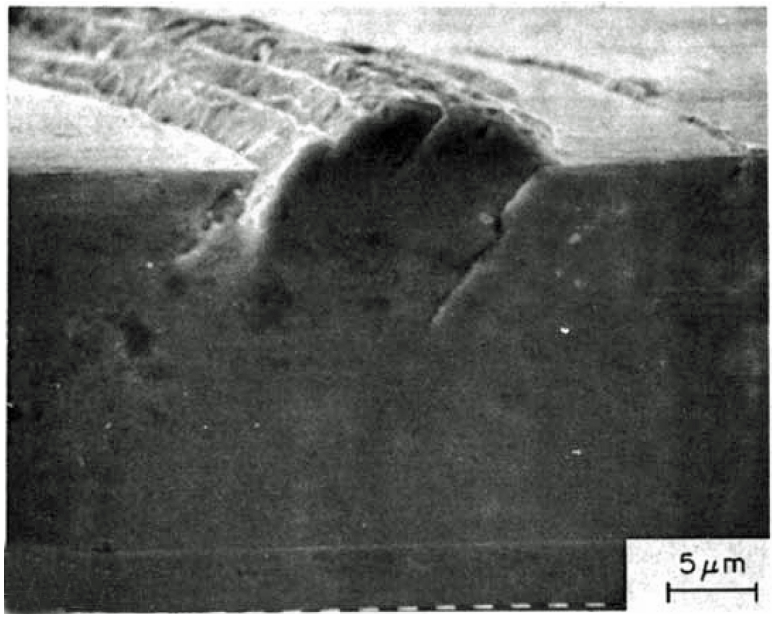

Figure 2.1: Fatigue crack formation at a PSB in a copper crystal fatigued at 60000 cycles at 0.002 strain at 20°C (Reprinted from [17], with permission, copyright Elsevier).

processing are sites for fatigue crack formation. Across the spectrum of various alloy systems used in engineering applications a plethora of mechanisms can drive fatigue crack nucleation and early growth.

MSCs are defined as cracks having size and/or crack tip cyclic plastic and damage process zone sizes on the scale of the dominate microstructural barriers such as grain/phase size or precipitate size/spacing [11, 12]; moreover, MSCs are often surrounded by a zone of relatively significant cyclic plastic deformation relative to the crack size. However, the damage process zone of MSCs is relatively small and confined to a crack tip zone that is increasingly well characterized by singular fields of fracture mechanics as these cracks lengthen [21]. MSCs interact strongly with local microstructure attributes as they grow, and their growth rates vary greatly depending on the strength of barriers that they encounter. MSCs typically have lengths up to three or four grain diameters [11,12] and have a tortuous front. In many cases, these MSCs may be arrested by a sufficiently strong barrier such as a grain or phase boundary [11, 12, 22–25]. In contrast, once cracks reach a certain length (typically on the order of several grain sizes) their growth rate is less sensitive to details of

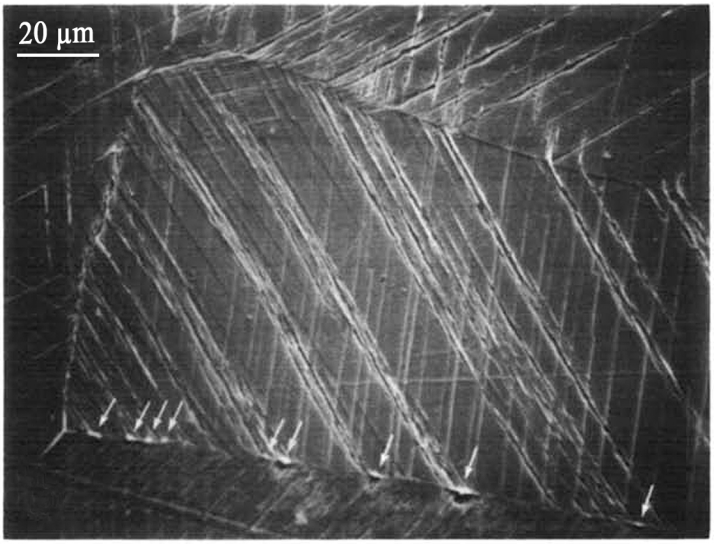

Figure 2.2: Fatigue crack formation (indicated by arrows) along a grain boundary in copper (Reprinted from [18], with permission, copyright Elsevier).

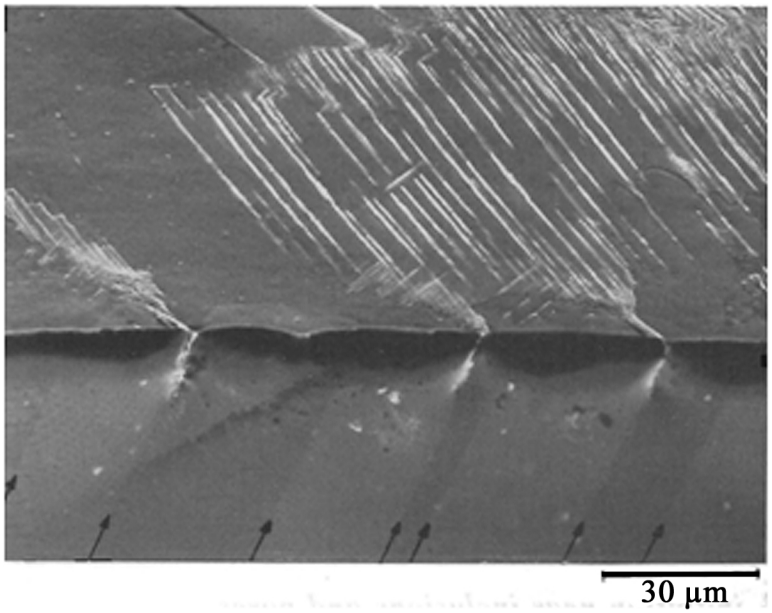

Figure 2.3: Fatigue crack formation along every other twin boundary (indicated by arrows) in polycrystalline Cu at room temperature. (Reprinted from [19], with permission, copyright Pergamon)

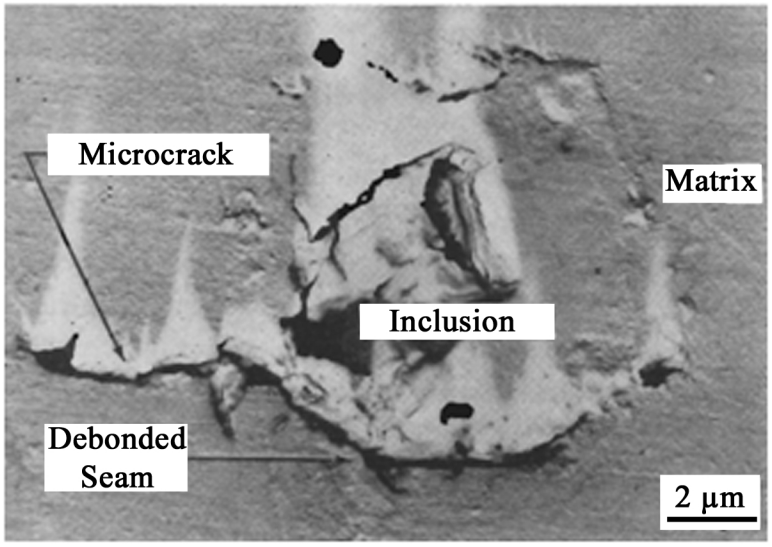

Figure 2.4: Fatigue crack formation at site of a partially debonded MnO-SiO_2- Al_2O_3 inclusion in matrix of 4340 steel (denoted by M) (Reprinted from [20], with permission, copyright Springer).

the inhomogeneity field as more microstructure is sampled across the crack front [26], and the probability of intermittent bypass of microstructural barriers is enhanced. Generally, MSC growth is considered to be most appropriately modeled by correlation with the cyclic crack tip displacement range, ΔCTD [6, 23, 27, 28].

Various modeling approaches have been applied to simulate fatigue crack nucleation and MSC growth. One class of models where the fatigue cracks are represented by continuously distributed dislocations have been developed to model small cracks in both isotropic materials [29, 30] and in anisotropic crystalline materials [31–34]. Idealized models of fatigue crack formation in single crystals have also been developed by Mura and Nakasone [35], Mura [36], Venkataraman *et al.* [37, 38], and Repetto and Ortiz [39], but are not applicable to the scale of analysis of polycrystals (and related multislip characteristics). More recently, Serebrinsky and Ortiz [40] have developed cohesive-laws that account for the number of cycles required for fatigue crack nucleation with applicability to finite element simulations of more complex (*i.e.*, realistic) microstructures. Additionally, Brinckmann and Van der Giessen [41] introduced a computational framework that uses both dislocation dynamics and cohesive surfaces to model near atomic separation that leads to crack

nucleation. Although in their infancy, such efforts are helping to shed light on the processes of fatigue crack nucleation and MSC growth, which are very difficult to detect or observe experimentally.

2.2.2 Physically Small and Mechanically Long Crack Growth

Mechanically long cracks (MLCs) are sufficiently large relative to the size of the dominant microstructural features and crack tip plastic zone size such that they can be characterized via linear elastic fracture mechanics (LEFM) (particularly in the high cycle fatigue or HCF regime). LEFM was first applied to crack growth by Paris [42], who linked the emerging field of fracture mechanics to cyclic fatigue through a power law relationship between average crack advance per cycle and the range of stress intensity factor, ΔK, *i.e.*,

$$\frac{da}{dN} = C_1 \Delta K^m \tag{2.2}$$

where C_1 and m are material constants.

Similar to MLCs, physically small cracks (PSCs) are typically larger than the spacing between dominant microstructural barriers, but are not so large that their growth is unaffected by the crack tip plastic zone that influences crack closure. Thus, although PSCs may be amenable to LEFM they are often better characterized via elastic-plastic fracture mechanics (EPFM), especially at higher amplitudes of applied stress. EPFM as an alternative to ΔK was first presented by Lamba who applied the ΔJ-integral to elastic-plastic fatigue crack growth [43]. Crack tip opening displacement principles of EPFM can effectively capture the behavior of PSCs but must be modified to account for the distribution of slip among the grains which also affects the scale of crack tip plasticity [21]. In the case of the PSC and MLC growth regimes, fatigue life is modeled in terms of the growth of a single dominant crack by an appropriate cyclic fracture mechanics parameter (*e.g.*, ΔK or ΔJ) along with the corresponding material constants and loading parameters (*e.g.*, stress/strain ratio, R, of minimum to maximum loads). These damage tolerant approaches, which only consider the

growth of a single dominate flaw, have been reviewed in more detail elsewhere [5, 44].

2.2.3 LCF, HCF and VHCF

Damage progression in uniaxial fatigue may be classified into two or three categories depending on the stress amplitude (and R) relative to the material yield strength. Under completely reversed loading, low cycle fatigue (LCF) is characterized by cyclic stresses well above the yield point. Plastic flow is uniformly distributed among the grains, and fatigue life is largely determined by the material's ability to resist propagation of cracks in the presence of extensive crack tip plasticity. In LCF, small fatigue cracks are uniformly distributed, resulting in a more homogeneous response, and fatigue life is dominated by multi-site crack propagation and coalescence. In contrast, completely reversed HCF is typically categorized by peak cyclic stresses well below the macroscopic yield strength and fatigue life is dominated by fatigue crack nucleation and MSC growth. In HCF the material response is dominantly elastic; however, local yielding occurs in grains that are favorably oriented for slip and in regions near grain boundaries, triple junctions, inclusions or inclusion clusters. Local cyclic slip is highly heterogeneous in HCF and the life is determined by the *weakest link* microstructure attribute(s) from which a single dominant flaw forms and/or propagates.

Traditionally, fatigue lives beyond 10^6 to 10^7 cycles were considered run-outs or infinite life, but many current engineering applications require fatigue lives up to 10^8 cycles and beyond. For example, the Engine Structural Integrity handbook [45], which contains the published standards for the United States Air Force to guide original equipment manufacturers, now requires lifetimes of 10^9 cycles for certain aircraft turbine engine components. In the past, fatigue lives in this range have been difficult to measure due to experimental limitations, but ultrasonic fatigue testing has enabled high frequency tests that can be carried out in a reasonable time frame [46]. Recent observations indicate that although some materials have a plateau around 10^6 cycles, the S-N curve then continues to decrease at

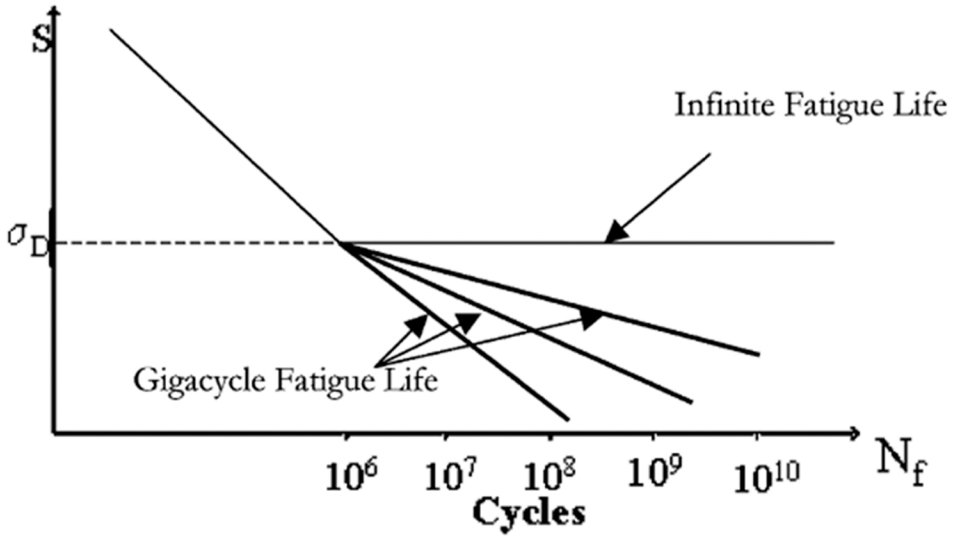

Figure 2.5: The concept of infinite fatigue life is questioned when experiments with fatigue lives greater than 10^6 cycles are considered (Reprinted from [49], with permission, copyright Elsevier).

higher numbers of cycles [47, 48]; this recently categorized fatigue regime (*i.e.*, above 10^6 cycles) is sometimes referred to as very high cycle fatigue (VHCF) or gigacycle fatigue (see Figure 2.5).

In this work, fatigue crack formation is considered in the HCF and VHCF regimes. The majority of HCF or VHCF lifetime is often spent in the crack formation regime. For example, in a Ti-6Al-4V alloy, it has been observed that up to 85% of the total HCF life is spent nucleating and growing a crack up to a detectable flaw size [50]. PSC and MLC regimes typically comprise a very small fraction of component life, particularly in the HCF regime. As the focus here will be on on HCF and VHCF, this work will emphasize crack formation and will not consider PSC and MLC growth.

2.2.4 Fatigue Crack Formation and Polycrystalline Microstructure

In this dissertation, we are primarily concerned with how the crystallographic attributes of the microstructure (*e.g.*, grain orientation, grain disorientation, grain size, and grain shape distributions) affect local driving forces for fatigue crack formation and early growth in

HCF. In general, plastic strain inhomogeneity at the grain level in polycrystals subjected to cyclic loading is directly linked to crystallographic texture. Winter *et al.* [51] observed that plasticity occurs preferentially in grains having slip systems with high Schmid factors, with slip localized within slip bands. Using crystal plasticity simulations to calculate distributions of cyclic slip in polycrystals, Bennett and McDowell [52] demonstrated that distributions of slip could be quite heterogeneous in HCF. This heterogeneity is directly related to complex interactions between grains of differing orientations. Sauzay and Jourdan [53] explored these types of interactions between grains by computationally characterizing the distributions of elastic stress fields around small grain clusters at the free surface using elastic FE simulations. They predicted that grain interactions could affect the local resolved shear stress by as much as 16% in copper and austenitic steels depending on the local orientations of the neighboring grains. Inhomogeneity of elastic stress fields corresponds to localization of plastic strain in regions of stress concentration associated with the jump of the elastic stiffness across grain boundaries and compatibility requirements of the polycrystal. Specifically, the effects of local crystallography (*e.g.*, phase, grain orientation, grain misorientation, grain topology, *etc.*) are considered here.

2.3 Mechanics of Fatigue in Polycrystals

Understanding the mechanical response of metallic polycrystals subjected to cyclic loads is essential for modeling fatigue crack formation and growth. In polycrystals, at low enough applied strain amplitudes, the stress-strain curve will stabilize after an initial transient period to a response for which no additional plastic strain will accumulate after subsequent cycles. This stabilization of the stress-strain curve is termed elastic or plastic shakedown. The elastic shakedown limit is the applied stress or strain amplitude below which no continued accumulation of plastic strain occurs; whereas, the cyclic plastic shakedown limit is the strain amplitude below which only reversed cyclic plastic straining will occur within the microstructure. If the plastic shakedown limit is exceeded, ratcheting will occur where

plastic strains continue to accumulate over subsequent cycles. These shakedown limits depend on R of the applied stress or strain. In terms of the plastic strain tensor, the ratcheting strain can be defined as

$$\left(\Delta\epsilon_{ij}^{p}\right)_{ratch} = \left(\epsilon_{ij}^{p}\right)\Big|_{end\ of\ cycle} - \left(\epsilon_{ij}^{p}\right)\Big|_{beginning\ of\ cycle} \tag{2.3}$$

where the cyclic plasticity is defined as the change in plastic strain over a cycle or

$$\left(\Delta\epsilon_{ij}^{p}\right)_{cyc} = \left(\Delta\epsilon_{ij}^{p}\right)_{max}\Big|_{over\ the\ cycle} - \left(\Delta\epsilon_{ij}^{p}\right)_{ratch} \tag{2.4}$$

Elastic shakedown, cyclic plasticity (plastic shakedown) and ratcheting are all depicted in Figure 2.6. To correctly model fatigue in polycrystals these phenomena must be accounted for via polycrystalline numerical simulations. In HCF in particular, the regimes of cyclic plasticity and ratcheting are of great interest as a function of applied stress state, stress amplitude and mean stress.

2.3.1 Fatigue Indicator Parameters

Crystallographic fatigue crack formation in ductile polycrystalline metals under multiaxial loading conditions generally is associated with a critical plane on which the cyclic plastic shear strain is maximum under proportional loading (*i.e.*, components of principal stress tensor vary in constant proportion to one another over the stress cycle) [13, 14]. Accordingly, fatigue indicator parameters (FIP) have been established relative to the criteria that define these critical planes. In the HCF regime, the material is nominally elastic, which has led to the introduction of stress-based parameters for correlation of fatigue crack initiation. For example Findley [54] proposed the HCF stress-based parameter

$$P_F = \tau_a + k_F\sigma_{n,\max} \tag{2.5}$$

where $\tau_a = \Delta\tau_{\max}/2$ is the maximum allowable alternating shear stress and $\sigma_{n,\max}$ is the stress normal to the plane of maximum alternating shear stress. The constant k_F accounts

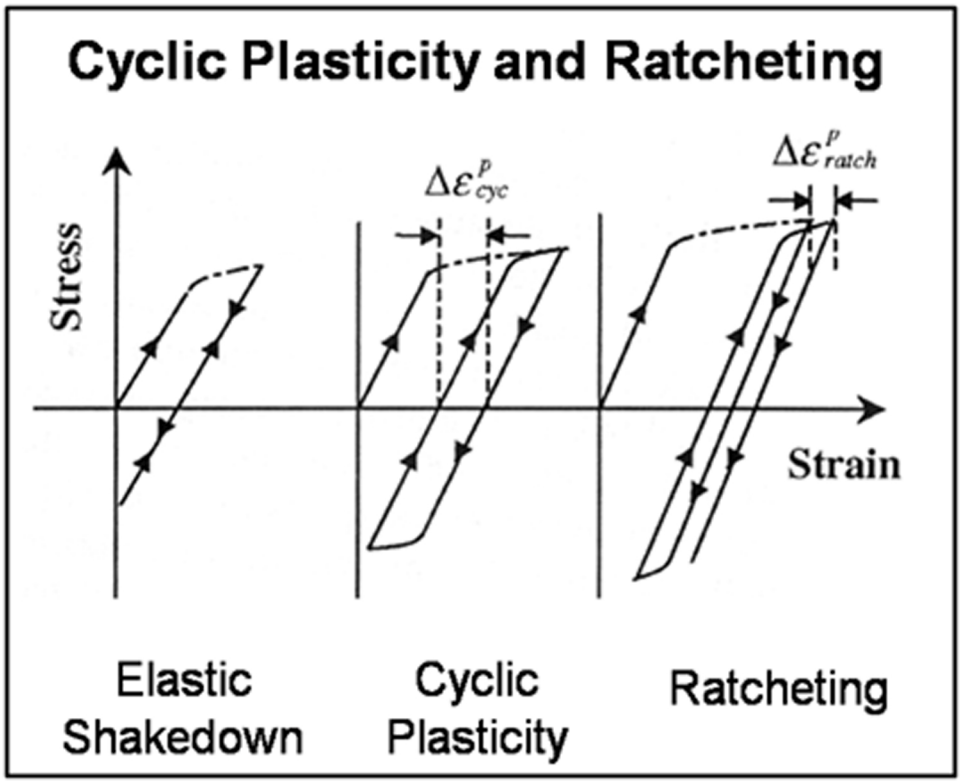

Figure 2.6: Schematic stress-strain curves depicting shakedown, cyclic plasticity and ratcheting in an arbitrary volume of material.

for the influence of the range in the stress normal to the plane of maximum shear. The value of P_F is constant for a given fatigue life. Both Dang Van [22] and Papadopoulos [55–57] have applied versions of the Mohr-Coulomb (MC) parameter at the grain scale, *i.e.*,

$$P_{MC} = \tau_a + k_{MC}\sigma_{hyd} \tag{2.6}$$

which is constant for a given fatigue life. Here, σ_{hyd} is the hydrostatic stress and k_{MC} is a material constant. This parameter originally was used to predict behavior in soils or other similar granular materials [58], and is assumed to be related to fatigue by the observations of the influence of normal stress on decohesion of PSBs, or the opening of microstructurally small stage I cracks in shear. Socie has argued, however, that peak hydrostatic stress likely does not directly influence crack initiation [14]. Papadopoulos *et al.* [59] compared several such stress-based fatigue indicator parameters (FIPs), demonstrating varying degrees of effectiveness.

Strain-life approaches have been applied mainly in the low cycle and transition fatigue regimes. However, when one considers microplasticity (distributed plasticity in the microstructure), they are attractive from a fundamental perspective even in HCF where localized plastic flow controls fatigue crack formation and crack propagation [6, 16]. Strain-life approaches were initiated by Coffin [60] and Manson [61], who independently proposed characterizing fatigue life based on plastic strain amplitude. A power law relation of average plastic strain amplitude $\Delta\epsilon_p/2$, with the number of cycles for fatigue crack initiation (formation plus small crack growth to some predefined size) has been established as

$$\frac{\Delta\epsilon_p}{2} = \epsilon'_f (2N_F)^c \tag{2.7}$$

where ϵ'_f is the fatigue ductility coefficient and c is the fatigue ductility exponent [62].

Critical plane plastic strain-based FIPs have also been developed that consider plastic cyclic straining as the primary driving force for fatigue crack nucleation and early growth. The simplest of these parameters based on the observation that fatigue cracks initiate on

planes of maximum plastic shear for multiaxial loading conditions is the maximum cyclic plastic shear strain range (MPSS) FIP, *i.e.*,

$$P_{MPSS} = \frac{\Delta\gamma_{p,max}}{2} \tag{2.8}$$

where $\Delta\gamma_{p,max}$ is the maximum change in the plastic shear strain range over a cycle, which can be calculated directly from the ordered principal plastic strain ranges over a cycle, $\left(\Delta\epsilon_i^p\right)_{cyc}$ for $i = 1, 2, 3$, according to

$$\Delta\gamma_{p,max} = \left| \frac{\left[\left(\Delta\epsilon_1^p\right)_{cyc} - \left(\Delta\epsilon_3^p\right)_{cyc}\right]}{2} \right| \tag{2.9}$$

Fatemi and Socie [63] and Fatemi and Kurath [64] proposed a parameter that also accounts for the maximum plastic shear strain range as well as the affect of the stress normal to the plane of maximum plastic shear, *i.e.*,

$$P_{FS} = \frac{\Delta\gamma_{p,max}}{2}\left(1 + k_{FS}\frac{\sigma_{n,\max}}{\sigma_o}\right) \tag{2.10}$$

where $\sigma_{n,\max}$ is the maximum stress normal to the plane of the maximum plastic shear strain range $\Delta\gamma_{p,max}$. The stress normal to the plane of maximum plastic shear strain range $\sigma_{n,max}$ promotes slip plane decohesion and subsequent crack nucleation and microstructurally small crack growth. The parameter described by k_{FS} is a material constant. The reference stress σ_o used to normalize $\sigma_{n,max}$ is typically the yield strength σ_y. The larger magnitudes of Fatemi-Socie (FS) FIP indicate a higher driving force for fatigue crack formation. The FS parameter has been used to correlate fatigue damage formation over a large number of grains for a range of multiaxial loading conditions for materials with extended Stage I dominant regions such as IN718 and 1045 steel [14, 65].

Although many of these FIPs were originally applied at the macroscale, several workers have applied these parameters at the microscale using crystal plasticity simulations.

For example, Bennett *et al.* [66] correlated microslip and mixed-mode behavior of microstructurally small crack growth to the MC and FS FIPs and demonstrated that they distribute differently over the grains; moreover, the FS parameter correlated better with distributions of microcracks within the grains. Bennett *et al.* [52] also used the MC and FS parameters to explore local grain orientation distribution effects on microslip in HCF. Other workers [67, 68] observed good agreement between the locally applied FS parameter (determined using crystal plasticity calculations) and microstructurally small crack growth within the first few grains with experiments in structural steel S460N. Additionally, Dunne *et al.* [69] used detailed simulations coupled with experiments to show that crystal plasticity can correlate precisely to localized plastic slip (and subsequent fatigue crack initiation) in realistic microstructures. More recently Findley and Saxena [70] used the FS parameter to examine the effect microstructure attributes such as grain size have on the local driving forces for fatigue damage formation. Such work demonstrates the ability of locally applied FIPs determined via crystal plasticity simulations to correlate microstructural scale slip with fatigue crack formation and microstructurally small crack growth. As argued by McDowell [6], these types of critical plane approaches for shear-dominated microcracking is related to Stage I propagation of MSCs. Early work by Hoshide and Socie [71] considered the affect of microplastic strain on fatigue damage formation and MSC crack growth under mixed-mode (I-II) loading via FEM simulations. They correlated ΔJ from EPFM via a Paris type law with fatigue crack growth behavior of small cracks. Moreover, Hoshide and Socie related ΔJ to the ranges of crack opening displacement (COD) and/or crack sliding displacement (CSD) for mode I and mode II, respectively. Later, McDowell and Berard [65] using ΔJ argued for similarity of ΔCTD with the FS parameter.

2.4 Summary

In polycrystalline metals, the mechanisms that accommodate cyclic straining in fatigue have been investigated extensively over the past several decades. Different regimes of

fatigue crack growth are observed depending on the size of the crack relative to the prevailing microstructural barriers (*e.g.*, grain/phase boundaries) within the material. Microstructurally small cracks have size/length on the order of the barrier spacing between dominate microstructural features; growth of microstructurally small cracks strongly depends on local microstructure attributes near the crack tip. Larger cracks are less sensitive to individual microstructure attributes at the crack tip since they sample considerable numbers of barriers within the zone of crack tip plastic deformation. The formation of distinct dislocation structures such as persistent slip bands can lead to fatigue damage formation both on external surfaces and/or in subsurface grains depending on the strain amplitudes and material system being considered; moreover, some material systems exhibit multiple mechanisms of fatigue damage formation that change depending on the strain amplitude (*i.e.*, the high cycle fatigue (HCF) regime versus the very high cycle regime (VHCF) fatigue regime). When there is significant fatigue life associated with the fatigue crack formation regime, scatter in the overall fatigue life is extremely dependent on how the mechanisms of fatigue crack formation are influenced by variations in local microstructure.

Stress and strain based fatigue indicator parameters (FIPs) derived based on experimental observations have been developed to capture the mechanics of fatigue response. Although stress based FIPs have been used with some success, fatigue crack formation is driven by plasticity on the scale of the dominant microstructural barriers even in HCF. As such, various plasticity based critical plane FIPs have been demonstrated to capture the mechanisms of fatigue crack nucleation and microstructurally small crack growth such as the Fatemi-Socie (FS) FIP. These types of FIPs have been computed over nonlocal volumes at the microscale to study the relative influence of local microstructure attributes like inclusions, grains, phases, *etc.* on the local driving forces for fatigue crack formation.

CHAPTER III

EXTREME VALUE PROBABILITIES OF FATIGUE

3.1 Introduction

Variability of fatigue response is primarily due to the extreme value probabilities of existing microstructure attributes (*i.e.*, phase, grain orientation/misorientation, inclusions, *etc.*) most important to the operant mechanisms of crack formation. Chapter 3 reviews the microstructure-dependent scatter of fatigue life in metals and the current methods used to characterize this variability. To offer the appropriate context for some of the extreme value approaches discussed and used in this dissertation, extreme value probability theory is first briefly reviewed. Classical statistical models are then considered that characterize variability of fatigue response. These models tend to be empirical and based on extensive experimentation; they do not consider microstructure explicitly. More recent approaches have been introduced that are based on the distributions of a single microstructure attribute; however, the scatter in fatigue life in many advanced engineering alloys is dependent on the distributions of multiple coupled interacting microstructure attributes. Moreover, many of these approaches lack any clear connection between the extreme value response and the microstructure attributes that most influence that extreme value response. Next, various methods of characterizing the microstructure of random heterogeneous materials is considered. The coupling of multiple microstructure attributes is well described by correlation functions. The use of these correlation functions to characterize material microstructure is briefly reviewed. Finally, a novel extreme value marked correlation function is introduced to describe the influence of coupled microstructure attributes on extreme value response. The newly introduced extreme value marked correlations are based on previously developed marked correlation functions that link correlated microstructure attributes with

mean value response. In contrast to these previously introduced marked correlation functions, these extreme value marked correlation functions correlate coupled microstructure attributes with extreme value response.

3.2 Extreme value statistics

The statistics of extremes or *extreme value statistics* refers to the class of probability problems that consider the extreme values (*i.e.*, largest and/or smallest) of multiple sets of random variables. Gumbel developed much of the early theory and application of the statistics of extremes in his seminal work [72]. In what follows, an understanding of the basic terms of probability theory are assumed (*e.g.*, random variable, population, sample, probability density, cumulative distribution, *etc.*) Such terms are readily defined in any standard text on probability theory (*e.g.*, [73]).

Assuming that X is a random variable that is associated with a known cumulative distribution function $F_X(x)$, the maximum extreme value of a sample from X of size n can be defined as

$$Y_n(y) = \max(X_1, X_2, \ldots, X_n) \tag{3.1}$$

If it is required that Y_n is less than some value y, than all the random variables in the same sample associated with Y_n must also be less than y. The cumulative distribution function of Y_n is defined as the probability that for a sample of size n, Y_n is less than or equal to y, *i.e.*,

$$F_{Y_n}(y) \equiv P(Y_n \leq y) = P(X_1 \leq y, X_2 \leq y, \ldots, X_n \leq y) \tag{3.2}$$

If it is assumed that $X_1, X_2, \ldots, X_n$ are statistically independent and identically distributed, *i.e.*,

$$F_{X_1}(x) = F_{X_2}(x) = \cdots = F_{X_n}(x) = F_X(x) \tag{3.3}$$

the cumulative distribution function F_{Y_n} is related to F_X according to

$$F_{Y_n}(y) = [F_X(y)]^n \tag{3.4}$$

Thus, the maximum extreme value will also be a random variable and have an associated distribution (*cf.*, [72, 74, 75]). A distribution function for the minimum extreme values can be constructed in a similar manner. The probability density function corresponding to the cumulative distribution function of the extreme maximum value is given by

$$f_{Y_{\max}}(y) = \frac{\partial F_{Y_{\max}}(y)}{\partial y} = n\,[F_X(y)]^{(n-1)}\, f_x(y) \tag{3.5}$$

Extreme value statistics are a subset of the more general discipline of order statistics [72, 74–76]. The r^{th} order statistic can be defined as the r^{th} member of a sequence of random variables $(X_1, X_2, \ldots, X_n)$ from a sample of size n arranged in order of increasing magnitude, *i.e.*, $X_{1:n} \leq X_{2:n} \leq X_{n:n}$. Assuming these variables to be independent and identically distributed, the distribution function of $X_{r:n}$, which relates to the probability that the r^{th} order statistic is smaller than or equal to x, can be expressed as

$$F_{X_{r:n}}(x) = P(X_{r:n} \leq x) = \sum_{k=r}^{n} \left(\begin{array}{c} n \\ k \end{array} \right) [F_X(x)]^k\, [1 - F_X(x)]^{(n-k)} \tag{3.6}$$

Here the binomial coefficient is defined as

$$\left(\begin{array}{c} n \\ k \end{array} \right) = \begin{cases} \frac{n!}{k!(n-k)!} & \text{if } 0 \leq k \leq n \\ 0 & \text{otherwise} \end{cases} \tag{3.7}$$

Assuming the population of the initial variate is absolutely continuous, the probability density function is

$$f_{X_{r:n}}(x) = r \left(\begin{array}{c} n \\ k \end{array} \right) [F_X(x)]^{(r-1)}\, [1 - F_X(x)]^{(n-r)}\, f_x(x) \tag{3.8}$$

Equations 3.6 and 3.7 reduce to Equations 3.4 and 3.5, respectively, when $r = k$ (*i.e.*, $X_{n:n} = Y_n$). These types of order statics can be used to explore the probabilities of having a

certain number of exceedances over a specified value or threshold.

The characteristics of extreme value statistics have been explored in some detail. The extreme value cumulative distribution function and probability density functions shift to the right (*i.e.*, increasing magnitudes of y) with increasing sample sizes (*i.e.*, increasing n). This is shown in Figure 3.1 for the exponential cumulative distribution function and exponential probability density function, *i.e.*,

$$F_X(x) = 1 - e^{-\lambda x} \tag{3.9}$$

and

$$f_X(x) = \lambda e^{-\lambda x}, \text{ for } x \geq 0 \tag{3.10}$$

The parameter λ used to plot Equations 3.9 and 3.10 in Figure 3.1 was set to unity. As the sample size n becomes large, the distributions described by Equations 3.4 and 3.5 above have been observed in some cases to converge to certain limiting distributions or asymptotic distributions.

A method to derive analytical forms of the asymptotic extreme value distributions (*i.e.*, as $n \to \infty$) was proposed by Cramer [77]. Following his methodology, a transformed random variable ξ_n can be defined for the random variable Y_n, *i.e.*,

$$\xi_n = n\left[1 - F_X(Y_n)\right] \tag{3.11}$$

Using this transformed variable, it can be shown that (*cf.* [74, 77])

$$F_{\xi_n}(\xi) = P(\xi_n \leq \xi) = 1 - \left(1 - \frac{\xi}{n}\right)^n \tag{3.12}$$

Taking the limit as $n \to \infty$ of the right hand side of the previous expression yields

$$\lim_{n\to\infty}\left(1 - \frac{\xi}{n}\right)^n = \exp(-\xi) \tag{3.13}$$

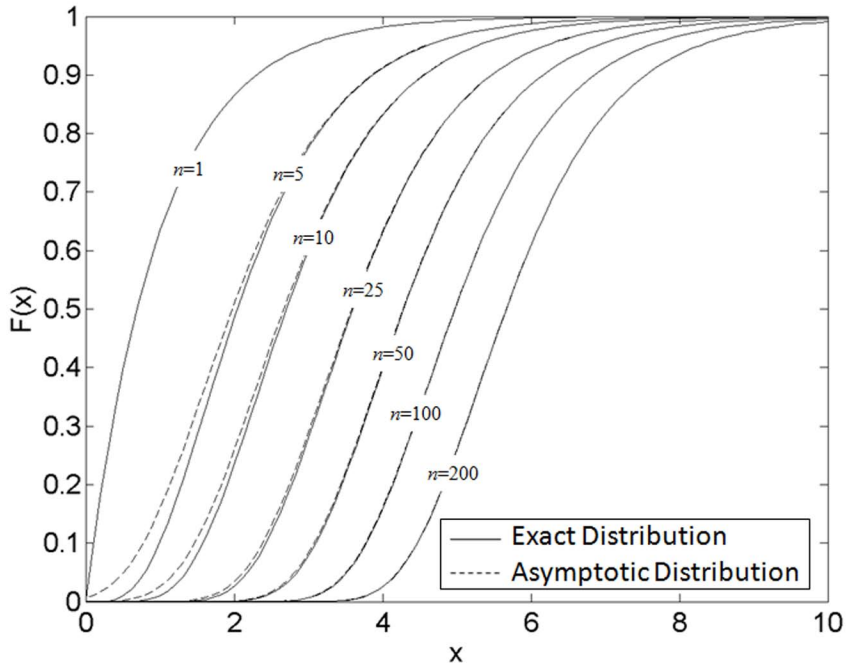

(a)

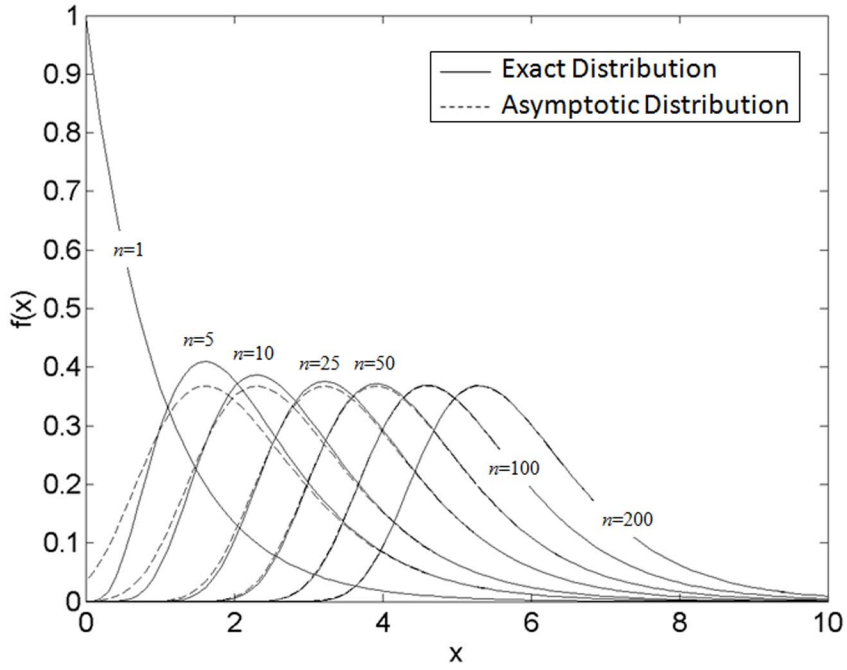

(b)

Figure 3.1: The exact and asymptotic extreme value distributions for several different sample sizes n taken from the exponential distribution function for the (a) cumulative probability function, and (b) the probability density function.

or as $n \to \infty$

$$F_{\xi_n}(\xi) = 1 - \exp(-\xi) \tag{3.14}$$

The corresponding asymptotic probability density can be expressed as

$$f_{\xi_n}(\xi) = \exp(-\xi) \tag{3.15}$$

Inverting Equation 3.11 results in

$$Y_n = F_X^{-1}\left(1 - \frac{\xi_n}{n}\right) \tag{3.16}$$

Therefore for sufficiently large sample sizes n, the asymptotic distribution of Y_n may be determined from that of ξ_n as given in Equations 3.14 and 3.15 for the cumulative distribution function and probability density function, respectively, based on the relationship given in Equation 3.16. In this manner, it can be observed that ξ_n decreases as Y_n increases, *i.e.*,

$$P(Y_n \leq y) = P\{\xi_n < n[1 - F_X(Y_n)]\} \tag{3.17}$$

Therefore, the cumulative distribution function of Y_n can be determined from that of ξ_n according to

$$F_{Y_n}(y) = 1 - F_{\xi_n}\{n[1 - F_X(Y_n)]\} = \exp\{-n[1 - F_X(Y_n)]\} \tag{3.18}$$

The associated probability density function is given as

$$f_{Y_n}(y) = -\frac{d\{n[1 - F_X(Y_n)]\}}{dy} \exp\{-n[1 - F_X(Y_n)]\} \tag{3.19}$$

For example, Cramer's method can be applied to derive the analytical form of the asymptotic extreme value distribution for the previously introduced exponential distribution defined by Equations 3.9 and 3.10. In this case, Equation 3.11 can be expressed as

$$\xi_n = n\{1 - [1 - \exp(-\lambda Y_n)]\} = n\exp(-\lambda Y_n) \tag{3.20}$$

Therefore, the asymptotic extreme value cumulative probability function and probability density are given by

$$F_{Y_n}(y) = \exp[-n\exp(-\lambda y)] \tag{3.21}$$

and

$$f_{Y_n}(y) = n\lambda\exp(-\lambda y)\exp[-n\exp(-\lambda y)] \tag{3.22}$$

respectively. These asymptotic forms for the exponential distribution are also plotted in Figure 3.1 for several different sample sizes n.

For distributions of a single variable, it has been shown that there are only three types of non-degenerated distributions to which the extreme value distributions can converge for large n [75, 78]. The three possible non-degenerated asymptotic distributions for the maximum extreme value distributions can be expressed as:

1. Gumbel (Type I):

$$F^I_{Y_n}(y) = \exp\left[-e^{-\alpha_n(y-u_n)}\right] \tag{3.23}$$

2. Fréchet (Type II):

$$F^{II}_{Y_n}(y) = \exp\left[-\left(\frac{v_n}{y}\right)^k\right] \tag{3.24}$$

3. Weibull (Type III):

$$F^{III}_{Y_n}(y) = \exp\left[-\left(\frac{\omega - y}{\omega - w_n}\right)^k\right] \text{for } z \leq \omega \tag{3.25}$$

For the Gumbel distribution, u_n is the characteristic largest value of the initial variate X and α_n is an inverse measure of dispersion of Y_n. The number of samples of the initial variate X in the set of distributions of X from which Y_n is sampled is n. For the Fréchet distribution,

v_n is the characteristic largest value of the underlying variable X and k is a shape parameter or inverse measure of the dispersion. In the Weibull distribution, ω is the upper bound of the initial variate X (*i.e.*, $F_X(\omega) = 1$), w_n is the characteristic largest value and k is the shape parameter. The extreme value asymptotic distribution for the maxima of the exponential distribution derived previously and given in Equation 3.21 was of Type I. The desire is to characterize a dataset as belonging to one of these three types of distributions so that mathematical properties can be used to better understand the data.

There are similar forms of these asymptotic distributions to which the minimum extreme value distributions can converge. The important implications of these limiting asymptotic distributions, as summarized by Castillo [75], are as follows:

- Only these three distributions can occur as asymptotic distributions for maxima of independent trials for distributions of a single random variable.
- There are specific mathematical tests that can be applied to the distribution of the initial variate (*i.e.*, $F_X(x)$) to determine if the distribution of the extremes associated with the distribution of the initial variate $F_{Y_n}(y)$ will converge onto one of the three known asymptotic distributions.
- There exists certain distributions that will not converge onto one of these three asymptotic distributions or which degenerate as the sample size n goes to infinity; however, such distributions rarely occur in practice.
- A distribution of the initial variate with a non-finite end-point in the tail in the direction of the desired extreme cannot converge to a Weibull type asymptotic distribution.
- A distribution of the initial variate with a finite end-point in the tail in the direction of the desired extreme cannot converge to a Fréchet type asymptotic distribution.

Defining the limiting or asymptotic character of the distribution of the initial variate is not always trivial, especially when the distribution of the initial variate itself is unknown.

Strategies to estimate the character of the extreme value distributions when the distribution of the initial variate is unknown using probability papers and various least-squares methods have been described [75]. Additionally, the tails of distributions that converge in a specific manner are known to be fit by specific asymptotic extreme value distributions. The tails of distributions that converge exponentially are described by the Gumbel or Type I extreme value distributions. Both the maximum and minimum tails of the normal (*i.e.*, Gaussian) distribution that has an exponential term converge exponentially. Distributions with a polynomial tail in the direction of the extremes are described by the Fréchet or Type II distribution. A log-normal distribution is an example of a distribution whose maximum tail converges to a Type II maximum extreme value distribution. The Weibull or Type III distributions describe the tails of distributions that are bounded. Thus, if the convergence of the tails of a distribution is known, then in some cases the asymptotic extreme value distribution that describes those tails can be inferred.

In this work, the focus is on the extreme value statistics of various material response parameters and correlations between the microstructure attributes associated with the regions of extreme value response. Thus, some type of multivariate extreme value framework is required. Work has also been done to mathematically define multivariate extreme value statistics [75, 79]. However, due to the increased complexity, the application of multivariate extreme value statistics has been limited. A method will be proposed in Section 3.5 that utilizes importance sampling to selectively sample the microstructure correlation functions at regions of observed extreme value behavior to couple single variate extreme value statistics with special marked correlation functions with minimum added complexity.

3.3 Microstructure-dependent scatter of fatigue life

In most advanced metallic polycrystalline alloys, significant scatter is observed in the overall fatigue life. Much of this scatter is directly related to the stochastic microstructure. For example, Marines *et al.* observed a transition in fatigue mechanisms between 10^6 and 10^7

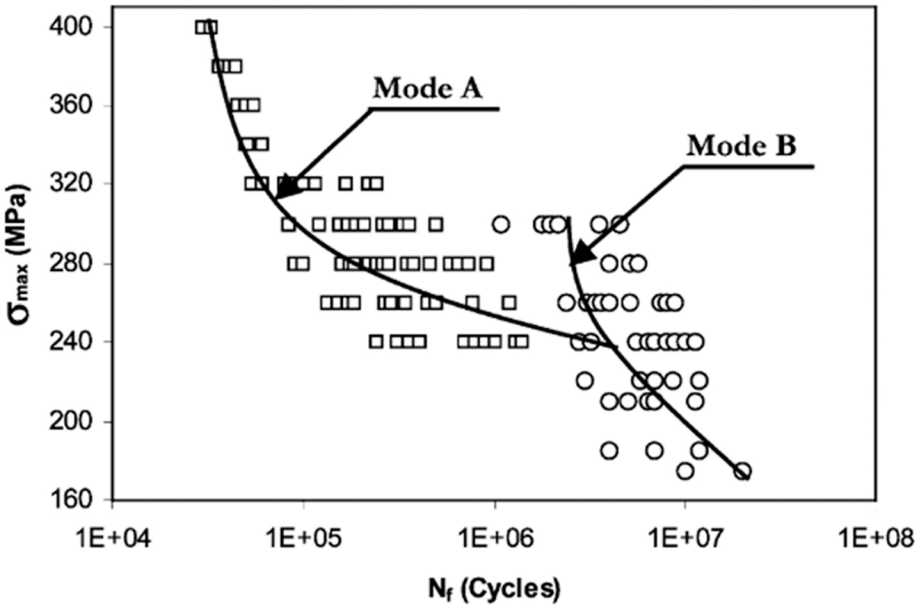

Figure 3.2: S-N curve for Al 2024-T3 (R=0.1), exhibiting two distinct failure modes depending on the number of cycles at failure (Reprinted from [49], with permission, copyright Elsevier).

cycles in aluminum alloys [49]. In the Al 2024-T3, life limiting cracks in samples that exhibited fatigue lives with fewer numbers of cycles were observed to form at broken inclusions, but in samples with longer fatigue lives, the life limiting crack were observed to form at PSBs near the surface (see Figure 3.2). The transition region in this material system where these competing mechanisms were observed, appears to exhibit a much higher scatter in the overall fatigue life than either the LCF or VHCF regimes. A transition from surface to subsurface fatigue crack initiation between 10^6 and 10^9 cycles has also been observed in titanium alloys [80]. Ravi Chandran and Jha [81] reported that two competing mechanisms of fatigue damage formation were observed in Ti-10V-2Fe-3Al. The probability of ultimate failure was shown to relate to the probably of clusters of primary α existing at the surface. Shorter lives were observed if these primary α clusters exist at the specimen surface than if they did not. Monte-Carlo simulations based on Poisson defect statistics supported these observations. Jha *et al.* [82] observed a dramatic increase in the overall scatter in fatigue life as lives increased from LCF to VHCF in Ti-6246 as can be seen in

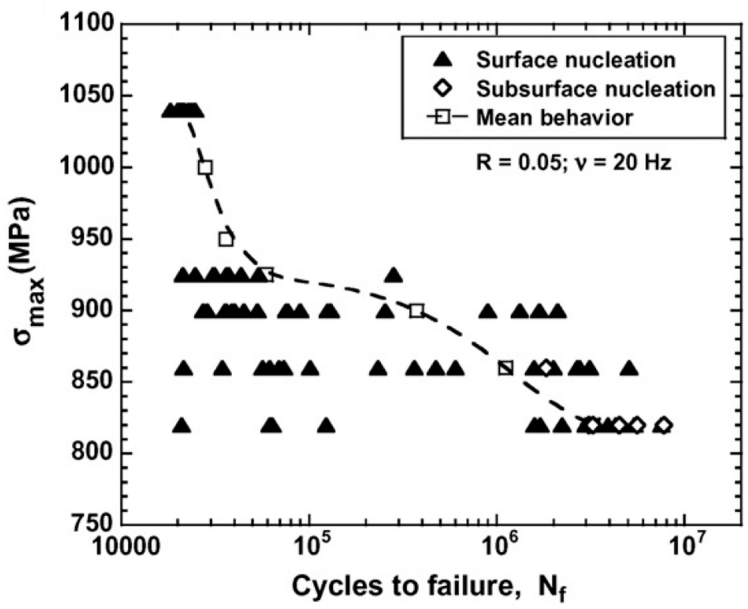

Figure 3.3: The fatigue variability of Ti-6246 characterized from repeated testing at several stress magnitudes showing mean versus life limiting behavior (Reprinted from [82], with permission, copyright Elsevier).

Figure 3.3. Similar observations were made in Ni-base superalloys and are given in Figure 3.4 [82, 83].

There is significant scatter in experimentally measured HCF life because attributes that govern failure lie in the tails (*i.e.*, extreme values) of joint distributions of attributes and responses. For example, if the key feature of the fatigue life in a particular material is determined by the largest inclusion of a certain type, an understanding of the distribution of inclusion sizes in the critically stressed regions would be essential to modeling the fatigue life for that particular material. Additional scatter can also be attributed to competing mechanisms that change depending upon the applied loading conditions.

3.3.1 Empirical probabilistic approaches to estimate fatigue variability

Classical statistical treatments of fatigue variability have primarily been based on large numbers of experiments. The variability of fatigue life is assessed by extensive experimentation to obtain a statistically significant sample. Designers then use these data to predict

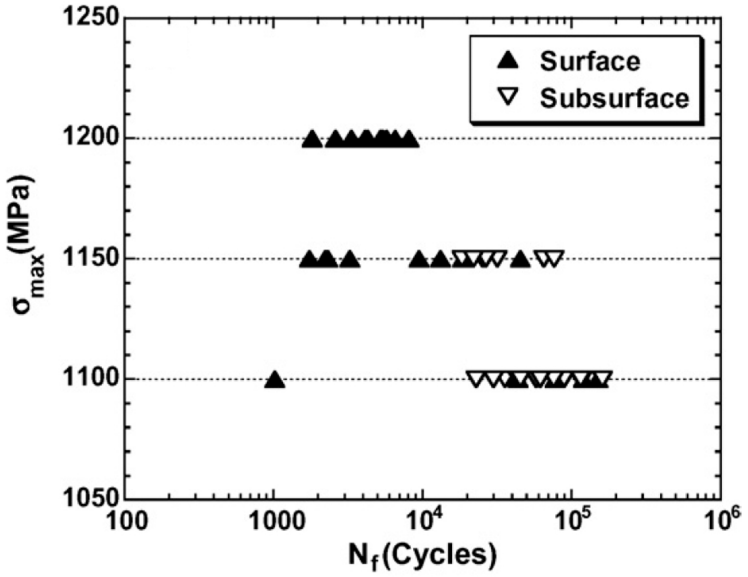

(a)

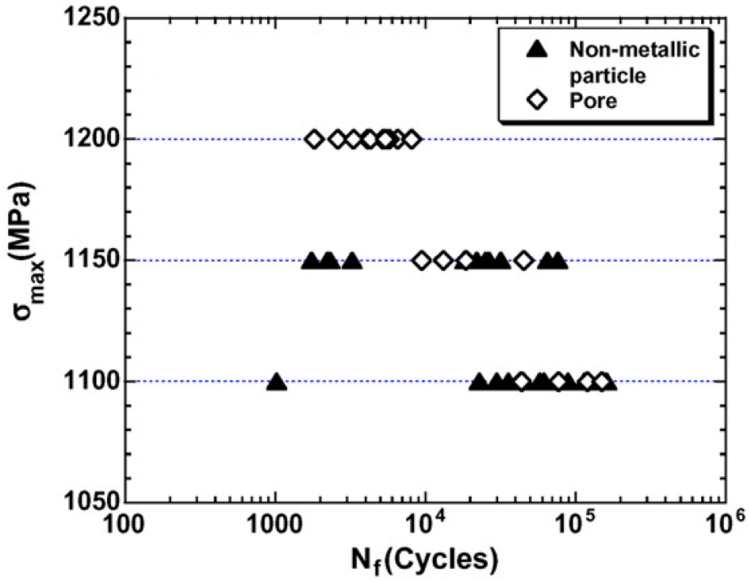

(b)

Figure 3.4: Competing failure mechanisms in a Ni-based superalloy: (a) surface vs. subsurface initiated failures and (b) non-metallic particle vs. void related failures (Reprinted from [82], with permission, copyright Elsevier)

component life with an acceptable level of risk. Such data collection requires significant time and resources and does not necessarily provide understanding of the mechanism(s) involved in dictating variability. In addition, the resulting predictions often change with varying sample sizes. A widely used probability of failure in fracture and fatigue was established by Weibull [4], *i.e.*,

$$P = 1 - \exp\left[-\left(\frac{\sigma_f}{\sigma_o}\right)^{m_w}\right] \tag{3.26}$$

where σ_f is the failure strength normalized by a reference strength σ_o and m_W is the Weibull modulus. The probability of failure P tends to zero if σ_f is small or to unity for high values of σ_f. Thus, P describes the the fraction of samples that will fail below σ_f. This model relies on fitting parameters to experimental data and does not explicitly link variations in the microstructure to variations in component life. Newer microstructure-sensitive probabilistic models have been developed that offer a better description of the variability of fatigue response that are based on the underlying distributions of microstructure attributes important to the processes of fatigue crack formation.

3.3.2 Single variate microstructure-sensitive probabilistic approaches to estimate fatigue variability

There are existing probabilistic methods that utilize single variate distributions of certain microstructure attributes to describe scatter in the fatigue response of metals. For example, in clean steels fatigue strength has been linked to the size of the largest inclusions within a given component or specimen [84]; moreover, various distribution functions describing inclusion size have been utilized to predict the resulting variability of fatigue response. Atkinson and Shi [3] reviewed some of these probabilistic methods.

The first class of models considered are based on the log-normal distribution (or any standard distribution) of the initial variate such as inclusion size (see Figure 3.5). Accuracy of these types of models, however, is limited by the experimental difficulty of correctly capturing the tails of the distribution for inclusion size because of the paucity of extreme

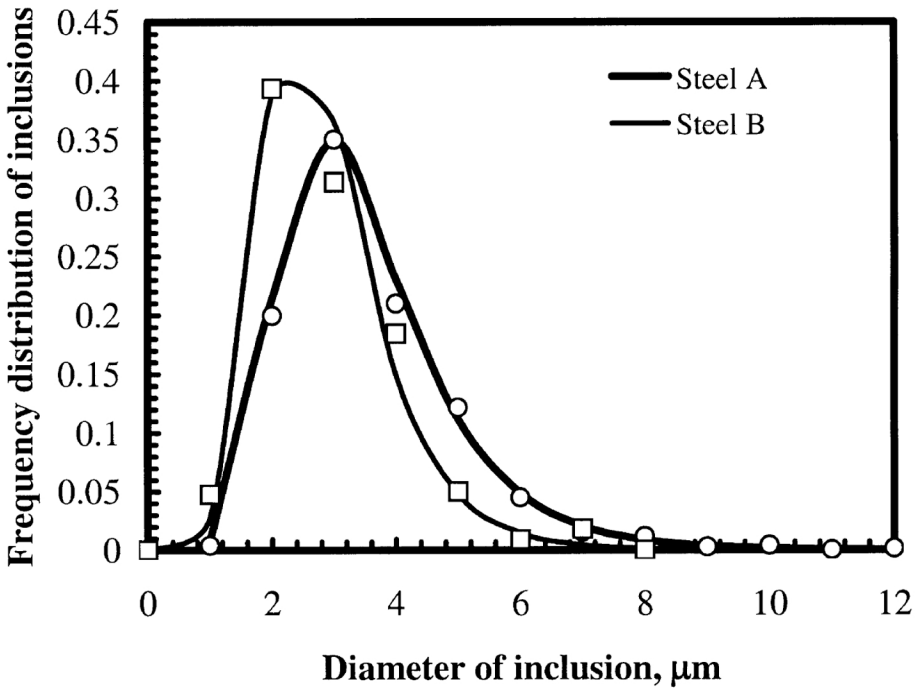

Figure 3.5: Distribution of inclusion diameter in clean steels with extreme value statistics indicated (Reprinted from [3], with permission, copyright Elsevier).

value data. In other words, a good fit of a standard distribution (including the tails) to measurements of the distribution of inclusion size requires measurement of rare events within the tail of the distribution, which is simply not practical in most applications.

The second class of models considered by Atkinson and Shi [3] are based on the extreme value Gumbel distribution. For example, Murakami and coworkers [85, 86] used classical Gumbel extreme value statistics to estimate the size of the largest inclusion based on specimen volume, which was subsequently used to estimate fatigue strength. The lower limit of fatigue strength of high strength steels was estimated as

$$\sigma_w = \frac{d_s\,(H_v + 120)}{\left(\sqrt{A_{max}}\right)^{\left(\frac{1}{6}\right)}} \tag{3.27}$$

where H_v is the Vickers hardness of the steel and A_{max} is the size of the maximum inclusion in the test volume. The experimentally determined parameter d_s accounts for the location of the inclusion relative to the surface and is 1.43, 1.41, or 1.56 depending on whether

the inclusion is on the surface, just below the surface or in the interior, respectively. This class of models has also been used to correlate fatigue crack formation in Al 7050-T7451 based on the maximum pore size and to investigate the fatigue limit of surfaced hardened 1.05Cr-0.23Mo steel alloy based on the maximum flaw size, respectively [87, 88].

The third class of models discussed by Atkinson and Shi [3] are based on the generalized Pareto distribution. The generalized Pareto distribution encompasses the standard family of distributions used to model data expressed in terms of exceedances over some threshold. To apply the generalized Pareto distribution, a predetermined threshold (*e.g.*, maximum inclusion size in this case) must be chosen; making this choice is not trivial. Atkinson and Shi argue that this class of models is more effective than models based on the extreme value Gumbel distribution because it incorporates a limit on the maximum inclusion size. In contrast, the extreme value Gumbel distribution predicts a monotonically increasing inclusion size for increasingly larger volumes.

Although these types of models have been shown to correlate with some experiments, consideration of purely geometric attributes such as largest inclusion size, grain size, or even correlations of nearest neighbor type between attributes is in general insufficient to quantify the scatter in HCF life. The additional attribute(s) of material response (*e.g.*, FIPs as defined Section 2.3.1) coupled with geometric attributes of microstructure provide the coupling necessary to pursue joint statistics of extreme value type that are relevant to minimum life design. Little work has been done to correlate individual microstructure attributes to response.

3.4 Statistical representations of random heterogeneous materials

A *random heterogeneous material* or random medium is defined based on the assumption that any sample of the medium is a realization of a specific random or stochastic process (*i.e.*, random field) [7]. The collection of all possible realizations of the random medium is defined as an *ensemble*. Most materials used in engineering applications can be classified

as random heterogeneous materials including polycrystalline metals. This is particularly true when one considers variations in the material structure of polycrystalline metals on the length scale of microns such as the phases, grains, grain/phase boundaries, inclusions, *etc.* In this dissertation, the attributes on this scale are considered collectively as the material microstructure.

Let Ω be defined as a particular realization (*i.e.*, sample) of the ensemble or point in the sample space represented in three dimensional real space (*i.e.*, $\Omega \in \Re^3$). Let the local state h describe the set of random variables that describe the state of Ω in the neighborhood $N(\vec{x})$ of the material point defined by the position $\vec{x}$ [89–91]. In other words, the local state h describes the physical state of the local structure and the attributes thereof in the neighborhood $N(\vec{x})$. The concept of a neighborhood is introduced because certain material structure variables can only be resolved to some volume about a given material point. For example, to consider the local state described in part by the orientation of the ordered lattice of a crystal, a volume containing a sufficient number of atoms is required to define the ordering of the lattice. The local state is a subset of H or the complete space of all possible local states (*i.e.*, $h \in H$). An example of a local state might consist of a description of the attributes at $N(\vec{x})$ including the phase ϕ and the local lattice orientation of the phase g. In this case, the local state in the neighborhood $N(\vec{x})$ is represented by the ordered set

$$h(\vec{x}) = \{\phi(\vec{x}), g(\vec{x})\} \tag{3.28}$$

Each of the parameters describing the various attributes of the local state (*i.e.*, microstructure attributes) resides in a fundamental set or fundamental zone depending on whether the parameter belongs to a discrete set, or a continuous one. The fundamental set for a two phase medium would be described by $\phi \in \{1, 2\} = \Phi$. The fundamental zone for the respective phases are distinguished by the symmetry subgroup of the phase (*i.e.*, $g \in SO(3)/G_\phi = \Gamma_\phi$ where $SO(3)$ is the special orthogonal group in three-dimensions and G_ϕ is the point symmetry subgroup of the lattice for phase ϕ [92]).

The main goal here is to briefly consider some of the various statistical measures that can be used to describe the distribution of certain local states or attributes of the local state for a given material microstructure. A common description of the local state h is given by the local state distribution function $f(h)$ which here is represented as the probability density of local state h. Thus,

$$f(h)\,dh = \frac{dV_{h|\Omega}}{V_{\Omega}} \tag{3.29}$$

describes the volume fraction of h in Ω. The total volume of Ω is defined by V_{Ω} and $dV_{h|\Omega}$ is the volume of Ω occupied by the local state h. The invariant measure of the local state space is dh ensures each increment of the local state space is weighted equally. The invariant measure has been discussed in more detail by others [91, 93].

Up to this point, no assumptions have been made regarding the size of Ω. If the size of Ω is sufficiently large or if $f(h)$ is averaged over a sufficient number of samples Ω, the local state distribution function will tend to describe the volume fraction of the the local state h for the entire ensemble. The size of Ω will be considered in more detail in Chapter 5.

Although the local state distribution function describes the density of the local state in the material, it does not give any description of the relative locations of any given local state to another. In contrast, various correlation functions have been constructed that describe statistical coupling between various local states or individual attributes of the local state.

3.4.1 Correlation functions

Correlation statistics have been used extensively to characterize random heterogeneous materials. The advantage of correlation statistics over classical single point descriptors like the local state distribution function is that correlation statistics provide information about coupling between local states. A few examples of various correlation functions that have been used to characterize the stochastic microstructure of random heterogeneous materials are

introduced here assuming a discrete tessellation of the local states h and h' for simplicity, *i.e.*,

- The radial distribution probability function can be expressed in terms of its probability density as $R\left(h, h'|r\right)$ such that $R\left(h, h'|r\right) dr$ and is associated with the probability of finding a local state h' within a distance of r to $r + dr$ of local state h in any direction. A schematic of the radial distribution function is given in Figure 3.6 for the arbitrary microstructure attributes β and β' associated with the local states h and h', respectively (*i.e.*, $\beta \in h$ and $\beta' \in h'$) [7].

- The 2-point correlation function can be expressed in terms of its probability density as $f_2\left(h, h'|\vec{r}\right)$ (a subset of n-point correlation functions [7, 94, 95]) and is associated with the probability of finding a randomly positioned vector $\vec{r}$ whose tail lies within the local state h and head lies within local state h' [7, 96, 97]. A schematic of the 2-point correlation function and its description is given in Figure 3.7 for the arbitrary microstructure attributes β and β'.

- The the lineal path correlation function can be expressed in terms of its probability density as $L\left(h, h'|\vec{r}\right)$ as shown schematically in Figure 3.8 for the arbitrary microstructure attributes β and β'. The lineal path correlation function is associated with the probability of finding a vector $\vec{r}$ completely within the local state h if $h = h'$ or the probability that the vector $\vec{r}$ crosses the boundary between the local states h and h' only once if $h \neq h'$ [7, 98, 99].

- The nearest neighbor correlation function can be expressed in terms of its probability density function as $N_n\left(h|r\right)$ such that $N_n\left(h|r\right) dr$ is the probability of finding the n^{th} nearest-neighbor of the local state h that is also associated with the local state h at an arbitrary material point in the range r to $r + dr$ [100–102]. In Figure 3.9 the nearest-neighbor correlation function is depicted for the arbitrary microstructure attributes β and β'.

Using these statistical constructs, the local states or specific attributes of the local states and their interrelationships can be described in great detail. The choice of which correlation function to use to describe the microstructure depends on the local state of interest for the considered material system. Consideration should be given as to the zone of influence and/or anisotropy in the correlation between local states. For example, some correlation functions are better at describing short range interactions between coupled attributes and vice versa (*e.g.* lineal path correlation function versus the 2-point correlation function, respectively). Other correlation functions are directionally independent and insensitive to local anisotropy (*e.g.*, radial correlation function, nearest-neighbor correlation function) or directionally dependent (*e.g.*, 2-point correlation function, lineal path correlation function).

Collection of these types of correlation statistics in real microstructures has traditionally been difficult because of material opacity. In most cases, to completely characterize the microstructure of engineering alloy systems, destructive serial sectioning has been required (*e.g.*, [103–108]). More recent methods based on the use of a synchrotron light source have been able to characterize small volumes of polycrystalline microstructure non-destructively, but such methods are presently possible in only a few locations throughout the world [109–112]. Others have used a synchrotron x-ray source to characterize stress/strain response in situ in three-dimensions in a polycrystal [113, 114]. Additional methods have been developed to characterize microstructures, statistically based on a limited set of planes sectioned at particular orientations. For example, Gao *et al.* [115] demonstrated that multiple oblique section planes cut around a fixed axis could be used to obtain a complete 2-point orientation correlation function in three-dimensions. Thus, the collection of correlation statistics in three-dimensions does not necessarily require a complete three-dimensional dataset. Automation of the measurement of lattice orientation has been particularly helpful in collecting statistical data of the crystallography in polycrystalline materials [116–118].

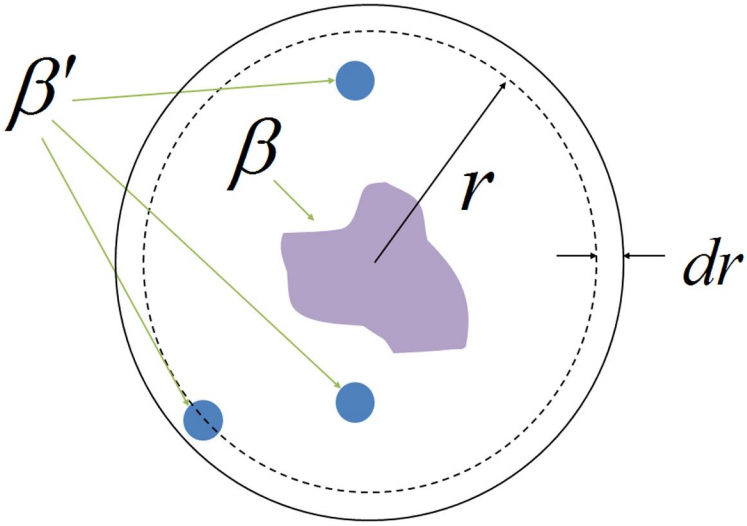

- Radial correlation function:

$$R(\beta, \beta' | r)$$

- Such that $R(\beta, \beta' | r)\, dr$ Is the probability of finding an attribute β and another attribute β' within a distance of r to $r + dr$ in any direction from the first attribute β.

- The radial correlation function has the following property:

$$\lim_{r \to 0} R(\beta, \beta' | r) = f(\beta)\, \delta(\beta - \beta')$$

where $\delta(\beta - \beta')$ is the Dirac delta function.

Figure 3.6: Radial correlation function for the arbitrary microstructure attributes β and β'.

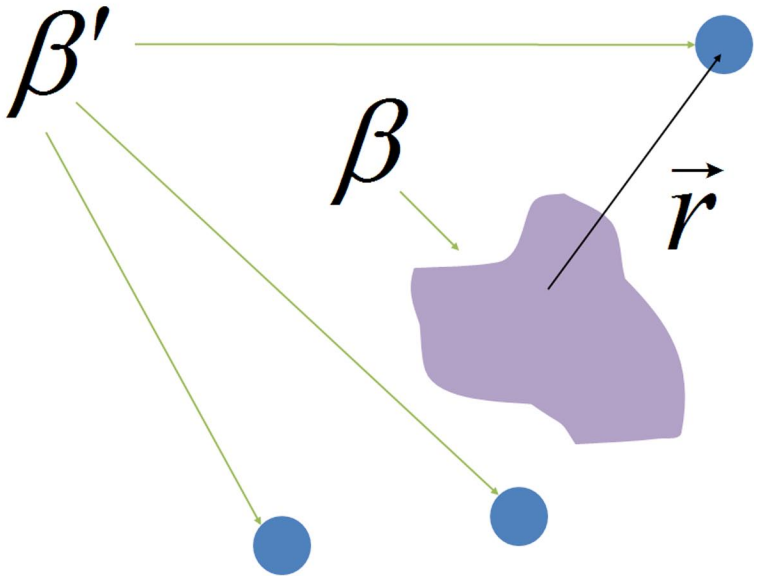

- 2-point correlation function:

$$f_2(\beta, \beta' | \vec{r})$$

- Is the probability of finding a randomly placed vector $\vec{r}$ whose tail falls withing a microstructure attribute β and whose head falls within the microstructure attribute β'.

- The 2-point correlation function has the following properties:

$$\lim_{\vec{r} \to 0} f_2(\beta, \beta' | \vec{r}) = f(\beta)\, \delta(\beta - \beta')$$

$$f_2(\beta, \beta' | \vec{r}) = f_2(\beta', \beta | -\vec{r})$$

where $\delta(\beta - \beta')$ is the Dirac delta function.

Figure 3.7: 2-point correlation function for the arbitrary microstructure attributes β and β'.

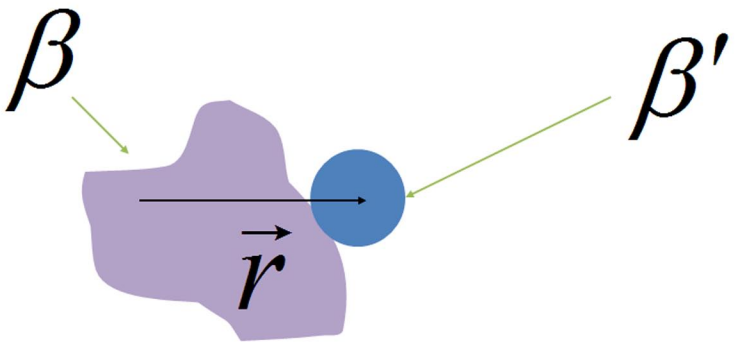

- Lineal path correlation function:

$$L(\beta, \beta' | \vec{r})$$

- The lineal path correlation function is associated with the probability of finding a vector $\vec{r}$ completely within the microstructure attribute β if $\beta = \beta'$ or the probability that the vector $\vec{r}$ crosses the boundary between the microstructure attributes β and β' only once if $\beta \neq \beta'$.

- The lineal path correlation function has the following properties:

$$\lim_{\vec{r} \to 0} L(\beta, \beta' | \vec{r}) = f(\beta)\, \delta(\beta - \beta')$$

$$L(\beta, \beta' | \vec{r}) = L(\beta', \beta | -\vec{r})$$

where $\delta(\beta - \beta')$ is the Dirac delta function.

Figure 3.8: Lineal path correlation function for the arbitrary microstructure attributes β and β'.

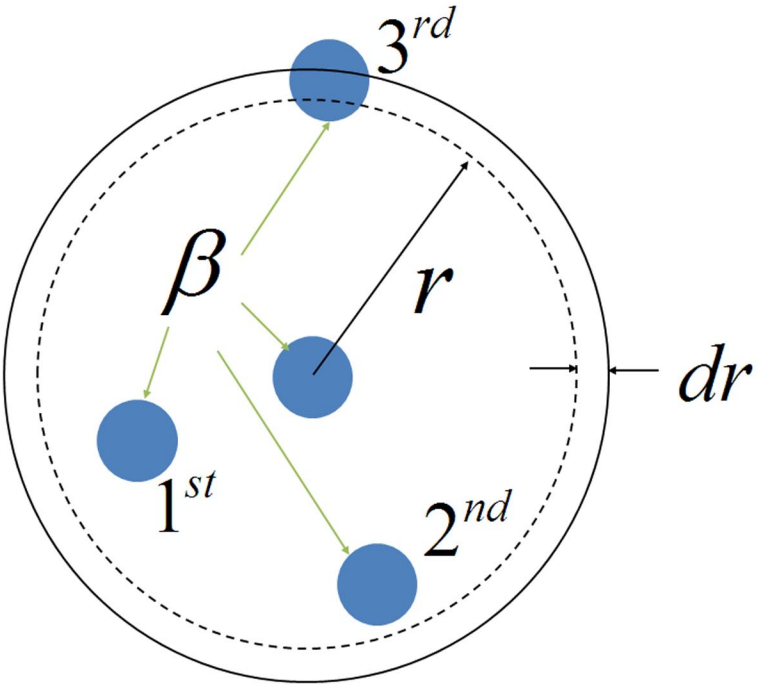

- Nearest neighbor correlation function:

$$N_n(\beta|r)$$

- Is associated with the probability of finding the nth nearest-neighbor of the same microstructure attribute to the microstructure attribute β located at an arbitrary material point in the range r to $r + dr$.

Figure 3.9: Nearest neighbor correlation function for the arbitrary microstructure attribute β.

3.4.2 Marked correlation functions

Recent work has attempted to link spatial correlations between geometrical attributes that describe the previously defined local state with various response parameters (*e.g.*, stress, strain). Based on concepts from marked point processes, Pyrz [119] constructed what he called marked correlation functions (MCF) that are expressed as the ratio between the distribution of a state variable and spatial correlations between geometrical attributes, *i.e.*,

$$M(r) = \frac{h(r)}{g(r)} \tag{3.30}$$

This MCF $M(r)$ measures correlations between geometrical attributes and the marks attached to those attributes. The mark on each attribute can be derived from a variety of different numerical tags that represent specific response parameters or state variables such as stress, elastic strain, and plastic strain. Pyrz describes the correlations between structural attributes using the a pair distribution probability density function $g(r)$, such that $g(r)\,dr$ is the probability of finding a point whose center lies between two concentric spheres of radii r and $r + dr$ about another point. The pair distribution function can be expressed as

$$g(f) = \frac{1}{2\pi r}\left[\frac{dK(r)}{dr}\right] \tag{3.31}$$

where $K(r)$ is the second order intensity function [120] defined as

$$K(r) = \frac{A}{N^2}\sum_{i=1}^{N} I_i(r) \tag{3.32}$$

and $I_i(r)$ is the number of additional points that lie inside a circle of radius r about an arbitrarily selected point. N is the total number of points in the observation area A. The distribution of the marks is described by the second order mark intensity function, *i.e.*,

$$H(r) = \frac{1}{\bar{m}^2}\left(\frac{A}{N^2}\right)\sum_{i=1}^{N}\sum_{j=1}^{j_i} m_i m_j \tag{3.33}$$

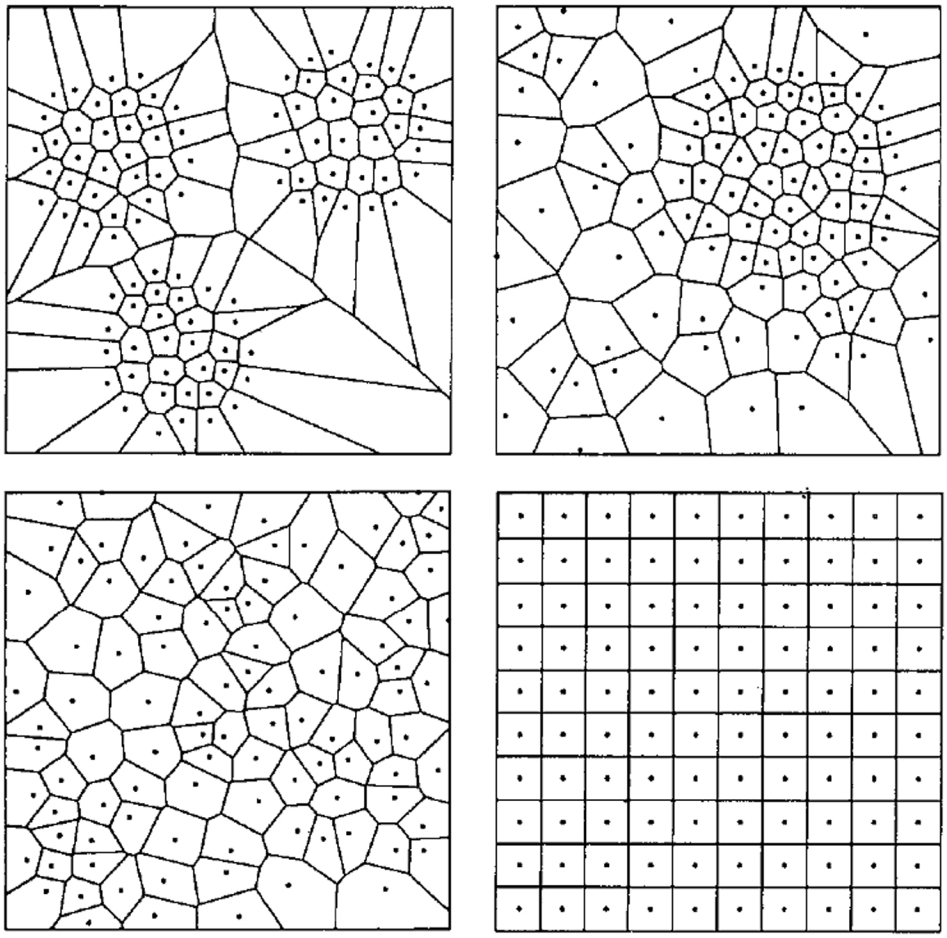

Figure 3.10: Point patterns and corresponding Dirichlet tessellations. On the the patterns for a triple and single cluster on the left and right, respectively. On the bottom are the hard-core and regular patterns on the left and right, respectively (Reprinted from [119], with permission, copyright Elsevier).

where $\bar{m}$ is the mean value of the marks on all of the marked attributes in the observation area A. Note that $H(r)$ reduces to $K(r)$ if the marked attributes all have the same mark. Similarly, $h(r)$ is the derivative of $H(r)$ with respect to dr, *i.e.*,

$$h(r) = \frac{1}{2\pi r}\frac{dH(r)}{dr} \tag{3.34}$$

Pyrz applied this MCF to understand the relationship between the distribution of composite fibers aligned along a common axis with the components of stress for different clustering patterns of the fibers as shown in Figure 3.10. If the mark on each of the geometrical

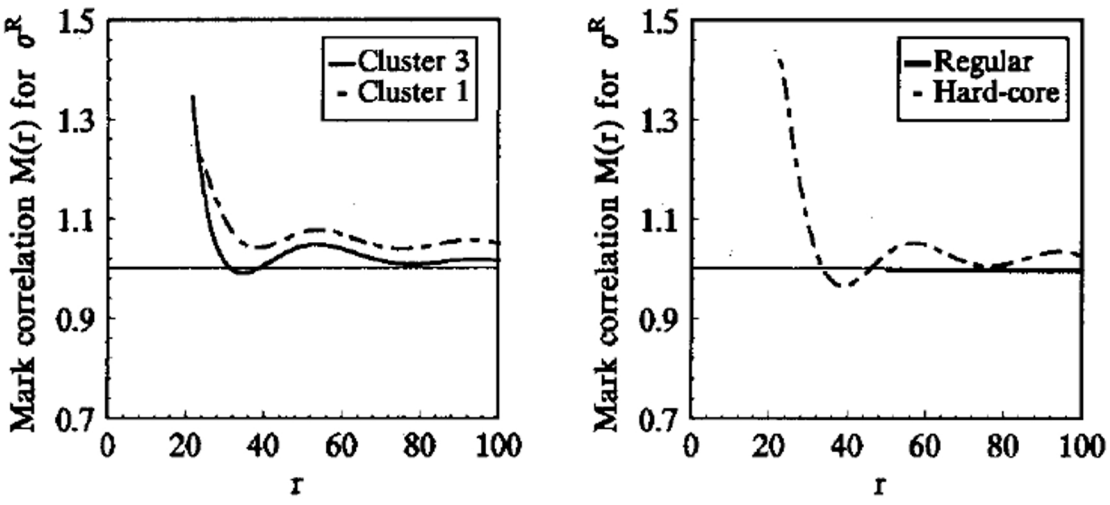

Figure 3.11: Marked correlation function $M(r)$ for maximal radial stresses around composite fibers for a transversely loaded unidirectional composite material (Reprinted from [119], with permission, copyright Elsevier).

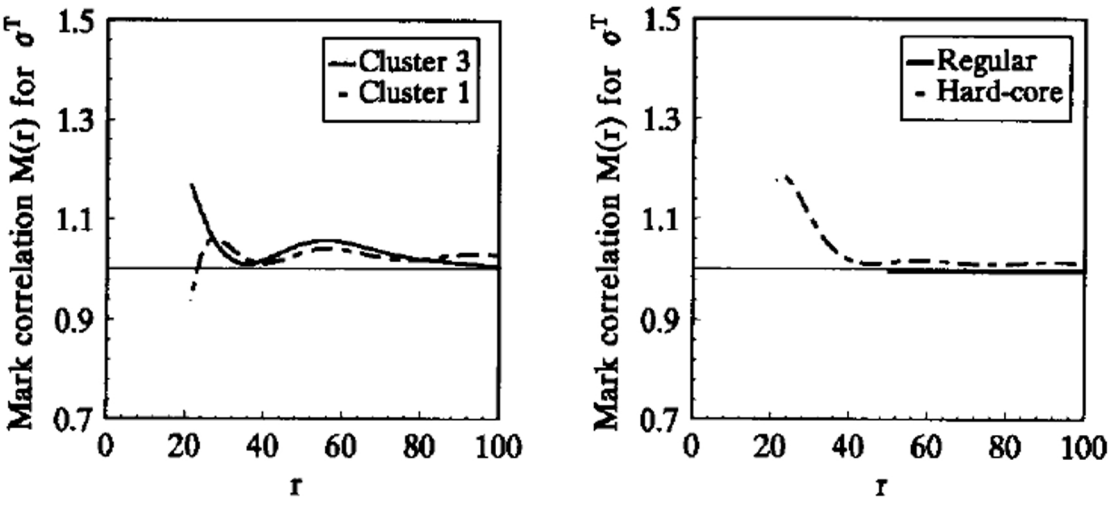

Figure 3.12: Marked correlation function $M(r)$ for maximal tangential stresses around composite fibers for a transversely loaded unidirectional composite material (Reprinted from [119], with permission, copyright Elsevier).

attributes in the volume are identical, then $h(r)$ reduces to $g(r)$ and $M(r)$ is unity. Values of $M(r)$ greater than unity indicate positive correlation between the marked attributes and values less than unity indicate repulsion. In Figures 3.11 and 3.12, are shown the MCF for the radial and tangential stresses around the composite fibers in the transversely loaded unidirectional composite material, respectively. Higher radial and tangential stresses correlate with fibers that are closer together as would be expected. Similar correlation functions could conceivably be constructed to examine correlations between response parameters and geometrical attributes for an infinite number of scenarios.

3.5 Extreme value marked correlation functions

The extreme value marked correlation function (EVMCF) describes the probability of finding correlated local states or attributes of the local state (*i.e.*, microstructure attributes) coincident with the extreme value response for a given volume. This EVMCF is based in part on the concept of the MCF as introduced by [119, 120]. In contrast to the MCF, which describes correlation of mean value response coupled microstructure attributes, the EVMCF describes how coupled microstructure attributes correlate with the extreme value response. Although, the concept of the EVMCF can be applied to a myriad of different types of correlation functions including the radial correlation function, n-point correlation function, lineal path correlation function, nearest neighbor distribution function *etc.*, it is demonstrated here in terms of the radial correlation function.

Given a response of interest parameterized by α, the EVMCF defined in terms of a radial distribution probability density function can be expressed as $R_{\max(\alpha)}(h, h'|r, \Omega)$ such that $R_{\max(\alpha)}(h, h'|r, \Omega)\,dr$ is the probability of finding a local state h coincident with the maximum response $\max(\alpha)$ and a second local state h' within a distance of r to $r + dr$ of the first local state h for a given volume of microstructure Ω. Here a discrete tessellation the local states h and h' is assumed. The estimation of $R_{\max(\alpha)}(h, h'|r, \Omega)\,dr$ is depicted for the microstructure attributes β and β' associated with the local states h and h', respectively,

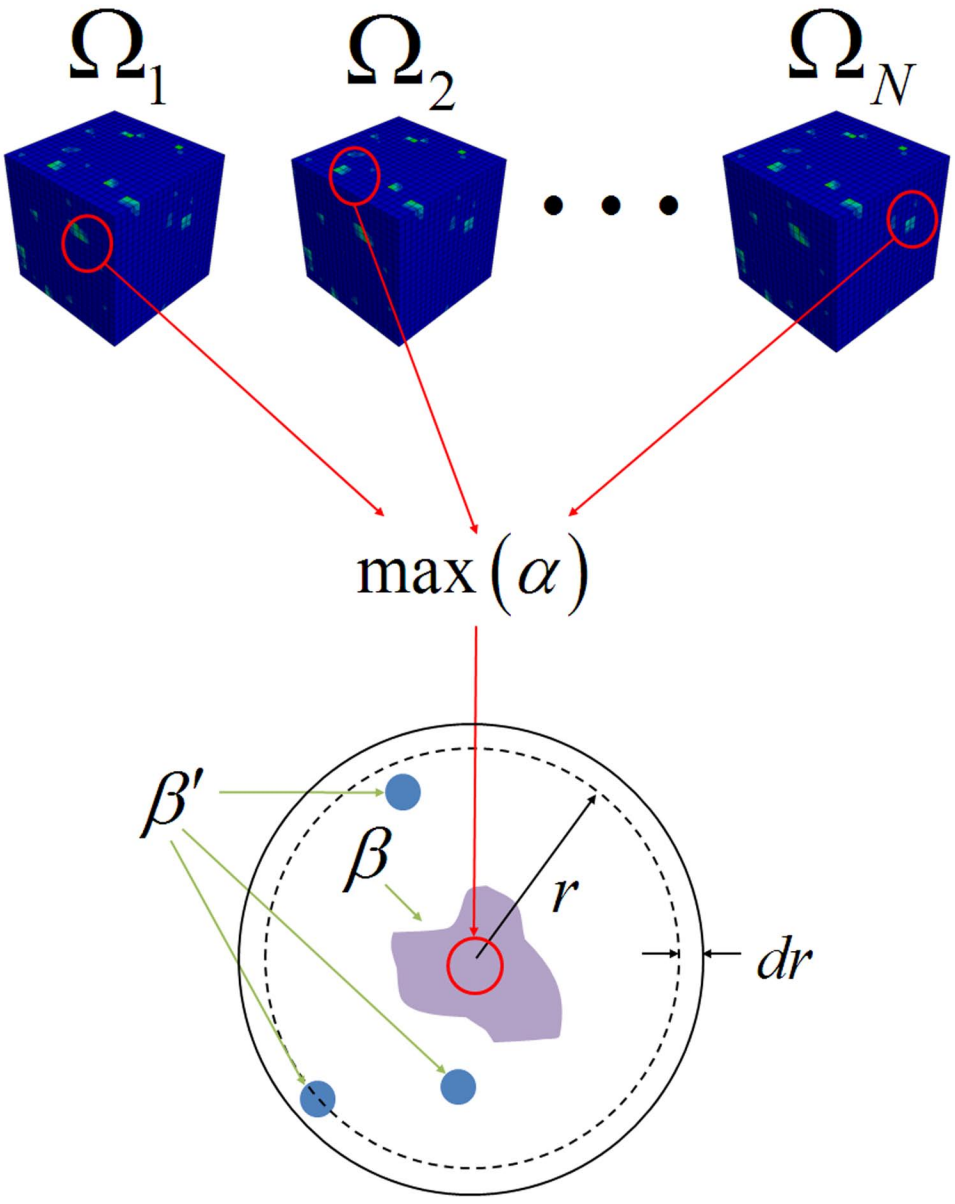

Figure 3.13: Extreme value marked radial correlation function for the extreme value response parameterized by α and the arbitrary microstructure attributes β and β'.

in Figure 3.13 and can be carried out as follows:

1. Instantiate a statistically significant number of samples N of volumes sampled from the ensemble or bulk material (*i.e.*, Ω_i for $i = 1, 2, \ldots, N$). The determination of N will be discussed later in Chapter 6.

2. In each sampled volume Ω_i the extreme value response $\max(\alpha)$ must be determined. The extreme value response is simply the maximum value of α observed/estimated in Ω_i.

3. The extreme value marked radial correlation function of attributes β and β', $R_{\max(\alpha)}(\beta, \beta'|r, \Omega)$, is selectively sampled at the locations where β is coincident with the extreme value response $\max(\alpha)$ in each sample Ω_i.

In the process of determining $R_{\max(\alpha)}(h, h'|r, \Omega)$, the distribution of the extreme value response is also characterized, which can be expressed as the probability density $f_{\max(\alpha)}(\alpha|\Omega)$. In other words, $f_{\max(\alpha)}(\alpha|\Omega)$ is the probability that the response parameter of value α is the maximum extreme value for a sampled volume Ω. The extreme value distribution of the response $f_{\max(\alpha)}(\alpha|\Omega)$ is related to the probability density of the extreme value distribution function described by Gumbel [72, 75].

The EVMCF described by $R_{\max(\alpha)}(h, h'|r, \Omega)$ coupled with the extreme value distribution of response $f_{\max(\alpha)}(\alpha|\Omega)$ together describes both the extreme value response of the microstructure as represented by the response parameter and the probabilities of existing correlated local states h and h' (or microstructure attributes β and β' associated with the local states h and h' such that $\beta \in h$ and $\beta' \in h'$) relative to the observed extreme values of α in a microstructure window Ω. Moreover, the EVMCF directly identifies the correlated local states that have a high probability of existing in the neighborhood of an extreme value response parameter. By comparing $R_{\max(\alpha)}(h, h'|r, \Omega)$ with the correlation function for the same local states sampled from the ensemble or $R(h, h'|r)$, the correlated local states most unique to the locations of extreme value response can be identified.

This sampling is limited to a prespecified microstructure volume Ω and is expected to change with varying sizes of Ω. The expected challenge of estimating $R_{\max(\alpha)}(h, h'|r, \Omega)$ is that multiple samples of Ω are required. Such sampling performed experimentally can be extremely time intensive or even infeasible. Estimation of $R_{\max(\alpha)}(h, h'|r, \Omega)$ is most accessible computationally because of the experimental difficultly of measuring response in situ in three dimensions. However, computational calculations can be time intensive depending on the complexity of the models and material system being analyzed. Additionally, it is noted that the number of samples required could be different depending on the response and material being analyzed.

The introduction of the EVMCF achieves the primary objective of linking the extreme value distributions of damage response to the coupled microstructure attributes of the local states that are associated with that response. Specifically, the extreme value distribution of response $f_{\max\alpha}(\alpha|\Omega)$ coupled with the EVMCF $R_{\max(\alpha)}(h, h'|r, \Omega)$ achieves three primary objectives, namely:

1. A description is given of both the distributions of microstructure attributes and potential interactions or correlations between multiple microstructure attributes.

2. The distributions of microstructure attributes and correlations between various microstructure attributes are quantifiably linked to the distributions of the damage response.

3. The extreme value nature of damage type scenarios (*e.g.*, fatigue) that depends on variations in the local microstructure can be characterized.

3.6 Summary

The mathematical framework for extreme value statistics is well defined for both single random variables and multiple random variables and has been applied across a wide range of disciplines. Classical extreme value probability theory describes the distributions of the

maxima or minima of finite sized samples or sets taken from the distribution of the initial variate. As the size of the sample sets becomes large, there are three known asymptotic distributions to which the distributions of the maxima or minima can converge. These asymptotic distributions are described by the Gumbel (Type I) distribution, the Fréchet (Type II) distribution, and Weibull (Type III) distribution. If the distribution of extremes can be classified as being associated with one of these types of asymptotic extreme value distributions, then the mathematical properties of that asymptotic distribution can be used to describe the data.

Although fatigue has been studied extensively, much remains to be understood about how statistical variation of microstructure affect scatter in fatigue lives. This scatter in fatigue life in HCF is primarily a function of the probability of finding regions within the microstructure that exhibit a high driving force for and/or weak resistance to fatigue damage formation. These regions can depend on multiple microstructure attributes that may or may not be coupled in terms of their effects on the mechanisms of fatigue damage formation such as grain size, grain orientation/misorientation, phase distribution, *etc.* Little work has been reported in the literature concerning how the interactions between slip bands and/or small cracks and microstructure attributes alter the local driving forces for fatigue damage formation.

Statistical variability in fatigue life has traditionally been determined experimentally. Simple models such as the Weibull distribution account for probability of failure, but are empirical in nature and do not explicitly account for microstructure. Others have considered the effect that single parameter extreme value statistical distributions such as inclusion size can have on fatigue life in clean steels. It is likely, however, that the necessary statistics will be of multivariate character, given the likely effect of coupling between microstructure attributes, but very little work has been reported in the literature on multivariate extreme value statistics either for fatigue or any other subject. The shapes of the tails of the distribution of the various fatigue response parameters (*e.g.*, cyclic plastic strain, FIPs) are

not well understood, nor is it clear how coupling between various microstructure attributes influences the extreme value distributions of the fatigue response parameters computed on the scale of the dominant microstructure attributes.

Various correlation functions have been used to describe random heterogeneous materials. Experimental methods have been developed to estimate the correlation statistics of real microstructures in three dimensions. Marked correlation functions have been introduced which describe how coupled microstructure attributes correlate with mean value response. In this work, extreme value marked correlation functions are introduced to describe how coupled microstructure attributes correlate with extreme value response. EVMCF describe the correlations between coupled microstructure attributes and extreme value response. These EVMCF are best estimated computationally due to the experimental difficulty of measuring in situ response in three dimensions, but are equally applicable to computational and/or experimental estimation.

CHAPTER IV

CYCLIC POLYCRYSTAL PLASTICITY MODELS FOR ENGINEERING ALLOYS

4.1 Introduction

This dissertation will apply the EVMCF introduced in Chapter 3 to study the influence of the crystallographic attributes of polycrystalline metals on the distribution of the extreme value FIPs. Specifically, the sensitivity of the extreme value FIPs to the crystallographic attributes in the Ni-base superalloy IN100 and the Ti alloy Ti-6Al-4V will be considered in Chapters 6 and 7, respectively. As noted in Chapter 2, fatigue crack formation in metals is most often associated with localized plasticity which occurs at the predominant microstructural barriers. In lieu of extensive experimentation, the approach taken here is to estimate the distribution of the extreme value driving forces for fatigue crack formation via computational simulation with experimental validation. To simulate distributed cyclic plasticity in metals, specially derived constitutive relations for cyclic plasticity are implemented into the commercially available FE package ABAQUS [121] via a user material subroutine (UMAT).

Effective predictive models of cyclic stress-strain response must be able to mimic the underlying mechanisms affecting that response, either explicitly or implicitly. Predicting the cyclic stress-strain response in metallic crystalline materials has been very challenging because the overall material response depends on various complex mechanisms at multiple scales. Macroscopically, the response is often best visualized in terms of the cyclic stress strain curve which describes the relationship between the saturated resolved shear stress

amplitude and resolved shear strain amplitude. Initial cyclic loading is typically accompanied by either cyclic hardening or softening which occurs when the maximum stress amplitudes increase or decrease during subsequent cycling, respectively. The point at which the curve becomes stable (repeatable) has been termed saturation. At low enough applied stress or strain amplitudes, the stress-strain response will stabilize after an initial transient or elastic shakedown period after which no additional plastic strain will accumulate after subsequent cycles. The cyclic plastic shakedown limit is the strain amplitude below which only reversed cyclic plastic straining will occur within the microstructure. If the plastic shakedown limit is exceeded, ratcheting will occur (*i.e.*, plastic strains will continue to accumulate over subsequent cycles). These shakedown limits depend on the R-ratios of the applied stress or strain. Shakedown, cyclic plasticity (plastic shakedown) and ratcheting were formally defined in Section 2.3 in terms of the cyclic plastic strain tensor and are repeated here for convenience, *i.e.*,

$$\left(\Delta\epsilon_{ij}^{p}\right)_{ratch} = \left(\epsilon_{ij}^{p}\right)\Big|_{end\ of\ cycle} - \left(\epsilon_{ij}^{p}\right)\Big|_{beginning\ of\ cycle} \tag{4.1}$$

$$\left(\Delta\epsilon_{ij}^{p}\right)_{cyc} = \left(\Delta\epsilon_{ij}^{p}\right)_{max}\Big|_{over\ the\ cycle} - \left(\Delta\epsilon_{ij}^{p}\right)_{ratch} \tag{4.2}$$

Macroscopically it is also observed that in some materials subject to cyclic loading after a certain amount of forward plastic flow (tension or compression), the material yields at a lower stress when the direction of loading is reversed. This phenomenon is called the Bauschinger effect.

To understand these experimentally observed macroscopic trends, the mechanisms operating on the scale of dominant microstructure attributes must be considered. Many of these mechanisms were briefly reviewed in Chapter 2. Although exact mechanisms vary from one material system to the next, when metallic crystalline materials are subjected to cyclic loads, the microstructure evolves due to the generation, motion and interactions of dislocations with themselves and other microstructure attributes such as second phase

inclusions or grain boundaries. Suresh [5] reviewed the various microscopic structural changes which can occur in many metallic material systems due to the motion and interactions of dislocations. For example, in metals under cyclic loads dislocations have been observed to arrange into bands of ladder like arrays of dislocations called persistent slip bands (PSBs) or distributed cellular structures called dislocation cells. Different dislocation structures develop and evolve depending on the amplitude of applied cyclic stress to minimize internal energy while still allowing the accommodation of the cyclic plastic flow. Dislocation generation and motion typically occur when the magnitudes of stress are sufficient to induce flow. Generally, plasticity is considered only when externally applied loads exceed the effective yield strength, but in polycrystalline materials local plasticity is possible in grains favorably oriented for slip even when the external loads are well below the effective yield strength of a material. This is the case with elastic shakedown. After initial cycling at low to moderate amplitudes of loading (relative to the materials macroscopic yield strength), hardening occurs in regions of localized flow which prevents further plasticity. Subsequent cycling after elastic shakedown is primarily elastic. Plastic shakedown at sufficient magnitudes of loading and R-ratios occurs until the dislocations organize into stable arrangements such as PSBs or dislocations cells that are able to accommodate the cyclic straining with minimal continued microstructural rearrangement. The Bauschinger effect is microstructurally due to changes in the structural arrangement of dislocations and localized stress fields which occur upon load reversal which decrease a materials inherent resistance to flow in the reverse direction. Certain dislocation structures like walls form upon forward loading, but can be dissolved upon stress reversals [122]. In material systems with impermeable particles or precipitates, dislocations pileup upon loading in one direction creating a backstress that resists further dislocation pileup. Upon reversal of the loading, this backstress assists dislocation motion away from pileups at these barriers [123].

Crystal plasticity models are one class of models that have been successful in capturing experimentally observed cyclic stress-strain response by incorporating the physics of

plastic flow on the scale of the individual grains. These models attempt to capture the fundamental mechanisms of slip on individual slip planes. Finer scale behavior has also been incorporated though various internal state variables (ISVs) which describe, for example, hardening due to dislocation pileup. Several examples of ISV based cyclic crystal plasticity models will be considered here. First, the general framework for large strain based crystal plasticity models will be presented including a description of the relevant kinematic, kinetic, and thermodynamic relationships. A few formulations of various ISV based crystal plasticity models will then be reviewed that have been developed to model cyclic plasticity in polycrystalline metals including pure Cu, the Ni-base superalloy IN100, and duplex $\alpha + \beta$ Ti-6Al-4V. Note that standard tensor notation is used throughout with vectors indicated by bold lower case letters and second rank tensors indicated by bold upper case letters. Fourth-rank tensors are expressed as upper case letters in a block letter font.

4.2 Crystal plasticity framework for large strain based models

Development of the pertinent theory of crystal plasticity can be traced through several papers, *i.e.*, [124–134]. Here we start with the kinematical description of the elastic-plastic deformation of single crystals based on large strain theory. The primary objective is to link the physics of slip along crystallographic slip planes to the micromechanical behavior of a deforming single crystal or an aggregate of crystals.

Consider an arbitrary body composed of material points each initially at position $\mathbf{x}$ at time t_n. At any later time t_{n+1}, the current position of a point originally at $\mathbf{x}$ is now at $\mathbf{y}$ (*i.e.*, $\mathbf{y} = \hat{\mathbf{y}}(\mathbf{x}, t_n)$. The deformation gradient $\mathbf{F}$ is a tensor defined such that when it operates on the infinitesimal material vector $d\mathbf{x}$ the result is the same infinitesimal material vector in the current deformed configuration $d\mathbf{y}$, *i.e.*,

$$d\mathbf{y} = \mathbf{F} \cdot d\mathbf{x} \tag{4.3}$$

The central tenant of large strain based crystal plasticity is that the total deformation gradient can be decomposed into elastic $\mathbf{F}^e$ and plastic $\mathbf{F}^p$ parts such that

$$\mathbf{F} = \mathbf{F}^e \cdot \mathbf{F}^p \tag{4.4}$$

This mathematical decomposition (*cf.* [125]) breaks up the specific mechanisms of deformation in crystalline materials into two separate parts. Specifically, $\mathbf{F}^p$ is constructed to capture the plastic flow by dislocation motion along the various slip planes without lattice distortion (*i.e.*, plastic incompressibility is assumed such that $\det[\mathbf{F}^e] = 1$). The rigid body rotation and elastic stretching are separately described by $\mathbf{F}^e$. This decomposition is purely for mathematical convenience; in reality all deformation modes are occurring simultaneously. This decomposition is shown schematically in Figure 4.1. The slip direction for slip system α is defined as $\mathbf{s}_o^\alpha$ and the slip plane normal is given by $\mathbf{n}_o^\alpha$ in the original reference and intermediate configurations. Application of $\mathbf{F}^e$ transforms $\mathbf{s}_o^\alpha$ and $\mathbf{n}_o^\alpha$ from their unstretched and unrotated state in the intermediate configuration to their rotated and stretched state in the current configuration $\mathbf{s}^\alpha$ and $\mathbf{n}^\alpha$, respectively, *i.e.*,

$$\mathbf{s}^\alpha = \mathbf{F}^e \cdot \mathbf{s}_o^\alpha \tag{4.5}$$

$$\mathbf{n}^\alpha = \mathbf{n}_o^\alpha \cdot (\mathbf{F}^e)^{-1} \tag{4.6}$$

Accounting for the kinematics of dislocation motion, the time rate of change of the plastic deformation gradient can be expressed as

$$\dot{\mathbf{F}}^p = \left(\sum_{\alpha=1}^{N_\alpha} \dot{\gamma}^\alpha \mathbf{P}^\alpha \right) \cdot \mathbf{F}^p \tag{4.7}$$

where $\mathbf{P}^\alpha$ is defined such that $\mathbf{P}^\alpha \equiv \mathbf{s}_o^\alpha \otimes \mathbf{n}_o^\alpha$ or the Schmid tensor in the reference or intermediate configurations. The slip rate for slip system α is defined by $\dot{\gamma}^\alpha$ and N_α is the

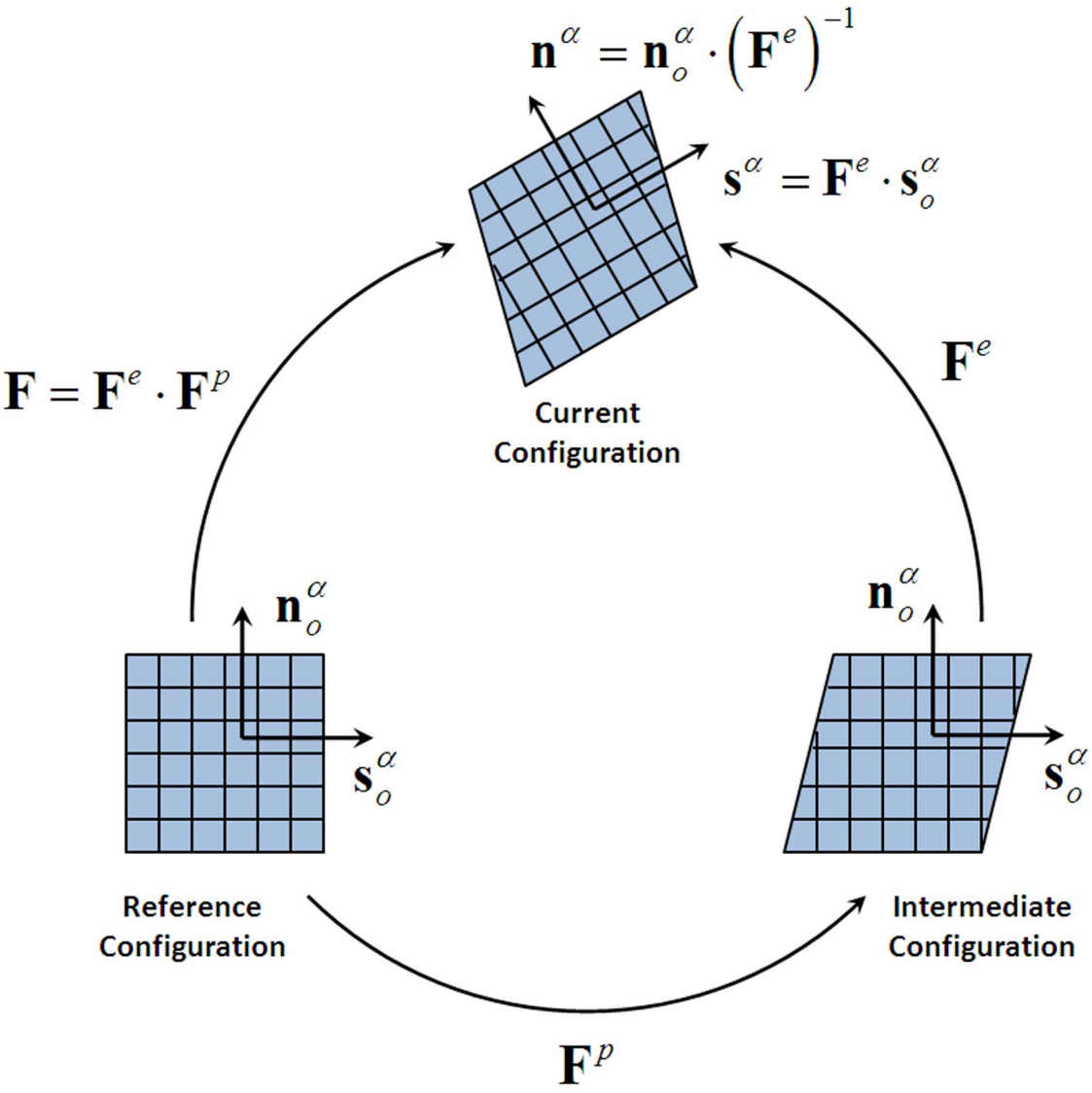

Figure 4.1: Elastic-plastic decomposition of the deformation gradient.

total number of active slip systems. The plastic velocity gradient $\mathbf{L}_o^p$ in the intermediate configuration is expressed in terms of the plastic deformation gradient as

$$\mathbf{L}_o^p = \dot{\mathbf{F}}^p \cdot (\mathbf{F}^p)^{-1} = \sum_{\alpha=1}^{N_\alpha} \dot{\gamma}^\alpha \mathbf{P}^\alpha \tag{4.8}$$

The plastic velocity gradient in the current configuration $\mathbf{L}^p$ is then given by

$$\mathbf{L}^p = \mathbf{F}^e \cdot \mathbf{L}_o^p \cdot (\mathbf{F}^e)^{-1} \tag{4.9}$$

Additionally, the elastic velocity gradient in the current configuration $\mathbf{L}^e$ is expressed as

$$\mathbf{L}^e = \dot{\mathbf{F}}^e \cdot (\mathbf{F}^e)^{-1} \tag{4.10}$$

Combining the elastic velocity gradient $\mathbf{L}^e$ with the plastic velocity gradient $\mathbf{L}^p$ additively yields the total velocity gradient $\mathbf{L}$, *i.e.*,

$$\mathbf{L} = \dot{\mathbf{F}} \cdot (\mathbf{F})^{-1} = \mathbf{L}^e + \mathbf{L}^p \tag{4.11}$$

The rate of deformation $\mathbf{D}$ and the spin tensor $\mathbf{W}$ are defined as the symmetric and antisymmetric parts of $\mathbf{L}$, respectively, *i.e.*,

$$\mathbf{D} = \frac{1}{2}\left(\mathbf{L} + \mathbf{L}^T\right) \tag{4.12}$$

$$\mathbf{W} = \frac{1}{2}\left(\mathbf{L} - \mathbf{L}^T\right) \tag{4.13}$$

Equations 4.12 and 4.13 are also valid for the elastic and plastic rates of deformation and spin tensors, respectively.

The constitutive equation is written in the intermediate configuration as

$$\mathbf{T} = \mathbb{C} : \mathbf{E}^e \tag{4.14}$$

where $\mathbf{T}$ is the second Piola-Kirchhoff stress in the intermediate configuration that is work conjugate to the elastic Green strain tensor $\mathbf{E}^e$. The fourth rank elastic stiffness is given by $\mathbb{C}$. The elastic Green strain tensor is defined as

$$\mathbf{E}^e = \frac{1}{2}\left[(\mathbf{F}^e)^T \cdot \mathbf{F}^e - \mathbf{I}\right] \tag{4.15}$$

where $\mathbf{I}$ is the second rank identity tensor. Note that $\mathbf{T}$ and $\mathbf{E}^e$ are both defined in terms of the intermediate configuration. The Cauchy stress in the current configuration $\boldsymbol{\sigma}$ is related to the second Piola-Kirchhoff stress in the intermediate configuration $\mathbf{T}$ according to

$$\boldsymbol{\sigma} = \frac{1}{\det\left[\mathbf{F}^e\right]}\mathbf{F}^e \cdot \mathbf{T} \cdot (\mathbf{F}^e)^T \tag{4.16}$$

The second Piola Kirchhoff stress in the intermediate configuration $\mathbf{T}$ is related to the second Piola-Kirchhoff stress in the reference configuration $\mathbf{T}_o$ according to

$$\mathbf{T} = \mathbf{F}^p \cdot \mathbf{T}_o \cdot (\mathbf{F}^p)^T \tag{4.17}$$

Recall that $\det\left[\mathbf{F}^p\right] = 1$ due to plastic incompressibility.

The fourth rank elastic stiffness in the crystal coordinate system $\mathbb{C}^c$ is related to the fourth rank elastic stiffness in the sample coordinate system $\mathbb{C}$ according to

$$\mathbb{C} = \mathbf{R}\underline{\otimes}\mathbf{R} : \mathbb{C}^c : \mathbf{R}^T\underline{\otimes}\mathbf{R}^T \tag{4.18}$$

where the lower tensor product is defined as $\left(\mathbf{A}\underline{\otimes}\mathbf{A}\right)_{ijkl} = A_{ik}A_{jl}$ for an arbitrary second rank tensor $\mathbf{A}$. $\mathbf{R}$ rotates the base vectors in the crystal coordinate system $\hat{\mathbf{e}}^c$ to the sample initial reference coordinate system $\hat{\mathbf{e}}$ (*i.e.*, the undeformed global reference frame). The rotation $\mathbf{R}$ is calculated using the direction cosigns according to

$$R_{ij} = \cos\left(\hat{e}_i, \hat{e}^c_j\right) = \hat{e}_i \cdot \hat{e}^c_j \tag{4.19}$$

where $\hat{e}_i$ and $\hat{e}^c_j$ are the components of the base vectors of the crystal coordinate frame and reference coordinate frame, respectively. Defined in this manner, the rotation matrix $\mathbf{R}$ is the transpose of the orientation matrix defined by Bunge [93]. Thus, $\mathbf{R}$ in terms of Euler angles ϕ_1, Φ, and ϕ_2 is defined as

$$\begin{aligned}
R_{11} &= \cos(\phi_1)\cos(\phi_2) - \sin(\phi_1)\sin(\phi_2)\cos(\Phi) \\
R_{12} &= -\cos(\phi_1)\sin(\phi_2) - \sin(\phi_1)\cos(\phi_2)\cos(\Phi) \\
R_{13} &= \sin(\phi_1)\sin(\Phi) \\
R_{21} &= \sin(\phi_1)\cos(\phi_2) + \cos(\phi_1)\sin(\phi_2)\cos(\Phi) \\
R_{22} &= -\sin(\phi_1)\sin(\phi_2) + \cos(\phi_1)\cos(\phi_2)\cos(\Phi) \\
R_{23} &= -\cos(\phi_1)\sin(\Phi) \\
R_{31} &= \sin(\phi_2)\cos(\Phi) \\
R_{32} &= \cos(\phi_2)\sin(\Phi) \\
R_{33} &= \cos(\Phi)
\end{aligned} \tag{4.20}$$

The current orientation matrix that rotates the crystal base vectors to the current global reference frame (after deformation) $\mathbf{R}'$ can be calculated according to

$$\mathbf{R}' = \mathbf{F}^e \cdot \mathbf{R} \tag{4.21}$$

Finally, the resolved shear stress τ^α is calculated according to

$$\tau^\alpha = \left[(\mathbf{F}^e)^T \cdot \mathbf{F}^e \cdot \mathbf{T}\right] : \mathbf{P}^\alpha \tag{4.22}$$

When the elastic stretches are small, $(\mathbf{F}^e)^T \mathbf{F}^e \cong \mathbf{I}$, which is the case for most metals. Therefore, the resolved shear stress can be approximated as

$$\tau^\alpha \doteq \mathbf{T} : \mathbf{P}^\alpha \tag{4.23}$$

Remaining to be defined is the relationship between the slip rates and the resolved shear stress (*i.e.*, flow rule) and the evolution of the internal state variables (ISVs) that describe

the local structural rearrangement of the microstructure (see the following section). Typically, the ISVs appear as terms that describe the hardening of the slip systems. Evolution of these hardening variables must be defined in the intermediate configuration. Various forms of the flow rule and hardening laws have been proposed. Forms for cyclic slip in pure copper, the Ni-base superalloy IN100 and duplex $\alpha + \beta$ Ti-6Al-4V will be considered. However, first the thermodynamic requirements of large strain based ISV crystal plasticity will briefly be considered.

4.2.1 Thermodynamic requirements of large strain based ISV crystal plasticity theory

To describe the irreversible path dependence of crystal plasticity, internal microstructure variables (*i.e.*, internal state variables) are introduced to describe local structural rearrangement within the microstructure. Several have discussed this general class of *internal state variable* (ISV) based constitutive theories and the thermodynamic requirements of their formulation (*e.g.*, [135, 136]). In short any physically based constitutive equation must satisfy the second law of thermodynamics. The second law provides the Clausius-Duhem inequality. For isothermal deformation, the Clausius-Duhem inequality can be expressed in terms of the second Piola-Kirchhoff stress as [137]

$$\frac{1}{2}\mathbf{T} : \left[\mathbf{C}^e + 2\left(\mathbf{C}^e \cdot \mathbf{L}_o^p\right)_{\text{sym}}\right] - \dot{\psi} \geq 0 \tag{4.24}$$

where the elastic right Cauchy-Green tensor $\mathbf{C}^e$ is given by

$$\mathbf{C}^e = \left(\mathbf{F}^e\right)^T \cdot \mathbf{F}^e \tag{4.25}$$

and $\dot{\psi}$ is the rate of change of the Helmholtz free energy ψ. The remaining terms have been defined previously. The Helmholtz free energy can be expressed in terms of an elastic term ψ^e and a nonelastic (microelastic) term ψ^p [138], *i.e.*,

$$\psi = \hat{\psi}^e\left(\mathbf{C}^e, T\right) + \hat{\psi}^p\left(\boldsymbol{\xi}_i, T\right) \tag{4.26}$$

where $\hat{\psi}^e$ and $\hat{\psi}^p$ are the functional forms of ψ^e and ψ^p, respectively, and T is the temperature. The set of internal state variables is given by the set of tensors $\boldsymbol{\xi}_i$ of arbitrary rank for $i = 1, \ldots, N$ such that N is the total number of ISVs. For example, the variables ξ_i^α could describe hardening on the individual slip systems defined by α. Combining Equation 4.26 with the Clausius-Duhem inequality 4.24 yields

$$\frac{1}{2}\mathbf{T} : \dot{\mathbf{C}}^e + (\mathbf{C}^e \cdot \mathbf{T}) : \mathbf{L}_o^p - \frac{\partial \psi^e}{\partial \mathbf{C}^e} : \dot{\mathbf{C}}^e - \sum_i \frac{\partial \psi_p}{\partial \boldsymbol{\xi}_i} * \dot{\boldsymbol{\xi}}_i \geq 0 \tag{4.27}$$

where the operator $*$ denotes an appropriate scalar product for the Euclidean space of the components of tensor ξ_i as the different ISVs can be of different (arbitrary) rank. To ensure that Equation 4.27 must be satisfied for every kinematically admissible process

$$\mathbf{T} = 2\frac{\partial \psi^e}{\partial \mathbf{C}^e} \tag{4.28}$$

$$(\mathbf{C}^e \cdot \mathbf{T}) : \mathbf{L}_o^p - \sum_i \frac{\partial \psi_p}{\partial \boldsymbol{\xi}_i} * \dot{\boldsymbol{\xi}}_i \geq 0 \tag{4.29}$$

Assuming that elastic part of the Helmholtz free energy ψ^e can be expressed as a sum of the work due to elastic stretching, *i.e.*,

$$\hat{\psi}^e(\mathbf{C}^e) = \frac{1}{2}\mathbf{E}^e : \mathbb{C} : \mathbf{E}^e \tag{4.30}$$

Equation 4.28 is satisfied by the constitutive law defined in Equation 4.14, *i.e.*,

$$\mathbf{T} = 2\frac{\partial \psi^e}{\partial \mathbf{C}^e} = \mathbb{C} : \mathbf{E}^e \tag{4.31}$$

Combining the previous Equations 4.7, 4.8, 4.25, and 4.22 results in

$$(\mathbf{C}^e \cdot \mathbf{T}) : \mathbf{L}_o^p = \sum_\alpha^{N_\alpha} \tau^\alpha \dot{\gamma}^\alpha \tag{4.32}$$

Equation 4.32 can then be combined with Equation 4.29 to yield

$$\sum_{\alpha}^{N_\alpha} \tau^\alpha \dot{\gamma}^\alpha - \sum_i \frac{\partial \psi_p}{\partial \boldsymbol{\xi}_i} * \dot{\boldsymbol{\xi}}_i \geq 0 \tag{4.33}$$

which must be satisfied for all internal state variables $\boldsymbol{\xi}_i$.

4.3 Cyclic crystal plasticity models for specific material systems

4.3.1 Copper

In relatively pure face-centered cubic (fcc) copper (or other similar materials), single crystals oriented for single slip exhibit three regions of response in the cyclic stress strain curve which correspond to differences in the dislocation substructure which develops to accommodate the cyclic plastic straining. In Figure 4.2, Region A is indicative of work hardening as the dislocations organize into structures called veins. Region B is characterized by the formation of persistent slip bands (PSBs) [139], and increased hardening in Region C has been attributed to the formation of cellular structures. Polycrystals generally exhibit multiple slip and a multiaxial stress state, but even single crystals can exhibit multislip if they are oriented in a certain way (*e.g.*, [001] oriented copper single crystals [140–142]). Experimental observations of copper single crystals indicate significant variations in the cyclic hardening rate and saturated resolved stress for differently oriented crystals. Effective crystal plasticity models of copper and other similar fcc single phase materials must be able to mimic the response due to these various mechanisms

Xu and Jiang [144] incorporate a rate independent crystal plasticity model for Cu with a Armstrong-Frederick type kinematic hardening rule to capture the Bauschinger effect observed in this material under cyclic loads. Based on a rate-independent formulation, a slip system is considered active (*i.e.*, $\dot{\gamma}^\alpha > 0$) when the effective resolved shear stress for a particular slip system reaches a critical value, *i.e.*,

$$\gamma^\alpha = |\tau^\alpha - \chi^\alpha| - \tau^\alpha_{cr} \leq 0 \tag{4.34}$$

The total backstress for each slip system χ^α is divided into I additive parts for each slip

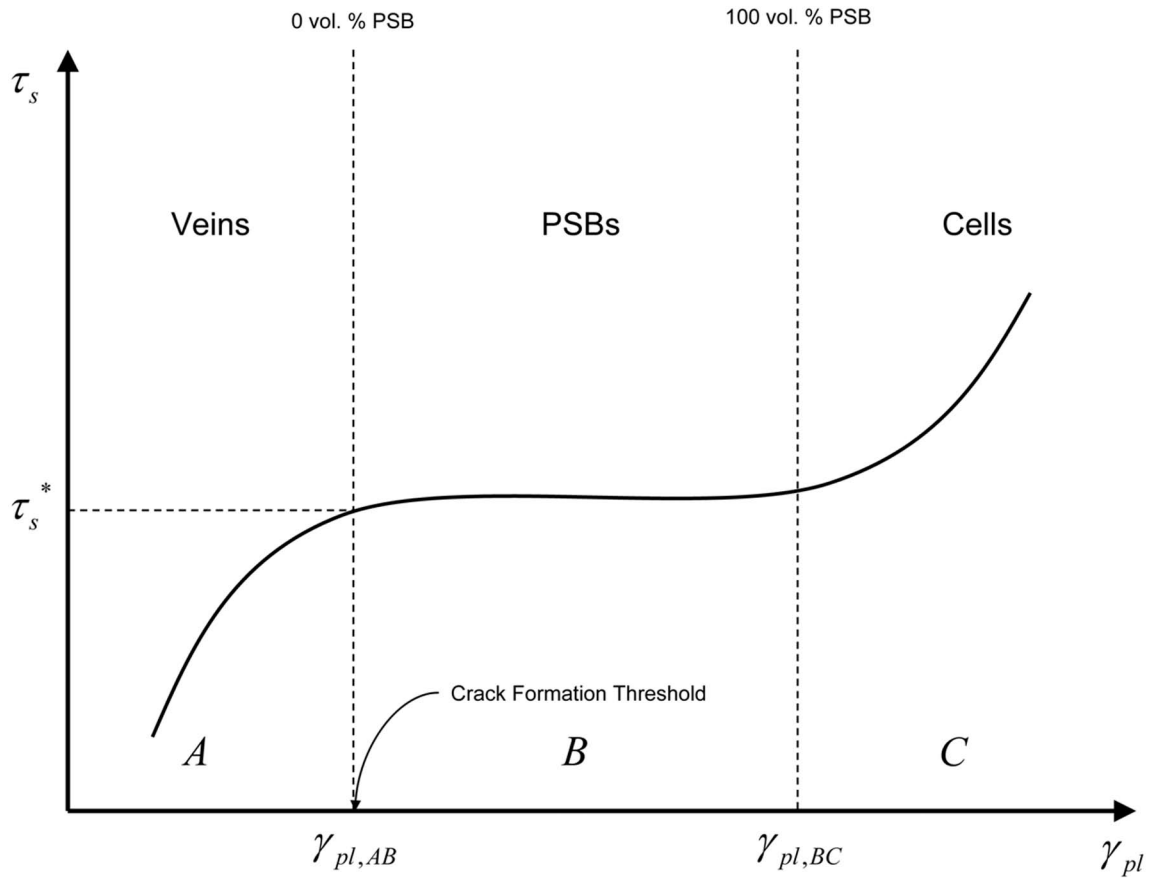

Figure 4.2: A schematic drawing of a cyclic stress strain curve for a typical single crystal which indicates the stress-strain regimes at which different mechanisms accommodate the plastic strain transitions. In copper at 295K, these transitions occur at strains of $\gamma_{pl,AB} = 6.0x10^{-5}$ and $\gamma_{pl,BC} = 7.5x10^{-3}$ with a saturation stress of $\tau_s^* = 14.0$ MPa [142]. In Nickel at 295K the transitions occur at strain magnitudes of $\gamma_{pl,AB} = 1.0x10^{-4}$ and $\gamma_{pl,BC} = 7.5x10^{-3}$ with a saturation stress of $\tau_s^* = 52.0$ MPa [143]. (Adapted from similar figure in [5]).

system, *i.e.*,

$$\chi^{\alpha} = \sum_{i=1}^{I} \chi_i^{\alpha} \tag{4.35}$$

The Armstrong-Frederick hardening rule here is expressed as,

$$\dot{\chi}_i^{\alpha} = c_i r_i \sum_{\beta} h^{\alpha\beta} \dot{\gamma}^{\beta} - c_i \chi_i^{\alpha} \sum_{\beta} \left| \dot{\gamma}^{\beta} \right| \tag{4.36}$$

where c_i and r_i are material constants. The latent hardening matrix $h^{\alpha\beta}$ used here is based on Bassani and Wu's [145] formulation, *i.e.*,

$$h^{\alpha\beta} = q^{\alpha\beta} G^{\beta} \tag{4.37}$$

where

$$G^{\beta} = 1 + \sum_{\kappa \neq \beta} f^{\beta\kappa} \tanh\left(\frac{\bar{\gamma}^{\kappa}}{\gamma_o}\right) \tag{4.38}$$

The material constants $f^{\beta\kappa}$ and $q^{\alpha\beta}$ represent the magnitudes of various slip interactions, $\bar{\gamma}^{\kappa}$ is the accumulated slip on slip system κ and γ_o is a constant.

A memory parameter is incorporated to describe the strain range dependent cyclic hardening. In the macroscopic plastic strain space the memory surface is described by,

$$F = \sqrt{(\boldsymbol{\epsilon}^p - \boldsymbol{\epsilon}_c) : (\boldsymbol{\epsilon}^p - \boldsymbol{\epsilon}_c)} - q \leq 0 \tag{4.39}$$

where $\boldsymbol{\epsilon}^p$ is the logarithmic plastic strain tensor and $\boldsymbol{\epsilon}_c$ and q are the center and radius of the memory surface, respectively. The memory surface evolves according to

$$\dot{\boldsymbol{\epsilon}}_c = (1 - \nu)\, H(F) \langle \mathbf{n} : \mathbf{n}^* \rangle \mathbf{n}^* dp \tag{4.40}$$

and

$$\dot{q} = \left[\nu H(F) - (1 - H(F)) (\xi q)^{\omega}\right] \langle \mathbf{n} : \mathbf{n}^* \rangle dp \tag{4.41}$$

where ν, ξ, and ω are material constants. H is the Heaviside function, $dp = \sqrt{\mathbf{D}^p : \mathbf{D}^p}$, and $\mathbf{n}$ and $\mathbf{n}^*$ are the unit normal of the plastic strain rate and memory surface, respectively, *i.e*,

$$\mathbf{n} = \frac{\mathbf{D}^p}{||\mathbf{D}^p||} \tag{4.42}$$

and

$$\mathbf{n}^* = \frac{\boldsymbol{\epsilon}^p - \boldsymbol{\epsilon}_c}{||\boldsymbol{\epsilon}^p - \boldsymbol{\epsilon}_c||} \tag{4.43}$$

To incorporate the strain-range dependent cyclic hardening or softening, the material constants in the backstress evolution are related to the memory parameters according to

$$\dot{r}_i = b\,(Q_i - r_i)\left|1 - \frac{r_i}{Q_i}\right|^m dp \tag{4.44}$$

where b, Q_i, and m are material constants. All constants are defined in [144].

Validation of this particular model was based on its ability to capture specific characteristics of saturated cyclic stress strain curves depending on changes in crystal orientation, transient strain hardening, dislocation structure evolution, and microstructural rearrangement due to high-low sequence loading. The model was compared to experimental data for Cu crystals oriented for single and multiple slip as seen in Figure 4.3. The authors considered the fact that different regions of the cyclic stress strain curve correlate with the development of varying dislocation structures as shown in Figure 4.2. Region A is associated with the formation of vein like dislocations and only the primary slip systems are experimentally observed to be active. Region B which is associated with the formation of PSBs can have multiple active slip systems, but one system will dominate. In Region C, the latent slip systems are active to the same degree as the primarily slip system. The simulations predicted similar results. In Region B, nine slip systems were predicted to be active but the slip amplitudes of the latent systems were very small. At larger resolved strain amplitudes in Region C, the simulation predicted again nine active slip systems, but

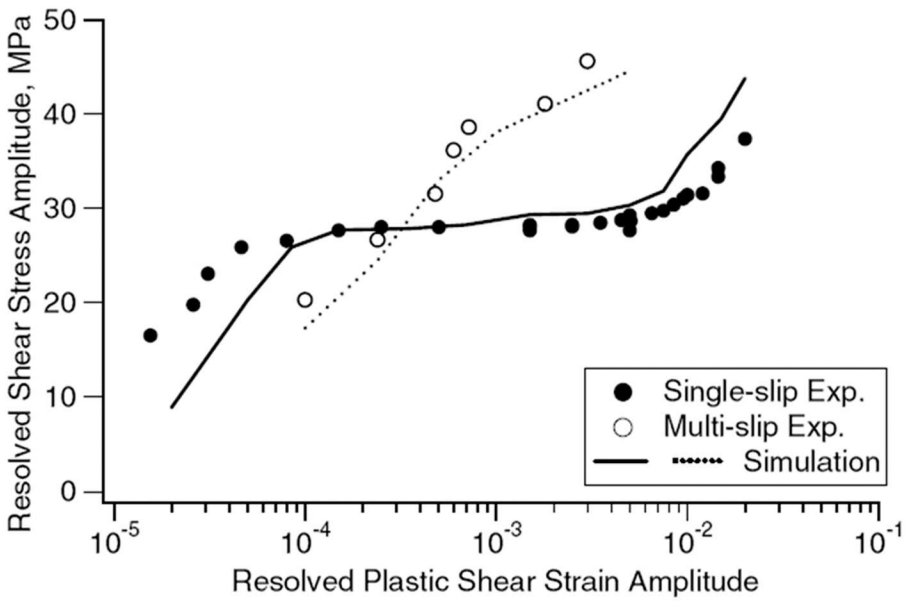

Figure 4.3: Resolved shear stress amplitude versus resolved plastic shear amplitude for Cu crystal plasticity model versus experiment (Reprinted from [144], with permission, copyright Elsevier).

three latent slip systems had slip amplitudes on the same order as that of the primary slip system. The model also correlated with the experimental observation that multiple slip is accompanied with additional latent hardening that is not present in single slip; this is captured by the latent hardening terms in $h^{\alpha\beta}$. The model was also able to capture the evolving hysteresis loops as the number of loading cycles increased as seen in Figure 4.4. The slip characteristics of the high-low sequence loading of the model also correlated well with experiments.

4.3.2 Ni-base superalloy IN100

Ni-base superalloys are typically used in aircraft gas turbine engines due to their high strength and creep resistance at high temperatures, primarily due to the existence of coherent γ' Ni_3Al precipitates of Ll_2 fcc structure dispersed in the γ austenitic Ni solid solution matrix which is of fcc crystal structure. Generally these alloys are more complex to model because of their tension-compression asymmetry and the non-Schmid characteristics of the Ni_3Al phase due to dislocation core spreading effects. The grain size of the primary γ

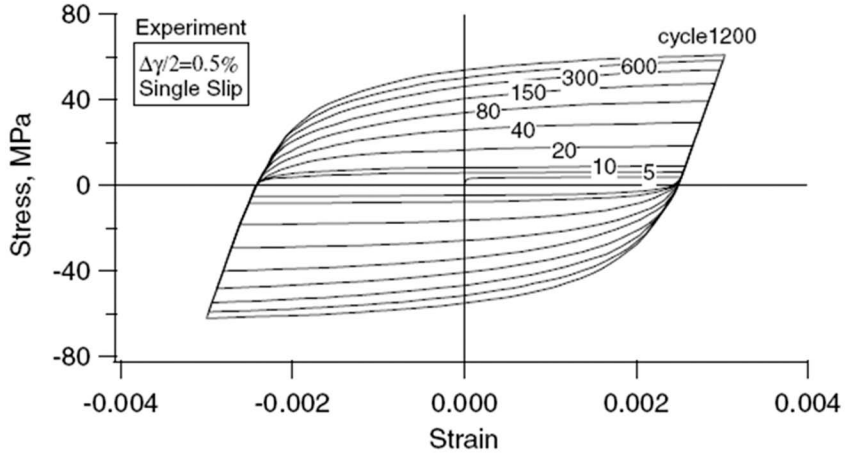

(a)

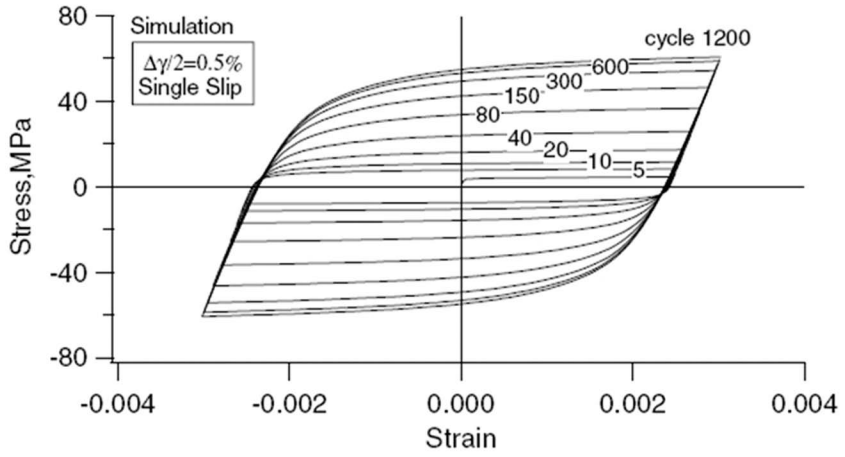

(b)

Figure 4.4: Cyclic stress-strain hysteresis loops for Cu: (a) experiment and (b) simulation (Reprinted from [144], with permission, copyright Elsevier)

phase along with the size and spacing of the coherent γ' precipitates can greatly affect the material response of these material systems. For example, dislocation mechanisms change from precipitate shearing to bypassing by Orowan looping depending on the spacing, size and volume fraction of the γ' precipitates.

Shenoy *et al.* [146–148] developed a crystal plasticity framework to model polycrystalline Ni-base superalloys. In this model the γ' precipitates are not explicitly modeled, but the influence of primary, secondary and tertiary γ' precipitates are included through ISVs. Also incorporated in the model, is the average effect of the grain size on the constitutive response and the dependence of the flow stress on crystallographic orientation. The version of the model presented here and in [149] is slightly different from what was originally introduced by Shenoy *et al.* [146–148].

A two term rate-dependent flow rule was applied based on the form proposed by Chaboche [150], *i.e.*,

$$\dot{\gamma}^{\alpha} = \left[\dot{\gamma}_1 \left\langle \frac{|\tau^{\alpha} - \chi^{\alpha}| - \kappa^{\alpha}}{D^{\alpha}} \right\rangle^{n_1} + \dot{\gamma}_2 \left\langle \frac{|\tau^{\alpha} - \chi^{\alpha}|}{D^{\alpha}} \right\rangle^{n_2} \right] \operatorname{sgn}(\tau^{\alpha} - \chi^{\alpha}) \tag{4.45}$$

where $\dot{\gamma}_1$ and $\dot{\gamma}_1$ are constants, n_1 and n_2 are flow exponents, κ^{α} is called the threshold stress and D^{α} is an constant average drag resistance. There is no embedded temperature dependence of these constants because the model was calibrated at a single temperature of 650°C. The advantage of this two term flow rule is that it is able to approximate the power law breakdown regime at higher strain rates [150]. The first term in the flow rule captures the dominant cyclic behavior while the second term incorporates the affects of thermally activated flow. The backstress χ^{α} captures the Bauschinger effect due to the homogenized response of the γ' precipitates in the γ matrix.

The threshold stress κ^{α} predicts initial flow for a given temperature, microstructural state and intrinsic slip resistance and is formulated as

$$\kappa_{\lambda}^{\alpha} = \kappa_{o,\lambda}^{\alpha} + \alpha_t \tilde{\mu} \tilde{b} \sqrt{\rho_{\lambda}^{\alpha}} \tag{4.46}$$

where λ indicates either octahedral or cubic slip. Shenoy *et al.* [146–148] consider both the standard 12 octahedral $\langle 110 \rangle \{111\}$ slip systems and 6 cube slip systems $\langle 110 \rangle \{100\}$. The cube slip systems describe "zig-zag" octahedral slip in the γ matrix or shearing of the γ' precipitates along {001} planes which has been observed at higher homologous temperatures for crystals/grains oriented for hard octahedral slip [151, 152]. ρ^{α} is the dislocation density, $\tilde{b}$ is the equivalent burgers vector and $\tilde{\mu}$ the equivalent shear modulus, *i.e.*,

$$\tilde{b} = \left(f_{p1} + f_{p2} + f_{p3}\right) b_{\gamma'} + f_{\gamma} b_{\gamma} \tag{4.47}$$

$$\tilde{\mu} = \left(f_{p1} + f_{p2} + f_{p3}\right) \mu_{\gamma'} + f_{\gamma} \mu_{\gamma} \tag{4.48}$$

where $b_{\gamma'}$ and b_{γ} and $\mu_{\gamma'}$ and μ_{γ} are the burgers vectors and shear moduli for the precipitate and matrix phases, respectively. The volume fractions of primary, secondary and tertiary γ' precipitates and the matrix phase are given by f_{p1}, f_{p2}, f_{p3} and f_{γ}, respectively. Also α_t is a statistical coefficient that accounts for the deviation from the regular spatial arrangements of the dislocation population. The initial critical resolved shear stress is given by

$$\kappa^{\alpha}_{o,oct} = \left[\left(\tau_{o,\gamma}\right)^{n_{\kappa}} + \Psi_{oct}\left(f_{p1}, d_2, f_{p2}, d_3, f_{p3}\right)^{n_{\kappa}}\right]^{\frac{1}{n_{\kappa}}} + \left(f_{p1} + f_{p2}\right)\tau^{\alpha}_{ns} \tag{4.49}$$

and

$$\kappa^{\alpha}_{o,cub} = \left[\left(\tau_{o,\gamma}\right)^{n_{\kappa}} + \Psi_{cub}\left(f_{p1}, d_2, f_{p2}, d_3, f_{p3}\right)^{n_{\kappa}}\right]^{\frac{1}{n_{\kappa}}} \tag{4.50}$$

where

$$\Psi_{oct} = \Psi_{cub} = \left[c_{p1}\sqrt{\zeta\frac{f'_{p1}}{d_1}} + c_{p2}\sqrt{\zeta\frac{f'_{p2}}{d_2}} + c_{p3}\sqrt{\zeta f'_{p3} d_3} + \frac{c_{gr}}{\sqrt{d_{gr}}}\right] \tag{4.51}$$

The normalized precipitate volume fractions are define as

$$
\begin{aligned}
f'_{p1} &= \frac{f_{p1}}{f_{p1}+f_\gamma} \\
f'_{p2} &= \frac{f_{p2}}{f_{p2}+f_\gamma} \\
f'_{p3} &= \frac{f_{p3}}{f_{p3}+f_\gamma}
\end{aligned}
\tag{4.52}
$$

In addition, ζ describes a normalize anti-phase boundary energy, *i.e.*,

$$
\zeta = \frac{\Gamma_{ABP}}{\Gamma_{APB_{ref}}} \tag{4.53}
$$

where $\Gamma_{APB_{ref}}$ is a reference anti-phase boundary energy. c_{p1}, c_{p2}, c_{p3}, and c_{gr} are parameters used to fit the initial experimentally observed yield. The average size of the primary, secondary, and tertiary precipitates is given by d_1, d_2, and d_3, respectively. The non-Schmid stress dependence of the octahedral slip systems is modeled as

$$
\tau^\alpha_{ns} = h_{pr}\tau^\alpha_{pr} + h_{cb}\left|\tau^\alpha_{cb}\right| + h_{se}\tau^\alpha_{se} \tag{4.54}
$$

where the resolved shear stresses on the primary, cubic and secondary slip systems are τ^α_{pr}, τ^α_{cb} and τ^α_{se}, respectively. h_{pr}, h_{cb} and h_{se} are constants. Evolution of dislocation density is modeled by

$$
\dot{\rho}^\alpha_\lambda = h_o\left(Z_o + k_1\sqrt{\rho^\alpha_\lambda} - k_2\rho^\alpha_\lambda\right)|\dot{\gamma}^\alpha| \tag{4.55}
$$

where Z_o is the initial geometrically necessary dislocation density which is calculated according to

$$
Z_o = \frac{k_\delta}{b d_{\delta_{eff}}} \tag{4.56}
$$

The equivalent precipitate spacing is approximated by

$$
d_{\delta_{eff}} \approx \frac{2}{d_{2\delta}}^{-1} \tag{4.57}
$$

The values k_1, k_2 and k_δ are constants. $d_{2\delta}$ is the secondary precipitate spacing. The self-hardening rate is given by h_o.

Finally, the backstress evolution is modeled as

$$\dot{\chi}_\lambda^\alpha = C_\chi \left(\eta \tilde{\mu} \tilde{b} \sqrt{\rho_\lambda^\alpha} \mathrm{sgn}\left(\tau^\alpha - \chi_\lambda^\alpha\right) - \chi_\lambda^\alpha \right) |\dot{\gamma}^\alpha| \tag{4.58}$$

where C_χ is a fitting parameter and

$$\eta = \frac{\nu_o Z_o}{Z_o + k_1 \sqrt{\rho_\lambda^\alpha}} \tag{4.59}$$

represents the ratio of backstress amplitude to the cyclic flow stress. ν_o accounts for the contribution due to the geometrically necessary dislocations.

Various material constants in the model were obtained from a range of experimental studies reported in the literature and the remaining parameters were obtained by fitting the response to experimentally measured stress-strain curves. The calibrated model parameters are given in Table 4.1 for the microstructure in the subsolvous condition at 650°C. The sizes and volume fraction of the γ' precipitates are given by $f_{p1} = 0.053$, $d_1 = 1 \times 10^{-3}$mm, $d_2 = 320 \times 10^{-6}$mm, $f_{p2} = 0.439$, $d_3 = 17 \times 10^{-6}$mm, $f_{p3} = 0.078$, and the mean grain size is $d_{gr} = 6.6 \times 10^{-3}$mm. The effective precipitate spacing is estimated to be $d_{\delta_{eff}} = 9.68 \times 10^{-6}$mm. Initial values of all slip system back stresses are set to zero. The model was calibrated for a range of microstructures with complex loading histories as described in [146–148].

4.3.3 Duplex Ti-6Al-4V

Ti-6Al-4V is also of significant importance in aerospace applications because of its high strength and desirable strength-to-weight ratio. Ti-6Al-4V exhibits favorable properties at elevated (but moderate) temperatures depending on heat treatments and thermomechanical processing. The microstructure of Ti-6Al-4V can range from bimodal to fully lamellar. A bimodal microstructure develops by applying deformation when the material is in the $\alpha + \beta$ regime (on a phase diagram) followed by recrystallization and aging. This processing route generates a microstructure that consists of equiaxed primary α grains dispersed

Table 4.1: Parameters of the microstructure- sensitive crystal plasticity model for IN100 at 650°C.

$\tau^{\alpha}_{o,oct}$ (MPa)	$\tau^{\alpha}_{o,cub}$ (MPa)	c_{p1}	c_{p2}	c_{p3}	c_{gr} (MPa $\sqrt{mm}$)	k_{δ}
85.1	170.2	1.351	1.351	1.22×10^5	9.432	2.5×10^{-3}

$b_{\gamma'}$ (nm)	b_{γ} (nm)	$\mu_{\gamma'}$ (MPa)	μ_{γ} (MPa)	k_1 (mm^{-1})	k_2	h_o
0.25	0.41	81,515	130,150	2.6×10^5	8.2	4.8 (oct), 2.4 (cub)

h_{pr}	h_{cb}	h_{se}	ν_o	$\Gamma_{APB}\left(=\Gamma_{APB_{ref}}\right)$ (J/m^2)	$\dot{\gamma}_1$ (s^{-1})	$\dot{\gamma}_2$ (s^{-1})
0.8	0.0	−0.4	2.82	164×10^{-3}	8.7	3.9×10^{-11}

$C_{11\gamma'}$	$C_{12\gamma'}$	$C_{44\gamma'}$	$C_{11\gamma}$	$C_{12\gamma}$	$C_{44\gamma}$	n_k
135,000	59,210	81,515	158,860	73,910	130,150	1

D^{α} (MPa)	n_1	n_2	$\rho^{\alpha}_{\lambda}(0)$ (mm^{-2})	α^{*}_{t} (MPa)	C^{*}_{χ} (MPa)
150 (oct), 180 (cub)	15	9	1.0×10^5	0.0385	2.713

* Specific values for this microstructure, with all other parameters independent of microstructure

among regions containing transformed β grains with embedded α laths. Texture effects in these alloys are particularly pronounced due to the low symmetry of crystallographic slip and anisotropic elasticity, as well as the contrast of properties between the α and β phases. In addition, despite their greater number of available slip systems, the colony regions containing α and β laths tend to be more resistant to slip than the primary α grains due to the presence of the $\alpha - \beta$ interfaces and, in some cases, finer α precipitates.

The crystal plasticity model considered here for duplex Ti-6Al-4V was initially developed by Mayeur and McDowell [153], extended by Zhang and McDowell [154] and then Bridier *et al.* [155]. In particular, Bridier *et al.*, tailored the model specifically for application to the HCF loading regime for peak stresses at or below the macroscopic yield strength. The duplex microstructure simulated here consists of a primary hexagonal closed packed (hcp) α grains and colony grains with secondary α phase intermittent with body-centered cubic (bcc) β phase in the form of a lamellar structure. In hcp primary α, there are four different families of slip systems: three $\left\langle 11\bar{2}0\right\rangle (0001)$ basal, three $\left\langle 11\bar{2}0\right\rangle \left\{10\bar{1}0\right\}$ prismatic, six $\left\langle 11\bar{2}0\right\rangle \left\{10\bar{1}1\right\}$ first order pyramidal $\langle a\rangle$ and twelve $\left\langle 11\bar{2}3\right\rangle \left\{10\bar{1}1\right\}$ first order pyramidal $\langle a+c\rangle$ slip systems. However, slip is dominate in the basal and prismatic slip systems due to a relatively low critical resolved shear stress when compared to the other slip systems.

The lamellar $\alpha + \beta$ colonies are homogenized in this model since the individual laths range in thickness from hundreds of nanometers to several microns. A crystallographic burgers orientation relation (BOR) is maintained between the secondary α and β lathes defined such that $(0001)_\alpha \,//\, \{101\}_\beta$ and $\left\langle 11\bar{2}0 \right\rangle_\alpha \,//\, \langle 111 \rangle_\beta$. The 24 possible slip systems in the lamellar region include three $\left\langle 11\bar{2}0 \right\rangle (0001)$ basal , three $\left\langle 11\bar{2}0 \right\rangle \left\{ 10\bar{1}0 \right\}$ prismatic, six $\left\langle 11\bar{2}0 \right\rangle \left\{ 10\bar{1}1 \right\}$ first order pyramidal $\langle a \rangle$ and twelve $\langle 111 \rangle \{110\}$ bcc slip systems. The bcc slip systems are transformed into the hexagonal coordinate system via the BOR. Hard systems in these colonies are those that intersect the $\alpha - \beta$ interface. Soft deformation modes are those on which dislocations glide parallel to the $\alpha - \beta$ interface or have parallel slip planes in both the secondary α and β phases.

The slip rate $\dot{\gamma}^\alpha$ for each slip system α is defined according to the flow rule of the form

$$\dot{\gamma}^\alpha = \dot{\gamma}_o \left\langle \frac{|\tau^\alpha - \chi^\alpha| - \kappa^\alpha}{D^\alpha} \right\rangle^M \operatorname{sgn}(\tau^\alpha - \chi^\alpha) \tag{4.60}$$

where $\dot{\gamma}_0$ is the reference shearing rate, χ^α is the backstress, κ^α is the threshold stress, and D^α is the drag stress, each for slip system α. The Macaulay bracket in the flow rule is defined such that $\langle x \rangle = x$ if $x \geq 0$ and $\langle x \rangle = 0$ otherwise, for any real number x (*i.e.*, $x \in \Re$). The inverse strain-rate sensitivity exponent M controls the rate sensitivity of the flow.

The initial backstress of each slip system is zero and evolves according to a modified Armstrong-Fredrick direct hardening/dynamic recovery relation, *i.e.*,

$$\dot{\chi}^\alpha = h\dot{\gamma}^\alpha - h_D \chi^\alpha |\dot{\gamma}^\alpha| \tag{4.61}$$

with $\chi^\alpha (t = 0) = 0$.

The threshold stress is defined as

$$\kappa^\alpha = \frac{\kappa_y}{\sqrt{d^\alpha}} + \kappa_s^\alpha \tag{4.62}$$

where the first term employs a Hall-Petch type formulation with d^α defined as the microstructural dimension of the free slip length and κ_y as the Hall-Petch slope. The second term is a softening parameter. Evolution of the threshold stress is governed by

$$\dot{\kappa}_s^\alpha = -\mu\kappa_s^\alpha |\dot{\gamma}^\alpha| = \dot{\kappa}^\alpha = -\mu\left(\kappa^\alpha - \frac{\kappa_y}{\sqrt{d^\alpha}}\right)|\dot{\gamma}^\alpha| \tag{4.63}$$

where μ is a constant. There is no evolution of the drag stress, *i.e.*, $\dot{D}^\alpha = 0$. The constant value of the drag stress is obtained as the difference between the critical resolved shear stress and the initial threshold stress on slip system α, *i.e.*,

$$\tau_{CRSS}^\alpha = \kappa^\alpha(t=0) + D^\alpha = \frac{\kappa_y}{\sqrt{d^\alpha}} + \kappa_s^\alpha(t=0) + D^\alpha \tag{4.64}$$

The model parameters estimated by Bridier *et al.* based on experiments [155] are given in Table 4.2.

As slip was observed experimentally to be more limited in the colonies than in the primary α grains, the initial CRSS values were assumed to be related to the same values in the primary α grains according to

$$\tau_{CRSS}^\alpha(\alpha+\beta \text{ colonies}) = 1.25\tau_{CRSS}^\alpha(\text{primary } \alpha \text{ grains}) \tag{4.65}$$

4.4 Integration of large strain based crystal plasticity relations

The relations for these types of large strain based crystal plasticity constitutive relations can be very stiff to integrate numerically. Both explicit and implicit schemes have been applied. Explicit schemes estimate the independent variables at the end of the time step based on the the values and derivatives of the independent variables at the start of the time step. Implicit schemes estimate the values of the independent variables at the end of the time step based on their values at some time greater then the start of the time step and less then or equal to their value at the end of the time step. Explicit integration schemes typically require

extremely small time steps to ensure proper convergence and that the Courant-Friedrichs-Lewy condition [156] is satisfied. The Courant-Friedrichs-Lewy condition ensures that the numerical domain of dependence includes the analytical domain of dependence so that the information necessary for the solution is accessible. Because of this requirement, application of explicit integration schemes is typically limited to dynamic problems. In contrast, implicit integration schemes require iterative approaches to estimate the values of the independent variables because the independent variables are only known with any certainty at the start of the time step. Because implicit schemes are not extrapolating to estimate the solution, typically much larger time steps can be taken. Thus, implicit schemes are typically preferred for static or quasi-static problems.

Some recent explicit schemes used to estimate dynamic response have been derived by many authors (*e.g.*, [157–161]). Implicit integration schemes for large strain base crystal plasticity relations have also be demonstrated by many (*e.g.*, [162–165]). Approximate implicit schemes based on numerical estimates of the global tangent stiffness matrix are outlined by Kalidindi and Anand [134]. McGinty [166] proposed a scheme with implicit update of the slip rates and explicit update of the hardening terms. The crystal plasticity models for IN100 and Ti-6Al-4V exercised in this work are integrated using the scheme presented by McGinty [166]. This integration scheme is presented in detail for the Ti-6Al-4V crystal plasticity model in Appendix A.

4.5 Summary

Here the relations for large strain based crystal plasticity constitutive relations based on the multiplicative decomposition of the deformation gradient into the elastic and plastic parts are reviewed. These types of constitutive models must satisfy the second law of thermodynamics. Specifically, flow rules and hardening laws formulated to simulated cyclic plasticity on the scale of the individual grains were considered for pure copper, the Ni-base

superalloy IN100 and the duplex $\alpha + \beta$ Ti alloy Ti-6Al-4V. The reviewed constitutive models for the specific material systems consider here each demonstrated a predictive ability to simulate macroscale cyclic stress-strain response. Additionally, these models are formulated to estimate the localized slip dependent behavior, particularly due to changing grain orientation relative to the loading direction and the evolving resistance to slip. Formulations were considered for both direct and latent hardening. The relations defining the evolution of the backstress for the various models were shown to capture the Bauschinger effect on the macroscale. Research into constitutive laws beyond what has been covered here is beyond the scope of this dissertation. The objective here is to apply these types of models to simulate the local cyclic plastic strain response in polycrystalline microstructure on the scale of the grains to estimate the driving forces for fatigue crack formation via certain FIPs as introduced in Section 2.3.1. The latter two models discussed for the Ni-base superalloy IN100 and duplex Ti-6Al-4V will be applied in this manner in Chapters 6 and 7, respectively.

Table 4.2: Model parameters for the duplex $\alpha + \beta$ Ti-6Al-4V crystal plasticity model.

Elastic Stiffness	C_{11}	162,400 MPa
	C_{12}	92,000 MPa
	C_{13}	69,000 MPa
	C_{33}	180,700 MPa
	C_{44}	49,700 MPa
Flow Rule	$\dot{\gamma}_o$	0.001 s^{-1}
	M	15
Backstress	$\chi^{\alpha}(0)$	0
	h	40,000
	h_D	8000
Threshold Stress	κ_y	17.3 MPa $mm^{-0.5}$
	$\kappa_s^{\alpha}(0)$	150 MPa
	μ	50
CRSS	$\tau_{CRSS}^{\langle 11\bar{2}0\rangle(0001)}\left(\alpha_p\right)$	420 MPa
	$\tau_{CRSS}^{\langle 11\bar{2}0\rangle\{10\bar{1}0\}}\left(\alpha_p\right)$	370 MPa
	$\tau_{CRSS}^{\langle 11\bar{2}0\rangle\{10\bar{1}1\}}\left(\alpha_p\right)$	490 MPa
	$\tau_{CRSS}^{\langle 11\bar{2}3\rangle\{10\bar{1}1\}}\left(\alpha_p\right)$	590 MPa

CHAPTER V

INSTANTIATION OF MICROSTRUCTURE VOLUME ELEMENTS FOR FE SIMULATION

5.1 Introduction

In Chapter 5 consideration is given regarding the instantiation and simulation of microstructure volume elements via the FEM. FE simulation of microstructure on a scale sufficient to resolve micron size features (*e.g.* grains, grain boundaries, phases, inclusions) is an active area of research and there are many fundamental questions that are currently being pursued. Some of the questions pertinent to this dissertation include:

- How to properly scale simulation volumes to effectively estimate distributions in response for damage type processes (*e.g.*, fatigue) that are dependent on extreme value microstructure attributes?
- How to instantiate statistical realizations of experimentally characterized volumes of microstructure?
- How to appropriately mesh microstructure such that the response fields around the microstructural features of interest are sufficiently resolved?
- How to appropriately apply boundary conditions to estimate response for various loading and service conditions?

Much of the on going work into the development of appropriate statistically representative microstructure volumes elements for FE simulations is beyond the scope of this dissertation. The purpose here is to apply currently available methods (published in the literature) to instantiate microstructure volumes such that the extreme value driving forces on the

scale of the crystallographic attributes can be estimated. It is not in the scope of this dissertation to evaluate the effectiveness of these methods beyond their applicability to the microstructure-sensitive extreme value probabilistic framework as it is presented in this dissertation.

In this chapter, proper scaling of simulation volumes to estimate distributions of extreme value response will first be considered. Representative volume element (RVE) and statistical volume element (SVE) will be defined. Of particular interest is the ability to estimate the extreme value tails of the response distribution via multiple simulated SVEs. Next, currently available methods for microstructural reconstruction will be considered. Specifically, two different methods will used in this work to instantiate microstructure volume elements for FE simulation of polycrystalline microstructures. First, a method based on the Voronoi tessellation is applied to partition space into a set of convex grains. Optimization routines are applied to then fit distributions of grain size by perturbing the grain centers via a simulated annealing approach. The grain orientation and disorientation distributions can also be fit to prespecified distributions. Another algorithm to instantiate microstructure volume elements is also considered based on packing ellipsoids representative of grains into a volume. These ellipsoids are constructed based on the distributions of major ellipsoidal axis generated by fitting ellipsoids to a set of experimentally characterized grains in three dimensions. The grain orientation and disorientation distributions of the polycrystalline microstructures instantiated based on the ellipsoid packing algorithm are also fit to prespecified distributions. Simple voxellated meshing of these instantiated microstructure volume elements will be discussed. Formal definitions of the periodic boundary conditions applied to simulate subsurface volume elements will be presented. Finally, this chapter will consider the mesh quality of the simple voxellated meshes used in this work and the determination of minimum SVE size to study the grain scale cyclic plastic response as estimated via crystal plasticity constitutive relations.

5.2 Statistical volume elements

To effectively simulate the microstructure-induced variability of the extreme value driving forces for fatigue crack formation, it is desired to construct multiple instantiations of microstructure volume elements such that each volume element becomes a statistical sample of the underlying distribution of the response of interest (*e.g.* stress, elastic strain, plastic strain). In other words, these simulated volumes are a statistical volume element (SVE) for the locally varying heterogeneous response at the scale of the individual microstructure attributes. The concept of an SVE is in contrast to that of a representative volume element (RVE) that is defined such that the distribution of local response or effective response of the volume will not change based on where the RVE is sampled from the microstructure ensemble (*i.e.*, bulk material), or if it is further increased in size.

The concept of a representative volume element was originally proposed by Hill [167] who considered an RVE as representative of the entire microstructure ensemble in an average sense. Hashin and Shtrikman [168, 169] considered an RVE as a reference cube that is small relative to the entire body such that the volume average variables are the same in the reference cube and bulk. Various statistical measures have also been considered to define an RVE. For example, Li *et al.* [170] applied marked correlation functions (as described previously in Section 3.4.2) using cracked/uncracked particles as marks to define the size of a "representative material elements" (*i.e.*, RVEs) in a particle reinforced metal matrix composite. The length scales at which the marked correlation functions of the cracked/uncracked particles tended to unity were argued to be associated with the length scale required for a RVE. Shan and Gokhale [171] determined RVE size based on the nearest neighbor and stress distributions. Kanit *et al.* [172] defined a RVE based the variances of the topology, and elastic and thermal properties. Moreover, they showed that multiple SVEs can be employed to approximate the response of the RVE within some tolerance for mean property values. This is important because often it is more computationally favorable to simulate multiple SVEs than a single large RVE. Ostoja-Starzewski [173] has also considered the

relationship between the SVE and RVE in more detail. They note that as the size of the SVE increases it eventually approaches that of the RVE. Additionally, it is noted that because there is no periodicity in real heterogeneous random media, at finite scales the RVE can only be approximated. Willis [174] formally defined the RVEs based on statistical distributions as a statistically equivalent representative volume element or SERVE. In his work he used two-point correlation statistics to define a SERVE such that the statistical distributions of the samples SERVEs are equivalent regardless of where they are sampled in the microstructure. Similarly, Swaminathan *et al.* [175, 176] used marked correlation functions to define SERVEs for fiber reinforced composites. These SERVEs are described by the authors such that:

- Each SERVE has certain macroscopic response variables such as the macroscopic stress-strain response that are equivalent to the same properties of the bulk material.
- Distribution functions describing the local microstructure attributes are equivalent to those sample from the entire microstructure ensemble.
- The SERVE is independent of location in the local microstructure and applied loading direction.

In the previously listed approaches the RVE/SVE size was determined all or in part based on the distribution of response on the scale of the microstructure. Others have defined the RVE/SVE size based only on the heterogeneity of the microstructure regardless of the response. For example, Tschopp *et al.* [177] use area fractions of gray levels from gray scale micrographs to determine RVEs for orthotropic microstructures. This approach (that only considers heterogeneity of the microstructure) defines the RVE size based on the fact that when a sufficient area of gray level pixels from a micrograph are averaged, the resulting gray level is homogenized across the micrograph. The length scale of the averaging area at which the gray level is homogenized is argued to correspond to the length scale of the appropriate RVE for that microstructure volume. Additionally, Niezgoda *et al.* [178] define

an RVE/SVE based on the 2-point statistics of a certain microstructure function which describes the locally varying local state of the material. It is argued that because mapping from microstructure to properties as many-to-one that if the microstructure is represented to a high degree of accuracy then a broad range of properties will automatically be captured.

RVEs (or SERVEs) for distributions of extreme value response parameters are typically untenably large. This is particularly true when trying to capture extreme value distributions of microstructure-dependent response that affect rare event damage formation and growth. This implies that complete characterization of the tail of the probability distribution function for fatigue response requires a very large RVE. It is also noted that an RVE for one type of response might not be a RVE for another type of response. In contrast, SVEs for extreme value response of a responsible size are more tenable because it is not required to be able to characterize the entire distribution from one volume element. Each SVE for a given response response can be designed to be large enough such that the response parameter of interest at a particular location is unaffected by statistical variations in the microstructure at distances on the order of the size of the volume (*i.e.*, correlation length is less than size of SVE); however, the volume is not so large that it contains a statistically representative set of responses for that particular response parameter. Thus, each instantiated SVE provides a sample of the extreme value distribution for the entire ensemble. It is likely that with a sufficient number of SVEs the character of the extreme value distribution of a particular response can be adequately characterized for the ensemble.

In the present case, to estimate the local driving forces for fatigue crack formation in polycrystalline metallic alloys, cyclic plasticity on the scale of the individual grains is considered (a key driving force for fatigue damage formation as reviewed in Chapter 2). Crystal plasticity constitutive models such as those introduced in Chapter 4 can be applied to estimate the distributed plastic response over a set of simulated SVEs. These multiple simulated SVEs must be of sufficient size such that the lower order moments of the cyclic plastic response on the scale of the grains are unaffected by further increasing the volume

of the SVE. It is also desired that the SVE be suitably large to serve as a RVE in terms of the overall macroscopic (*i.e.*, effective) elastic/plastic response. In other words, the stress-strain response taken from any instantiation of the microstructure should be representative of any other. The RVE for this effective response is insensitive to the higher order moments of the slip distribution, and is not the same as a RVE for the extreme value distribution of FIPs. The SVE construct incorporates some of the logic behind the definition of the before mentioned SERVEs. However, SVEs do not require the distribution of response to be identical across a set of SVEs sampled from the microstructure ensemble. Being able to simulate variations in the local response via these types of SVEs allows the computational exploration of how microstructural heterogeneity affects fatigue variability.

Here it is noted that the the extreme value distributions of a given response variable will be dependent on the size of the SVE. As noted in Section 3.2, the the extreme value distribution will depend on sample size n. Moreover, as the sample size n tends to a very large size, the extreme value distribution will likely converge to one of the asymptotic forms listed in Section 3.2 (*i.e.*, the Gumbel (Type I) distribution, the Fréchet (Type II) distribution, or the Weibull (Type III) distribution). The SVEs for extreme value response introduced here are effectively samples each of size n. Sample size for a specific extreme value response parameter for a given SVE depends on the size of the dominant microstructure attributes that most influence the extreme value response. For example, to characterize the extreme value distribution of plasticity as parameterized by the effective plastic strain in polycrystalline metals, the dominant microstructure attribute could be that of the individual grains. Therefore, the sample size of an SVE for the extreme value distribution of the effective plastic strain would be dictated by the number of grains within that SVE. If the number of grains in the SVE is large enough, then the extreme value distribution of the effective plastic strain sampled over many SVE of the same size would likely converge to one of the three types of asymptotic extreme value distributions. SVEs could also be instantiated with fewer numbers of grains that might still satisfy the requirements of an SVE listed above

(the size is sufficient so that the lower order moments of the response of interest at any one location is not significantly effected by further increasing the volume); however, the number of grains or sample size might not be sufficient to estimate the asymptotic extreme value distribution of the response of interest. Depending on the application, a large sample size is not always desired. For example, if the application is dependent on the volume at a notch root, then it is not desirable to consider volumes larger than that of the notch root even if the extreme value distribution is not described by one of the standard asymptotically converged extreme value distributions.

5.3 Instantiation of microstructure volume elements

Much consideration has been given to the reconstruction of microstructure volumes based on various statistical parameters. Groeber *et al.* [8, 9, 103, 179] considered a variety of statistical measures to characterize and reconstruct volumes of the Ni-base superalloy IN100 including distributions of grain size, grain orientation and grain misorientation. Consideration was also given concerning the statistics of contiguous neighbors and grain shape. Distribution of grain shape, in this work, was characterized by considering the distribution of the ratios of the major elliptical axis of ellipsoids fit to a set of experimentally characterized grains (in three dimensions). Ellipsoids were also used to reconstruct a polycrystalline aluminum alloy with a rolled texture by Brahme *et al.* [180]. In this case, the morphology of the grains was determined from multiple EBSD scans taken on orthogonal sections.

The problem of reconstructing microstructure volume elements from special correlation statistics, particularly two-point correlation functions, has also been explored by several groups. Torquato and coworkers have considered reconstruction of two phase composites from two-point correlation functions in two and three dimensions [181, 182]. Others have shown how the efficiency of these reconstructions can be enhanced though an update of the two-point correlation functions rather than measuring it during each iterative step during the reconstruction [183]. Reconstruction of polycrystalline materials [184, 185], metal matrix

composites [186], and TiB whiskers in Ti-6Al-4V-1.0B [99], has also been accomplished from measured spatial correlation functions.

Here two methods will be considered to instantiate microstructure volume elements based on distributions of grain size, grain orientation and grain disorientation. The Voronoi tessellation based algorithm for the instantiation of polycrystalline microstructure volume elements employs the Voronoi tessellation to partition space into a set of convex grains. The grain size distribution is optimized via a simulated annealing algorithm by perturbing the grain centers via a Monte Carlo approach. The grain orientation and disorientation distributions are also fit to prespecified distributions using a simulated annealing optimization algorithm. The ellipsoid packing microstructure volume element instantiation constructs polycrystalline microstructure by packing ellipsoids representative of grains into a prespecified volume. These ellipsoids are constructed based on the distributions of major ellipsoidal axis that are generated by fitting ellipsoids to a set of experimentally characterized grains in three dimensions. The grain orientation and disorientation for this microstructure builder can also be fit to prespecified distributions via a simulated annealing algorithm.

5.3.1 Voronoi tessellation based polycrystalline microstructure volume element instantiation

A Voronoi tessellation is a mathematical construct that describes a space partitioned around predefined centers such that all points closer to a given center than any other is associated with that center. In this manner, the space is divided up into a set of space filling convex polyhedrons. The Voronoi tessellation is the duel of the Delaunay triangulation. Voronoi tessellations have been employed in many different applications and the geometrical concept behind this construction is well defined in the literature (*e.g.*, [187]). Fast Voronoi tessellation generation algorithms are readily available [188]. Gross and Li [189] evaluated Voronoi tessellations based on structure, topology and statistics relative to typical polycrystalline materials and observed that both topology and various statistical properties do not

agree well with those measured experimentally. They suggest that more realistic polycrystalline microstructure volume elements can be instantiated using optimization methods to randomly perturb the centroids of the Voronoi tessellated cells to match certain statistical distributions measured from actual material systems like grain size, grain volume, grain boundary length, *etc.* It was also suggested that optimization methods could be used to match various texture measurements such as orientation or misorientation/disorientation (*cf.* [118]). Modifying random Voronoi tessellations to match more realistic distributions of grain size has also been performed earlier by others [190, 191] to create RVEs for FE simulations. Recently, Zhang et al. [154] used modified Voronoi tessellations that were optimized with a simulated annealing algorithm to fit experimentally characterized statistics of orientation, disorientation, and phase volume fraction in multiphase Ti-6Al-4V to construct FE models for crystal plasticity simulations. Additionally, Shenoy *et al.* [147] constructed digital instantiations of the microstructure for IN100 using the same methods. Similar algorithms are used here to fit distributions of grain size, orientation and disorientation to construct SVEs for simulation of the microstructure.

The Voronoi tessellation microstructure volume element instantiation (VorPolycrystalGen) developed in this work was written in C++. This software instantiates SVEs for polycrystalline microstructures based on predefined distributions of grain size, grain orientation, and grain disorientation (*cf.* [192]). The logic of VorPolycrystalGen is as follows:

1. Using a Monte Carlo approach, a number of *grain centers* are randomly placed in a prespecified cuboidal volume.

2. The Voronoi tessellation is calculated based on the current location of the grain centers.

3. The grain volume distribution is determined for the grains defined by the Voronoi tessellation.

4. If the error tolerance between the difference of the target grain volume distribution

and model grain volume distribution is not satisfied, a grain center is selected at random and its position is perturbed on the order of a fraction of the average grain size in the three dimensional sample space. Acceptance of the change in the location of the grain center is determined by the simulated annealing algorithm based on the amount of improvement of the grain volume distribution of the instantiated SVE to the target grain volume distribution of the microstructure ensemble.

5. Steps 2 through 4 are repeated until the error tolerance is satisfied.

6. The crystal lattice of each grain is assigned an orientation randomly sampled from a predefined orientation distribution.

7. The disorientation distribution is calculated for the misorientation of the crystal lattices between all grain neighbors.

8. If the error tolerance between the target disorientation distribution and the model disorientation distribution is not satisfied, the orientation of two randomly selected grains are exchanged. Acceptance of the orientation change is determined by the simulated annealing algorithm.

9. Steps 7 - 8 are repeated until the error tolerance is satisfied.

The Voronoi tessellation is computed in VorPolycrystalGen using QHULL [188] (see www.qhull.org). By using the Voronoi tessellation, all points closer to a defined grain center than to any other grain center is associated with a single grain. An additional parameter is also input by the user that defines the ratio of the minimum distance between any two grain centers to average distance between the grain centers. This prevents grain centers from lying too close, thus also preventing the generation of very small Voronoi cells (*i.e.*, grains). A SVE instantiated for a typical polycrystalline microstructure can be seen in Figure 5.1. The target and optimized distributions for an arbitrary grain volume distribution normalized by an average grain volume are shown in Figure 5.2.

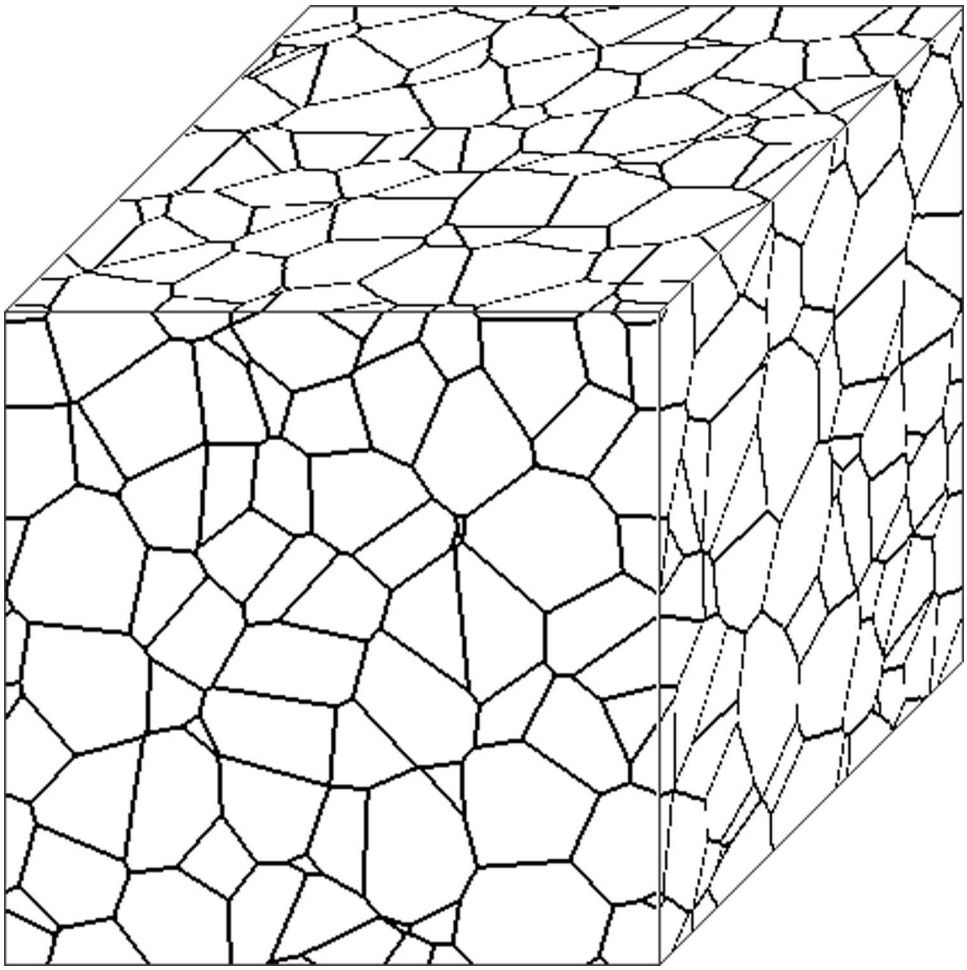

Figure 5.1: A SVE instantiated using VorPolycrystalGen.

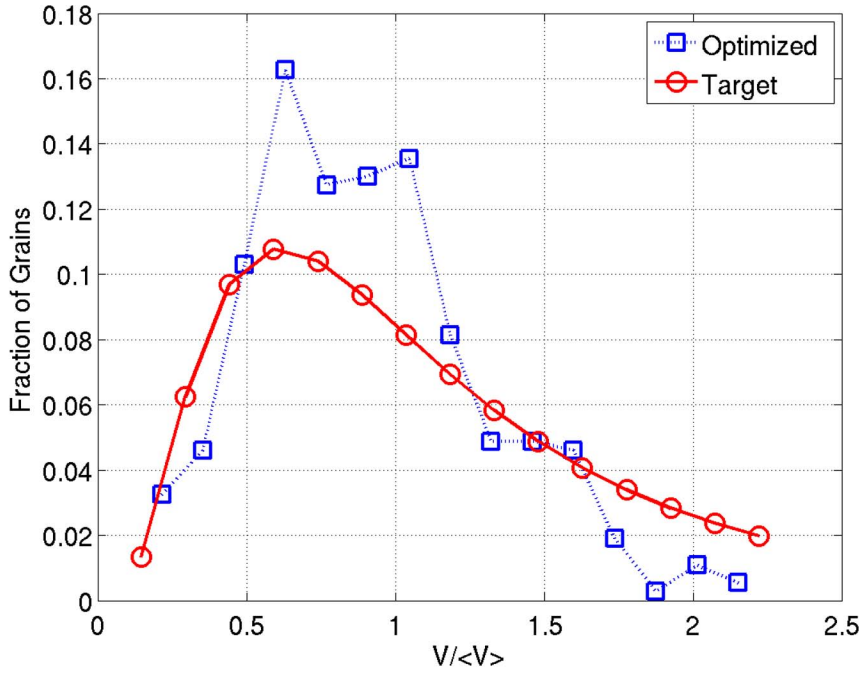

Figure 5.2: Target and optimized grain volume distributions generated using VorPolycrystalGen. The grain volume distribution is normalized by an average grain volume.

5.3.2 Ellipsoidal packing based microstructure volume element instantiation

Grain shape in general is difficult to quantify because of the general challenges associated with describing shape in three dimensions [193]. One way to describe approximate shape is to fit an ellipsoid in three dimension to an experimentally characterized grain [180, 185]. A systematic method has been developed to fit ellipsoids to voxel data describing three dimensional grain structure obtained via serial sectioning [8,9]. These *grain equivalent ellipsoids* offer a first order description of grain shape, aspect ratio, and volume. The approach taken here randomly generates grain equivalent ellipsoids based on predefined distributions of the ratios of the major ellipsoidal axis.

The the major axis of a grain equivalent ellipsoid $(2a, 2b, 2c)$ (defined such that $a > b > c$) can be estimated from the zeroth order moment (μ_{000}), the first-order moments ($\mu_{100}, \mu_{010}, \mu_{001}$) and the second-order moments ($\mu_{200}, \mu_{020}, \mu_{002}$) of a grain. Following MacSleyne *et al.* [194], the three dimensional moments μ_{pqr} of an object can be described by

$$\mu_{pqr} = \iiint x^p y^q z^r D(\mathbf{r})\, d\mathbf{r} \tag{5.1}$$

such that the position $\mathbf{r}$ is given in three dimensional real space defined by the basis $\hat{e}_i$ for $i = 1, 2, 3$ according to $\mathbf{r} = x\hat{e}_1 + y\hat{e}_2 + z\hat{e}_3$ (*i.e.*, $\mathbf{r} \in \Re^3$) and (p, q, r) is a triplet of positive integers. The indicator or characteristic function $D(\mathbf{r})$ defines an object or arbitrary shape at position $\mathbf{r}$, *i.e.*,

$$D(\mathbf{r}) = \begin{cases} 1 & \text{for } \mathbf{r} \text{ inside object} \\ 0 & \text{otherwise} \end{cases} \tag{5.2}$$

The order n of the moment is calculated by $n = p + q + r$.

The zeroth order moment corresponds to object volume, *i.e.* $V \equiv \mu_{000}$. The center-of-mass (COM) $(x_{COM}, y_{COM}, z_{COM})$ is given by the first order moments, *i.e.*,

$$\begin{aligned} x_{COM} &\equiv \tfrac{\mu_{100}}{V} \\ y_{COM} &\equiv \tfrac{\mu_{010}}{V} \\ z_{COM} &\equiv \tfrac{\mu_{001}}{V} \end{aligned} \tag{5.3}$$

If the object is located (or translated) so that its COM is coincident with the origin of the coordinate system $\hat{e}_i$, the moments calculated with respect to the COM are called *central moments*. Assuming hereafter all moments are calculated with respect to the COM, the second order moments can be defined in terms of a second rank tensor called the moment-of-inertia tensor $\mathbf{N}$, *i.e.*

$$\mathbf{N} = \begin{bmatrix} \mu_{020} + \mu_{002} & -\mu_{110} & -\mu_{101} \\ -\mu_{110} & \mu_{200} + \mu_{002} & -\mu_{011} \\ -\mu_{101} & -\mu_{011} & \mu_{200} + \mu_{020} \end{bmatrix} \tag{5.4}$$

When the object is oriented such that its principal axes are aligned with the coordinate basis $\hat{e}_i$, all non-diagonal moments vanish in the moment-of-inertia tensor. In this manner, the

ellipsoid with axes $(2a, 2b, 2c)$ aligned along the coordinate basis $\hat{e}_i$, respectively, is related to the second order moments according to

$$\begin{aligned} \mu_{200} &= a^5 \tfrac{4\pi}{15} \tau_1 \tau_2 \\ \mu_{020} &= a^5 \tfrac{4\pi}{15} \tau_1^3 \tau_2 \\ \mu_{002} &= a^5 \tfrac{4\pi}{15} \tau_1 \tau_2^3 \end{aligned} \tag{5.5}$$

where $b = a\tau_1$ and $c = a\tau_2$. Given a voxel dataset of experimentally characterized grains via serial sectioning, a distribution of equivalent grain aspect ratios b/a and b/c can be determined based on the calculated aspect ratios according to Equation 5.5.

Ellipsoidal packing polycrystalline microstructure volume element instantiation (EllipPolycrystalGen) was developed to instantiate polycrystalline microstructure volume elements based on distributions of the aspect ratios b/a and b/c of the equivalent ellipsoids. EllipPolycrystalGen employs an ellipsoidal packing based algorithm followed by an annealing algorithm to fill the remaining free space to instantiate polycrystalline models. The aspect ratio of the randomly placed ellipsoids b/a and b/c are determined by randomly sampling the experimentally characterized distributions of the aspect ratios. Using grain equivalent ellipsoids instead of other space filling methods like the Voronoi tessellation allows construction of more complex grain morphologies such as elongated grains common in rolled ductile metals, and facilitates more accurate reconstruction of two phase microstructures with bi-modal size distribution such as duplex Ti-6Al-4V. The logic of EllipPolycrystalGen is as follows:

1. An ellipsoid is generated by randomly selecting the aspect ratios of the major axes of the ellipsoid b/a and b/c from a predefined distribution (*e.g.*, beta distribution). The size of the ellipsoidal grain placed in the volume is taken to be some fraction of the size of the ellipsoid as determined by the random sample of the distribution of aspect ratios to account for the later annealing step that fills in the empty space of the model.

2. The orientation of the major axes of the ellipsoid relative to the sample coordinate system is randomly selected based on a predefined distribution.

3. The ellipsoid is randomly placed in the volume. If the ellipsoid overlaps with any previously placed ellipsoid, a new random location is selected repeatedly until no overlap exists (see Figure 5.3).

4. Steps 1 through 3 are repeated until the jamming limit is reached and no more non-overlapping ellipsoids can be placed in the volume.

5. The ellipsoids are then allowed to grow uniformly during an annealing step until all the space in the microstructure volume is filled (see Figure 5.4).

6. The crystal lattice of each grain is assigned an orientation by randomly sampling a predefined orientation distribution.

7. The disorientation distribution is calculated for the misorientation of the crystal lattices between all grain neighbors.

8. If the error between the target disorientation distribution and the model disorientation distribution is not satisfied, the orientation of two randomly selected grains are exchanged. Acceptance of the change is determined by the simulated annealing algorithm.

9. Steps 7 - 8 are repeated until the error tolerance is satisfied.

Instantiation of the microstructure volume elements is performed in MATLAB [195] and optimization of the orientation and disorientation distributions is performed in a C++ based program.

It is noted that there are some considerations that should be taken when instantiating microstructure volume elements Via EllipPolycrystalGen. Because the structure is generated with non-overlapping ellipsoids, care must be taken to appropriately define the size

fraction of the initial ellipsoids that are packed into the volume relative to the experimentally characterized (or target) grain equivalent ellipsoids. This helps to ensure that the final grain size distribution is representative of the experimentally characterized microstructures after the uniform growth algorithm is applied to fill in the empty space after no more non-overlapping ellipsoids can be placed in the volume (*i.e.*, the jamming limit is reached). Additionally, it is recognized that the microstructure will vary depending on how the ellipsoids are packed into the volume. For example, for a two phase structure different packing densities will be achieved depending on whether the larger phase is packed first, the smaller phase is packed first, or both phases are simultaneously packed into the volume. The jamming limit for these different approaches will vary significantly. More rigorous statistical parameters can be applied to ensure the instantiated microstructure volume element is sufficiently representative of the real experimentally characterized microstructure. For example, it might be important to consider the number of grain neighbors or ensure agreement between the correlation statistics for certain microstructure attributes between the experimentally characterized microstructures and the instantiated microstructure volume elements. Such consideration would of course increase the complexity of the algorithm. In this work, these types of more detailed statistical requirements are neglected.

A two-dimensional section of a microstructure volume element instantiated via EllipPolycrystalGen with a bi-modal grain size distribution is shown in Figure 5.5. Comparing the aspect ratios of the ellipsoids and final grains after applying uniform grain growth, the distributions of the aspect ratios of the original ellipsoids and the equivalent ellipsoids fit to the final grains were essentially the same for a typical bi-modal microstructure with near equiaxed grains, as shown in Figure 5.6. EllipPolycrystalGen gives the user much more control over grain morphology than other commonly used microstructure volume element instantiation algorithms like those based on the Voronoi tessellation and allows one to more easily generate bi-modal grain size distributions. Here, the tails of the distributions are captured with higher fidelity than the tails of the grain size distribution for the microstructure

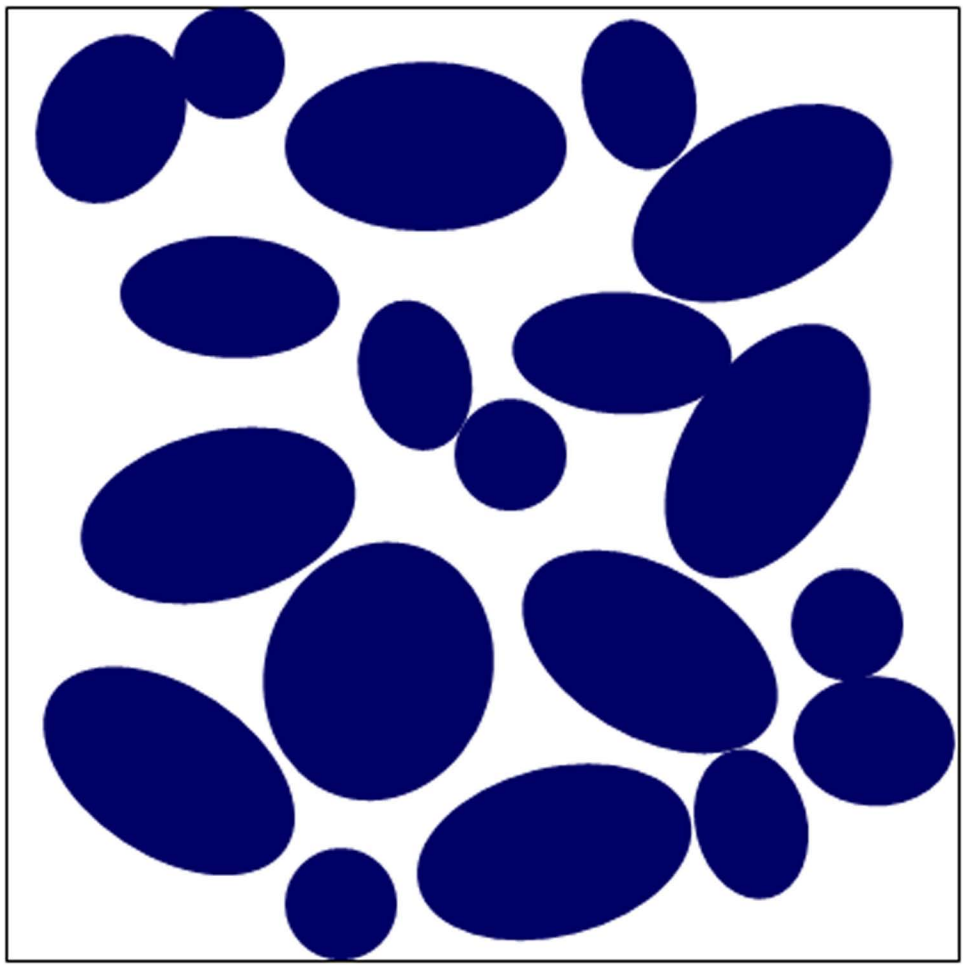

Figure 5.3: A schematic in two dimensions showing the packing of grain equivalent ellipsoids in an predefined area.

volume elements instantiated using the VorPolycrystalGen as can be seen by comparing Figures 5.2 and 5.5.

5.4 Applied FE mesh for instantiated microstructure volume elements

In this work, all instantiated SVEs are simulated in the commercially available FE package ABAQUS [121]. The microstructures are meshed by an array of evenly spaced linear eight node brick elements (type C3D8R) with reduced integration [121]. Once the polycrystalline microstructure is instantiated (via VorPolycrystalGen or EllipPolycrystalGen), the nodes and associated brick elements are automatically placed according to the mesh density input by the user (see Figure 5.7). In all cases the simulated SVEs are constructed as

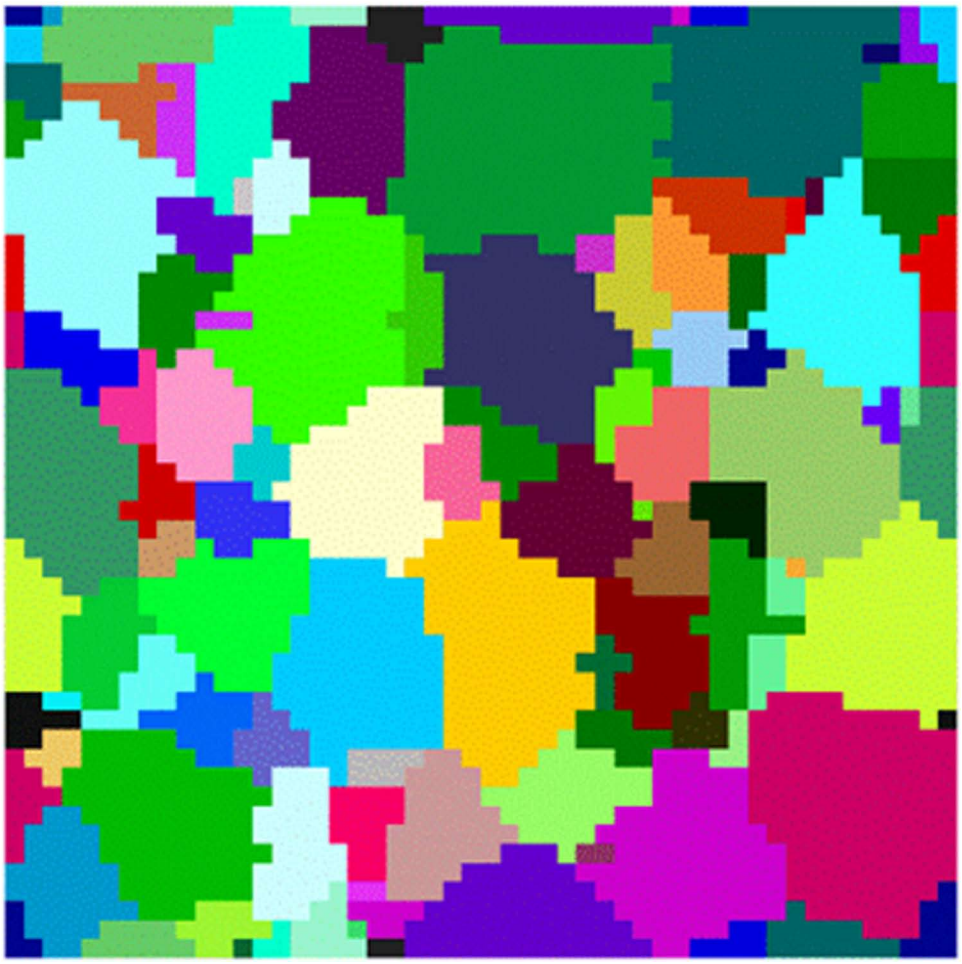

Figure 5.4: A two dimensional section of a microstructure instantiated using the ellipsoid packing algorithm with a bi-modal grain size distribution.

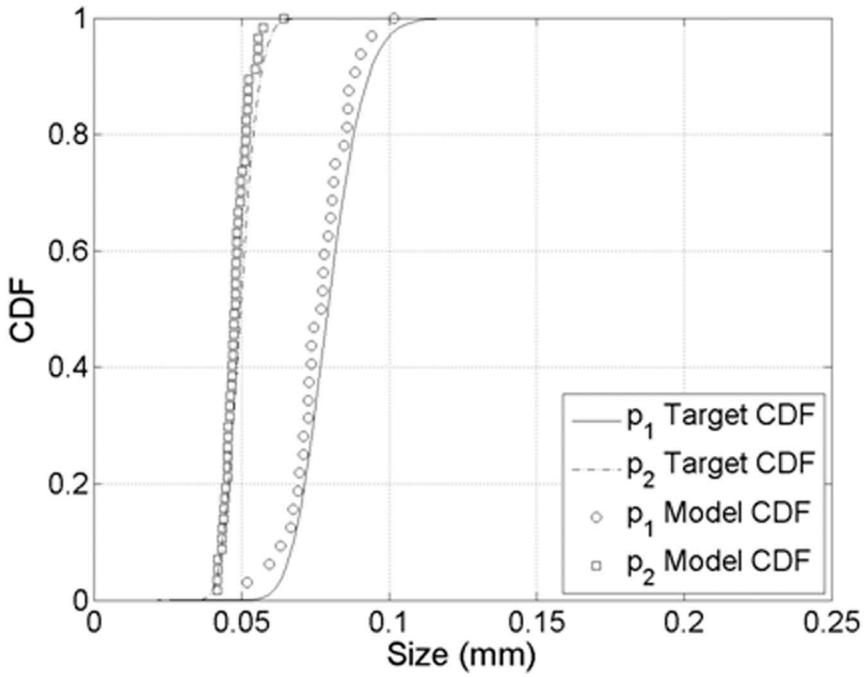

Figure 5.5: Target log-normal and fit model distributions for an arbitrary bi-modal grain size distribution generated via EllipPolycrystalGen.

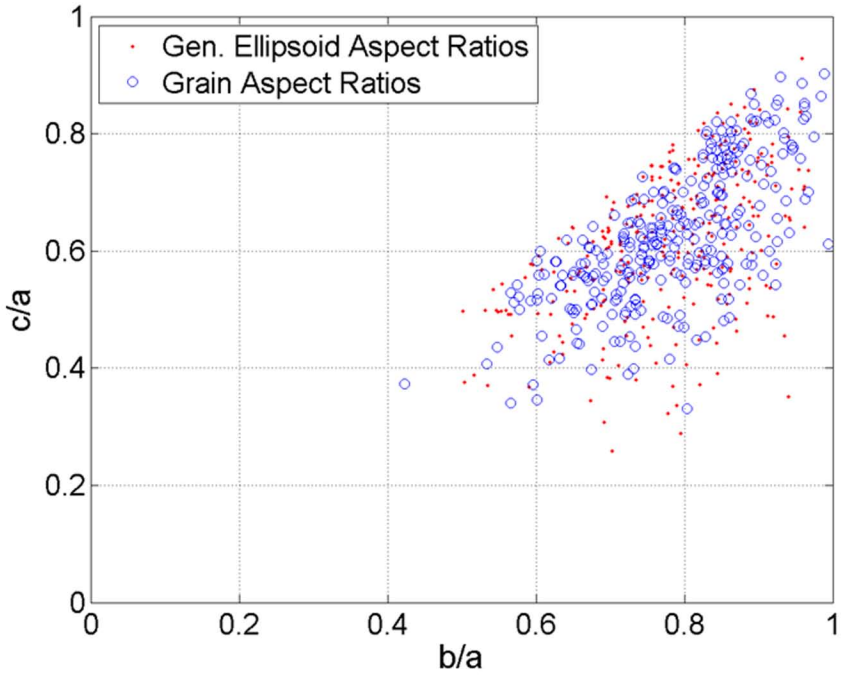

Figure 5.6: Aspect ratios of the initial generated ellipsoids (dots) and grains (circles) after uniform grain growth.

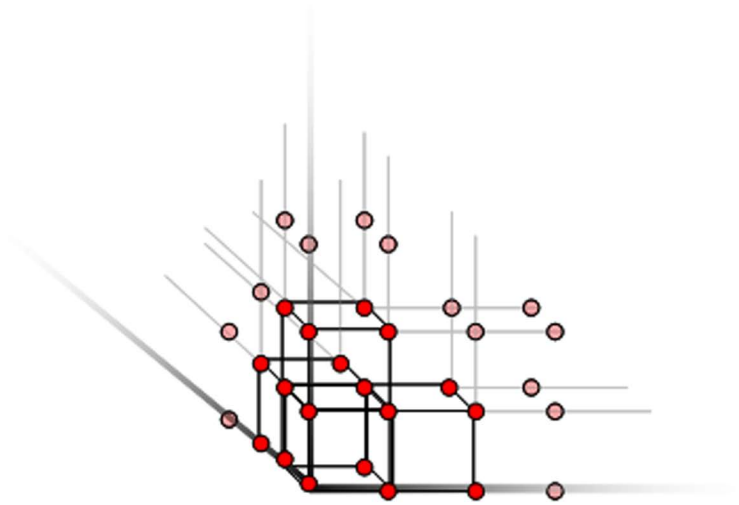

Figure 5.7: A view of the eight node brick elements and their nodal locations in a corner region of the model

cuboidal volumes, thus the voxellated mesh is easily overlaid on the volume with high quality elements throughout. Coordinate values of each node and element are calculated and stored along with a numeric tag value for future identification. The element sets for each grain are defined such that all elements whose centroid falls within a given grain, belong to that grain set. The resulting mesh is written as an INP file for use with ABAQUS [121]. A voxellated meshed overlaid on an arbitrary polycrystalline microstructure instantiated by VorPolycrystalGen is shown in Figure 5.8.

5.5 Periodic boundary conditions to simulate subsurface microstructure volume elements

For the majority of the simulated SVEs, periodic boundary conditions were proscribed in all directions. With periodicity assumed on all sides, the microstructure volumes were simulated to be subsurface. The notation used to describe the nodal sets of the nodes on the faces, edges and vertices of the model are given in Table 5.1 and Figure 5.9. Note that the nodal sets of the nodes on the faces do not include the nodes at the edges and the nodal sets for the edges do not include the nodes at the vertices. The nodal equations that forced periodicity on the model are given in Tables 5.2 to 5.5.

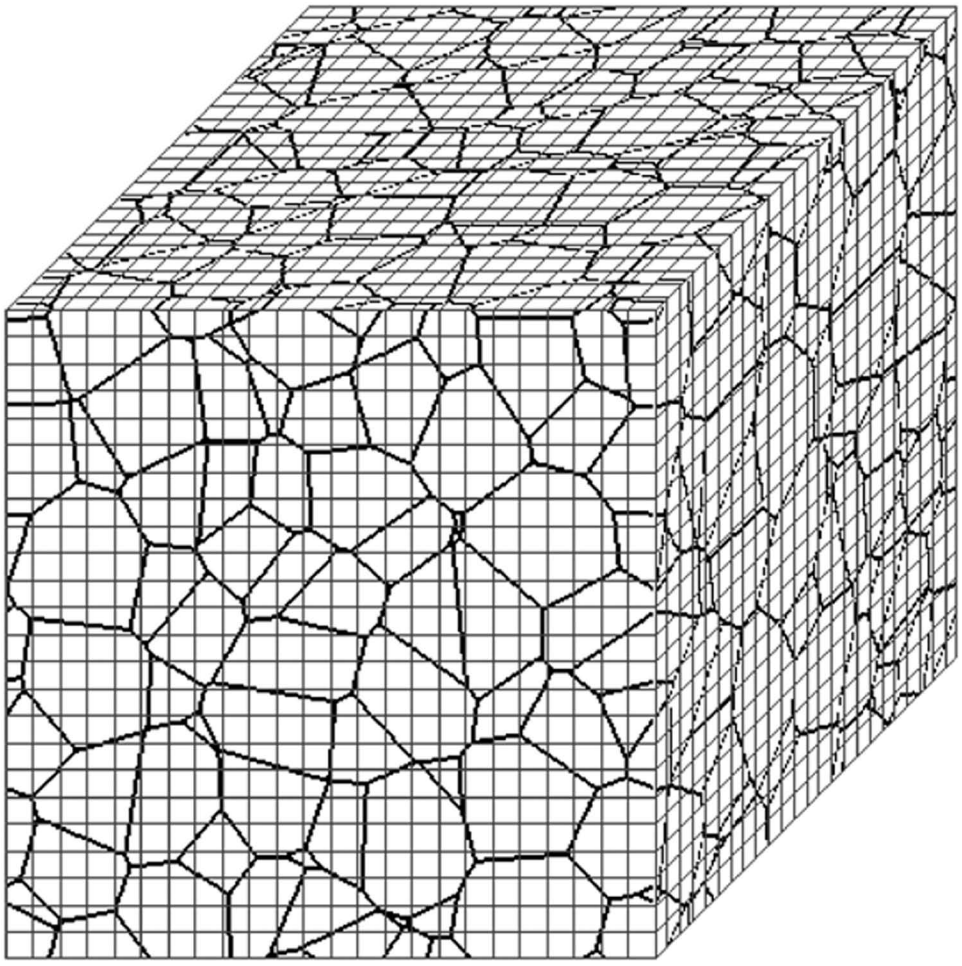

Figure 5.8: SVEs instantiated via Voronoi tessellation microstructure volume element instantiation with associated FE mesh. Note that the meshes are voxellated and do not exactly correspond to the boundaries as defined by the Voronoi tessellation.

Table 5.1: Description of symbols used to describe nodes sets at vertices and faces.

Symbol	Description
REF	Reference node located at $x = 0$, $y = 0$ & $z = 0$
V000	Node at vertex located at $x = 0$, $y = 0$ & $z = 0$
V001	Node at vertex located at $x = 0$, $y = 0$ & $z = h$
V010	Node at vertex located at $x = 0$, $y = h$ & $z = 0$
V100	Node at vertex located at $x = h$, $y = 0$ & $z = 0$
V011	Node at vertex located at $x = 0$, $y = h$ & $z = h$
V101	Node at vertex located at $x = h$, $y = 0$ & $z = h$
V110	Node at vertex located at $x = h$, $y = h$ & $z = 0$
V111	Node at vertex located at $x = h$, $y = h$ & $z = h$
FXP	Face nodes excluding edges and vertices for surface normal to x axis at $x = h$
FXN	Face nodes excluding edges and vertices for surface normal to x axis at $x = 0$
FYP	Face nodes excluding edges and vertices for surface normal to y axis at $y = h$
FYN	Face nodes excluding edges and vertices for surface normal to y axis at $y = 0$
FZP	Face nodes excluding edges and vertices for surface normal to z axis at $x = h$
FZN	Face nodes excluding edges and vertices for surface normal to z axis at $x = 0$

Table 5.2: Nodal equations for constraint on the nodal sets of the nodes on the faces for the proscribed periodic boundary conditions. The symbol u represents the nodal displacements with associated degree of freedom 1, 2, or 3 represented as a subscript on u. The superscript on u describes the associated nodal set.

$$
\begin{array}{c}
u_1^{FXP} - u_1^{FXN} - u_1^{V111} + u_1^{V011} = 0 \\
u_2^{FXP} - u_2^{FXN} - u_2^{V111} + u_2^{V011} = 0 \\
u_3^{FXP} - u_3^{FXN} - u_3^{V111} + u_3^{V011} = 0 \\
u_1^{FYP} - u_1^{FYN} - u_1^{V111} + u_1^{V101} = 0 \\
u_2^{FYP} - u_2^{FYN} - u_2^{V111} + u_2^{V101} = 0 \\
u_3^{FYP} - u_3^{FYN} - u_3^{V111} + u_3^{V101} = 0 \\
u_1^{FZP} - u_1^{FZN} - u_1^{V111} + u_1^{V110} = 0 \\
u_2^{FZP} - u_2^{FZN} - u_2^{V111} + u_2^{V110} = 0 \\
u_3^{FZP} - u_3^{FZN} - u_3^{V111} + u_3^{V110} = 0
\end{array}
$$

Table 5.3: Nodal equations for constraint on the nodal sets of the nodes on the edges for the proscribed periodic boundary conditions. The symbol u represents the nodal displacements with associated degree of freedom 1, 2, or 3 represented as a subscript on u. The superscript on u describes the associated nodal set.

1-direction
$u_1^{EX000} - u_1^{EX001} - u_1^{V100} + u_1^{V101} = 0$
$u_1^{EX010} - u_1^{EX011} - u_1^{V100} + u_1^{V101} = 0$
$u_1^{EY100} - u_1^{EY000} - u_1^{V111} + u_1^{V011} = 0$
$u_1^{EY101} - u_1^{EY001} - u_1^{V111} + u_1^{V011} = 0$
$u_1^{EZ100} - u_1^{EZ000} - u_1^{V111} + u_1^{V011} = 0$
$u_1^{EZ110} - u_1^{EZ010} - u_1^{V111} + u_1^{V011} = 0$
2-direction
$u_2^{EX010} - u_2^{EX000} - u_2^{V111} + u_2^{V101} = 0$
$u_2^{EX011} - u_2^{EX001} - u_2^{V111} + u_2^{V101} = 0$
$u_2^{EY000} - u_2^{EY100} - u_2^{V010} + u_2^{V110} = 0$
$u_2^{EY001} - u_2^{EY101} - u_2^{V010} + u_2^{V110} = 0$
$u_2^{EZ010} - u_2^{EZ000} - u_2^{V111} + u_2^{V101} = 0$
$u_2^{EZ110} - u_2^{EZ100} - u_2^{V111} + u_2^{V101} = 0$
3-direction
$u_3^{EX011} - u_3^{EX010} - u_3^{V111} + u_3^{V110} = 0$
$u_3^{EX001} - u_3^{EX000} - u_3^{V111} + u_3^{V110} = 0$
$u_3^{EY001} - u_3^{EY000} - u_3^{V111} + u_3^{V110} = 0$
$u_3^{EY101} - u_3^{EY000} - u_3^{V111} + u_3^{V110} = 0$
$u_3^{EZ000} - u_3^{EZ100} - u_3^{V001} + u_3^{V101} = 0$
$u_3^{EZ010} - u_3^{EZ110} - u_3^{V001} + u_3^{V101} = 0$

Table 5.4: Nodal equations for constraint on the nodal sets of the nodes on the vertices for the proscribed periodic boundary conditions. The symbol u represents the nodal displacements with associated degree of freedom 1, 2, or 3 represented as a subscript on u. The superscript on u describes the associated nodal set.

1-direction
$u_1^{V110} - u_1^{V010} - u_1^{V111} + u_1^{V011} = 0$
$u_1^{V100} - u_1^{V000} - u_1^{V111} + u_1^{V011} = 0$
$u_1^{V101} - u_1^{V001} - u_1^{V111} + u_1^{V011} = 0$
2-direction
$u_2^{V010} - u_2^{V000} - u_2^{V111} + u_2^{V101} = 0$
$u_2^{V110} - u_2^{V100} - u_2^{V111} + u_2^{V101} = 0$
$u_2^{V011} - u_2^{V001} - u_2^{V111} + u_2^{V101} = 0$
3-direction
$u_3^{V001} - u_3^{V000} - u_3^{V111} + u_3^{V110} = 0$
$u_3^{V101} - u_3^{V100} - u_3^{V111} + u_3^{V110} = 0$
$u_3^{V011} - u_3^{V010} - u_3^{V111} + u_3^{V110} = 0$

Table 5.5: Nodal equations to eliminate rigid body motion for the proscribed periodic boundary conditions. The symbol u represents the nodal displacements with associated degree of freedom 1, 2, or 3 represented as a subscript on u. The superscript on u describes the associated nodal set.

1-direction
$u_1^{V011} = 0$
$u_2^{V101} = 0$
$u_3^{V110} = 0$
$u_2^{V100} = u_3^{V100} = 0$
$u_1^{V000} = u_3^{V000} = 0$
$u_1^{V010} = u_3^{V010} = 0$
$u_1^{V001} = u_2^{V001} = 0$

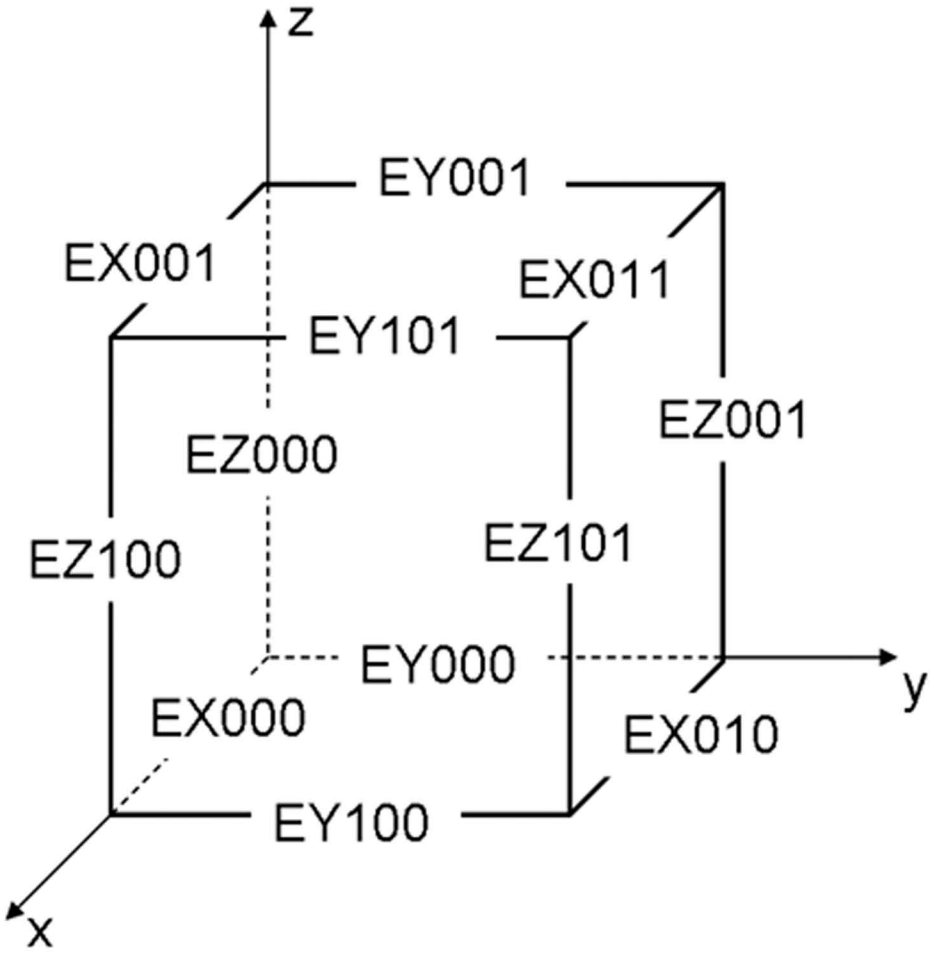

Figure 5.9: Location of edge node sets. Note that these edge node sets do not include the nodes at the vertices of the model.

The three main components of these periodic boundary conditions include constraints on the opposing faces, parallel edges and vertices. Additional constrains are also imposed to prevent any rigid body motion. Displacements between corresponding nodes on opposing faces are constrained to be identical in the direction perpendicular to those faces. Displacements for corresponding nodes on each set of four parallel edges are constrained to be identical in the two directions perpendicular to the direction in which the edges are parallel. Displacements for the vertices in all directions are required to be the same. In all cases these constraints account for any contraction or expanding of the dimensions of the actual microstructure volume. Unless the nodal positions on the corresponding surfaces or edges are the same, these boundary conditions will not be valid. The uniform mesh makes alignment of the nodes across the periodic boundary conditions trivial.

5.6 Mesh quality study

As described in Section 5.4, a voxellated mesh is imposed to model the instantiated microstructures. A detailed study was performed to investigate the sensitivity of the convergence of the extreme value driving forces for fatigue crack formation to these types of voxellated meshes. For this study, the extreme value driving forces for fatigue crack formation was estimated via the Fatemi-Socie FIP as previously introduced. The material systems considered was the Ni-base superalloy IN100. The parameters for the microstructures that were instantiated using VorPolycrystalGen are given in Table 5.7.

Four different microstructure volume elements were instantiated using VorPolycrystalGen for this mesh study and are hereafter referred to as volume elements A, B, C and D. Two of the meshes with different numbers of elements for volume element C are shown in Figures 5.10 and 5.11 with contours of accumulated plastic strain after three cycles. In each case, the elements belonging to the grain with the extreme value grain averaged Fatemi-Socie parameter of highest magnitude among all of the grains in the volume is highlighted

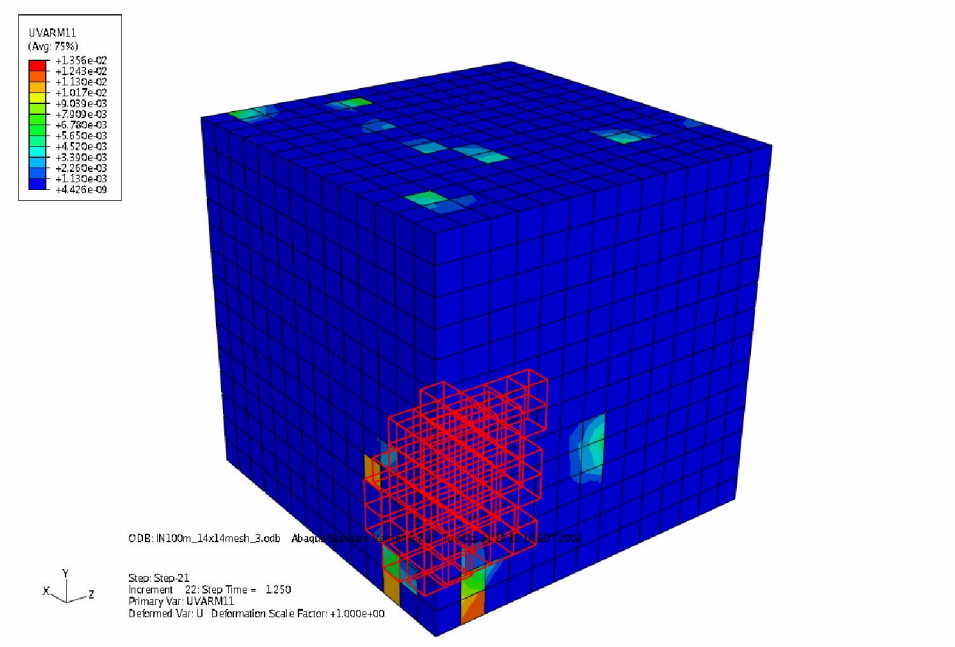

Figure 5.10: The mesh and contours of accumulated plastic strain after three cycles at 0.5% strain with $R = -1$ for the 77 grain model for Microstructure C 28 elements along each edge. The elements belonging to the grain with the extreme value FIP are highlighted in red.

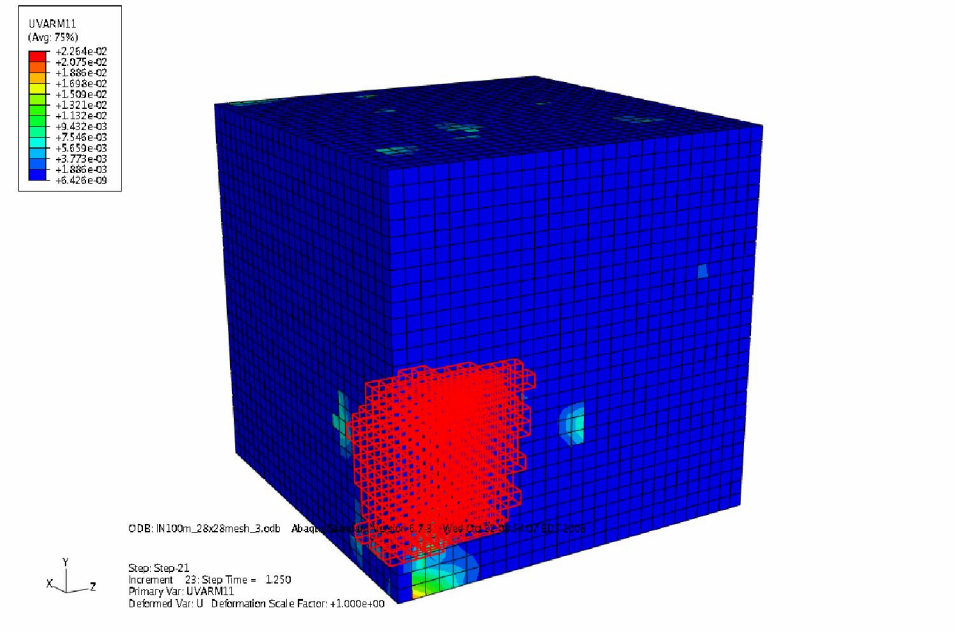

Figure 5.11: The mesh and contours of accumulated plastic strain after three cycles at 0.5% strain with $R = -1$ for the 77 grain model for Microstructure C with 28 elements along each edge. The elements belonging to the grain with the extreme value FIP are highlighted in red.

Table 5.6: Description of the different meshes considered in the mesh study for volume element A.

Number of Elements Along Edge	**Tot. Elements**	**Element Vol.** (mm^3)	**Ratio of Element Vol. to Ave. Grain Vol.**
8	512	1.25×10^{-7}	0.1250
10	1000	6.40×10^{-8}	0.0640
12	1728	3.70×10^{-8}	0.0370
14	2744	2.33×10^{-8}	0.0233
16	4096	1.56×10^{-8}	0.0156
18	5832	1.10×10^{-8}	0.0110
20	8000	8.00×10^{-9}	0.0080
22	10648	6.01×10^{-9}	0.0060
24	13824	4.63×10^{-9}	0.0046
26	17576	3.64×10^{-9}	0.0036
28	21952	2.92×10^{-9}	0.0029

in red. In the case of volume element C as seen in Figures 5.10 and 5.11, the grain highlighted in red is contained entirely in the interior of the volume (*i.e.* the grain does not intersect the boundary) except for one element on the 1-2 surface. A description of the different meshes considered is given in Table 5.6. For the simulations, periodic boundary conditions were imposed in all directions as defined in Section 5.5. The simulations were cycled in strain control with a maximum strain of 0.5% under completely reversed loading (*i.e.*, R=-1). The distribution of the grain volume normalized by the target average grain volume of $1.0 \times 10^{-6} mm^3$ was fit to a log-normal distribution with the mean and standard deviation of the natural logarithm of the normalized grain volume given by -14.0 and 0.7, respectively. A strain rate of $0.002 s^{-1}$ was employed in these simulations. All calculations were performed over the entire volume.

The convergence of the extreme value Fatemi-Socie FIP as calculated over a single element and over all the elements of each grain is given in Figures 5.12 and 5.13. In Figure 5.12, it can be observed that the magnitude of the extreme value Fatemi-Socie FIP changes by as much at 20% across the meshes with 20 to 28 elements along an edge and convergence is not achieved. However, with grain size averaging volumes, variation in the extreme value

Table 5.7: Model parameters used for all simulated volume elements in the mesh quality study.

Edge Length of Volume Element	40 μm
Average Cube Root Grain Size	10 μm
Number of Grains	77
Ratio of Minimum Spacing to Average Distance Between of Grain Centers	0.3

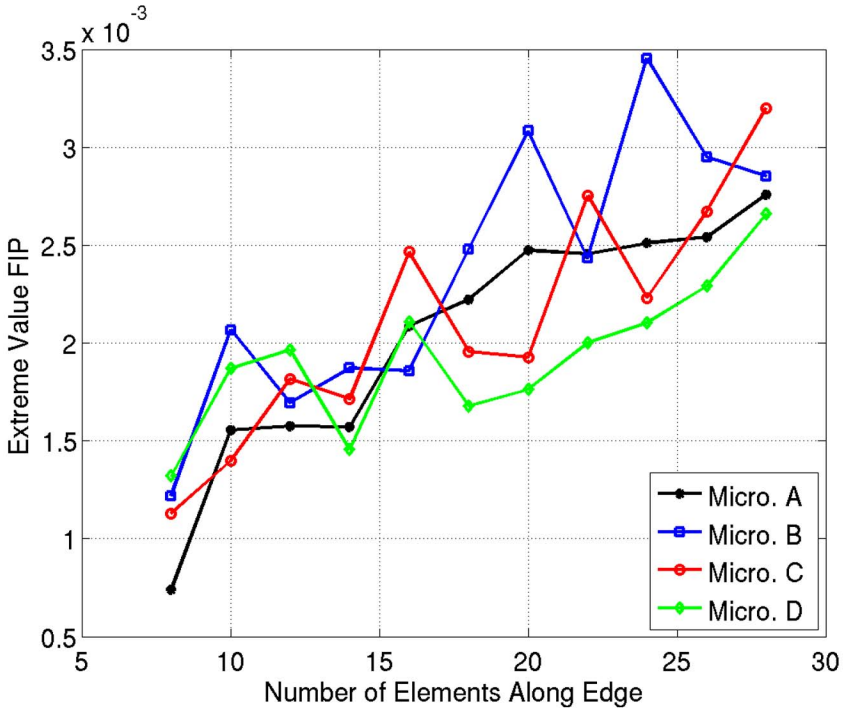

Figure 5.12: Convergence of the extreme value Fatemi-Socie FIP for the FIP calculated over a single element.

FIP reduces to less than 5% in most cases across meshes with 14 to 28 elements along an edge. The grain with the observed extreme value FIP did not change when there were 12 or more elements along an edge or when the ratio of the element volume to average grain volume was greater than or equal to 0.064.

5.7 Minimum statistical volume element size for grain scale cyclic plastic response

As mentioned previously, SVEs of sufficient size are required such that the local plastic response on the scale of the grains is unaffected by further increasing the volume of the SVE.

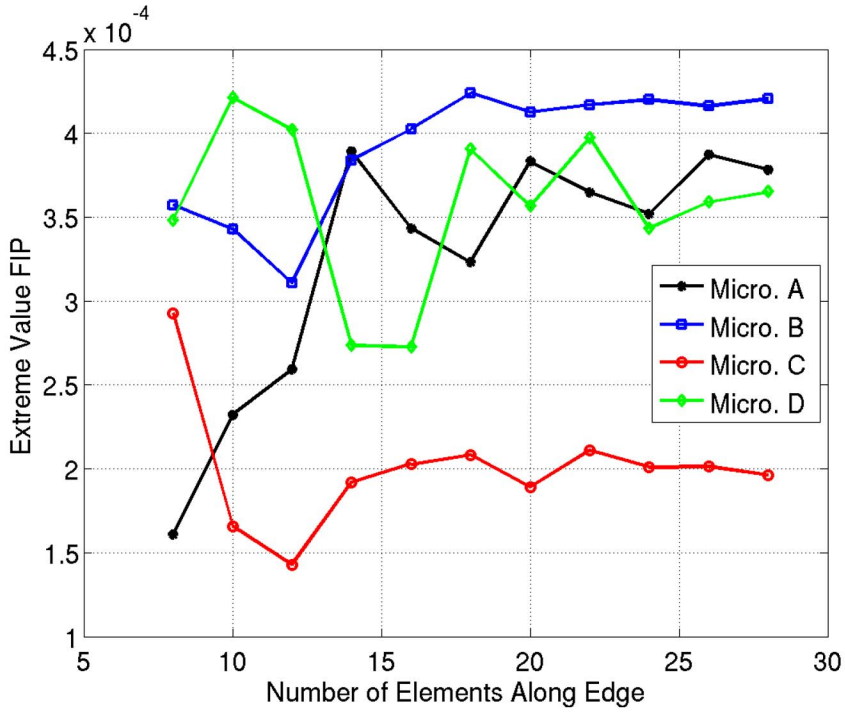

Figure 5.13: Convergence of the extreme value Fatemi-Socie FIP for the FIP calculated over all the elements in a single grain.

Additionally, it is desired that the overall macroscopic elastic/plastic response is nearly the same for each SVE. It has been shown by others that local crystallography can have a large influence on the local elastic stress fields due to the influence of neighboring grains. For example, Sauzay *et al.* [53, 196, 197] considered the effect of nearest neighbor grains on the stress distribution at the free surface of polycrystals and found that grain interactions could affect the local resolved shear stress by as much as 16% in copper and austenitic steels depending on the local orientations of the neighboring grains. Bennett and McDowell [52] also demonstrated that distributions of slip could be quite heterogeneous in HCF. This heterogeneity is directly related to complex interactions between grains of differing orientations. Specifically, here it is desired to determine the number of grain neighbor interactions that have a significant influence on the plastic response for a nominal grain.

To quantify the influence of SVE size on the FIPs, several SVEs of different size were

simulated. Specifically, the simulated SVE were constructed of cuboidal arrays of randomly oriented grains, as can be seen in Figure 5.14. These cuboidal grain arrays consisted of blocks with 3, 5, 7, and 9 grains, respectively, along each edge with random periodic boundary conditions applied in all directions. In this manner the center grain has 1, 2, 3, and 4 neighbors, respectively, in each direction between itself and the applied periodic boundary conditions. In these simulations, these SVEs were cycled one time under completely reversed loading (*i.e.*, R=-1) with a maximum strain magnitude of 1.0%. It is noted that although one cycle is probability insufficient to estimate the stable cycle by cycle ratcheting of the plasticity that is expected in fatigue, it is assumed here that the range of influence of the microstructure attributes on the local plastic response on the scale of the individual grains due to the interactions between grain neighbors is similar before and after shakedown. In other words, the main concern here is not the particular magnitudes of the cycle by cycle ratcheting, but the range of interactions between grain neighbors that influence the averaged plastic response on the scale of a single grain. The quasistatic strain rate of $0.004s^{-1}$ was used in these simulations. The grains were dimensioned 9 micrometers along each edge and consist of a total of 27 quadrilateral elements with reduced integration (type C3D8R in ABAQUS [121]) or 3 elements along each edge. The orientation of the individual grains was random except for the center grain which was oriented in the $\langle 001 \rangle$, $\langle 21\,(25) \rangle$, and $\langle 111 \rangle$ directions, respectively. We can see in Figure 5.15 that crystals oriented near the $\langle 21\,(25) \rangle$, and $\langle 111 \rangle$ directions exhibit the maximum apparent Schmid factors for octahedral and cube slip, respectively. The Fatemi-Socie FIP averaged over the differently oriented center grains for the differently sized SVEs are given in Figure 5.16. In all cases, there is a significant change in the grain averaged FIP of the center grain when the SVE is increased from 3 to 5 grains along each edge. However, as the number of grains along each edge are increased further from 4 to 5, 5 to 7, or 7 to 9, further changes grain averaged FIP of the center grain are much less. Thus, for the purposes of this work, we assume that only up to the 2nd nearest neighbor interactions are important. The SVEs for

the microstructures for all subsequent studies are scaled accordingly.

It is noted that the approach given here to specify a minimum SVE size possibly neglects longer range or higher order influences on the cyclic plastic response. For example, these volumes simulated here are likely too small to pick up shear banding that can occur at higher applied plastic strains. Additionally, the periodicity eliminates the long range influence of a free surface on the driving forces for subsurface crack formation which may be important. The first approach taken here only considers interactions within the local neighborhood on the scale of a few grains. Thus, the actual magnitudes of the response could change significantly if longer range interactions are considered, particularly in the case of shear banding. However, it is also recognized that such interactions likely are not as important for the applied stresses considered here which are just at or less then the effective yield stress. At stresses below the effective yeild stress, plasticity is much more heterogeneous and localized; therefore, the longer range or higher order moments of cyclic plasticity are expected to be less important.

5.8 Summary

Various aspects important to the instantiation and simulation of microstructure volume elements has been considered. Proper scaling of simulation volumes to estimate distributions of extreme value response is essential. As RVEs for extreme value response are typically untenably large, in this dissertation SVEs are utilized. Specifically, SVEs are constructed such that the macroscopic stress/strain behavior is similar between any two SVEs sampled from the same material; however, the lower order moments of cyclic plasticity on the scale of the individual grains changes minimally with increasingly larger volumes. In this manner, multiple SVEs can be constructed to sample the underlying character of the extreme value distribution for a given microstructure volume element. It is recognized that this definition of a SVE does not guarantee that the instantiated SVEs will be sufficiently large to estimate the asymptotic extreme value distribution of the response of interest. To estimate

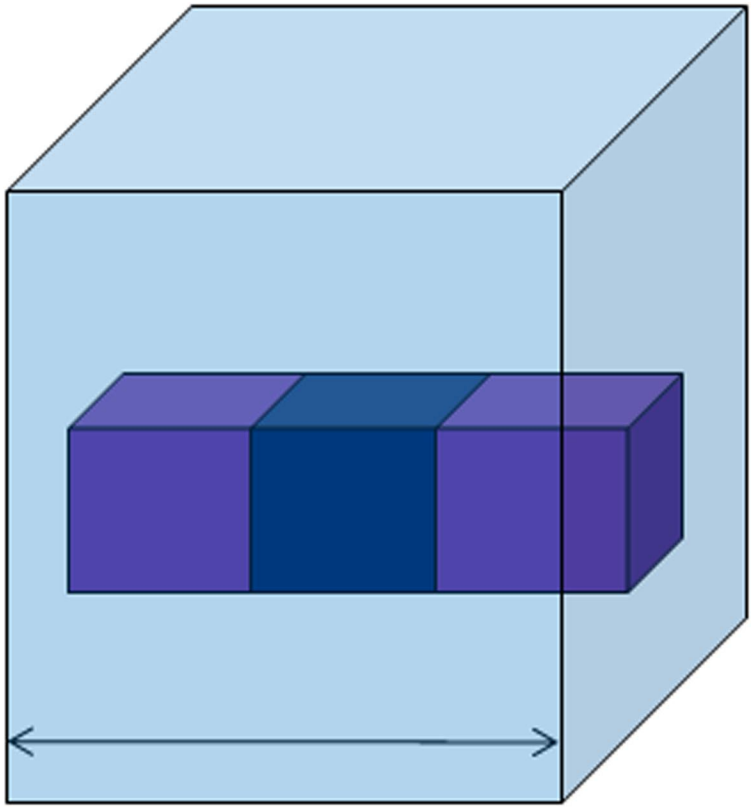

Figure 5.14: Microstructure model with cuboidal grains used to estimate the minimum necessary size for an SVE for the Fatemi-Socie FIP. The minimum number of grains between a single cuboidal grain and itself was determined such that the grain average Fatemi-Socie parameter changed minimally with increasing number of grain neighbors.

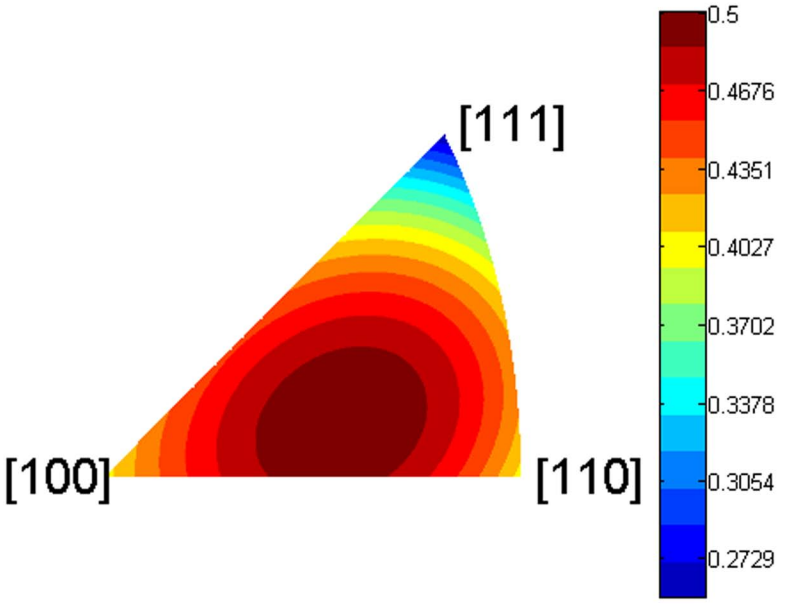

(a)

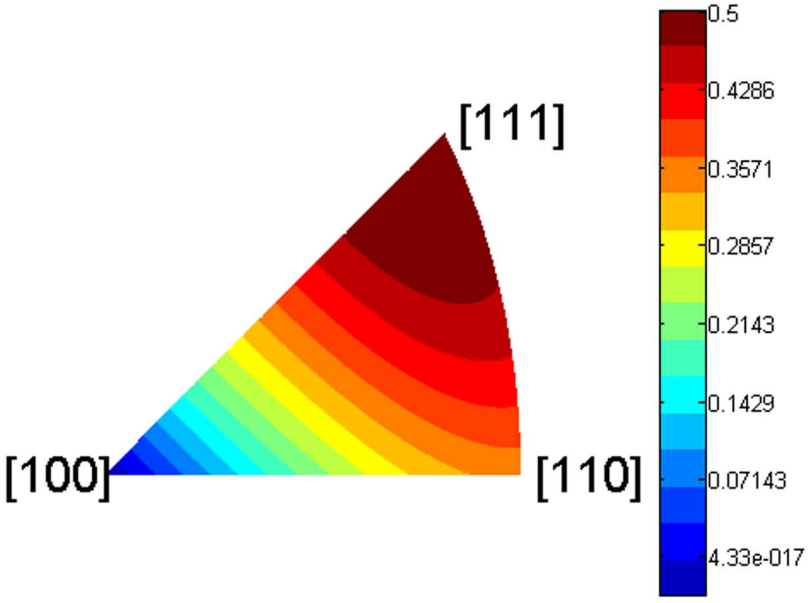

(b)

Figure 5.15: Contours of Apparent Schmid factors based on crystallographic orientation for the (a) octahedral and (b) cube slip systems.

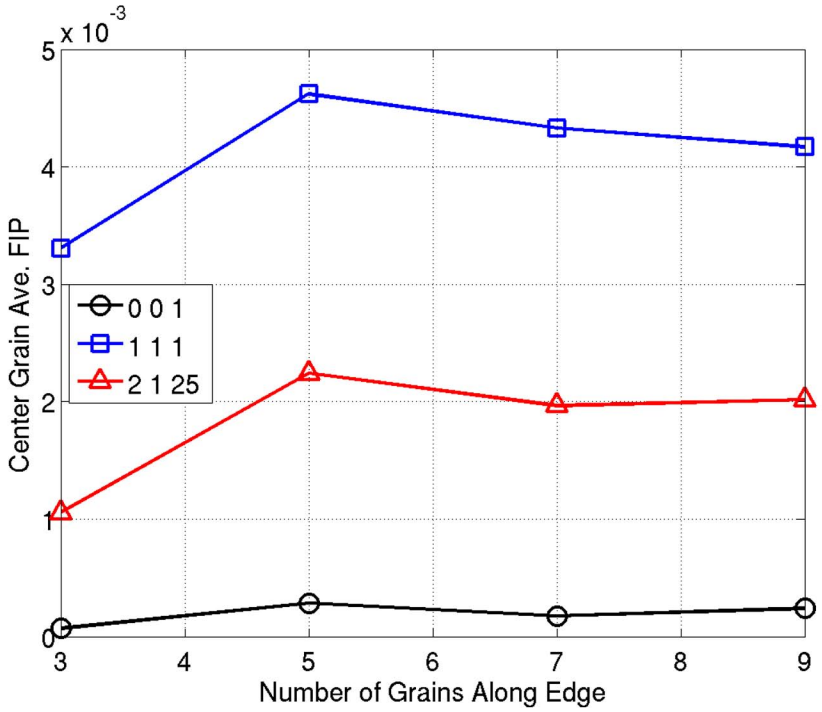

Figure 5.16: Comparison of the grain averaged Fatemi-Socie FIP of the center grain oriented with its {001}, {111} and {21 (25)} planes perpendicular to the loading directions, respectively, versus the number grains along the edge of the SVE. These SVEs consisted of arrays of cuboidal grains each grain dimensioned 9μm along an edge.

the asymptotic extreme value distribution of response for a particular SVE size, the SVE must contain a sufficiently large sample size n of the microstructure attributes that most influence the extreme value response. Depending on the application, it may not always be desirable to construct an SVE of sufficient size to sample the asymptotic extreme value distribution of the desired response. Such a case might exist when considering the extreme value response at a notch root. The extreme value distribution of the response of interest in this case should correlate with the size of the critically stress volume at the notch root regardless of whether the asymptotic extreme value distribution can be characterized based on the size of that particular microstructure volume element.

Much research has examined the instantiation of microstructure volume elements that are statistically representative of real materials. The two different methods introduced in this work to instantiate microstructure volumes for FE simulation of polycrystalline microstructures are based on the Voronoi tessellation and packing grain equivalent ellipsoids into a fixed volume, respectively. The first method based on the Voronoi tessellation can be applied to instantiate microstructure volume elements with space filling convex polyhedrons representative of the grain structure. Distributions of grain size/volume for microstructure volume elements instantiated via the Voronoi tessellation can be optimized to fit experimentally determined grain size distributions by randomly perturbing the grain centers via a simulated annealing algorithm. Grain orientation and grain disorientation can also be fit to the respective target distribution prespecified by the user using a simulated annealing technique. It is noted that significant modification of the morphology of the polyhedrons generated via the Voronoi tessellation is not possible. Additionally, the topology of the instantiated grains is very approximate and is not representative of real polycrystalline microstructure. Moreover, it is very difficult to instantiate microstructure volume elements with multi-modal grain/phase distributions.

The second method applied here to instantiate microstructure volume elements that are

statistically representative of real microstructures is based on packing grain equivalent ellipsoids into a volume. These grain equivalent ellipsoids can be generated by randomly sampling the distributions of aspect ratios of the major elliptical axes calculated from grain equivalent ellipsoids fit to a set of experimentally characterized grains in three dimensions. These randomly generated grain equivalent ellipsoids are oriented based on the orientation distribution of experimentally characterized grains and placed into a volume until no more non-overlapping ellipsoids can be placed. When no more non-overlapping ellipsoids can be placed into the volume, all the ellipsoids are allowed to grow uniformly until all space is filled. The distributions of the orientation of the lattice of the grains and disorientation between grain neighbors can then be optimized using a simulated annealing algorithm. Using grain equivalent ellipsoids to instantiate polycrystalline microstructure volume elements allows much greater control over grain topology. For example, rolling textures with elongated grain can be generated, which was not the case with the microstructure volume elements instantiated based on the Voronoi tessellation. Additionally, multi-modal grain/phase size distributions can be generated with much higher fidelity.

Simulations were performed to consider both mesh quality and minimum required SVE size of several instantiated microstructure volume elements for the Ni-base superalloy IN100. The simulated SVEs in this work are meshed using a simple voxellated mesh with periodic boundary conditions. Several different mesh densities were considered to determine the sensitivity the of FIPs to the mesh. The response calculated over nonlocal averaging volumes converges sufficiently when the averaging volumes are on the scale of the grains. If the averaging volumes are on the scale of the individual elements, no convergence was achieved. To determine minimum SVE size, several sample microstructure volume elements were instantiated for IN100 with cuboidal arrays of grains. The lower order moments of the cyclic plasticity on the scale of the individual grains is relatively stable when the SVEs are large enough to consider interactions up to the second nearest neighbor before periodicity. It is noted that the procedure used here to estimate the minimum SVE

size did not necessarily account for longer range or the higher order moments of cyclic plasticity that might result from shear banding, for example. However, as the maximum appled loads are hereafter set to be below the yeild point, such longer range interactions are expected to be less important because plasticity will be more heterogeneous and localized.

CHAPTER VI

MICROSTRUCTURE-SENSITIVE EXTREME VALUE PROBABILITIES OF FATIGUE IN THE NI-BASE SUPERALLOY IN100

6.1 Introduction

In Chapter 6 the microstructure-sensitive extreme value probabilistic framework based on the newly introduced extreme value marked correlation functions (EVMCF) is applied to characterize the extreme value HCF response of the PM Ni-base superalloy IN100 at 650°C. The objective of this framework as it is applied here is to quantify the effects of interactions between the crystallographic microstructure attributes on fatigue life in the HCF regime. By using the EVMCF, this framework quantifies the statistical correlation between the extreme value distributions of cyclic plastic strain based FIPs to the coupled microstructure attributes that exist at the location of the extreme value FIPs. To accomplish this task, multiple SVEs are constructed to compute the cyclic plastic response on the scale of the grains in the Ni-base superalloy IN100. These SVEs for extreme value FIPs are constructed and simulated via the finite element method with crystal plasticity constitutive relations formulated to capture microstructure-sensitive grain scale cyclic plasticity in IN100 as outlined in Chapter 4. The results of the simulations are used to explore the extreme value statistics of the FIPs for IN100. This chapter is designed to be self supporting for the convenience of the reader; therefore, some background covered previously may be repeated. Much of the work described here has been published previously [149, 198].

The dependence of fatigue crack formation on various microstructure attributes was briefly reviewed in Chapter 2. For example, second phase inclusions or pores, large grains that are favorably oriented for slip, or grains adjacent to grains that are unfavorably oriented

for slip have each been linked to fatigue crack formation in several metallic polycrystalline material systems. Identifying the underlying microstructure attributes that drive fatigue crack formation in material systems with multiple phases, complex processing histories, *etc.*, however, is often complicated by the fact that multiple interacting microstructural features couple with the imposed cyclic plastic deformation and stress state to increase the local driving forces for fatigue crack formation. In most cases, this dependence cannot merely be deduced from direct quantitative image analysis of various microstructure attributes. Assessment of the coupling of microstructure attributes with the driving forces for fatigue crack formation requires a combination of experiments and computational simulation, along with a connective framework based on extreme value statistics.

In general, fatigue crack formation in polycrystalline metallic materials is primarily driven by irreversible slip on the scale of the microstructure. In addition, interacting microstructure attributes (*e.g.*, grains, phases, inclusions, and voids) can increase local slip and associated driving forces for fatigue damage at the scale of the dominant microstructure attributes. In HCF, where stress amplitudes remain below the macroscopic flow stress and cyclic plasticity is quite heterogeneous, fatigue lives are dominated by fatigue crack formation rather than by physically small or large crack propagation. Accordingly, the emphasis is placed on cyclic plasticity-based Fatigue Indicator Parameters (FIPs) as introduced in Section 2 that reflect probability of fatigue crack nucleation and microstructurally small crack growth.

As reviewed in Chapter 3, the scatter in the High Cycle Fatigue (HCF) life of specimens or components depends on the extreme value probabilities of having existing hot spots or regions with increased local driving forces for fatigue crack formation (*i.e.*, fatigue crack nucleation and microstructurally small crack propagation). Specifically, the probability of fatigue crack formation in a particular volume of material is established by the extreme value (*i.e.*, rare event) probability of a particular existing combination of microstructure attributes that couple with the applied stress state such that fatigue cracks form

and propagate. Coupling of microstructure attributes with loading conditions and the resulting fatigue response is the main source of both scatter and size effects in fatigue in the absence of other random environmental factors (*e.g.*, temperature, atmosphere). As such, scatter is commonly observed in the fatigue response between multiple material volumes (or components) even when they are fabricated from the same batch of processed material and tested in nearly identical environments. Although environmental effects can also contribute to the probability of surface to subsurface transition of crack formation, they are not considered here. The main emphasis of the study covered in this chapter to exercise the developed microstructure-sensitive extreme value probabilistic framework characterize correlations of microstructure attributes that exist with high probability relative to the nominal microstructure in regions where the fatigue driving forces are maximum (*i.e.*, extreme value) in IN100.

For most applications, large numbers of experiments are necessary to meaningfully quantify any variability in fatigue life and to identify any change in the mechanism of fatigue crack formation as a function of applied loading conditions for a given specimen size. Typically, insufficient experimental data are available to support this quantification. Moreover, the mathematical form of the tails of the probability distributions for the driving forces for fatigue crack formation, such as the local distributions of stress/strain, are not well characterized; moreover, the dependence of the character of those tails on single and/or interacting microstructure attributes are not well understood.

In this chapter, the focus is on how the crystallographic attributes of the polycrystalline microstructure (*e.g.*, grain orientation, disorientation, size, and shape distributions) affect the local driving forces for fatigue crack formation in HCF. In general, plastic strain inhomogeneity at the grain level in polycrystals subjected to cyclic loading is directly linked to crystallographic texture. Winter *et al.* [51] observed that plasticity occurs preferentially in grains having slip systems with high Schmid factors, with slip localized within slip bands. Using crystal plasticity simulations to calculate distributions of cyclic slip in polycrystals,

Bennett and McDowell [52] demonstrated that distributions of slip could be quite heterogeneous in HCF. This heterogeneity is directly related to complex interactions between grains of differing orientations. Sauzay and Jourdan [53] explored these types of interactions between grains by computationally characterizing the distributions of elastic stress fields around grain clusters at the free surface using elastic FE simulations. They predicted that grain interactions could affect the local resolved shear stress by as much as 18% in copper and austenitic stainless steels depending on the local orientations of the neighboring grains. Inhomogeneity of elastic stress fields corresponds to localization of plastic strain in regions of stress concentration associated with the jump of the elastic stiffness across grain boundaries and compatibility requirements of the polycrystal. In this chapter, the effects of local crystallography (*e.g.*, phase, grain orientation, grain disorientation, grain topology, *etc.*) on the extreme value driving forces for fatigue crack formation are estimated via simulation in a powder metallurgy (PM) Ni-base superalloy, IN100.

Ni-base superalloys are predominantly used in aircraft gas turbine engines due to their high strength and creep resistance at high temperatures that is conferred by coherent γ' Ni_3Al precipitates of Ll_2 face-centered cubic (fcc) structure. These precipitates are dispersed in the γ austenitic Ni solid solution matrix of fcc crystal structure and provide excellent resistance to slip. Commonly, fatigue crack formation in polycrystalline superalloys has been linked to the existence of large pores or nonmetallic inclusions introduced during processing. Often, inclusions debond from the matrix or crack during primary forming processes. During loading, the stress concentrations at inclusions/pores often lead to the formation of fatigue cracks [199–201]. However, as processing techniques improve, cleaner Ni-base superalloys are being developed that have lower number density of inclusions/pores; consequently, fatigue cracks are increasingly observed to form along crystallographic planes. For example, Jha *et al.* [202] noted that subsurface fatigue crack formation occurs in individual grains absent of any voids/inclusions in René 88DT, particularly at

lower stress amplitudes (*i.e.*, in the HCF regime). In this case, the nucleation region associated with the size of the crystallographic facets at the sites of fatigue crack formation was observed to be much larger than the average grain size. This suggests that cracks tend to form in larger grains. In the same alloy, Shyam *et al.* [203] noted that cracks form predominantly in larger grains or at inclusions near large grains. Additionally in René 88DT, Miao *et al.* [204] also observed that most critical (*i.e.*, life limiting) fatigue cracks in the HCF/VHCF regime initiate crystallographically away from the surface. The grains in which these cracks form were observed to be large in size relative to the average grain size. Here these grains were associated with higher Schmid factors, indicating they are oriented favorably for slip. Others have shown that slip bands associated with shearing of the second phase γ' precipitates and subsequent fatigue crack formation have been observed to be more common in coarser grained superalloys, while deformation in the smaller grains has been observed to be more homogeneous [205, 206].

The analysis of the slip character in Ni-base superalloys has provided some insight into fatigue crack formation in these materials systems. As mentioned previously, the γ austenitic phase in these Ni-base superalloys has a fcc crystalline lattice. As typical in fcc materials, slip is expected on the 12 octahedral $\langle 110 \rangle \{111\}$ slip systems. However, contributions of an additional 6 cube $\langle 110 \rangle \{100\}$ slip systems have been observed in the γ phase in many Ni-base superalloys at certain elevated temperatures. In single crystal SC16, Bettge and Österle [151] observed "zig-zag" slip along along {100} planes. They postulated that this cube slip is due to cross slip of screw dislocations on {111} planes when blocked at the $\gamma - \gamma'$ interfaces. Phillips *et al.* [152] observed similar "zig-zag" slip in the γ matrix of polycrystalline Ni-based turbine rotor material René 104. In this case, the "zig-zag" slip in the γ matrix occasionally causes shearing of the γ' precipitates on {001} planes when the γ' precipitates are encountered as depicted schematically in Figure 6.1.

Cube slip has been observed in several single crystal Ni-base superalloys over a wide range of temperatures. For example, Miner et al. [207] investigated slip traces in single

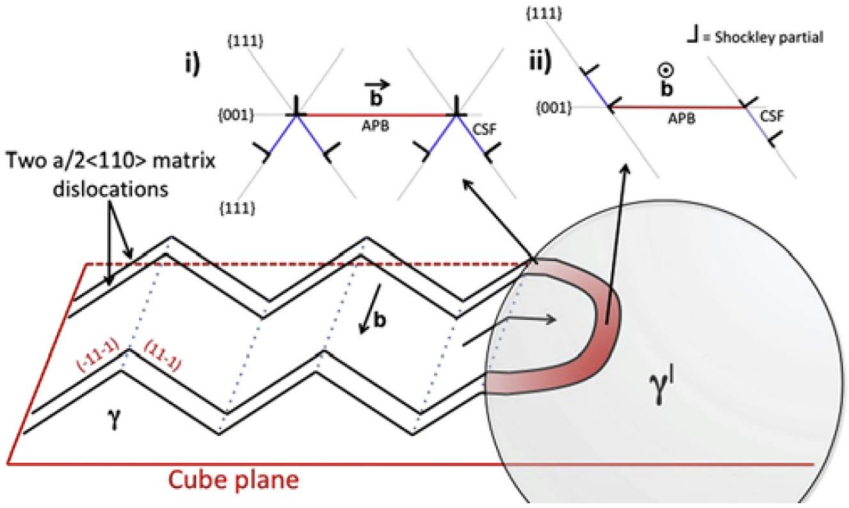

Figure 6.1: Model for cube-slip propagation as proposed by Phillips *et al.* [152] (Reprinted from [152], with permission, copyright Elsevier).

crystal of René N4 at room temperature, 650°C, 760°C, 870°C, and 980°C. They observed slip traces along {100} planes for all the temperatures considered when the crystals were oriented with the {111} slip planes perpendicular to the loading direction. Additionally, at increasingly higher temperatures, {100} slip traces were observed with increasing frequency in the crystals oriented in directions other than ⟨111⟩ relative to the loading direction. Cube slip accommodates deformation for grains in hard crystallographic orientations. At 870°C {111} slip traces were only observed for crystals oriented near [001] and [011] and all others were of {100} character. Bettge and Österle [151] observed "zig-zag" cube slip in single crystals of SC16 oriented with the {111} slip planes perpendicular to the loading direction. Westbrooke *et al.* [208] observed slip bands traces along {100} planes in single crystals of a Pratt & Whitney alloy for a crystal unfavorably orientated for slip on {111} planes and octahedral slip for a crystal oriented for loading in the $\left[1\bar{1}0\right]$ direction. They also observed slip traces for the crystal tested in the [100] direction that were neither of {111} or {100} character. The morphology and distribution of γ' appears to dictate the character of slip in these types of superalloys. For example, Nitz *et al.* [209] examined slip in single crystals of NIMONIC 105 at temperatures from 10°C to 877°C via TEM analysis and only

observed octahedral slip. It is noted that in this particular material the γ' precipitates are small relative to the other materials discussed here (17 nm) and are spherical in their morphology whereas in most single crystals the γ' precipitates are an order of magnitude larger and tend to have a cuboidal morphology. The slip character of these single crystals is summarized in Table 6.1.

Various slip modes have also been observed in fatigue tests of various polycrystalline Ni-base superalloys. The slip behavior of various polycrystalline alloys is summarized in Table 6.2. Generally in these alloys fatigue cracking propagates along {111} planes at lower homologous temperatures and along {100} planes at moderate temperatures (*i.e.*, between 500°C to 800°C). It is emphasized that this is what was observed in fatigue tests of IN100 [210]. In contrast, when the γ' precipitates are more spherical and smaller in size and have lower volume fraction, slip and cracking along {100} planes has not been observed, such as in René 88DT [211].

As reviewed in Chapter 3, statistical treatments of fatigue have primarily been based on large numbers of experiments. Typically, one observes a wide range of scatter for a given component in the number of cycles to failure, particularly in HCF. For example, in Figure 6.2 significant variability can be observed in the overall fatigue lives in IN100 across a range of applied stress magnitudes [83]. The variability of fatigue life is assessed by extensive experimentation to obtain a statistically significant sample. Designers then use these data to predict component life with an acceptable level of risk. Such data collection requires significant time and resources and does not necessarily provide understanding of the mechanism(s) that have the most influence on the variability of the response. In addition, the resulting predictions often change with sample size. The problem is further complicated when multiple mechanisms of damage formation are observed [82, 83, 202]. In these cases, multiple competing mechanisms of fatigue crack nucleation and MSC crack growth make it difficult to accurately predict fatigue life because different mechanisms operate at

Table 6.1: The slip character of several different single crystal Ni-base superalloys.

Material	**Vol. Fraction** γ'	**Ave. Size of** γ' (nm)	γ' **Shape**	**Temp.** (C)	**Strain Rate** (s^{-1})	**Slip Character**	**Ref.**
Heat Treated PW alloy	0.51	500	Cuboidal	RT	10^{-5}	[110] oriented crystals exhibited {111} slip traces, [111] oriented crystal exhibited {100} slip traces and [100] oriented crystals exhibited neither	[208]
NIMONIC 105	0.47	17.2	Spherical	10 to 877	7×10^{-5}, 1.4×10^{-4}	No observed {100} slip traces, only {111} type	[209]
Rene N4	0.65	250	Cuboidal	RT, 650, 760, 870, 980	1 to 2.5×10^{-5}	[111] oriented crystals exhibited {100} slip traces at all temperatures and range of orientations exhibiting {100} slip traces (instead of {111}) increased with temperature	[207]
SC16	0.35, 0.05	450, 80	Cuboidal	650, 750, 850	10^{-5}	Observed slip traces on {100} planes at 650°C and 750°C for ⟨111⟩ oriented crystals	[151]

Table 6.2: The slip character of several different polycrystalline Ni-base superalloys. Because in many cases the volume fraction of the γ' precipitates was not reported, the combined weight % of Al+Ti is listed because Al and Ti are the limiting components for the formation of the γ' precipitates. * For this material the combined wt. % of Al+Nb+Ta is reported because these are the limiting components in this case for the formation of the γ' precipitates. ** Although this value was not reported in the paper it was given by the authors who wrote this paper. Values not reported in the respective references are listed as "nr" for not reported.

Material	**Grain Size** (μm)	**wt.%** Al+Ti	**Vol. Fraction** γ'	**Ave. Size of** γ' (nm)	γ' **Shape**	**Temp.** (C)	**Slip Character**	Ref.
IN100	30	10.2	0.6**	1000	Cuboidal	RT, 538	At RT cracks form on {111} and at 538°C cracks form on {100}	[210]
MARM 004	nr	10.55*	0.5	1000	Cuboidal	RT, 600	Facets on {111} at RT and facets on {100} at 600°C	[212]
NIMONIC AP1	40-50	7.4	nr	500	Cuboidal	RT	Most cracking on {111}, but cracking on {100} observed when slip is limited to single grains	[213]
René 88DT	26	5.8	nr	100-200	Spherical	593	Cracks form and propagate along {111} planes	[211]
René 104	nr	10	55%	307	nr	704	Observed "zig-zag" octahedral slip along {001} planes in γ matrix and shearing of γ' precipitates along {001} planes	[152, 214]
Udmit 700	nr	7.5	nr	200	Cuboidal	RT, 850	Crack growth observed only on {100} planes at both RT and 850°C	[215]

different stress magnitudes and often microstructure attributes vary spatially in the material. For example, multiple modes of failure are evident in the cumulative probability plot in Figure 6.2(b) at the stress magnitude of 1150MPa. In this case, the authors assert that the bi-modal nature of the failure probability relates to the fact that there exist two different competing failure mechanisms [83].

Processes of HCF crack formation and early growth depend on a few key attributes (or sets of attributes) such as the largest inclusion or void within an entire population of such features. There is significant scatter in experimentally measured HCF life because the attributes that govern failure lie within the tails of joint distributions of attributes and responses, necessitating consideration of extreme value statistics. For example, if the key feature of the fatigue life in a particular material is determined by the largest inclusion of a certain type, an understanding of the distribution of inclusion sizes in the critically stressed regions would be essential to modeling the HCF life for that particular material.

The problem of the largest inclusion size in clean steels has been considered by several different workers as was reviewed in Section 3.3.2. All of these methods, however, assume failure based on a single attribute (*e.g.*, inclusion size) and do not consider how interacting attributes affect the damage processes of interest. For example, in many cases the driving forces for damage formation around an inclusion might depend as much on the orientation of the grains that affect the local slip processes in the matrix around an inclusion as on the size of the inclusion itself. It is argued that a framework that only considers purely geometric attributes such as inclusion size, grain size, or grain orientation is in general insufficient to quantify the scatter in HCF life. The additional attribute(s) of material response (*e.g.*, stress, strain, plastic strain and other driving force parameters) coupled with the geometric attributes of the microstructure facilitate pursuit of joint statistics of extreme value type that are relevant to minimum fatigue life design.

Next, the microstructure-sensitive extreme value probabilistic framework is exercised via computational simulation on multiple instantiated SVEs for the Ni-base superalloy

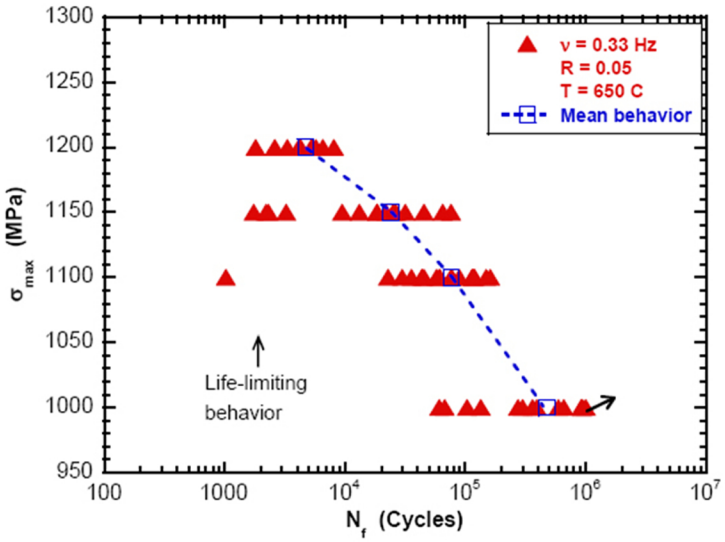

(a)

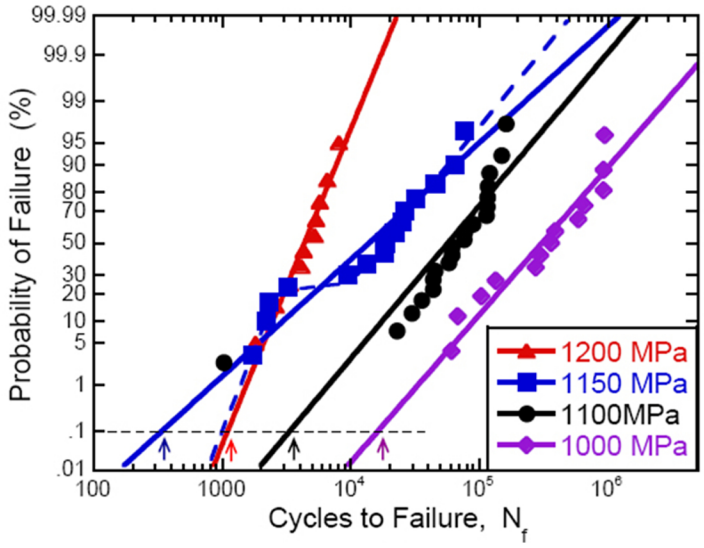

(b)

Figure 6.2: The fatigue variability of IN100 characterized from repeated testing at several stress magnitudes; (a) The mean versus life-limiting behavior and (b) Cumulative distribution functions for tests at different stress magnitudes (Reprinted from [83], with permission, copyright The Minerals, Metals and Materials Society (TMS)).

IN100. Simulations are performed that estimate the cyclic deformation response via a crystal plasticity model formulated and calibrated for IN100 at 650°C. The model is implemented using the finite element (FEM) method. Finally, the results are compared to a limited number of fatigue experiments available in the literature for this particular material system.

6.2 Methodology

6.2.1 Extreme value marked correlation functions

The extreme value distributions of the driving forces for fatigue crack formation as estimated by the FIPs (see Section 2.3.1) are first considered. Given a spatial window Ω, the probability density of the extreme value distribution of an arbitrary FIP, P_α, can be expressed as $f_{\max(P_\alpha)}(P_\alpha|\Omega)$ such that $f_{\max(P_\alpha)}(P_\alpha|\Omega)\,dP_\alpha$ is the probability that P_α between some range described by dP_α (calculated over an averaging volume on the scale of the dominate microstructural features like grains, for example) is the extreme value for a sampled SVE of volume Ω. The basic procedure to construct the extreme value distribution of the FIPs is to sample the extreme maximum value FIP across a number of samples in time and/or space. Here, the distribution of the maximum response parameters is considered by sampling the maximum FIP in a number of equal volumes sampled from the microstructure ensemble.

To quantify correlation between the extreme value driving forces for fatigue crack formation (*i.e.*, FIPs) and the coupled crystallographic microstructure attributes (*e.g.* grain size, grain orientation, grain misorientation, phase) that most influence that extreme value response, the EVMCF are used. Here, the EVMCF introduced in Section 3.5 are constructed in terms of the radial distribution function. Thus, for the purposes here, the probability density of the extreme value marked radial correlation function $R_{\max(P_\alpha)}(\beta,\beta'|r,\Omega)$ for the arbitrary microstructure attributes β and β' is defined such that $R_{\max(P_\alpha)}(\beta,\beta'|r,\Omega)\,dr$ is the probability of finding a sphere centered at the crystallographic microstructure attribute

β coincident to the location of the maximum value of P_α in the microstructure window Ω, with microstructure attribute β' at a distance within r to $r + dr$ from β in any direction. It is noted that radial correlation functions do not contain information regarding anisotropy of the morphology of the specific microstructure attributes considered; however, they do describe the correlation lengths between the specific crystallographic microstructure attributes being considered without regard to directionality, which is the primary focus in this chapter.

The extreme value distribution of the FIPs considered together with the EVMCF characterize the correlation between the extreme value FIPs and the coupled microstructure attributes β and β' for a SVE of size Ω. In this way, spatial correlations are identified between microstructure attributes that have a high probability of existing in the neighborhood of an extreme value FIPs. Multiple instantiations of Ω are required to effectively characterize and build up the tail of the probability distribution corresponding to extreme value response neighborhoods. From these statistical functions, the coupled microstructure attributes that are statistically the most relevant to the extreme value response can be identified. Moreover, the extreme value distributions of the response for different microstructure variants of a given material system can be compared; such a comparative analysis could support the materials design of new microstructures with improved extreme value response for a given application.

Statistically meaningful construction of the extreme value distribution of the FIPs along with the related EVMCF requires a significant number of simulations/experiments. This can require extensive processing time for both simulations and data analysis depending on the complexity of the models being analyzed. The number of samples required for statistical significance depends on the response parameter considered and material being analyzed. Analogous experimental data are not typically available and are very expensive to obtain. Typical fatigue experiments will not provide enough information to construct these coupled distribution functions because such experiments typically only consist of a few data

points at each stress/strain amplitude considered. In addition, fatigue hot spots are identified experimentally after failure and characterization of the sites of fatigue crack formation and their neighborhoods is very cumbersome and typically requires destructive sectioning. Thus, although this framework is general in its application to experiments and/or simulations, it is envisioned that it will be much more practically applied to simulations that are substantiated with limited experimentation. Such is the case here.

6.2.2 Simulation strategy

To exercise the aforementioned microstructure-sensitive extreme value probabilistic framework for polycrystalline Ni-base superalloys, the strategy implemented here estimates the extreme value distribution of the FIPs and the EVMCF via the simulation of multiple instantiations of the microstructure. As mentioned, the focus here is to characterize the dependence of the driving forces for fatigue crack formation on the crystallographic attributes of the microstructure in IN100. It is recognized that fatigue crack formation in IN100 is typically most associated with the presence of non-metallic inclusions and/or pores. However, as previously mentioned, Ni-base superalloys have been developed with much smaller populations of these types of inclusions/voids that fail predominantly crystallographically (*e.g.*, [211]). Thus, in this work consideration is given on how a variant of IN100 would fail crystallographically in the absence of non-metallic inclusions or voids. In addition, the improved understanding of extreme value behavior of the orientation dependent slip processes in IN100 developed here can later be coupled with the existence of inclusions/voids to improve current predictive models of fatigue crack formation in this material system. To accomplish this objective, instantiations of the microstructure are simulated via the FE package ABAQUS [121] coupled with a microstructure-sensitive crystal plasticity model for IN100 [147, 148].

The crystal plasticity model implemented here for IN100 was described in detail in Chapter 4 along with the associated constitutive relations. The primary, secondary and

tertiary γ' precipitates are not explicitly modeled, but their influence is accounted for in the proposed hardening laws and form of the flow rule. This model also accounts for the average effect of the grain size on the constitutive response and the dependence of the flow stress on crystallographic orientation. Both the standard 12 octahedral $\langle 110 \rangle \{111\}$ slip systems and 6 cube slip systems $\langle 110 \rangle \{100\}$ are explicitly considered. As previously mentioned, the cube slip systems describe "zig-zag" octahedral slip and shearing of the γ' precipitates that has been observed at higher homologous temperatures for crystals in hard orientations for octahedral slip [152, 214]. This particular model has been calibrated for IN100 at 650°C.

6.2.3 Simulation of microstructure volume elements

Using a crystal plasticity formulation allows these digital microstructure volume elements to serve as statistical volume elements (SVEs) for the cyclic plastic response on the scale of the individual grains (a key driving force for fatigue crack formation). Each SVE for a desired response (*e.g.*, grain scale plasticity) is designed to be large enough such that the response parameter of interest at a particular location is unaffected by statistical variations in the microstructure at distances on the order of the size of the volume (*i.e.*, correlation length is less than size of SVE); however, the volume is not so large that it contains a statistically representative set of responses for that particular response parameter. A discussion on appropriately defining SVE/RVE size can be found in Section 5.2.

Here the SVEs are constructed such that the lower order moments of the cyclic plastic response on the scale of the grains are unaffected by further increasing the volume of the SVE. Of course, the higher order moments affect the tail of the PDF and the RVE size for invariance of these moments would be quite large, in general. It is also desired that the SVE be suitably large to serve as a RVE in terms of the overall effective (*i.e.*, macroscopic) elastic/plastic response. In other words, the stress-strain response should be the same for any SVE. The RVE for this macroscopic response is insensitive to the higher order moments

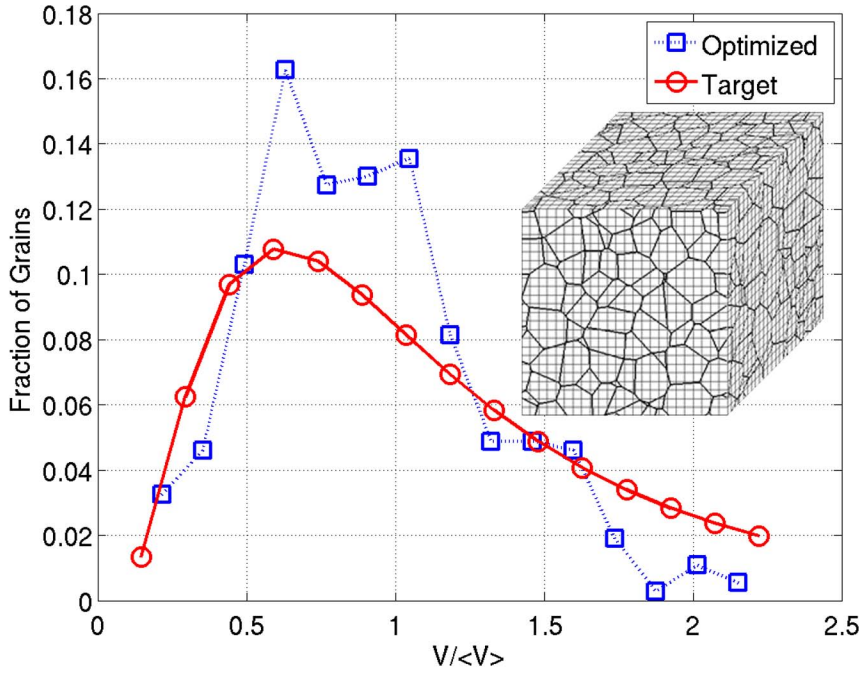

Figure 6.3: The target and optimized grain size distribution of a SVE instantiated for IN100 where V is the actual grain volume and $\langle V \rangle$ is the target average volume or 8.0×10^{-6}mm^3 or a cube root grain size of 0.02mm.

of the slip distribution, and is not the same as a RVE for the extreme value distribution of FIPs.

The SVEs for the simulations here were instantiated using VorPolycrystalGen as described in Section 5.3.1. Specifically, this program instantiates volumes of simulated polycrystalline microstructure based on the Voronoi tessellation whose distributions of grain size, orientation and disorientation are fit to prespecified targets. A SVE instantiated for IN100 along with an imposed voxellated mesh can be seen in Figure 6.3. The target and optimized distributions for the grain volume normalized by the target average grain volume are also shown in Figure 6.3. The orientation distribution was chosen as random as shown in Figure 6.4 (as commonly observed in IN100). The disorientation distribution was fit to a random Mackenzie disorientation distribution function [216, 217].

Once the microstructure in a particular SVE is instantiated and optimized to fit the target distributions of grains size, grain orientation, and grain disorientation, the program

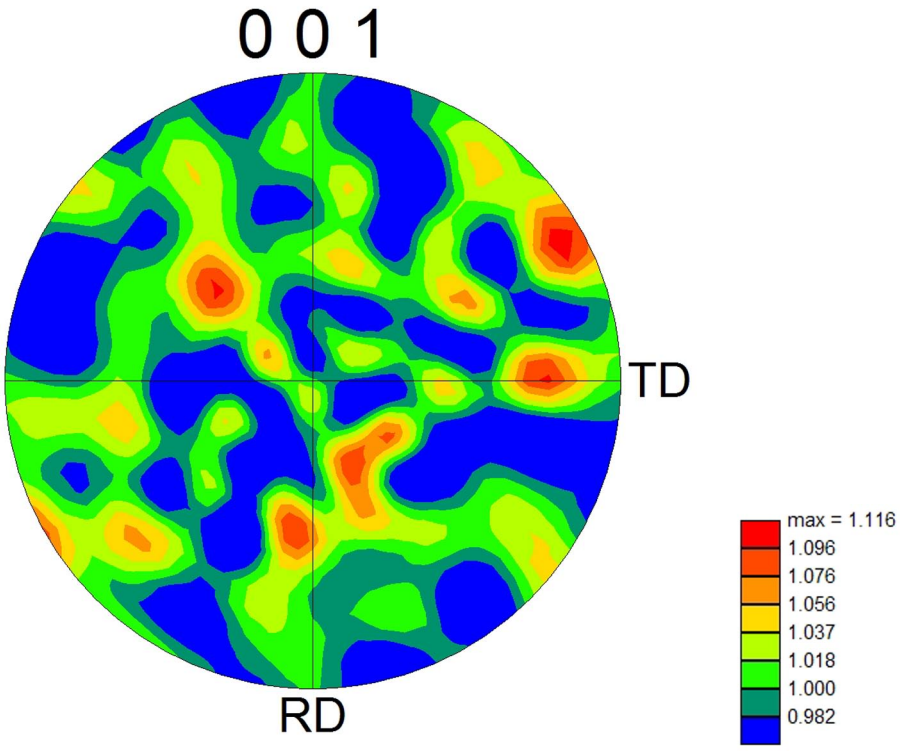

Figure 6.4: Pole figure representing the random texture of the instantiated microstructure volume elements for the Ni-base superalloy IN100.

writes the ABAQUS input files for the meshed microstructure that contain all the necessary information for the FE simulations. Information in these input files includes the details of the geometry, mesh, boundary and loading conditions. Meshing these SVEs was described in Section 5.4. The initial simulation cell geometry is defined by the user defined values of edge length and mesh density (the number of elements along each edge of the simulated block of microstructure). The user also defines the target distributions for the grain size, grain orientation and grain disorientation. Once the polycrystalline microstructure is instantiated for the volume element (with grain centers defined), the elements and nodes are created based on the mesh density input by the user. Using the known edge length and mesh density, the element edge length and total size is calculated. The elements are constructed as an array of cuboidal elements (type C3D8R in ABAQUS) each with identical dimensions. These particular elements employ reduced integration to speed up computation time. Cuboidal elements are also convenient because the overall simulation cell was assumed to be cubic in this model. In addition, a voxellated mesh greatly simplifies the application of periodic boundary conditions in all directions, as described in Section 5.5.

6.2.4 Microstructure attributes and fatigue indicator parameters

To estimate the driving forces for fatigue crack formation, the FIPs as introduced in Section 2.3.1 are applied. Specifically, here the critical plane cyclic plastic strain range based approaches are considered. As such the driving forces for fatigue crack formation are estimated via the MPSS and the FS [63] FIPs, *i.e.*,

$$P_{MPSS} = \frac{\left\langle \Delta\gamma_{p,max} \right\rangle_V}{2} \tag{6.1}$$

and

$$P_{FS} = \frac{\left\langle \Delta\gamma_{p,max} \right\rangle_V}{2} \left(1 + k_{FS} \frac{\sigma_{n,\max}}{\sigma_o} \right) \tag{6.2}$$

The nonlocal maximum cyclic plastic shear strain range is computed using the ordered

principal plastic strain ranges over a cycle, $\left\langle \Delta\epsilon_i^p \right\rangle_V\Big|_{cyc}$ for $i = 1, 2, 3$, as

$$\left\langle \Delta\gamma_{p,max} \right\rangle_V = \left| \frac{\left\langle \Delta\epsilon_1^p \right\rangle_V\Big|_{cyc} - \left\langle \Delta\epsilon_3^p \right\rangle_V\Big|_{cyc}}{2} \right| \tag{6.3}$$

where $\langle x \rangle_V$ is employed to denote averaging of a quantity "x" over a characteristic volume, V. Note that averaging is performed on each component of the plastic strain tensor, *i.e.*

$$\left\langle E_{ij}^p \right\rangle_V = \frac{1}{V} \int_V E_{ij}^p dV \tag{6.4}$$

where E_{ij}^p denotes the components of the plastic strain tensor $\mathbf{E}^p$. Larger magnitudes of these FIPs indicate a higher driving force for fatigue crack formation. In particular, the Fatemi-Socie (FS) parameter has been used to correlate fatigue crack formation over relatively significant number of grains for a range of multiaxial loading conditions for materials with extended Stage I dominant regions such as 1045 steel and IN718 [14, 66]. Although the Fatemi-Socie FIP was originally only applied at the scale of laboratory specimens, several workers have applied this and similar FIPs at the microscale using crystal plasticity simulations. For example, Bennett *et al.* [66] correlated microslip and mixed-mode behavior of microstructurally small crack growth to the Fatemi-Socie FIP and considered its distribution over the grains; moreover, the Fatemi-Socie FIP distributes heterogeneously over the grains. Moreover, they also observed that the Fatemi-Socie FIP correlates well with distributions of small fatigue cracks within the grains. Bennett *et al.* [52] also used the Fatemi-Socie FIP to explore local grain orientation distribution effects on microslip in HCF. Other workers [67, 68] observed good agreement between the locally applied Fatemi-Socie FIP (determined using crystal plasticity calculations) and microstructurally small crack growth within the first few grains based on experiments in structural steel S460N. Dunne *et al.* [69, 218] employed simulations coupled with experiments to show that crystal plasticity can correlate precisely to localized plastic slip (and subsequent fatigue crack formation) in

realistic Ni-base superalloy and Ti alloy microstructures. They used the cumulative plastic strain (see Equation 7.4 in Section 7.3) as a metric for correlating nucleation at a point within a grain, instead of a MPSS or FS FIP. Findley and Saxena [70] employed the Fatemi-Socie FIP to examine the effect microstructure attributes such as grain size have on the local driving forces for fatigue crack formation. Zhang *et al.* [219] and Prasannavenkatesan *et al.* [220] also used the Fatemi-Socie FIPs to look at the local processes of fatigue crack formation at primary inclusions in carburized and shot-peened martensitic steel. Such work demonstrates the ability of locally applied FIPs determined via crystal plasticity simulations to correlate microstructure scale slip with fatigue crack formation and early stages of microstructurally small crack growth for a range of ductile metallic polycrystalline material systems. In essence, there is similitude in scaling the relations between and the number of cycles to form and growth a fatigue crack to different length scales within the range of several microns to several hundred microns.

As discussed by McDowell [6], these types of critical plane approaches for shear-dominated microcracking are related to Stage I shear-dominated propagation of MSCs with an influence of the normal stress to the slip/crack plane. Early work by Hoshide and Socie [71] considered the affect of microplastic strain on fatigue crack nucleation and MSC crack growth under mixed-mode (I-II) loading. They correlated ΔJ from EPFM via a Paris type law with fatigue crack growth behavior of small cracks. Moreover, Hoshide and Socie [71] related ΔJ to the ranges of crack opening displacement (COD) and/or crack sliding displacement (CSD) for mode I and mode II, respectively. Later, McDowell and Berard [65] employed ΔJ and argued for similarity of ΔCTD with the Fatemi-Socie parameter.

6.3 Extreme value fatigue response and microstructure in IN100

To investigate the influence of grain orientation, disorientation and grain size on IN100, multiple SVEs were constructed using VorPolycrystalGen and simulated via FEM in

ABAQUS, as previously described. Multiple SVEs for the local plastic response were instantiated and strained uniaxially at 0.3%, 0.5% and 0.7% strain at a quasistatic strain rate of $0.002s^{-1}$. The macroscopic yield is observed for this particular IN100 at 1.0% strain. The cyclic strains were completely reversed (*i.e.*, R = -1). Each simulation was cycled three times to allow for an initial shakedown period before the results were analyzed. There is no provision in the current simulations to address cyclic hardening or softening behavior over large numbers of cycles. Periodic boundary conditions were applied in all directions. As described in Sections 5.6 and 5.7, the voxellated meshes of these instantiated microstructure volume elements consist of quadrilateral elements with reduced integration (type C3D8R in ABAQUS). Also the convergence of the response estimated via these voxellated meshes was demonstrated as long as the FIPs were calculated over volumes on the scale of the grains. As such all FIPs considered here in this chapter are averaged over each individual grain. The number of grains in the simulations was allowed to vary to best fit the imposed grain size distribution and ranged between 325-375 grains. Each SVE was dimensioned to 0.150mm along each edge. The distribution of grain volumes normalized by the target average grain volume of $8.0 \times 10^{-6}mm^3$ was fit to a log-normal distribution with a mean of -12 and standard deviation of 0.4. This corresponds to a target average cube root grain size of 0.020mm. There are 24 elements along each edge of the SVE or 13824 elements in all. The ratio of the element volume to the average target grain volume is 0.030. A total of 50 simulated SVEs were cycled at 0.3% strain, 100 at 0.5% and 50 at 0.7% strain.

6.3.1 Characterization of extreme value distributions of FIPs

It is of interest to first consider the character of the extreme value distributions of the FIPs as estimated from the simulated SVEs. Recalling from Section 3.2, there are only three possible non-degenerated asymptotic distributions for the maximum extreme value distributions. The goal is to be able to characterize a dataset as belonging to one of these three

types of distributions so that the mathematical properties of these distributions can be used to better understand the data. Here it will be demonstrated that the extreme value FIPs sampled from the simulated SVEs are well characterized by the asymptotic form of the extreme value Gumbel distribution.

It is important to first consider the number of simulated SVE that are required to accurately characterize the extreme value distribution of response. It was mentioned previously in Section 5.2, that Kanit *et al.* [172] demonstrated that a certain number of SVEs could be used to estimate the mean value response of an RVE. In other words, a sufficient number of simulated SVEs can be employed to estimate the effective average (*i.e.* macroscale) response for a given response function. Additionally, Niezgoda *et al.* [178] demonstrated that 2-point correlation functions could be employed to determine the best limited set of SVEs to estimate the mean value response of the ensemble (*i.e.* RVE). This limited number of SVEs selected to be representative of a single RVE was called an RVE set. Selectively choosing the best SVEs to estimate the effective average response is in contrast to the previous approach where the SVEs are randomly selected. The latter approach requires many more SVEs to estimate the effective average response of a single RVE.

However, very little work has been done to quantify how many SVEs of sufficient size are required to estimate the extreme value distributions of response. It is the objective here to determine how many SVEs are required such the character of the extreme value distribution does not significantly change as more SVEs are sampled. To visualize the extreme value distributions of the FIPs calculated in the SVE simulated here, the extreme value FIPs for each SVE are given on a probability plot that has been linearized for the extreme value Gumbel distribution. This is demonstrated in Figure 6.5, where the distributions of the extreme value Fatemi-Socie FIPs are shown for sample sizes of 25, 50, 75 and 100 SVEs. Here these SVEs were all cycled at 0.5% maximum strain strain. Estimation of the grain scale extreme value FIPs was done by calculating the FIP for each grain. In other words, the grain averaged FIP was calculated from the cyclic plastic strain tensor averaged over

the entire volume of each grain. In these simulations, the grains nominally had about 40 elements per grain. The critical plane is determined from the principal components of the cyclic plastic strain range tensor as described by Equation 2.9. In Figure 6.5, it is noted that the probability p is linearized for the extreme value Gumbel distribution by appropriately scaling the ordinate. The range of observed extreme values is then given by the abscissa. By scaling the plot in this manner, a true extreme value Gumbel distribution appears as a straight line. This linearizion procedure and the method used to fit the experimental data to the extreme value Gumbel distribution is outlined in Appendix B. The fits of these sampled distributions to the Gumbel distribution are shown in Figure 6.5. As can be observed from Table 6.3, these data are fit by the Gumbel distribution with high confidence (*i.e.*, $R^2 > 0.97$), even for a sample size of just 25 simulated SVEs; moreover, the fitting parameters do not change significantly with increased sample size. This suggests that the extreme value distribution of the FIPs can be estimated in some cases with as few as 25 simulated SVEs.

Thus, the approach presented here demonstrates that the minimum number of SVEs required to characterize the extreme value distribution for a given response can be determined by gradually increasing the number of simulated SVE until the character of the distribution is relatively unchanged even when more data points are added. In the case shown here, which is well described by the Gumbel (Type I) extreme value distribution, convergence of the extreme value distribution based on the number of simulated SVEs is quantified in terms of the difference between the parameters of the Gumbel fits for the different sample sizes or in terms of the R^2 values determined from the least squares regression when the data is plotted on the linearized Gumbel probability scale. Determination of convergence is likely much more difficult when the extreme value distributions do not fit one of the three known asymptotic extreme value distributions. In this case, many more data points are likely required to ensure that the extreme value distribution is well characterized because of the lack of linearity that results because the linearized probability scale is unknown when the

Table 6.3: The parameters for the least squares fit of the Gumbel distribution (*i.e.*, $F^I_{Y_n}(y) = \exp\left[-e^{-\alpha_n(y-u_n)}\right]$) for the extreme value distributions of the Fatemi-Socie FIPs sampled over 25, 50, 75, and 100 SVEs, respectively, for 0.5% maximum strain. These extreme value distributions are plotted in Figure 6.5. The goodness of fit is also given in terms of the R^2 value that ranges between 0 and 1 with 1 indicating a perfect fit.

#SVEs	α_n	u_n	R^2
25	8186.6	4.375×10^{-4}	0.973
50	8345.4	4.453×10^{-4}	0.988
75	8581.8	4.402×10^{-4}	0.987
100	8727.9	4.307×10^{-4}	0.991

Table 6.4: Fit Gumbel distribution parameters (*i.e.*, $F^I_{Y_n}(y) = \exp\left[-e^{-\alpha_n(y-u_n)}\right]$) for the extreme value maximum plastic shear strain (MPSS) and Fatemi-Socie (FS) FIPs for IN100 cycled at 0.5% maximum strain. These extreme value distributions are plotted in Figure 6.6. The goodness of fit is also given in terms of the R^2 value that ranges between 0 and 1 with 1 indicating a perfect fit.

FIP	α_n	u_n	R^2
FS	8.73×10^3	4.31×10^{-4}	0.991
MPSS	1.13×10^4	3.18×10^{-4}	0.993

extreme value distribution deviates from one of the three known asymptotic extreme value distributions.

A comparison of the extreme value FS and MPSS FIP distributions calculated from 100 simulated SVEs of IN100 are shown in Figure 6.6. This plot is similarly linearized for the Gumbel distribution. In IN100, the grains predicted to exhibit the extreme value response were different between the MPSS and FS FIPs in approximately 10% of the SVEs simulated. The parameters of the Gumbel distributions fit via least squares regression to the observed extreme value FIPs are given in Table 6.4. It likely that the FS parameter better characterizes the mechanisms of crystallographic fatigue crack formation. As previously discussed, it has been shown that the FS parameter appropriately captures shear-dominated microcracking related to Stage I shear-dominated propagation of MSCs with an influence of the normal stress to the slip/crack plane [65,71]. Hereafter, it is assumed that the driving forces for fatigue crack formation are best captured by the FS parameter.

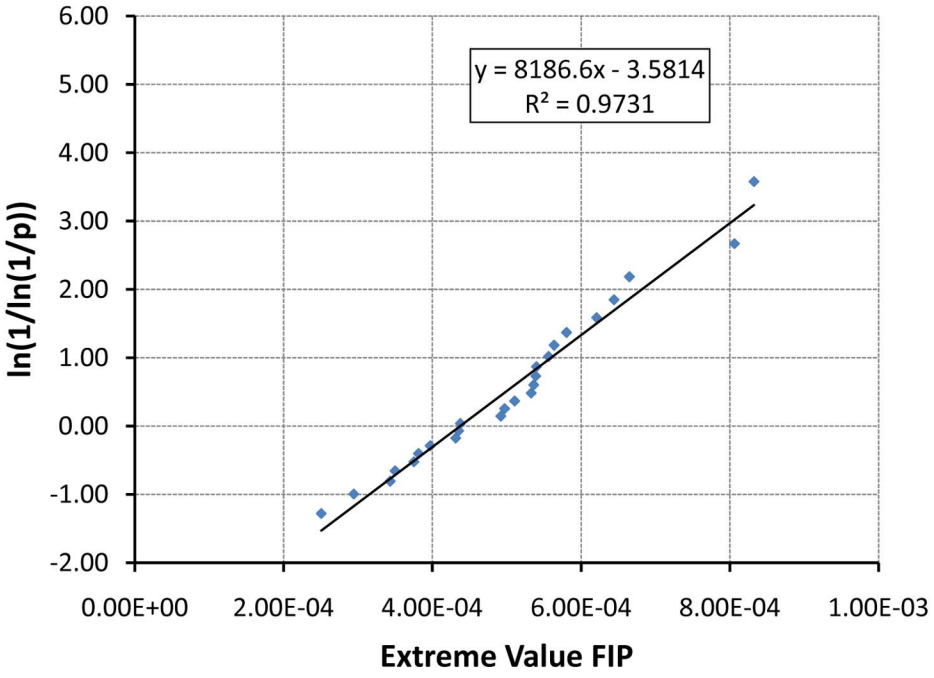

(a)

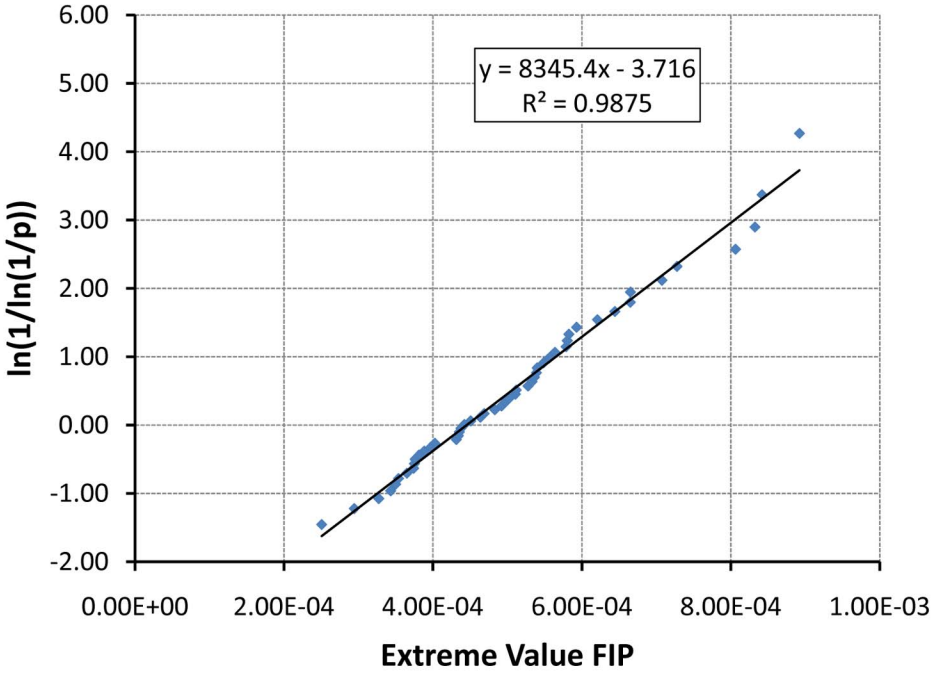

(b)

Figure 6.5: Extreme value distribution of the Fatemi-Socie FIP as estimated over grain sized averaging volumes for (a) 25, (b) 50, (c) 75, and (d) 100 SVEs for the simulations cycled at 0.5% strain. The extreme value Fatemi-Socie FIP was selected to be the FIP with the highest magnitude out of all the FIP calculated over each grain. The fit described by the linear equation $y = mx + b$ is such that x is the value of the FIP and $y = \ln(1/\ln(1/p))$ such that p is the probability

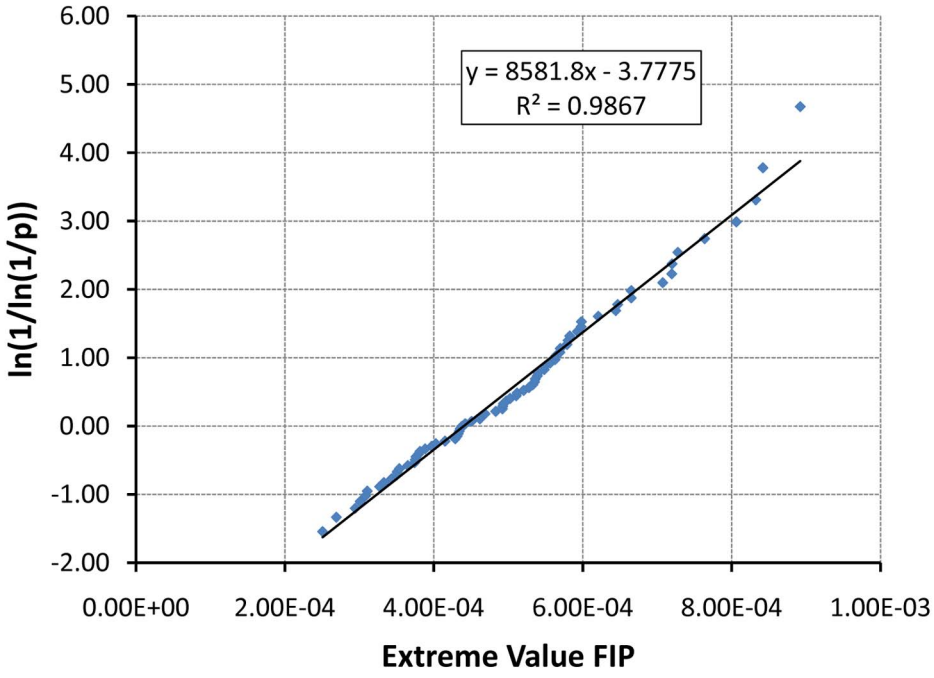

(c)

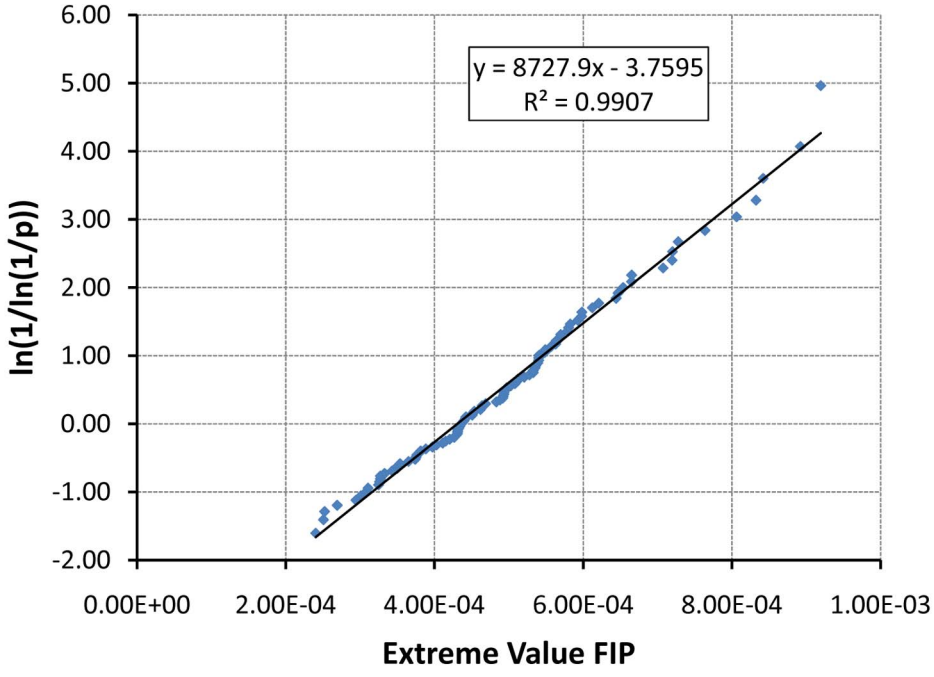

(d)

Figure 6.5: Extreme value distribution of the Fatemi-Socie FIP as estimated over grain sized averaging volumes for (a) 25, (b) 50, (c) 75, and (d) 100 SVEs for the simulations cycled at 0.5% strain. The extreme value Fatemi-Socie FIP was selected to be the FIP with the highest magnitude out of all the FIP calculated over each grain. The fit described by the linear equation $y = mx + b$ is such that x is the value of the FIP and $y = \ln(1/\ln(1/p))$ such that p is the probability

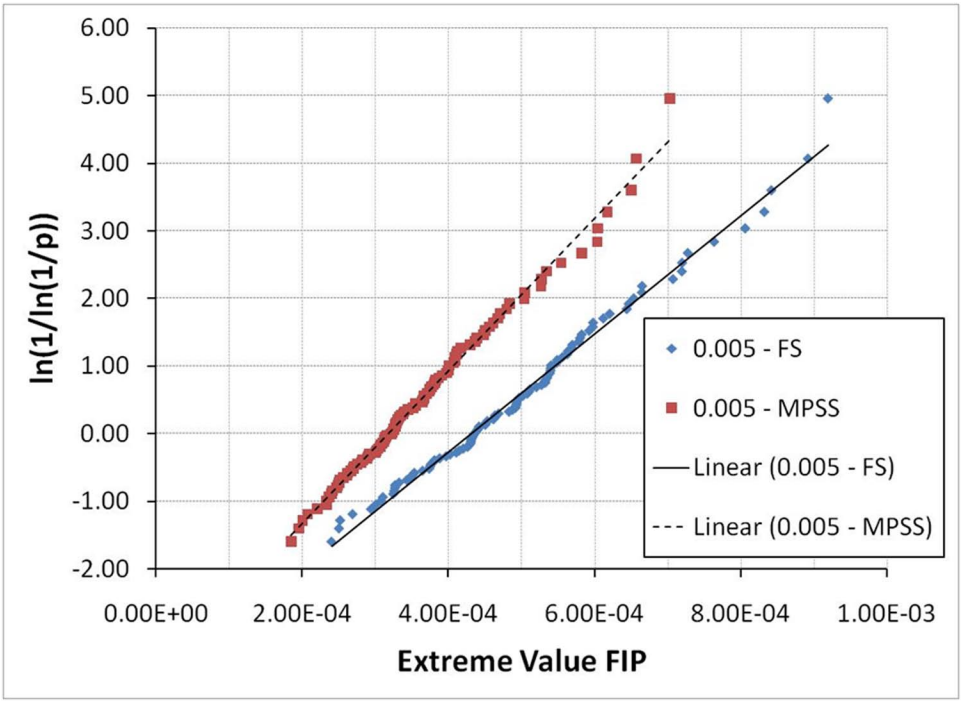

Figure 6.6: The extreme value grain averaged maximum plastic shear strain (MPSS) and Fatemi-Socie (FS) FIPs calculated over 100 simulated SVEs cycled at 0.5% maximum strain for IN100 plotted on a Gumbel probability scale.

Figure 6.7 shows the distributions of the extreme value Fatemi-Socie FIPs for the different strain magnitudes tested, 0.3%, 0.5%, and 0.7%. Again this plot is linearized for the Gumbel distribution as outlined in Appendix B. Additionally, the extreme values of the FIPs are plotted in Figure 6.7 on a log scale in order compare the distributions for the different strain magnitudes on the same plot. The parameters for the fit of the Gumbel distribution to these observations are given in Table 6.5. It is noted that as the strain magnitude increases, the extreme value distributions of the Fatemi-Socie FIP tend to shift to the right toward higher magnitudes of the FIPs. This correlates with the fact that as the strain magnitude increases the driving forces for fatigue crack formation are higher. Thus, fatigue cracks are estimated to form more rapidly and the portion of fatigue life attributed to fatigue crack formation is shorter.

The parameters for the Gumbel distribution fit to the extreme value distributions of the FIP estimated from the simulated SVEs can be applied to quantify the relative dispersion

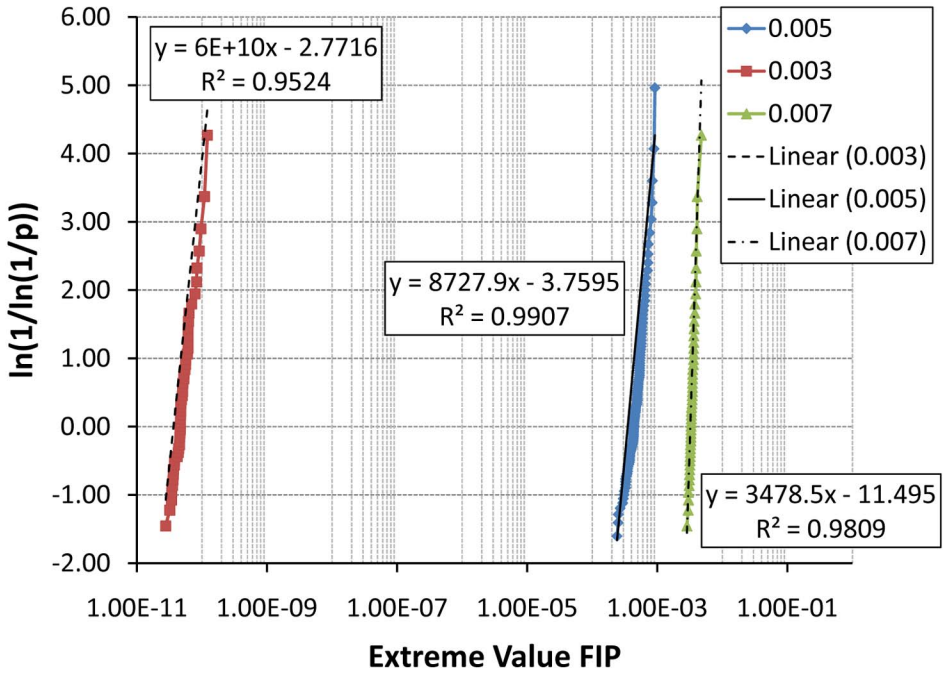

Figure 6.7: The extreme value distribution of the Fatemi-Socie FIP as estimated over a single element and over the entire grain for the simulations cycled at 0.3%, 0.5%, and 0.7% strain. The extreme value Fatemi-Socie FIP was selected to be the FIP with the highest magnitude out of all the FIP calculated over each element or over each grain in each SVE.

Table 6.5: The parameters for the least squares fit of the Gumbel distribution (*i.e.*, $F^I_{Y_n}(y) = \exp\left[-e^{-\alpha_n(y-u_n)}\right]$) for the extreme value distributions of the Fatemi-Socie FIP for the different maximum strain levels simulated. The goodness of fit is also given in terms of the R^2 value that ranges between 0 and 1, with 1 indicating a perfect fit.

% Strain	α_n	u_n	$(\alpha_n)^{-1}/u_n$	R^2
0.30%	6.0×10^{10}	4.619×10^{-11}	0.361	0.952
0.50%	8727.9	4.307×10^{-4}	0.266	0.991
0.70%	3478.5	3.305×10^{-3}	0.087	0.981

of the extreme value distributions for the different strain magnitudes considered. For the Gumbel distribution, recall that α_n is an inverse measure of the dispersion of the largest values of the initial population (*i.e.*, the parent distribution of the extreme value distribution) while u_n can be considered as the characteristic largest value of the initial population. Thus, the quantity $(\alpha_n)^{-1}/u_n$ is an indication of the dispersion of the extreme value distribution relative to the characteristic largest values of the initial population. In other words, larger values of $(\alpha_n)^{-1}/u_n$ indicate greater variation around the characteristic largest values than smaller values. In the case shown in Figure 6.7, as the strain magnitude increases the variation of the extreme value distributions of the distributions (*i.e.*, $(\alpha_n)^{-1}/u_n$ from Table 6.5) tends to decrease. These data corroborate the S-N curve for IN100, as seen in Figure 6.2 with the noted exception at 1150MPa where there are arguably two competing modes of failure. As the stress/strain magnitude increases the overall variation in the fatigue lives decrease. These results similarly show that variation of fatigue life associated with crack formation decreases as the magnitude of applied cyclic straining increases.

6.3.2 Microstructure attributes correlated with the extreme value FIPs

To understand how local attributes of microstructure influence the extreme value fatigue response as estimated via the FIPs, microstructure attributes in the neighborhoods of the extreme value FIPs are considered. Two forms of the Schmid factor are considered here. The *apparent* Schmid factor for the lattice orientation g, m_a^g, is calculated based only on the orientation of the slip plane relative to the loading direction, *i.e.*, $m_a^g = \max\left[\cos\left(\phi^i\right)\cos\left(\lambda^i\right), i = 1,\ldots,N\right]$, where ϕ^i is the angle between the i$^{\text{th}}$ slip plane normal and the uniaxial stress direction, and λ^i is the angle between the i$^{\text{th}}$ slip direction and the direction of SVE uniaxial applied stress. The total number of slip systems is N. In contrast, the *local* Schmid factor calculated over a volume ω, m_i^ω, is computed as the ratio between the maximum resolved shear stress (computed from the FE simulations) divided by the remote SVE uniaxial applied stress σ, *i.e.*, $m_i^\omega = \max\left(\tau_{rss}^i\right)/\sigma$ for $i = 1,\ldots,N$. In

comparison to the apparent Schmid factor, the local Schmid factor considers the local stress state as affected by intergranular interactions and microplasticity. Thus, although the apparent Schmid factor is typically bounded between 0.27 and 0.5 for $\langle 110 \rangle \{111\}$ octahedral slip, this is not the case for the local Schmid factor. In reality the local Schmid factor will be observed to be more broadly distributed between 0 and 1 due to load shedding or load shielding from neighboring grains, which affects the local stress fields in individual grains relative to the macroscopic applied loading conditions. For the calculations given below, the volumes over which the local Schmid factor are calculated correspond to the same volumes over which the FIPs are calculated. The apparent Schmid factor is calculated based on grain orientation relative to the SVE uniaxial applied stress.

Next, the focus is directed on the zones where the extreme value FIPs have been identified. In Figure 6.8, plots are given for the grain average extreme value Fatemi-Socie FIP versus the corresponding local Schmid factor for both the octahedral and cube slip systems for applied maximum strain magnitudes of 0.3%, 0.5% and 0.7%, respectively. In Figure 6.8, each extreme value Fatemi-Socie FIP is associated with two Schmid factors, one for octahedral slip and one for cube slip. It is noted that as the maximum cyclic strain amplitude increases, the local Schmid factors associated with the extreme value FIPs tend to decrease slightly. This is logical because even though the far field stress increases the flow stress may not change significantly. Therefore, the local Schmid factor will decrease in magnitude as the far field load increases. Secondly, it is noted that in all cases the Schmid factors for cube slip are of greater magnitude than the local Schmid factors for octahedral slip as seen in Figure 6.8. In other words, the grains in which the extreme value FIPs are identified all appear to be unfavorably oriented for octahedral slip.

6.3.3 Extreme value marked correlation functions of apparent Schmid factors

The correlated microstructure attributes at the locations are also considered in terms of the EVMCF. As discussed previously, the primary microstructure attribute considered in

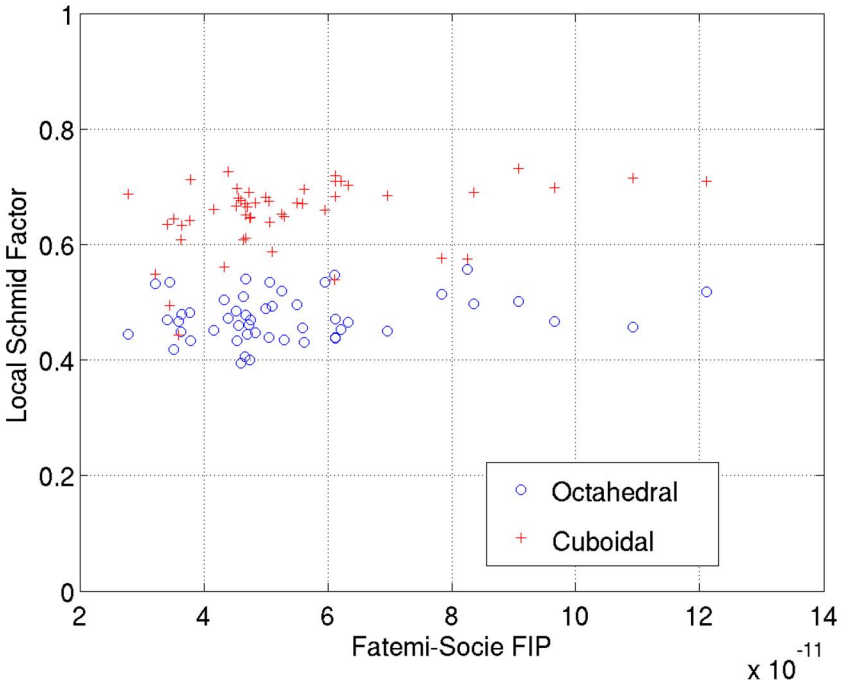

(a)

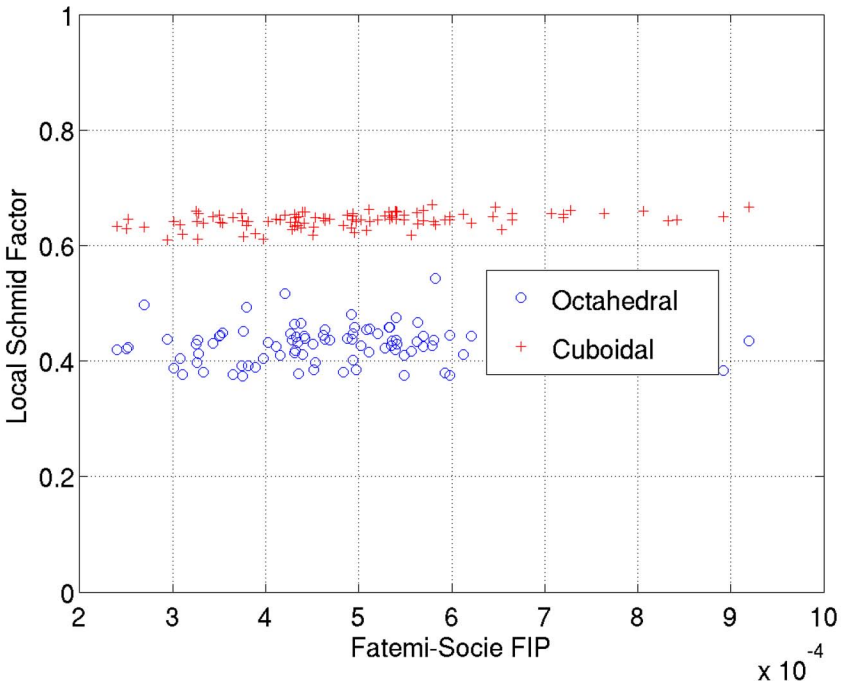

(b)

Figure 6.8: Scatter plot of the extreme value Fatemi-Socie FIP (abscissa) versus the local Schmid factor (ordinate) for (a) 50 simulated SVEs at 0.3% strain, (b) 100 simulated SVEs at 0.5% strain, and (c) 50 simulated SVEs at 0.7% strain for IN100.

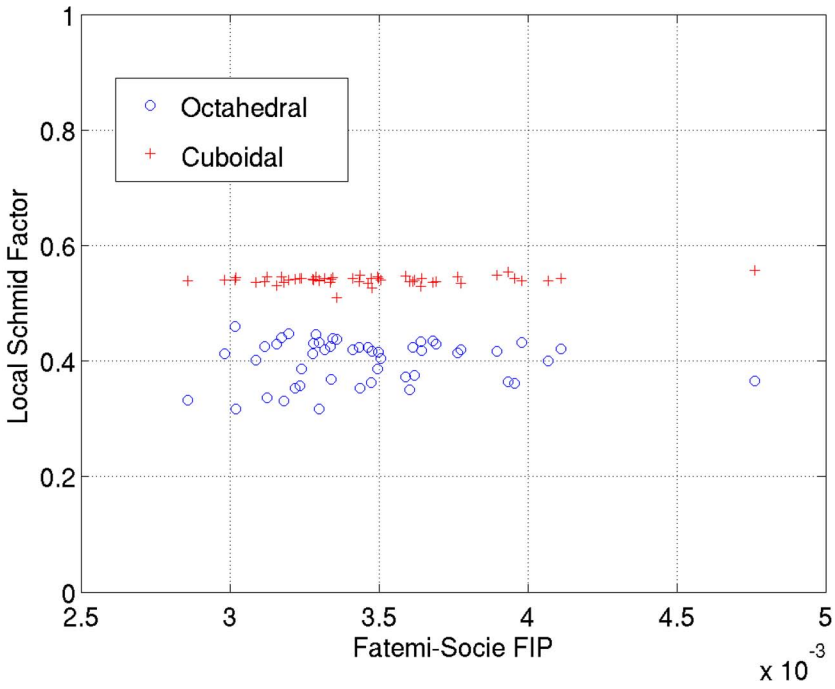

(c)

Figure 6.8: Scatter plot of the extreme value Fatemi-Socie FIP (abscissa) versus the local Schmid factor (ordinate) for (a) 50 simulated SVEs at 0.3% strain, (b) 100 simulated SVEs at 0.5% strain, and (c) 50 simulated SVEs at 0.7% strain for IN100.

this study is crystallographic orientation. As such, the extreme value marked radial correlation function for the FIPs are constructed in terms of the apparent Schmid Factor (*i.e.*, $R_{\max(FIP)}\left(m_a^g, m_a^{g'}|r,\Omega\right)$). In this way, the probabilities that specific grain orientations and misorientations exist coincident with the observed extreme value FIPs are indirectly quantified. As will be seen later, constructing the extreme value correlation function with the apparent Schmid factor instead of the more direct microstructure attribute of crystalline orientation simplifies the interpretation of the results. A choice was made to not use the local Schmid factor computed using the point wise stress tensor acting on slip systems at each point in the mesh because the local Schmid factor is a response parameter and not a direct description of the local microstructure attribute of interest (*i.e.*, grain orientation). Instead, the distributions of the response function reflect the local stress state information.

In Figures 6.9 to 6.11, the complete radial distribution estimated over the entire set of simulated SVEs and the extreme value marked radial distribution functions sampled only at the location of the extreme value FIPs for the 100 SVEs cycled at 0.5% strain are shown for several combinations of the apparent Schmid factor. In Figure 6.9, plots of the complete radial and extreme value marked radial correlation function are given for the apparent Schmid factors (a) $m_a^g = 0.45 - 0.5$ (cube slip) and $m_a^{g'} = 0.45 - 0.5$ (cube slip), (b) $m_a^g = 0.45 - 0.5$ (cube slip) and $m_a^{g'} = 0.40 - 0.45$ (cube slip), (c) $m_a^g = 0.45 - 0.5$ (cube slip) and $m_a^{g'} = 0.45 - 0.5$ (octahedral slip), and (d) $m_a^g = 0.45 - 0.5$ (cube slip) and $m_a^{g'} = 0.40 - 0.45$ (octahedral slip). The distance r that separates the two orientations is normalized against the average cube root grain size d (*i.e.*, 20 μm). In all cases, grains that have a high magnitude of the apparent Schmid factor for cube slip $m_a^g = 0.45 - 0.5$ near grains with a moderate to high apparent Schmid factor for cube or octahedral slip $m_a^{g'} = 0.4 - 0.5$ exist with a significantly higher probability at the locations of extreme value response than in the overall microstructure. The particular combination of apparent Schmid factors shown in Figure 6.9 were selected because they occurred with the highest probability at the extreme value location of the FIPs. In Figure 6.9(a), the auto-correlation

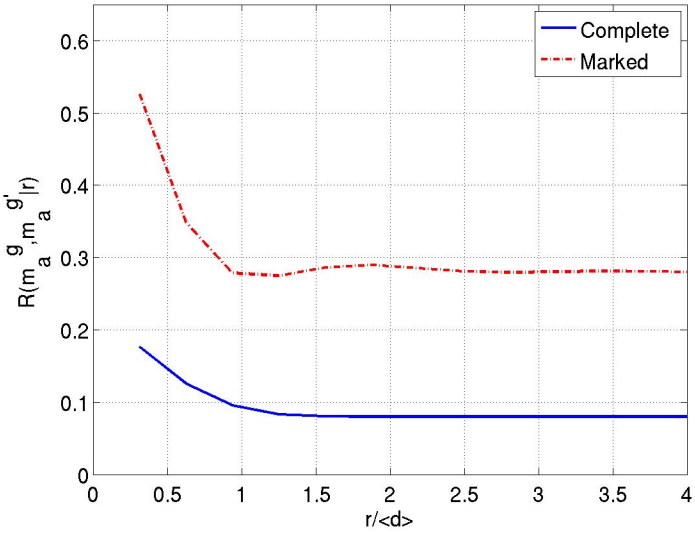

(a)

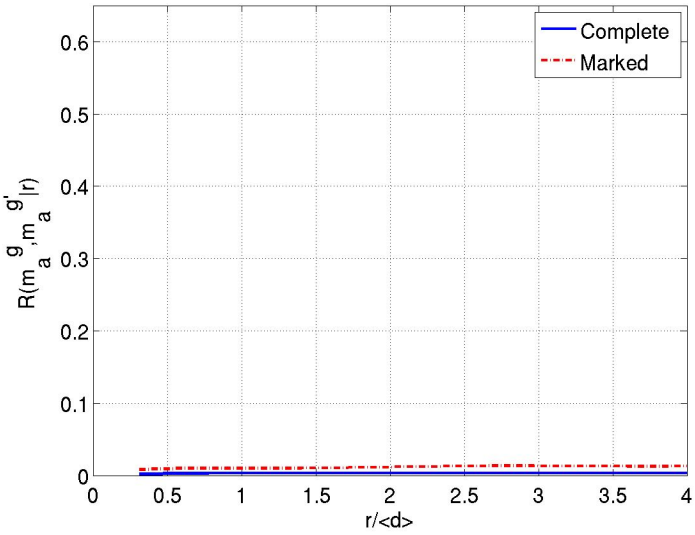

(b)

Figure 6.9: The complete radial and extreme value marked radial correlation function for the simulated SVEs of IN100 cycled at 0.5% maximum strain for the apparent Schmid factors (a) $m_a^g = 0.45 - 0.5$ (cube slip) and $m_a^{g'} = 0.45 - 0.5$ (cube slip), (b) $m_a^g = 0.45 - 0.5$ (cube slip) and $m_a^{g'} = 0.40 - 0.45$ (cube slip), (c) $m_a^g = 0.45 - 0.5$ (cube slip) and $m_a^{g'} = 0.45 - 0.5$ (oct. slip), and (d) $m_a^g = 0.45 - 0.5$ (cube slip) and $m_a^{g'} = 0.40 - 0.45$ (oct. slip). The distance r is normalized by the average grain size d of 20 μm.

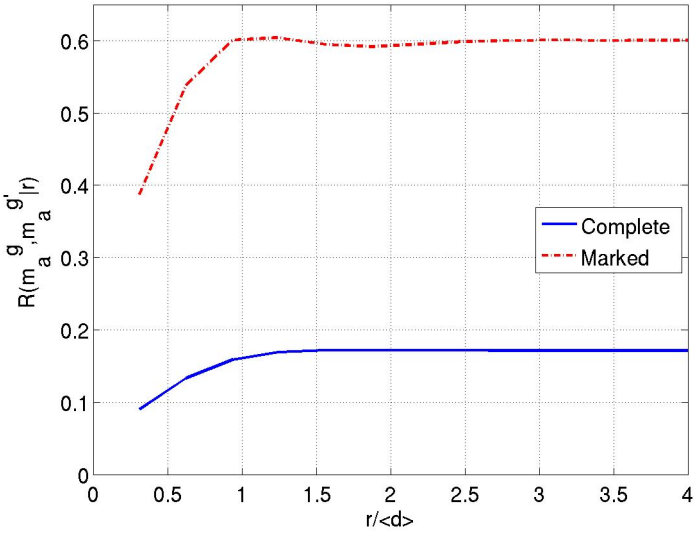

(c)

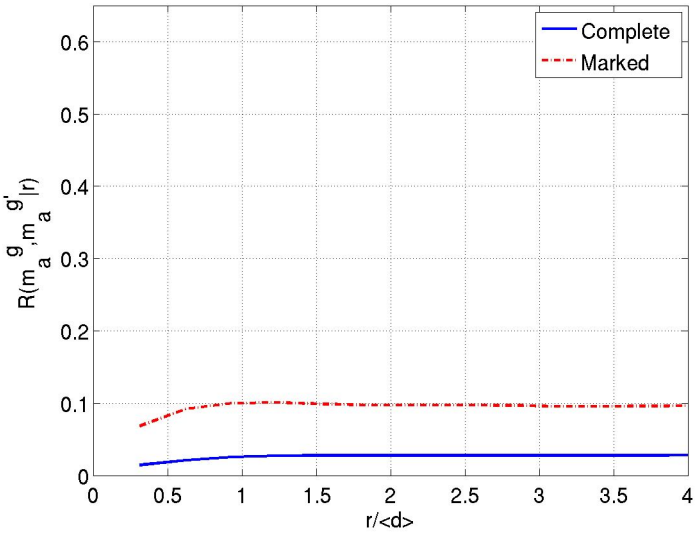

(d)

Figure 6.9: The complete radial and extreme value marked radial correlation function for the simulated SVEs of IN100 cycled at 0.5% maximum strain for the apparent Schmid factors (a) $m_a^g = 0.45 - 0.5$ (cube slip) and $m_a^{g'} = 0.45 - 0.5$ (cube slip), (b) $m_a^g = 0.45 - 0.5$ (cube slip) and $m_a^{g'} = 0.40 - 0.45$ (cube slip), (c) $m_a^g = 0.45 - 0.5$ (cube slip) and $m_a^{g'} = 0.45 - 0.5$ (oct. slip), and (d) $m_a^g = 0.45 - 0.5$ (cube slip) and $m_a^{g'} = 0.40 - 0.45$ (oct. slip). The distance r is normalized by the average grain size d of 20 μm.

is shown between the apparent Schmid factors $m_a^g = m_a^{g'} = 0.45 - 0.5$ (for cube slip). Below one average grain size it can be observed that the probability of finding $m_a^g = 0.45 - 0.5$ (for cube slip) at the location of the extreme value response is as high as 50%; in contrast, the probability of finding this particular orientation in the complete microstructure ensemble is only 20%. Similarly, the probability of finding $m_a^g = 0.45 - 0.5$ (for cube slip) near $m_a^{g'} = 0.45 - 0.5$ (for octahedral slip) (as can be seen in Figure 6.9(c)) is as high as 60% at a distance of one average grain size; whereas, the probability of these correlated orientation existing in the complete microstructure ensemble is less than 20%. Similar difference are observed in Figure 6.9 (b) and (d). These EVMCFs describe a high probability of finding a high FIPs in individual or clusters of grains for easy cube slip surrounded by grains oriented for easy octahedral slip.

It appears that grains oriented with moderate magnitudes of the Schmid factor for cube slip ($m_a^g = 0.4 - 0.45$) are not as critical to the extreme value FIPs as the grains with the highest magnitudes of the Schmid factor for cube slip (*i.e.*, with Schmid factors $m_a^g = 0.45 - 0.5$ (cube slip)). As see in Figure 6.10, grains oriented with moderate magnitudes of the Schmid factor for cube slip (Figure 6.10(a)),or grains with moderate magnitudes of the Schmid factor for cube slip near grains with the highest magnitudes of the Schmid factor for octahedral slip (Figure 6.10(b)), are not considered likely to exist coincident with the extreme value response. This indicates that the highest driving forces for fatigue crack formation develop only near grains with a very high magnitude of the apparent Schmid factor for cube slip. Other coupling between the Schmid factors for both cube and octahedral slip found not to exist with high probability coincident with the extreme value response are given in Figure 6.11. This suggests that there are many possible grain combinations that do not raise the driving forces for fatigue crack formation as significantly as do those described in Figure 6.9.

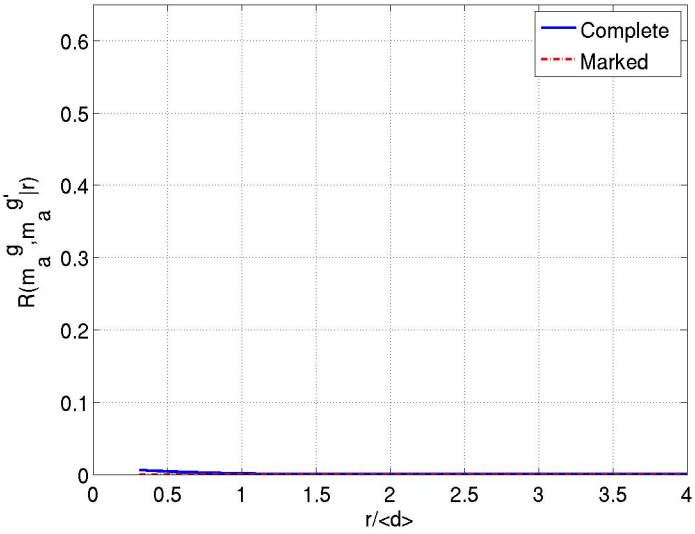

(a)

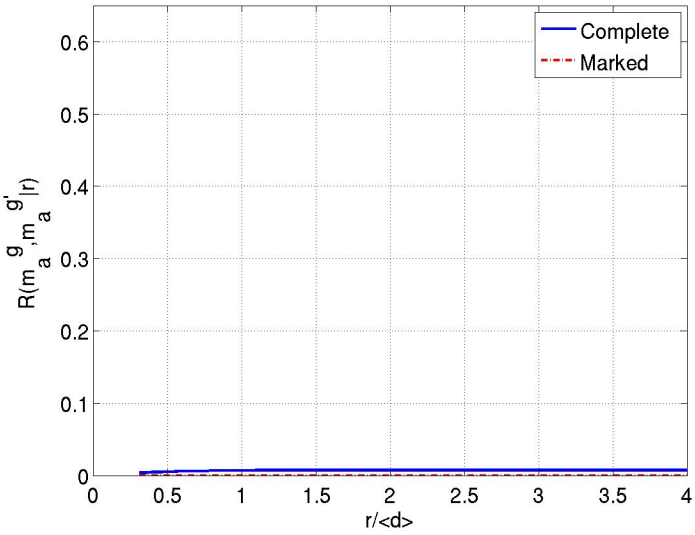

(b)

Figure 6.10: The complete radial and extreme value marked radial correlation function for the simulated SVEs of IN100 cycled at 0.5% maximum strain for the apparent Schmid factors (a) $m_a^g = 0.40 - 0.45$ (cube slip) and $m_a^{g'} = 0.40 - 0.45$ (cube slip) and (b) $m_a^g = 0.40 - 0.45$ (cube slip) and $m_a^{g'} = 0.45 - 0.5$ (oct. slip). The distance r is normalized by the average grain size d of 20 μm.

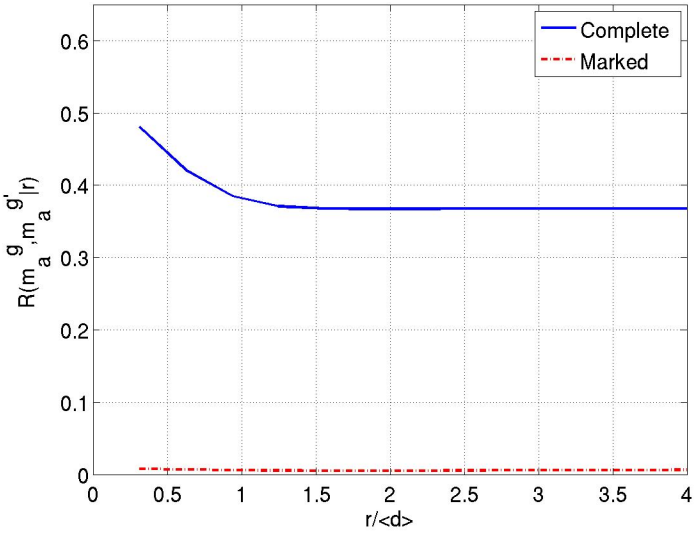

(a)

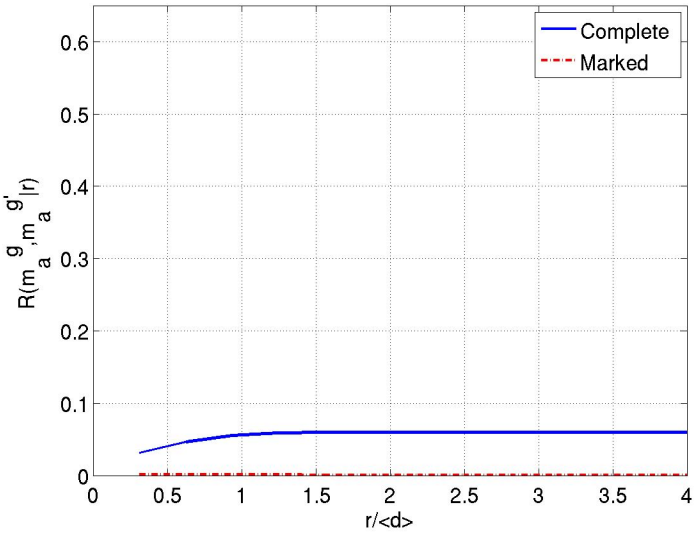

(b)

Figure 6.11: The radial and extreme value marked radial correlation function for the simulated SVEs of IN100 cycled at 0.5% maximum strain for the apparent Schmid factors (a) $m_a^g = 0.45 - 0.5$ (oct. slip) and $m_a^{g'} = 0.45 - 0.5$ (oct. slip), (b) $m_a^g = 0.45 - 0.5$ (oct. slip) and $m_a^{g'} = 0.40 - 0.45$ (oct. slip), (c) $m_a^g = 0.40 - 0.45$ (oct. slip) and $m_a^{g'} = 0.45 - 0.5$ (oct. slip), and (d) $m_a^g = 0.40 - 0.45$ (oct. slip) and $m_a^{g'} = 0.40 - 0.45$ (oct. slip). The distance r normalized by the average grain size d of 20 μm.

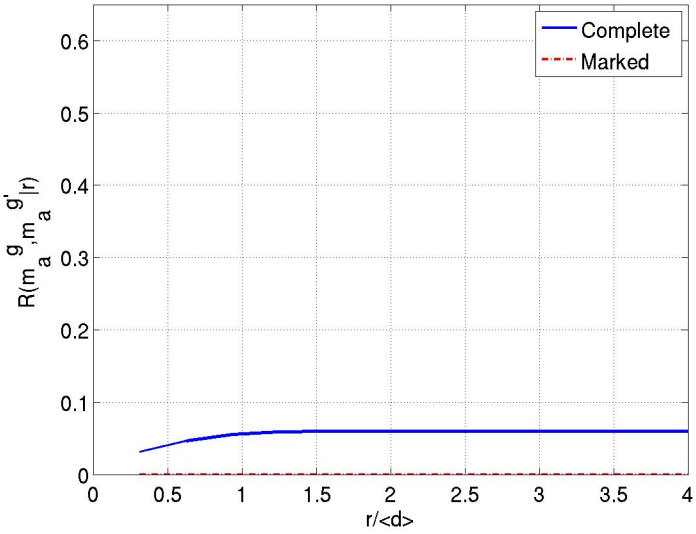

(c)

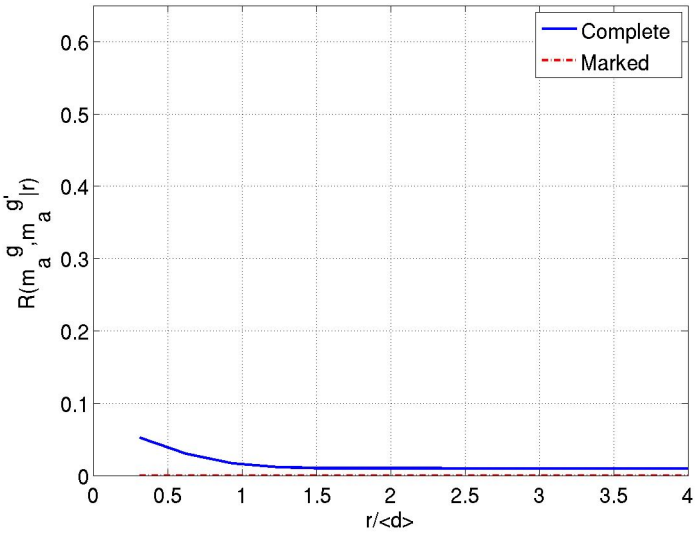

(d)

Figure 6.11: The complete radial and extreme value marked radial correlation function for the simulated SVEs of IN100 cycled at 0.5% maximum strain for the apparent Schmid factors (a) $m_a^g = 0.45-0.5$ (oct. slip) and $m_a^{g'} = 0.45-0.5$ (oct. slip), (b) $m_a^g = 0.45-0.5$ (oct. slip) and $m_a^{g'} = 0.40-0.45$ (oct. slip), (c) $m_a^g = 0.40-0.45$ (oct. slip) and $m_a^{g'} = 0.45-0.5$ (oct. slip), and (d) $m_a^g = 0.40-0.45$ (oct. slip) and $m_a^{g'} = 0.40-0.45$ (oct. slip). The distance r is normalized by the average grain size d of 20 μm.

With an understanding of how the slip planes are oriented relative to the loading direction as described by the apparent Schmid factor, it is also informative to explore the distributions of the local Schmid factors in the regions identified to be critical by the extreme value FIPs. In Figure 6.12, the probability density is shown for the local Schmid factors m_l for all the grains and for the grains with the apparent Schmid factors $m_a = 0.45 - 0.5$ for both the octahedral and cube slip systems, respectively. When the distribution of the local Schmid factor is considered over all of the grains, it can be observed that the maximum local Schmid factors for octahedral slip are less than the maximum local Schmid factors for cube slip. This suggests that the resolved shear stresses on the cube slip systems can be much larger than they are on the octahedral slip systems. As expected, when the apparent Schmid factor is larger (*i.e.*, between 0.45 and 0.5) for cube slip, the corresponding local Schmid factors are much more likely to be larger than the local Schmid factors for cube slip. However, when the magnitudes of the Schmid factors for octahedral slip are highest (*i.e.*, 0.45 to 0.5), it can be observed that the local Schmid factor for cube slip can be larger than the local Schmid factor for octahedral slip. Thus, in some cases even when the Schmid factors for octahedral slip are high, the actual resolved stresses are larger on some of the cube slip planes than on the octahedral slip planes.

It is hypothesized that the distributions of the extreme value Fatemi-Socie parameter are directly related to distributions of crystallographic fatigue crack formation in this and similar material systems. Thus, assuming an averaging volume for the relevant FIP that corresponds to crack incubation at the length scale of each grain, one may postulate a relation such as $P_{FS} = \tilde{\gamma}'_f (2N_{FOR})^c$, where $\tilde{\gamma}'_f$ is a fatigue ductility coefficient appropriate to crack formation at the scale considered. Recall that N_{FOR} indicated the number of cycles required to form a crack on the scale of several dominant microstructural barrier spacings (see Equation 2.1). This relation is related to the form of the Coffin-Manson law as defined in Equation 2.7, with rescaling of the parameters for a crack size on the order of dominant

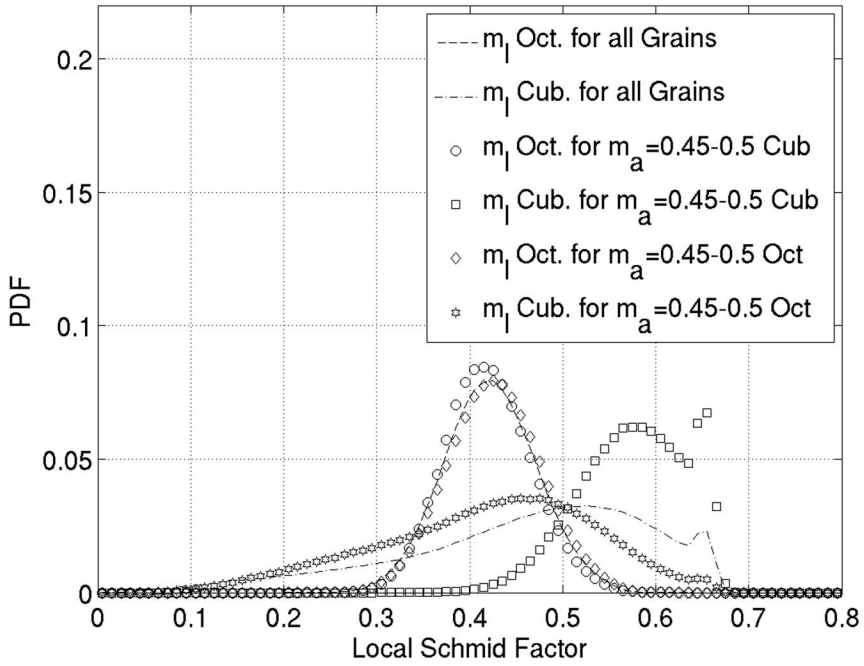

Figure 6.12: Probability density of the local Schmid factors m_l for the octahedral and cube slip systems for all grains and for the grains with the apparent Schmid factors $m_a = 0.45$ to $m_a = 0.5$ for both the octahedral and cube slip systems for the simulated SVEs for IN100, respectively.

microstructural attributes. Using this type of relation, optimization problems can be envisioned regarding polycrystalline orientation distributions to achieve target HCF lives or variability thereof.

Here only crystallographic fatigue crack formation has been considered; the effect of voids or non-metallic inclusions on the driving forces for fatigue crack formation has been neglected. Indeed, in IN100 the role of non-metallic inclusions is very important in forming life-limiting fatigue cracks. Each of these attributes can have an effect on overall variability of fatigue crack formation in this material system and must be considered for any new material development. The understanding of extreme value slip behavior in this material system, however, is very important to the understanding of fatigue crack formation around inclusions/voids. For example, one can imagine a sample of IN100 with two inclusions of very similar character (*i.e.*, phase, size, shape) where a fatigue crack forms at one of the inclusions and not the other when the material is subjected to some specified cyclic loading condition. Likely, an understanding of the local grain character (*i.e.*, size, shape, orientation, misorientation) near the inclusion where the fatigue crack formed relative to the inclusion void of fatigue damage will be sufficient to explain the different responses in the neighborhood around the two inclusions. Consideration of the extreme value marked radial distributions of the apparent Schmid factor allows us to readily observe the character of slip that is predicted to exist at the location of the extreme value response (*i.e.*, FIPs). Here we observed that grains oriented unfavorably for octahedral slip or favorably for cube slip are predicted to exist with high probability at the locations of extreme value fatigue response in IN100. Moreover, clusters of grains oriented for cube slip or clusters of grains oriented for cube slip surrounded by grains oriented favorable for octahedral slip are predicted to exist with high probability at the location of the extreme value fatigue response. These simulations support the observations made in IN100 by Li *et al.* [210] who observed fatigue crack formation along {100} planes in grains oriented unfavorable for octahedral slip. Thus, it is expected that clusters of grains oriented unfavorably for octahedral slip near inclusions

or voids are more susceptible to fatigue crack formation than inclusions or voids that are not located in such clusters.

6.4 Summary

The microstructure-sensitive extreme value probabilistic framework to evaluate variability of damage processes was applied to characterized HCF in the P/M Ni-base superalloy IN100. Specifically, this framework can be applied to characterize the extreme value distributions of the key response parameters and to characterized how the extreme value response relates to certain coupled microstructure attributes (*e.g.*, grain/phase size, grain orientation, grain misorientation). In this work, the driving forces for fatigue crack formation (*i.e.*, crack nucleation and microstructurally small crack growth) in polycrystalline IN100 are assessed using certain critical plane based FIPs. The cyclic plastic strain resolved on these critical planes has been observed to relate to processes of crack formation in crystalline metals.

Multiple microstructure volume elements are instantiated via a Voronoi tessellation algorithm and simulated via FEA with a cyclic polycrystal plastic constitutive model. These instantiated microstructure volume elements are optimized to fit pre-specified grain size, lattice orientation, and lattice disorientation distributions. In this manner, each of these instantiated microstructure volume elements constitute a SVE for the desired extreme value response of interest. In other words, each constructed SVE is designed to be a sample of the extreme value response from the microstructure ensemble and not intended to be representative of the entire distribution of response. This contrasts with the concept of a RVE that is constructed to exhibit the same representative response regardless of where it is sampled from in the microstructure ensemble. RVEs for extreme value behavior of reasonable size are typically untenable.

The multiple simulated SVEs for IN100 account for the material microstructure, applied strain amplitude and strain state, and critically stressed volume of interest in HCF

scenarios. Periodic boundary conditions are applied in all directions to simulate subsurface conditions. Here 100 SVEs for IN100 were constructed and cycled at 0.5% maximum strain under completely reversed loading (*i.e.*, R=-1). An additional 50 SVEs for IN100 were instantiated and cycled under completely reversed loading for 0.3% strain and 0.7% strain, respectively.

It was shown that the extreme value distributions of the Fatemi-Socie fatigue indicator parameters (FIPs) that estimate the driving forces for fatigue crack formation are fit with high confidence (*i.e.*, $R^2 > 0.97$) by the Gumbel distribution. Additionally, The shape of the extreme value distributions of the Fatemi-Socie FIPs appears to be well defined with as few as 25 simulated SVEs. This was demonstrated by considering subsets of the 100 SVEs cycled at 0.5% maximum applied strain of 25, 50 and 75 SVEs. The parameters of the fits of the observations to the Gumbel distributions for sample sizes of 25, 50, 75 and 100 SVEs varied little. Thus, a procedure was introduced to evaluate the minimum number of simulated SVEs required to adequately characterize a particular extreme value distribution by gradually increasing the number of data points until the character of the distribution remains unchanged. The quality of the characterized extreme value distribution can be easily quantified if the distribution is described by one of the three known asymptotic extreme value distributions by comparing the differences in the parameters of the known asymptotic extreme value distributions fit to increasingly larger sample sizes such as was demonstrated here. If the extreme value distribution is not well describe by one of the three know asymptotic extreme value distribution, it is much more difficult to determine if the number of simulated SVEs is sufficient to adequately characterize the extreme value distribution. However, if the characterized distribution remains relatively stable as the number of data points are increase significantly than it can be assumed that the number of simulated SVEs is sufficient.

The results from these simulations demonstrated that cube slip may play an important role in fatigue crack formation particularly when there are multiple grains oriented for cube

slip clustered in the same region or clusters of grains oriented for cube slip surrounded by other grains oriented favorable for octahedral slip. These observations support the results of previous experiments of fatigue in this material system [210]. Thus, as fatigue crack formation is dominated by the presence of non-metallic inclusions or voids for this particular material system, it is expected that given two inclusions of similar character that fatigue cracks will form preferentially near the inclusion that is surrounded by grains or grain clusters unfavorably oriented for octahedral slip. Additionally, there are many different grain combinations that do not increase the driving forces for fatigue crack formation as significantly as those with grains oriented with high magnitudes of the apparent Schmid factor (*i.e.* between 0.45-0.5) for cube slip. This understanding can inform the materials design of special textured materials for specific applications with well defined loading conditions.

CHAPTER VII

MICROSTRUCTURE-SENSITIVE EXTREME VALUE PROBABILITIES OF FATIGUE IN DUPLEX TI-6AL-4V

7.1 Introduction

In this chapter, the microstructure-sensitive extreme value probabilistic framework to characterize performance/variability for damage evolution processes is exercised using computational polycrystal plasticity models to compare the driving forces for fatigue crack formation (nucleation and early growth) at room temperature for several different microstructure variants of a duplex Ti-6Al-4V alloy. As discussed previously, this probabilistic framework employs the EVMCF to quantify the coupling between the extreme value driving forces for fatigue crack formation and the microstructure attributes at the fatigue critical sites. By applying this framework to study the driving forces for fatigue crack formation in these microstructure variants of Ti-6Al-4V, these microstructures can be ranked in terms of relative high cycle fatigue (HCF) performance and the correlated microstructure attributes that have the most influence on the predicted fatigue response can be identified. As introduced in Chapter 2, nonlocal FIPs based on the cyclic plastic strain averaged over domains on the length scale of the microstructure attributes (*e.g.* grains, phases) are employed to estimate the driving force(s) for fatigue crack formation at the scale of the individual grains. By simulating multiple SVEs using crystal plasticity constitutive models such as the model for duplex Ti-6Al-4V as introduced in Chapter 4, extreme value distributions of the predicted driving forces for fatigue crack formation can be estimated by considering the FIPs. This strategy of using multiple SVEs contrasts with simulation based on a single RVE, which is often untenably large when considering extreme value responses. This chapter is designed to be self supporting; therefore, some background material may be repeated for

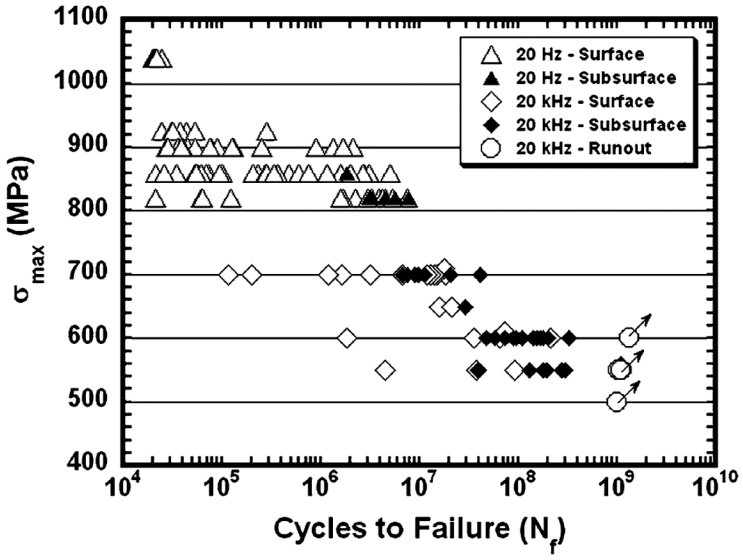

Figure 7.1: The fatigue variability of Ti-6246 characterized from repeated testing at several stress magnitudes from HCF to VHCF showing mean versus life limiting behavior (Reprinted from [221], with permission, copyright Springer).

convenience.

7.1.1 Extreme value statistics and metal fatigue

As can be seen in Figure 7.1 for Ti-6245 [221], considerable scatter has been observed in the number of cycles to failure in the HCF-VHCF regimes in duplex $\alpha + \beta$ Ti alloys. In the example given in Figure 7.1, there are three orders of magnitude between the maximum and minimum observed lives across most of the HCF-VHCF regime. Much of the observed scatter of the fatigue life of engineered components arises from microstructure stochasticity. This is particularly true for the processes of fatigue crack nucleation and microstructurally small crack growth in ductile metallic material systems such as Ti-6Al-4V. Fatigue crack formation is driven by localized plasticity and the accumulation of dislocations against obstacles or the development of particular dislocation structures (*e.g.*, persistent slip bands) [5]. As reviewed in Chapter 2, in the HCF regime of metals for which cyclic stress amplitudes are below the macroscopic yield stress, plasticity is quite heterogeneous and localized at microstructure attributes that raise the local stresses sufficiently to

induce flow [6], are favorably oriented for preferential yield, or both. Specific life limiting attributes can vary from specimen to specimen or from component to component due to the stochasticity of material microstructure. Thus, scatter in the HCF life of specimens or components depends on the extreme value probabilities of existing microstructure attributes that elevate the driving forces for fatigue crack formation, constituting size effects.

As reviewed in Chapter 3, current methods that estimate fatigue resistance as a function of the extreme value statistics of microstructure are limited to distributions of a single microstructure attribute; these methods do not consider the effect of multiple interacting microstructure attributes on the extreme value response distributions (*e.g.*, fatigue crack formation). For example, the review of Atkinson and Shi [3] outlined the various extreme value models that predict the fatigue resistance in clean steels based on the largest inclusions, which is the microstructure attribute that appears to most influence fatigue crack formation in this material system. Although some of the reviewed models have been applied with success in predicting variability of fatigue response in this material system, none of these current models account for the influence of the interactions between the inclusion and surrounding matrix. In other words, these approaches are limited to a single attribute and cannot describe how the interactions between multiple attributes influence the extreme value response. Although first order approaches based on a single microstructure attribute (*e.g.*, inclusion size) may be sufficient for some material systems or applications, the process of fatigue crack formation in many advanced engineering alloys is often complex and depends on the influence of multiple interacting microstructure attributes. In some cases, multiple interacting microstructure attributes exert influence at different material length scales.

Some recent computational work has considered effects of multiple microstructure attributes on fatigue response. Liao [222] used a Monte Carlo technique to generate microstructure instantiations with distributions of particle size, grain size, and grain orientation that have been randomly sampled from experimental data with known distributions. These

multiple microstructure instantiations are then used to simulate the variation in fatigue response in 2024-T351 aluminum sheets. The response was estimated using FEA with elastic constitutive laws. Fatigue-relevant attributes, including particle size, grain size and grain orientation, were identified in each simulated instantiation and the distribution of these attributes was considered. These fatigue-relevant attributes were selected a priori based on experiments. The results of this Monte Carlo method correlated well with other methods based on extreme value statistics and with experiments. However, as with the previous methods discussed, correlations between the important microstructure attributes relative to their influence on the driving forces for fatigue crack formation were neglected because each critical attribute was considered independent of the others.

7.1.2 Fatigue crack formation in duplex Ti-6Al-4V

In this work, the processes of fatigue crack formation will be considered in duplex $\alpha+\beta$ Ti-6Al-4V. Experimental observations for Ti-6Al-4V support the hypothesis that fatigue crack formation in this material system is not adequately described by a distribution of any single microstructure attribute. Fatigue crack formation in $\alpha+\beta$ Ti alloys has been associated with slip-dominated fatigue crack formation as early as the 1960s by Wells and Sullivan [223], who observed cracks form along slip bands in the α phase of Ti-6Al-4V. However, confusion persists regarding the fundamental mechanisms of fatigue crack formation in this material system. In short, it is not clear which specific microstructure attributes (or arrangements of attributes) is/are most important in the processes of fatigue crack formation. Relevant experiments that have investigated fatigue crack formation in $\alpha+\beta$ Ti alloys under typical cyclical loading conditions at room temperature are reviewed next.

In duplex $\alpha+\beta$ Ti alloys, the appearance of distinct facets in the primary α grains is commonly observed at sites of fatigue crack formation. In some cases, these facets have been associated with basal planes oriented perpendicular to the uniaxial loading axis in Ti-6Al-4V [224, 225]. Bache [226] argues that crack formation on basal planes in grains

that are unfavorably oriented for slip is due to shear stresses induced by dislocation pileup on the grain boundary in adjacent grains oriented for easy slip. This mechanism, originally postulated by Stroh [227], is thought to activate when a critical density of dislocations accumulate on the boundary such that the shear stresses in the adjacent grain (oriented for easy slip) are sufficient to induce slip on the hard oriented basal slip planes (oriented nearly perpendicular to the loading direction). Then under cyclic loading conditions a crack forms over many cycles in the hard oriented grain. This proposed mechanism is supported by the work of Baxter *et al.* [228] who observed slip on basal planes oriented nearly perpendicular to the loading axis in IMI 834.

In contrast, other studies have observed fatigue facet formation on basal planes favorably oriented for slip. Bridier *et al.* [229, 230] investigated fatigue crack formation in Ti-6Al-4V in both LCF and HCF, respectively, and observed that cracks mostly formed on basal slip planes and less frequently on prismatic slip planes. In all cases, these basal and prismatic planes exhibited high Schmid factors; however, a bias was observed toward primary α grains with orientation of applied stress more toward the c-axis, indicating a preference for crack formation on planes that are somewhat less favorably oriented for basal (or prismatic) slip but with somewhat higher stress normal to the basal (or prismatic) plane. Subsurface fatigue crack formation on pyramidal planes in primary α grains in Ti-6Al-4V was also observed by Gilbert and Piehler [231] in grains oriented for hard basal slip (*i.e.*, with c axis nearly parallel to the uniaxial loading direction); they noted that clusters of grains oriented favorable for slip on pyramidal $\langle a + c \rangle$ planes and grains oriented favorable for basal slip tend to favor fatigue crack formation. Jha and Larsen [232] observed in Ti-6246 that at moderate stress amplitudes (*i.e.*, close to the macroscopic yield stress), facets near the location of initial fatigue crack formation were all inclined 35-45° relative to the loading axis. In one sample, the facet near the location of initial fatigue crack formation appeared to be oriented about 35° relative to the loading direction in a grain oriented unfavorably for basal slip, suggesting the facet may have been formed by a $\langle c + a \rangle$ hard slip

mechanism (*i.e.*, pyramidal slip). In another sample, the facet near the location of initial fatigue crack formation developed on an apparent basal slip plane favorably oriented for slip. It is interesting to note that the grain unfavorably oriented for basal slip that developed the facet was surrounded by other grains more favorably oriented for easy slip (*i.e.*, prismatic or basal slip). Additionally, the sample with the facet that formed in the grain oriented for hard basal slip failed at 60,000 cycles; the other sample with the facet that formed in the grain oriented for easy basal slip failed at 2,000,000 cycles. Szczepanski *et al.* [221] also observed fatigue facet formation in the very high cycle fatigue (VHCF) regime of Ti-6246 on or near basal or prismatic slip planes favorably oriented for slip.

The size of the primary α grains also appears to play a role in fatigue crack formation in duplex $\alpha + \beta$ Ti alloys. Mahajan and Margolin [233] noted that larger fatigue cracks more readily formed in primary α grains with longer paths for slip. Jha and Larsen [232] and also Szczepanski *et al.* [221] noted in Ti-6246 that the primary α grains that form facets tend to be larger than average. However, these grains were not necessarily the largest primary α grains in the population. This suggests that grain size plays a role in fatigue crack formation in this material system, but other attributes must also be considered.

The process of fatigue crack formation in $\alpha + \beta$ Ti alloys is further complicated when one considers the existence of local textured regions on the scale of hundreds of microns to several millimeters. These microtextured regions are understood to develop during processing from larger prior β grains. Bridier *et al.* [230] observed that microtextured regions in Ti-6Al-4V that favor slip activation in grains oriented for basal or prismatic slip are associated with distributed fatigue cracks, near the interface of bands of texture. Similar observations were made by Le Biavant *et al.* [234], who found distributed fatigue cracks in microtextured regions favorably oriented for basal or prismatic slip and no cracking in regions unfavorably oriented for prismatic and basal slip. Because microstructure conditions in these microtextured regions appear to favor crack formation, multiple cracks form in these regions that coalesce into a critical life limiting crack. Szczepanski *et al.* [221] also

noted that accumulated slip in microtextured regions with high fractions of grains oriented favorably for basal or prismatic slip in Ti-6246 likely enhances fatigue crack formation in the VHCF regime. Bantounas *et al.* [235] observed that fatigue crack formation was favored in regions with grains oriented for easy basal slip that are adjacent to grains whose c-axis are within about 15° of the uniaxial loading direction. They argued that cracks form in grains that are oriented for easy slip and then propagate most effectively along basal planes in surrounding grains oriented for hard basal slip. This also supports the previously mentioned observations of Gilbert and Piehler [231], who noted fatigue cracking in Ti-6Al-4V in clusters of grains oriented for pyramidal $\langle a + c \rangle$ slip and grains oriented for easy basal slip.

Simulations have also given insight into understanding many of these experimental observations. Hasija *et al.* [236] and Venkataramani *et al.* [237, 238], using dwell sensitive crystal plasticity models for α-Ti-6Al and Ti-6246, respectively, demonstrated that grains favorably oriented for basal slip transfer stress to nearby grains that are unfavorably oriented for basal slip through load shedding. Simulations carried out by Dunne *et al.* [69, 218, 239] for α-Ti-6Al demonstrated that these types of rogue grain combinations can significantly increase the driving force for fatigue crack formation, particularly in dwell fatigue.

Based on these previous examples, it is apparent that several different microstructure attributes, including grain orientation/misorientation, grain size and local texture, have been identified as important relative to fatigue crack formation in $\alpha + \beta$ Ti alloys. In fact, Jha and Larsen [232] postulate a hierarchy of microstructure arrangements relative to their potency for localized accumulated plastic slip. Based on limited experiments, they suggest four possible underlying microstructure configurations in Ti-6246 whose probability of occurrence may relate to the observed variability in the overall fatigue life. A cluster of primary α grains and lamellar $\alpha + \beta$ colonies with aligned slip planes oriented for close to maximum shear or a cluster of primary α grains, each similarly oriented for basal slip

were observed at sites of subsurface fatigue crack formation in specimens with shorter fatigue lives. In contrast, the microstructure features described by a hard primary α grains (oriented unfavorably for basal slip) surrounded by soft lamellar colonies and/or primary α grains favorably oriented for slip or primary α grains favorably oriented for basal slip were observed to be associated with surface fatigue crack formation in specimens with longer fatigue lives. Likely, many more experiments would be needed to make any conclusions regarding the uniqueness of this set of critical microstructure configurations for fatigue damage formation in this material system.

This body of work indicates that the mechanisms of fatigue crack formation in these types of $\alpha + \beta$ Ti alloys are quite complex. Even in HCF, localized plastic slip is clearly linked to fatigue crack formation. Additionally, the multiplicity of competing failure modes increases fatigue variability, particularly in the HCF and VHCF regimes [82,240,241]. It is not likely that the single attribute extreme value approaches outlined previously will be able to capture the microstructure dependence of the fatigue crack formation and growth in these types of material systems. A new approach is needed to link extreme value distributions of interacting microstructure attributes that enables the identification and comparison of configurations of microstructure attributes that drive variability in fatigue life.

7.1.3 Correlated microstructure attributes and extreme value driving forces for fatigue crack formation

As presented in Chapter 3, EVMCFs have been introduced to quantify the interacting microstructure attributes that are the most statistically significant relative to the measured or simulated extreme value distributions of response [149, 198]. Specifically, correlation functions describing the microstructure attributes potentially relevant to the operant mechanism of fatigue crack formation are selectively sampled in regions marked by certain extreme value response parameters (*e.g.*, cyclic plastic strain range). These extreme value marked correlations can be compared to the same correlation functions sampled over the entire microstructure ensemble (without regard to response) to determine the particular

correlated microstructure attributes that are most significant relative to the extreme value response. In general, this methodology can be applied to quantify important microstructure attributes that correlate with strong influence on the extreme value distributions of fatigue response. This probabilistic framework was coupled with multiple simulated material volume elements to investigate orientation relationships important to fatigue crack formation in the P/M Ni-base superalloy IN100 [149, 198]. It was shown that the driving forces for fatigue crack formation were highest in clusters of grains oriented for cube slip near grains oriented for octahedral slip, which correlated well with experimental observations in the same material [210].

Simulation-based strategies for investigating the driving forces for fatigue crack formation at the scale of the dominant microstructure attributes have greatly expanded in recent years. McDowell [242] outlined the use of plastic shear strain- based FIPs to estimate the driving forces for fatigue crack formation in metals associated with plastic ratcheting and reversed cyclic plasticity as defined by Equations 2.3 and 2.4, respectively. As defined previously in Section 6.2.4 by Equations 6.1 and 6.2, the MPSS and FS [63] FIPs are similarly calculated here in an identical manner, *i.e.*,

$$P_{MPSS} = \frac{\left\langle \Delta\gamma_{p,max} \right\rangle_V}{2} \tag{7.1}$$

$$P_{FS} = \frac{\left\langle \Delta\gamma_{p,max} \right\rangle_V}{2}\left(1 + k_{FS}\frac{\sigma_{n,\max}}{\sigma_o}\right) \tag{7.2}$$

Here a value of $K = 1$ is used based on previous studies (*e.g.*, [149]), and is subject to refinement. Averaged over scales pertinent to the microstructure attributes relevant to the processes of fatigue crack formation, these types of FIPs have been used to investigate the relative fatigue crack formation potency of several different microstructure attributes. In martensitic gear steels, Prasannavenkatesan *et al.* [220] used these two parameters to characterize the relative potency of different kinds of inclusions to form grain/inclusion scale HCF cracks. Similar FIPs have also been used to characterize the influence of

microstructure on fatigue crack formation in structural steel [67, 68] and Ni-base superalloys [69, 70, 147, 149, 198]. These efforts have demonstrated the utility in using these types of parameters coupled with crystal plasticity simulations to correlate microstructure scale slip with fatigue crack formation at the scale of the individual grains or attributes that control slip intensification (*e.g.*, inclusions).

In this chapter, the same microstructure-sensitive extreme value probabilistic framework is used that was demonstrated previously for IN100 in Chapter 6 and [149, 198] to investigate the influence of the microstructure on the driving forces for crystallographic fatigue crack formation in duplex Ti-6Al-4V. A similar strategy of simulating multiple SVEs sampled from the same distributions of microstructure is used to characterize the extreme value distributions of FIPs. EVMCFs are sampled selectively at the locations of extreme value response (*i.e.*, hot spots). These statistical volume elements are simulated via the finite element method using a rate sensitive crystal plasticity model calibrated to experimental measurements.

7.2 Methodology

7.2.1 Extreme value marked microstructure correlation functions

As described previously in Chapter 6, the probability density of an arbitrary extreme valued FIP P_α is defined as $f_{\max(P_\alpha)}(P_\alpha|\Omega)$ given a window Ω (*i.e.*, SVE), such that $f_{\max(P_\alpha)}(P_\alpha|\Omega)\,dP_\alpha$ is the probability that P_α between some range described by dP_α is the extreme value for a sampled SVE of size Ω. Similar to the defined EVMCF in Chapter 6, the EVMCF introduced in Section 3.5 is defined for this chapter in terms of the radial distribution function $R_{\max(P_\alpha)}(\beta,\beta'|r,\Omega)$ such that $R_{\max(P_\alpha)}(\beta,\beta'|r,\Omega)\,dr$ is the probability that a microstructure attribute β located coincident with the extreme value FIP P_α is located within a distance of r to $r + dr$ of a second microstructure attribute β' in any direction.

This two part statistical construct describes both the extreme value response of the microstructure as represented by the FIPs and considers the probabilities of correlated

microstructure attributes, β and β', existing in the proximity of extreme values FIP P_α in a microstructure window Ω. By comparing $R_{\max(P_\alpha)}(\beta, \beta'|r, \Omega)$ with the correlation function for the same microstructure attributes sampled from the complete microstructure ensemble given by $R(\beta, \beta'|r, \Omega)$, the correlated microstructure attributes most probable to exist at locations of extreme value response can be identified. Sampling is performed on a predefined size of microstructure window Ω. In the case of periodic boundary conditions, the sampling volume is limited to the size of Ω so as to not bias the result.

Changing the size of the SVE will affect the resulting extreme value distribution of response and associated EVMCF. As discussed in Section 5.2, the minimum size of Ω is established by relevant spatial correlations of the neighborhood of extreme value response sites. For example, nearest and second nearest neighbor grains must be sampled to capture load shedding phenomena, while much larger values are perhaps required to capture phenomena associated with microtexture. In other words, the SVE size must be suitably large compared to the short range spatial interactions at microstructure hot spots. In general, if the SVE size is too small, the extreme value distribution resulting from compiling extreme values of a set of SVEs may not relate to the low probability tail region of interest, and may provide ambiguous information. Previous studies have shown that the lower order moments of cyclic plasticity on the scale of the individual grains are relatively unaffected beyond the second nearest neighbor grain interactions in certain polycrystalline material systems [149].

As mentioned previously, the SVE size determines the sample size n for which the extreme value distribution of response is characterized (see Section 5.2). Larger SVEs will sample more microstructure and will be associated with a larger sample size n for the extreme value distribution of the microstructure-dependent response. If the sample size is sufficiently large, the extreme value distributions of response will ideally converge to one of the known asymptotic extreme value distributions. If the lower order moments of cyclic plastic response are appropriately captured for a given SVE size, multiple SVEs could be

considered together as a single sample to increase the sample size n for a given data set. This would be in contrast to simply increasing the SVE size until a desired sample size n is achieved. In some cases it might be more computationally favorably to simulate multiple SVEs to achieve a given sample size n instead to simulating one large SVE. In this work, each sample of the extreme value distribution is limited to a single simulated SVE.

7.2.2 Duplex Ti-6Al-4V cyclic polycrystal plasticity model

In aerospace applications, $\alpha + \beta$ Ti alloys are important in view of their high strength and desirable strength-to-weight ratio. These alloys exhibit favorable properties at elevated (but moderate) temperatures depending on heat treatment and thermomechanical processing. The microstructure of typical $\alpha+\beta$ Ti alloys can range from bi-modal to fully lamellar. A bi-modal microstructure is generated by applying deformation when the material is in the $\alpha+\beta$ regime (on a phase diagram) followed by recrystallization and aging. This processing route generates a microstructure that consists of equiaxed primary α grains dispersed among regions containing transformed β grains with embedded α laths. Texture effects in these alloys are particularly pronounced due to the low symmetry of crystallographic slip and anisotropic elasticity, as well as the contrast of properties between the α and β phases. In addition, despite their greater number of available slip systems, the β regions containing α laths tend to be more resistant to slip than the primary α grains due to the presence of the α laths and, in some cases, finer α precipitates.

The particular crystal plasticity model used in this work for duplex Ti-6Al-4V was outlined previously in Chapter 4. This constitutive model was initially developed by Mayeur and McDowell [153], extended by Zhang *et al.* [154] and then Bridier *et al.* [155] specifically for application to the HCF loading regime for peak stresses at or below the macroscopic yield strength. In hcp primary α, there are four different families of slip systems: three $\left\langle 11\bar{2}0\right\rangle (0001)$ basal, three $\left\langle 11\bar{2}0\right\rangle \left\{ 10\bar{1}0\right\}$ prismatic, six $\left\langle 11\bar{2}0\right\rangle \left\{ 10\bar{1}1\right\}$ first order pyramidal $\langle a\rangle$, and twelve $\left\langle 11\bar{2}3\right\rangle \left\{ 10\bar{1}1\right\}$ first order pyramidal $\langle a+c\rangle$ slip systems. At

room temperature, slip is dominant in the basal and prismatic slip systems due to a lower critical resolved shear stress relative to the other slip systems. The lamellar $\alpha + \beta$ colonies are homogenized in this model since the individual laths range in thickness from hundreds of nanometers to several microns. A crystallographic burgers orientation relation (BOR) is maintained between the secondary α and β laths defined such that $(0001)_\alpha \,//\, \{101\}_\beta$ and $\left\langle 11\bar{2}0 \right\rangle_\alpha \,//\, \langle 111 \rangle_\beta$. The 24 possible slip systems in the lamellar region include three $\left\langle 11\bar{2}0 \right\rangle (0001)$ basal, three $\left\langle 11\bar{2}0 \right\rangle \left\{ 10\bar{1}0 \right\}$ prismatic, six $\left\langle 11\bar{2}0 \right\rangle \left\{ 10\bar{1}1 \right\}$ first-order pyramidal $\langle a \rangle$ and twelve $\langle 111 \rangle \{110\}$ bcc slip systems. The bcc slip systems are transformed into the hexagonal coordinate system via the BOR, as previously defined. Hard slip systems in these colonies are those that intersect the $\alpha - \beta$ interface. Soft deformation modes are those on which dislocations glide parallel to the $\alpha - \beta$ interface or have parallel slip planes in both the secondary α and β phases. In particular, Bridier's [155] extension of the model is formulated to favor single slip, which has been experimentally observed to dominate at low cyclic strain amplitudes. Additionally, slip in the $\alpha + \beta$ colonies is more restricted.

7.2.3 Instantiation of SVEs for simulation of duplex Ti-6Al-4V

The extreme value fatigue response of Ti-6Al-4V is characterized via the simulation of multiple SVEs to estimate $f_{\max(P_\alpha)}(P_\alpha|\Omega)$ and $R_{\max(P_\alpha)}(\beta, \beta'|r, \Omega)$. The cyclic plastic response is estimated over multiple three-dimensional instantiated SVEs simulated with the FE package ABAQUS [121]. The aforementioned crystal plasticity model for duplex Ti-6Al-4V that has been calibrated with experiments is implemented in ABAQUS as a user-material subroutine (*i.e.*, UMAT). Simulation of multiple SVEs that have been instantiated from predefined target distributions of key microstructure attributes (*e.g.* grain size distribution, phase distribution, orientation distribution, misorientation/disorientation distribution, *etc.*), can be used as a basis to characterize the microstructure dependence of the heterogeneously distributed plastic response. Application of three-dimensional periodic boundary conditions simulates a subsurface condition.

The SVEs for duplex Ti-6Al-4V are instantiated via the software EllipPolycrystalGen as described in Section 5.3.2. This method generates grains by sampling the distributions of the aspect ratios of grain equivalent ellipsoids fit to grains of experimentally characterized microstructures. Using grain equivalent ellipsoids instead of other space filling methods like a Voronoi diagram allows construction of more complex grain morphologies such as elongated grains common in rolled ductile metals, and facilitates more accurate reconstruction of two phase microstructures with bi-modal grain size distributions such that observed in duplex Ti-6Al-4V. For example, Brahme *et al.* [180] employed ellipsoids fit to experimentally characterized grains to reconstruct Al microstructures with elongated grains from orthogonal EBSD maps. Groeber *et al.* [8,9] used similar methods to reconstruct polycrystalline representations of IN100 characterized from three-dimensional serial sections.

7.2.4 Simulated microstructures

To explore the influence of stochastic microstructure on the distributions of FIPs, multiple SVEs were instantiated for each of the four microstructures with different grain size distributions and volume fractions of primary α. The target size of the primary α grains, $\alpha+\beta$ colonies, and the target volume fraction of the primary α phase are given in Table 7.1. Grain size is related to grain volume according to

$$\left\langle d_{grain} \right\rangle = 0.7 \left\langle V \right\rangle^{\frac{1}{3}} \tag{7.3}$$

where $\left\langle d_{grn} \right\rangle$ and $\langle V \rangle$ are the mean (volume averaged) grain size and grain volume, respectively [243]. The assumed mean (μ) and standard deviation (σ) of the grain size for these microstructures is also given in Table 7.1. In Figures 7.2 and 7.3, the target log-normal and fit cumulative distribution functions are shown for the primary α grains and $\alpha+\beta$ colonies for the instantiated fine and coarse bi-modal microstructures, respectively. Unless otherwise specified, the target orientation distribution was random as shown in Figure 7.4. The target disorientation distribution was also specified as random (*cf.* [244]). Optimization of

Table 7.1: Microstructures for Ti-6Al-4V along with the assumed log-normal fits for the grain volume distributions.

		Duplex Ti-6Al-4V Microstructures			**Assumed Mean and St. Dev. for Grain Size Distributions**			
					$\alpha+\beta$ **Colony**		**Prim.** α	
Micro.	**Description**	**Trans.** β **Size** (μ**m**)	**Prim.** α **Size** (μ**m**)	**Vol.** % **Prim.** α	μ (μ**m**)	σ (μ**m**)	μ (μ**m**)	σ (μ**m**)
A	Fine bi-modal low α	50	10-50	30%	50	5	25	10
B	Fine bi-modal high α	50	10-50	70%	50	5	25	10
C	Coarse bi-modal low α	80	40-60	30%	80	10	50	5
D	Coarse bi-modal high α	80	40-60	70%	80	10	50	5

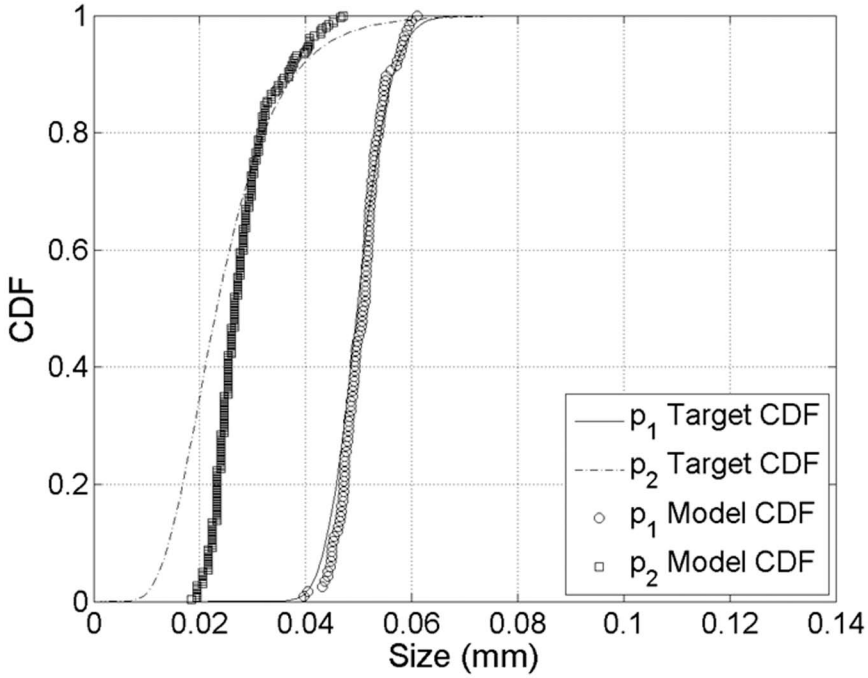

Figure 7.2: Target log-normal and fit model distributions of the grain size for the $\alpha + \beta$ colonies (p_1) and primary α grains (p_2) for an instantiated fine bi-modal microstructure.

the orientation distribution and disorientation distribution to fit the target distributions via a simulated annealing algorithm was described previously in Chapter 5.

7.3 Extreme value statistics of fatigue in duplex Ti-6Al-4V

In this section, it is considered how the crystallographic attributes of the microstructure (*e.g.*, grain orientation, grain disorientation, grain size, and grain shape distributions) affect the local driving forces for fatigue crack formation in HCF. Similarly to what was shown in Chapter 6, the MPSS and FS FIP (as defined previously in Equations 6.1 and 6.2) are employed to estimate the driving forces for fatigue crack formation. Additionally, in this chapter, the cumulative effective plastic strain (CEPS) calculated overall cycles is considered, *i.e.*,

$$P_{CEPS} = \int_0^t \sqrt{\left(\frac{2}{3}\right)\left\langle \dot{\mathbf{E}}^p \right\rangle_V : \left\langle \dot{\mathbf{E}}^p \right\rangle_V} dt \tag{7.4}$$

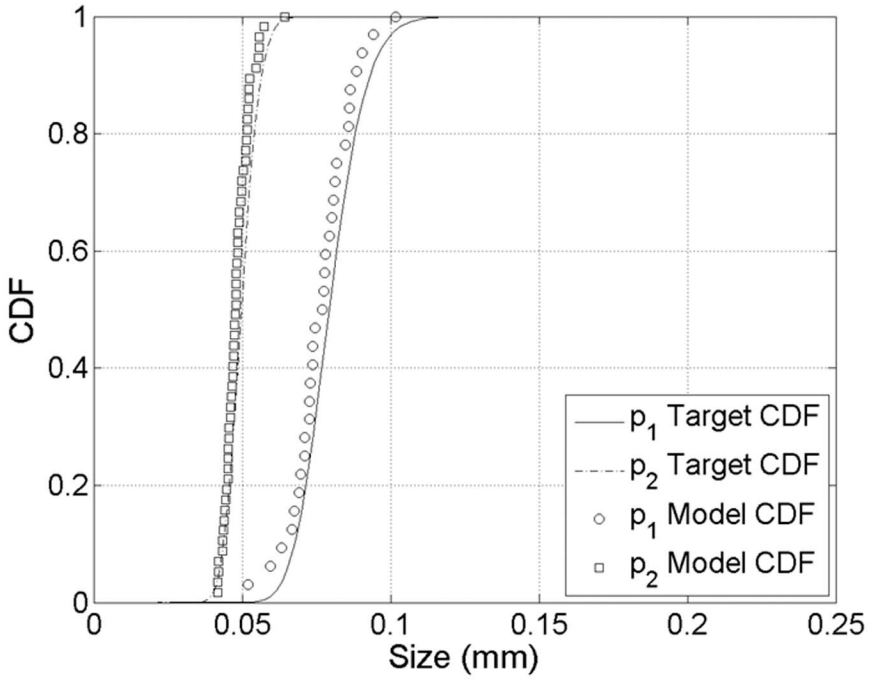

Figure 7.3: Target log-normal and fit model distributions of the grain size for the $\alpha + \beta$ colonies (p_1) and primary α grains (p_2) for an instantiated coarse bi-modal microstructure.

Table 7.2: Size of three different grain scale averaging volumes used to calculate FIPs. The equivalent grain size is calculated via Equation 7.3.

Ave. Vol.	**# of Elem.**	**Tot. Vol (mm^3)**	**Equiv. Grain Size (mm)**
1	27	9.83×10^{-5}	0.032
2	125	4.55×10^{-4}	0.054
3	343	1.25×10^{-3}	0.076

In each microstructure, these FIPs are calculated using each of three different sized averaging volumes, as defined in Table 7.2. The smallest averaging volume considered is slightly larger than the mean grain size of the smallest grains (*i.e.*, the primary α grains in Microstructures A and B). By using the same sized averaging volumes to compare the response across the range of simulated microstructure, a uniform comparison can be made between the driving forces for fatigue crack formation for the different microstructure considered on the scale of the averaging volume regardless of the differing distributions of grains/phases sizes.

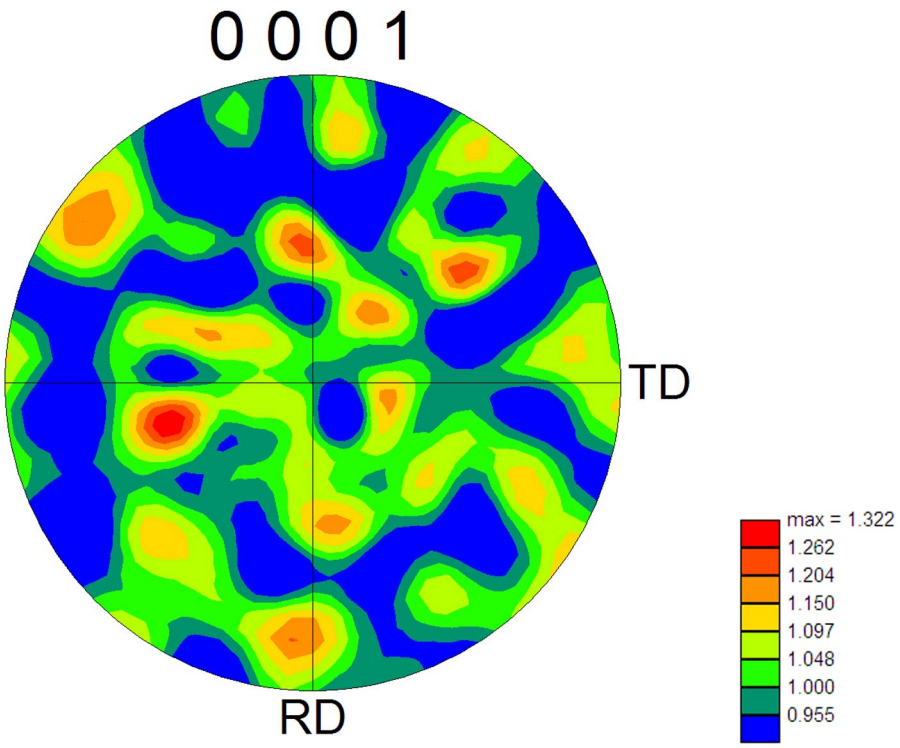

Figure 7.4: Pole figure representing random textures for the instantiated duplex Ti-6Al-4V microstructures.

Table 7.3: Approximate range in the number of grains and nominal number of elements per grain for primary α and $\alpha + \beta$ colonies for four different microstructure variants of duplex Ti-6Al-4V in cuboidal SVEs dimensioned 0.400mm along each edge

Micro.	Description	#. of Grains	Ave. # of Elem. Prim. α	Ave. # of Elem. Col.
A	Fine bi-modal low α	325-375	20	105
B	Fine bi-modal high α	625-675	20	105
C	Coarse bi-modal low α	75-100	96	400
D	Coarse bi-modal high α	125-175	96	400

The ellipsoidal packing algorithm EllipPolycrystalGen was used to instantiate multiple SVEs for Ti-6Al-4V which were then simulated via ABAQUS [121]. These SVEs dimensioned 0.400mm along each edge of the cuboidal microstructure block were subjected to uniaxial cyclic strain with zero minimum strain (*i.e.*, R=0) at a quasistatic strain rate of $0.002s^{-1}$ at room temperature. Unless otherwise specified, the peak applied strain was 0.6%. Each simulation was cycled at least ten and up to twenty times to explore how shakedown affects the extreme value distributions of the FIPs. In most cases, periodic boundary conditions were applied in all directions to simulate subsurface conditions. The voxellated meshes of these instantiated microstructure volume elements consisted of brick elements with reduced integration (type C3D8R in ABAQUS [121]). The specific range of the number of grains is given in Table 7.3 for the different microstructures considered. Also listed are the approximate average number of elements in each of the the primary α and $\alpha + \beta$ colonies for each microstructure. There were 26 elements along each edge of the SVE or 17576 elements in all. The volume of the SVE was maintained constant in this analysis across the range of microstructures. A meshed SVE for an arbitrary instantiation of Microstructure A is given in Figure 7.5 with contours of the Mises strain at the peak strain of 0.6% after 10 cycles. The variations in the stress fields shown in Figure 7.5 throughout the volume are primarily due to the mismatch of the anisotropic elastic stiffness for the differently oriented grains.

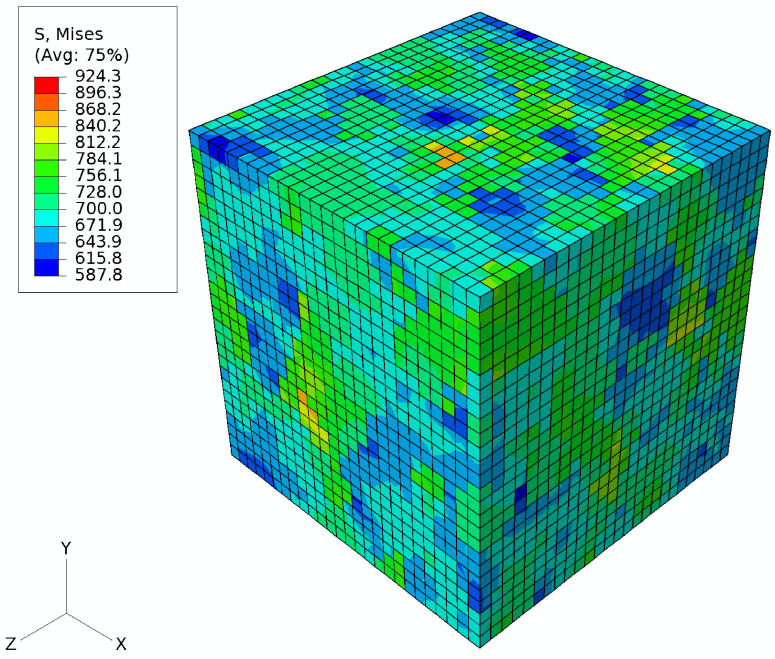

Figure 7.5: Meshed cuboidal SVE with an edge dimension of 0.400mm for an arbitrary instantiation of Microstructure A with contours of the Mises stress at the peak strain of 0.6% after 10 cycles.

7.3.1 Distributions of extreme value FIPs in randomly textured duplex Ti-6Al-4V

To understand the number of cycles required to approach a condition of plastic shakedown (*i.e.*, stabilization of cyclic plasticity at the grain scale), a single instantiation for Microstructure A was cycled 20 times using the conditions given previously. The percentage of primary α grains and $\alpha+\beta$ colonies that exhibit a cumulative effective plastic strain above (a) 1.0×10^{-10}, (b) 1.0×10^{-8}, and (c) 1.0×10^{-6} are shown in Figure 7.6. It can be observed in Figure 7.6(c) that the percentage of grains exhibiting a significant level of cumulative effective plastic strain (*i.e.* above 1.0×10^{-6}) is fairly stable after about 10 cycles. Additionally it can be observed that most significant plasticity occurs in the primary α grains and not in the $\alpha+\beta$ colonies. This is expected as slip was modeled to be more difficult in the $\alpha+\beta$ colonies (see Section 4.3.3). Based on the shakedown period in Figure 7.6, it was assumed that at least 10 cycles were required before relative stability was achieved for the cyclic plastic response.

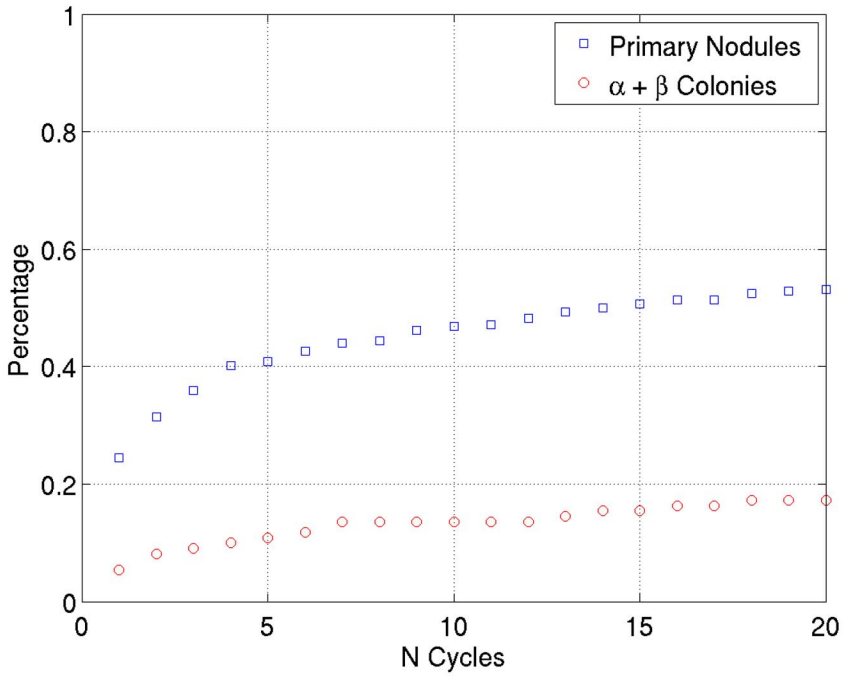

(a)

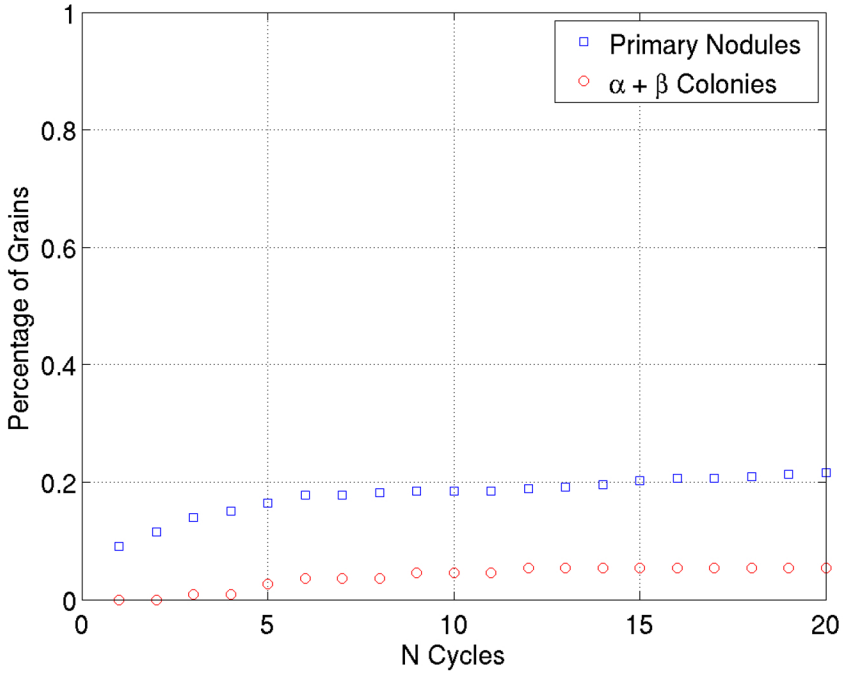

(b)

Figure 7.6: The percentage of primary α grains and $\alpha+\beta$ colonies that exhibit a cumulative effective plastic strain above (a) 1.0×10^{-10}, (b) 1.0×10^{-8}, and (c) 1.0×10^{-6} after 20 cycles at 0.6% maximum strain for $R = 0$.

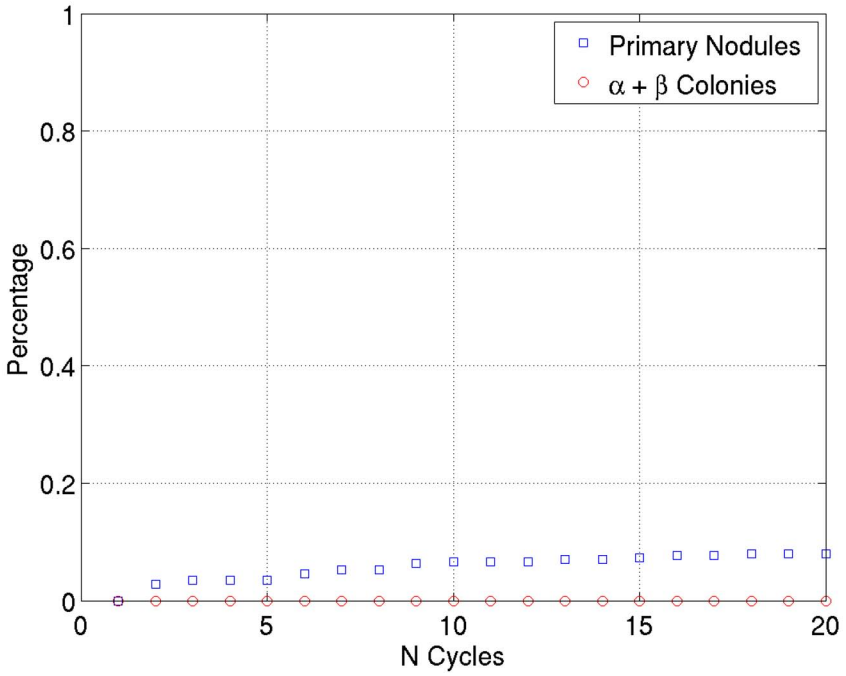

(c)

Figure 7.6: The percentage of primary α grains and $\alpha+\beta$ colonies that exhibit a cumulative effective plastic strain above (a) 1.0×10^{-10}, (b) 1.0×10^{-8}, and (c) 1.0×10^{-6} over for the first 20 cycles at 0.6% maximum strain for $R = 0$.

Table 7.4: The 0.01, 0.1 and 0.99 probability levels are given in terms of the linearized probability scale for Gumbel and Fréchet extreme value probability distribution functions.

Probability (p)	$\ln(1/\ln(1/p))$
0.01	-1.53
0.1	-0.83
0.99	4.60

Next, the extreme value distributions of the various FIPs described above are considered for the four different microstructures described in Table 7.1. A total of 100 SVEs were instantiated for each microstructure in Table 7.1. The FIPs were calculated over three different averaging volumes as defined in Table 7.2 along with the equivalent grain size for those averaging volumes as estimated via Equation 7.3. A volume average FIP centered at each element in each SVE was computed for each averaging volume. The maximum volume averaged FIP for a given SVE was defined as the extreme value FIP for that instantiation. The distribution of extreme value FIPs was then constructed for each microstructure based on values from each of the 100 simulated SVEs. For the smallest averaging volume, these distributions are plotted in Figure 7.7 on a Gumbel probability scale. The 0.01, 0.1 and 0.99 probabilities levels are also given in Figure 7.7 and specified explicitly in Table 7.4 for both the linearized Gumbel and Fréchet probability scales. The procedure to generate probability plots linearized for the extreme value Gumbel distribution is outlined in Appendix B. The distribution appears linear on the Gumbel scale if it fits that particular distribution exactly. Using linear least squares regression, the distribution parameters for the particular distribution of interest can be estimated.

Comparing the extreme value distributions for three different FIPs does not immediately reveal any significant differences between the distributions; the same general relative trends are observed across the range of microstructures. However, the grains predicted to exhibit the extreme value response varied between the different FIPs in as many as 14% of the SVEs simulated. The CEPS FIP assumes crack formation results only from total plastic strain accumulation and has been used in the literature [69,218,239]; however, unless it can be definitively shown that total plastic strain accumulation drives fatigue crack formation in very early cycles (unlikely in HCF), a measure of steady state directional cycle by cycle plastic strain reversal or accumulation is preferred. Although both the MPSS and FS FIPs account for directional cycle by cycle strain accumulation, the FS parameter is better suited to capture the effect of the normal stress that appears to promote formation of fatigue cracks

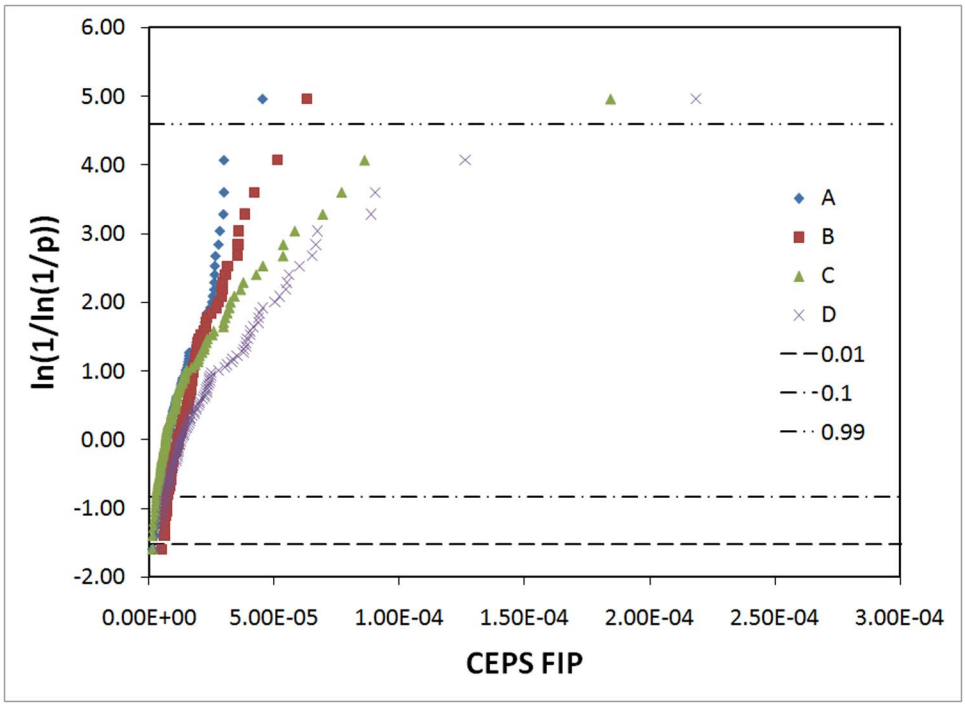

(a)

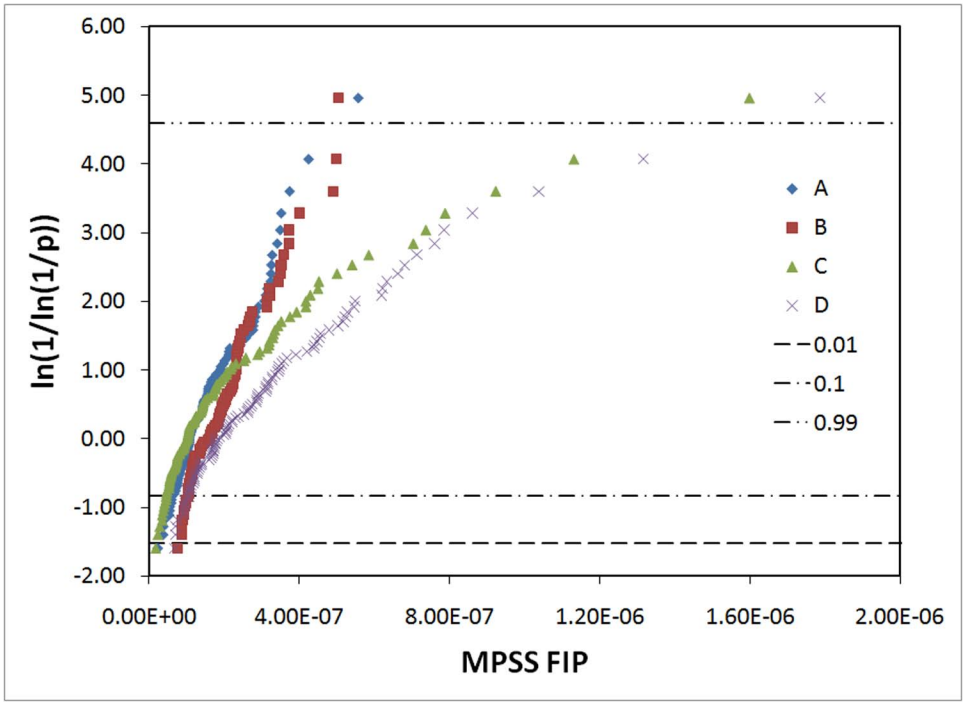

(b)

Figure 7.7: The extreme value FIP calculated over a cube shaped averaging volume with equivalent grain size of 0.032mm for Microstructures A-D plotted on a Gumbel probability scale for (a) the cumulative effective plastic strain (CEPS), (b) the maximum plastic shear strain (MPSS), and (c) the Fatemi-Socie (FS) FIPs. The 0.01, 0.1 and 0.99 probability levels are indicated.

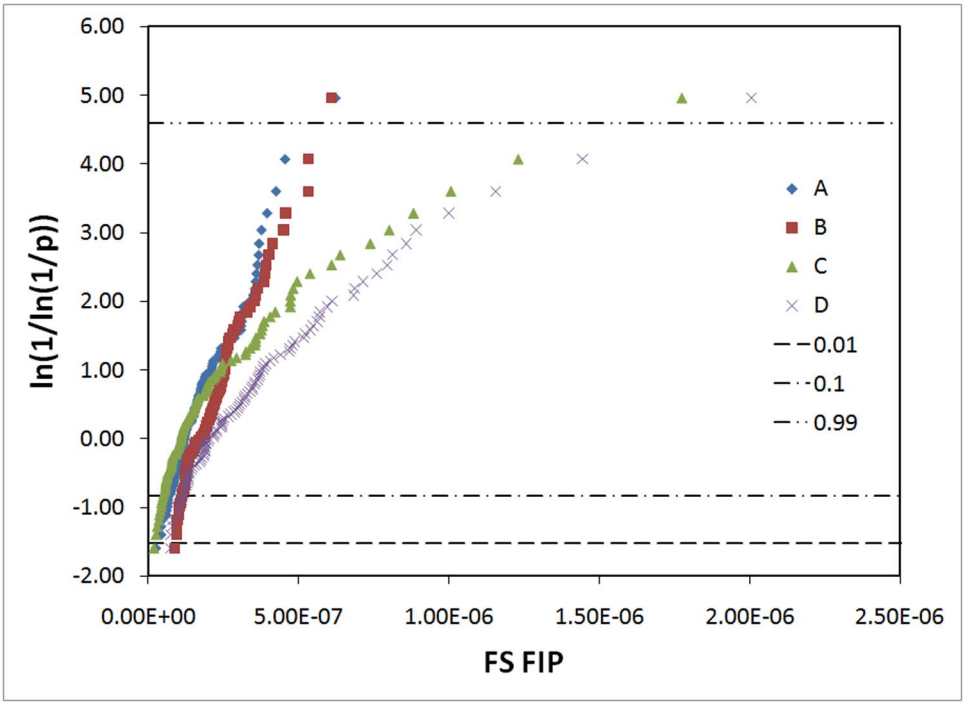

(c)

Figure 7.7: The extreme value FIP calculated over a cube shaped averaging volume with equivalent grain size of 0.032mm for Microstructures A-D plotted on a Gumbel probability scale for (a) the cumulative effective plastic strain (CEPS), (b) the maximum plastic shear strain (MPSS), and (c) the Fatemi-Socie (FS) FIPs. The 0.01, 0.1 and 0.99 probability levels are indicated.

on basal or prismatic slip planes with slip plane normals that tend to be closer aligned with the loading direction [155]. As shown by McDowell and Berard [65], the FS parameter reflects mixed mode growth of small fatigue cracks. For Ti-6Al-4V it is expected to be effective in reflecting combined effects of basal slip with elevated normal stress to this plane due to intergranular interactions.

It is also of interest to consider the mathematical character of the extreme value distributions of the FIPs as estimated from the simulated SVEs. As discussed in Chapter 3, for distributions of a single variable, there are only three types of non-degenerated distributions to which the extreme value distributions can converge for sufficiently large sample sizes. The three possible non-degenerated asymptotic distributions for the maximum extreme value distributions are the (i) Gumbel (Type I), (ii) Fréchet (Type II), or (ii) Weibull (Type III). The desire is to characterize a dataset as belonging to one of these three types of distributions so that mathematical properties can be used to better understand the data. Here the Type III Weibull distribution is not considered further because it is not clear how to quantify an upper bound for the present extreme value data at this time.

In Figure 7.8, the extreme value FS FIPs calculated for 100 simulated SVEs for each microstructure averaged over a cube shaped volume with equivalent grain size of 0.032mm are plotted on the (a) Gumbel (Type I) and (b) Fréchet (Type II) probability scale along with the linear fits estimated via least squares regression. The Fréchet probability scale is constructed in the same manner as the Gumbel probability scale that is described in Appendix B. The linearized Fréchet distribution is of the form $\ln\left[1/\ln\left(1/p\right)\right] = k\ln\left(y_n\right) - k\ln\left(v_n\right)$, where p is the probability. The fitting parameters for the maximum extreme value Gumbel distribution defined by Equation 3.23 and the Fréchet distribution defined by Equation 3.24 are given in Tables 7.5 and 7.6, respectively.

The fits (*i.e.*, R^2) in Figure 7.8(a) for the extreme value Gumbel distribution are better

Table 7.5: Fits of the extreme value Fatemi-Socie (FS) FIP distributions to the extreme value Gumbel (Type I) distribution for the duplex Ti-6Al-4V microstructures. The FS FIPs were calculated over averaging volumes with the equivalent grain size of 0.0032mm (see Table 7.2). The relative dispersion is calculated by $(\alpha_n)^{-1}/u_n$.

Micro.	α_n	u_n	**Rel. Disp.**	R^2
A	1.113×10^7	1.296×10^{-7}	0.69	0.973
B	1.177×10^7	1.740×10^{-7}	0.49	0.982
C	4.286×10^6	1.077×10^{-7}	2.17	0.854
D	3.968×10^6	2.141×10^{-7}	1.18	0.902

Table 7.6: Fits of the extreme value Fatemi-Socie (FS) FIP distributions to the extreme value Fréchet (Type II) distribution for the duplex Ti-6Al-4V microstructures. The FS FIPs were calculated over averaging volumes with the equivalent grain size of 0.0032mm (see Table 7.2).

Micro.	k	v_n	R^2
A	1.95	1.130×10^{-7}	0.917
B	2.74	1.635×10^{-7}	0.954
C	1.35	1.025×10^{-7}	0.970
D	1.76	2.004×10^{-7}	0.972

for Microstructure A and B than for Microstructures C and D. The extreme value distributions of the FS FIPs for these latter two microstructures almost appear bi-modal in character with the low probability regime exhibiting a differing slope than the higher probability regime. The instantiated SVEs for Microstructures A and B with the smaller relative grain size have many more grains in each SVE than Microstructures C and D which each have a larger relative average grain size (see Table 7.3). It is possible that the simulated SVEs with fewer numbers of grains are not as well described by the extreme value Gumbel distribution because they are further away from asymptotic convergence than the microstructures with more grains. As noted in Section 5.2, SVE size will affect the the extreme value distributions when the sample size of the microstructure attributes of interest is small relative to the large sample size required for asymptotic convergence of the extreme value distribution of response. In other words, as the size of the SVE increases and more microstructure is sampled, the extreme value distribution of the microstructure dependent response will shift

to higher values of the response until the asymptotic form of the extreme value distribution is achieved. This asymptotic convergence was demonstrated previously in the plot of the maximum extreme value distribution of the exponential distribution function shown in Figure 3.1. As the sample size increases, the extreme value distribution shifts to the left (toward higher magnitudes) until convergence is achieved. The sample size n of the extreme value distribution of a given response for the SVEs simulated here directly relates to the number of microstructure attributes that influence the response that exist in each SVE. In this work, the distributed plasticity is considered on the scale of the grains; therefore, the number of grains in each SVE dictates the sample size of the extreme value distributions of the plastic response (*i.e.*, FIPs). If the sample size n is sufficient, the extreme value distributions will likely converge to one of the three asymptotic forms listed in Section 3.2. Smaller samples sizes might not exhibit such convergence. It is noted that the particular simulations size employed here (*i.e.* 0.400mm along each edge of the simulation block) was chosen to both ensure that the lower order moments of the cyclic plastic response would change minimally with increasingly larger volumes and for computational convenience. The SVE size was held constant across all simulated SVEs here to compare the distributions of extreme value response for the range of microstructures considered here for that SVE size. Even if the SVE size is not sufficient for asymptotic convergence of the extreme value distributions, it does not mean that a larger SVE size should be used. For example, if it is of critical importance to consider the extreme value response in the volume of a notch root, it would not be prudent to consider volumes larger than the critically stress volume at the notch root even if the sample size of the considered volume is insufficient to produce asymptotically converged extreme value distributions. In this work, the size of SVE required for asymptotic convergence of the extreme value FIPs is not considered; although, the SVE size does likely play a role in the quality of fits to the known asymptotic extreme value distributions for the SVE with fewer numbers of grains.

The fits for the extreme value Fréchet distribution given in Figure 7.8(b) are all very

similar. Visual inspection of the extreme value distributions plotted on the Fréchet probability plot shows that the distributions tend to deviate from linearity at both the low probability and high probability regions of the plot. This lack of linearity, tends to suggest that the extreme value distributions of the FIPs for these simulated SVEs with periodic boundary conditions are better described by the extreme value Gumbel distribution than the extreme value Fréchet distribution. This is true even for the extreme value distributions of the FIPs for Microstructures C and D which appear bi-modal on the Gumbel probability scale.

The lower probability regime (*i.e.* < 0.1 probability) of the extreme value distributions of the FIPs shown in Figure 7.8 tend to be very similar in magnitude across the entire range of simulated microstructures. This lower probability regime where the FIPs are of lower relative magnitude is associated with greater numbers of cycles for fatigue crack formation N_{FOR}. In other words, the driving forces for fatigue crack formation are all nominally the same for larger magnitudes of N_{FOR}. There does appear to be a slight deviation in the low probability regime depending on the volume fraction of the primary α grains. Microstructures A and C both with 30% primary α tend to converge to the same lower probability extreme value FS FIPs. The extreme value FS FIPs of Microstructures B and D with both with 70% primary α similarly converge but to a value slightly higher than that of Microstructures A and C. Therefore, this low probability regime tends be most influenced by the nominal volume fraction of the primary α grains. The extreme value FIPs in this regime is likely most associated with the probability of finding nominal grains oriented for easy slip. Lower volume fractions of the primary α grains tends to exhibit the lowest driving forces for fatigue crack formation in this low probability regime.

In contrast to this low probability regime, there is much more scatter and separation between the extreme value distributions of the FIPs for the different microstructures considered in the higher probability regime of the cumulative distribution plots shown in Figure 7.8. This suggests that for crack formation, there will be more scatter in the shorter life

regime (*i.e.* for crack formation N_{FOR}) than in the longer life regime. Moreover, this scatter appears to be most influenced by the grain size distribution. For example, Microstructures A and B with similar grain size distributions tend to exhibit extreme value FIPs similar in magnitude in the high probability regime. Additionally, the extreme value FS FIPs for Microstructures C and D with larger relative grain sizes also tend to be similarly distributed. There is over an order in magnitude difference between the extreme value FIPs for Microstructures A and B versus those of Microstructures C and D above 0.99 probability. Consideration of the influence of the volume fraction of the primary α grains in the high probability regime appears to be much less significant. Thus, it appears that the extreme value FIPs for the microstructures with smaller primary α grain size are much lower in magnitude then the microstructures with larger primary α grains.

A demarcation between differing lower and higher probability regimes is especially significant for Microstructures C and D which exhibited bi-modal extreme value distribution of the FS FIPs with two different slops in the low and high probability regimes. As Microstructures C and D sample far fewer grains than Microstructures A and B (*i.e.*, n is much smaller for Microstructures C and D), it is likely that certain extreme value coupled microstructure attributes are devoid in a many of the instantiated SVEs. Thus, the extreme value FIPs in the lower probability region of these Microstructures is strongly dictated by the nominal microstructure; moreover, many important extreme value coupled microstructure attributes are not observed in this low probability regime. Higher cumulative probability of the extreme value FIPs is increasingly associated with more extreme value (*i.e.*, rare event) individual/coupled microstructure attributes, and in the case of Microstructures C and D exhibit a different slop than the low probability regime. As the SVE size (*i.e.*, sample size n) increases, this bi-modal distribution likely converges to a single asymptotic extreme value distribution that is completely dependent on the extreme value probabilities of the key individual/coupled microstructure attributes. Microstructure C which had the fewest number of grains in each SVE changes slop around 70% probability (*i.e.* $\ln(1/\ln(1/p)) = 1.0$) while

Microstructure D with the next fewest number of grains appears to change slope around 1% prbability (*i.e.* $\ln(1/\ln(1/p)) = -0.83$). This similar bi-modal separation was not observed to be strong with Microstructures A and B. It is likely that this separation was not observed in this case because Microstructures A and B sampled many more grains with each simulated SVE and were less influenced by the nominal microstructure than the key extreme value microstructure attributes.

Despite the bi-modal character the the extreme value distributions of the FS FIPs for Microstructures C and D, Microstructures A and B clearly exhibit lower relative magnitudes in the extreme value FIPs. Even if the size of the SVEs was increased to determine if a more linear asymptotically converged extreme value distribution could be characterized for Microstructures C and D, the distributions of the extreme value FIPs would likely shift to the left towards higher magnitudes and Microstructures A and B would still exhibit lower relative extreme value FIPs.

In Figure 7.9, the extreme value distribution of the FS FIP determined for each of the first 10 cycles for Microstructure A is given for the FIPs calculated over a cube shaped averaging volume with equivalent grain size of 0.032mm. From Figure 7.9, it can be observed that most of the shakedown occurs during the first 6-7 cycles; there is little change in the distributions for cycles 8-10. Shakedown of the extreme value distributions can be quantified by comparing the parameters of the linear fits for the Gumbel distribution that are extracted as previously explained. The inverse measure of the dispersion of these distributions, α_n, changes by as much as 40% between the initial and second cycles but changes by less than 5% between the cycles 9 and 10. Additionally, the grains predicted to exhibit the extreme value FS FIPs differed by as much as 15% between the 1st and 10th cycles. This indicates that although the location of the extreme value FIP can be estimated in the first few cycles, there is a significant probability that the location of the extreme value response may change after shakedown.

It can also be observed in Figure 7.9, that the lower probability region of the extreme

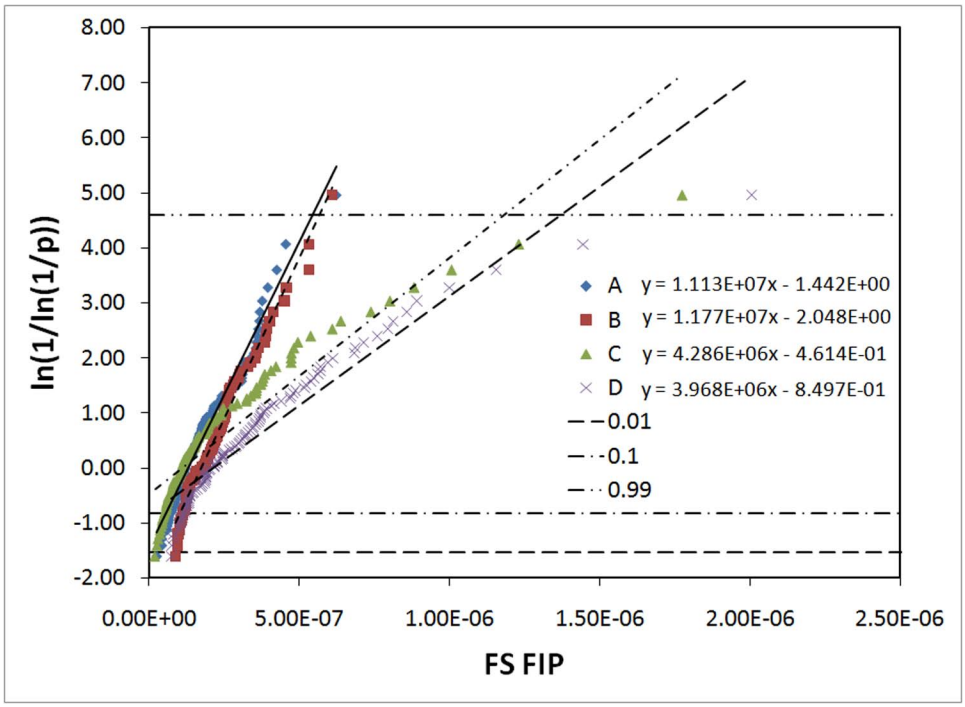

(a)

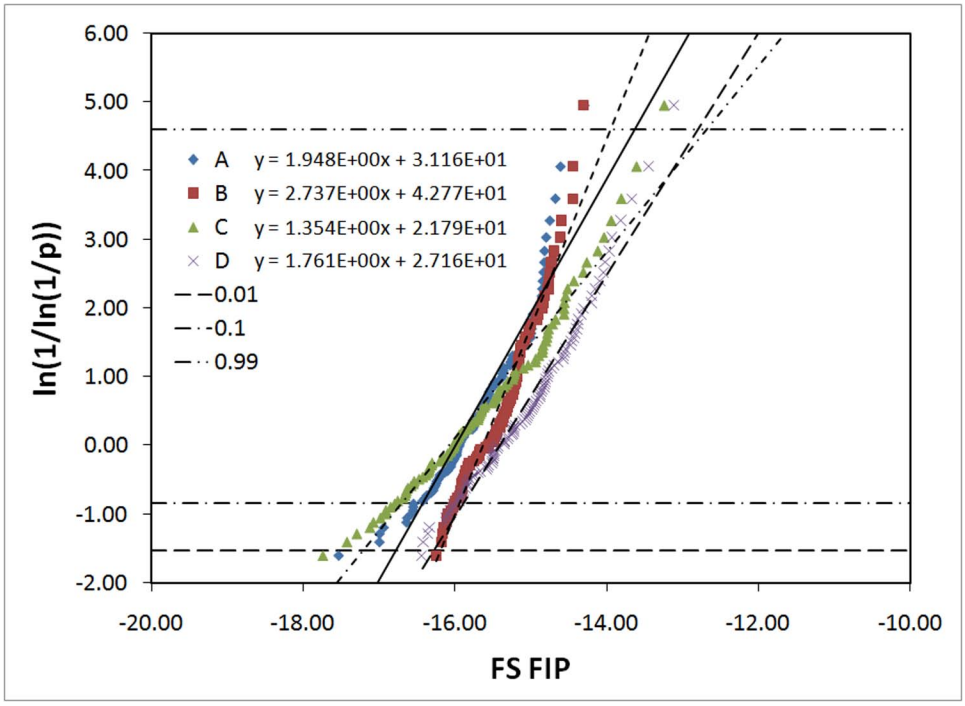

(b)

Figure 7.8: The extreme value Fatemi-Socie (FS) FIP calculated over a cube shaped averaging volume with equivalent grain size of 0.032mm for the four analyzed microstructures plotted on the (a) Gumbel (Type I) and (b) Fréchet (Type II) probability scales. Note that the equations given for the least squares linear regression are such that $y = \ln(1/\ln(1/p))$ and $x = FIP$ for the Gumbel probability plot and $x = \ln(FIP)$ for the Fréchet probability plot, respectively. The 0.01, 0.1 and 0.99 probability levels are indicated.

value distribution of the FIPs tends to converge to similar magnitudes of the extreme value FIPs across the range of cycles considered; whereas, most scatter in the extreme value distributions of the FIPs across the range of cycles is in the high probability regime. In the lower cumulative probability regime, the extreme value distributions change little from cycle to cycle even before shakedown is achieved. At higher cumulative probabilities, the scatter in the extreme value FIPs from cycle to cycle slowly decreases until a condition of shakedown is achieved. After shakedown the scatter is minimal between the extreme value distributions of the FIPs for further subsequent cycling. This indicates that most shakedown is occurring in the high probability regime, and that shakedown does not affect the driving forces for fatigue crack formation as significantly in the low probability regime. It is likely that the changes in the extreme value FIPs are more drastic in the high probability regime of the extreme value distributions of the FIPs because there is greater hardening and evolution of the microstructure in the regions with the most plasticity. Because the plasticity is less in the lower probability regime associated with lower magnitudes of the extreme value FIPs, there is less hardening and subsequent evolution in the plastic behavior from one cycle to the next. After shakedown, the extreme value distribution approaches linearity on the Gumbel probability scale for Microstructure A and is well described by the extreme value Gumbel distribution (*i.e.*, by cycle 10 the fit from Table 7.7 is $R^2 = 0.973$).

The distributions of the volume average Fatemi-Socie (FS) FIP calculated over an averaging volume with equivalent grain size of 0.032mm, 0.054mm and 0.076mm for Microstructure A are given on a Gumbel probability scale in Figure 7.10. In comparing the relative extreme value distributions, there is no significant difference in predicted trends. The magnitude of the FIPs tend to decrease as the size of the averaging volumes increase. In other words, the larger the averaging volume for the FIP calculations, the lower the overall magnitude of the extreme value FIPs tends to be. This is reasonable because larger averaging volumes will wash out the extreme value response over a larger area. Using larger averaging volumes, however, allows one to consider the average driving forces for

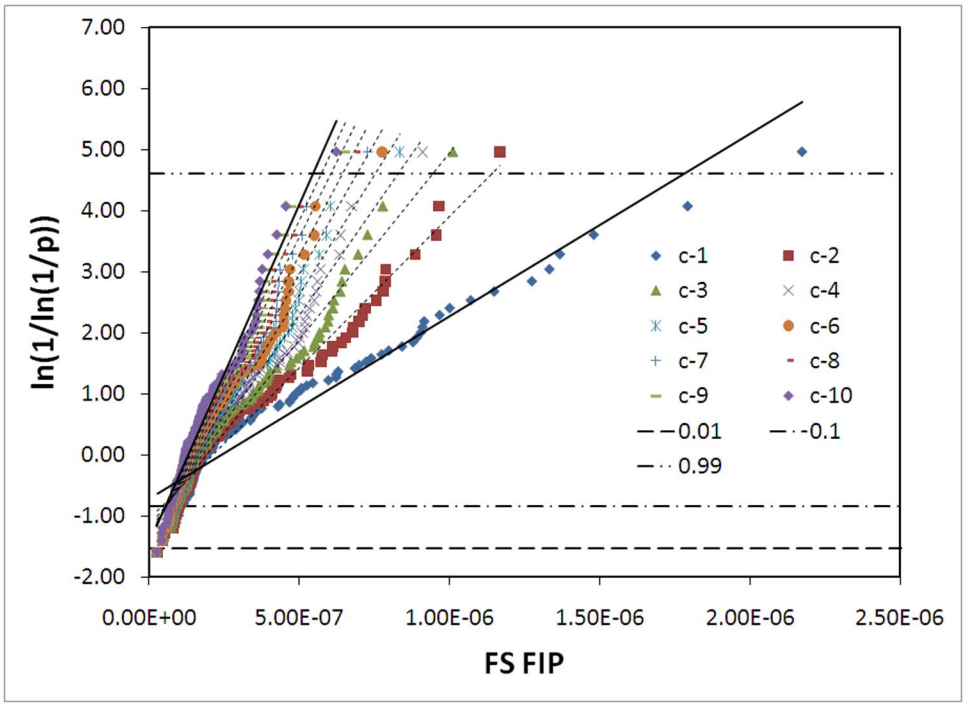

Figure 7.9: The extreme value Fatemi-Socie (FS) FIP calculated over a cube shaped averaging volume with equivalent grain size of 0.032mm for Microstructure A on a Gumbel probability scale for the first 10 cycles. Note that the equations given for the least squares linear regression are such that $y = \ln(1/\ln(1/p))$ and $x = FIP$. The 0.01, 0.1 and 0.99 probability levels are indicated.

Table 7.7: Fits of the extreme value Fatemi-Socie (FS) FIP distributions to the extreme value Gumbel (Type I) distribution for cycles 1 through 10 of Microstructure A. The FS FIPs were calculated over averaging volumes with the equivalent grain size of 0.0032mm (see Table 7.2). The relative dispersion is calculated by $(\alpha_n)^{-1}/u_n$.

Cycle	α_n	u_n	**Rel. Disp.**	R^2
1	2.991×10^6	2.402×10^{-7}	1.39	0.936
2	4.968×10^6	2.124×10^{-7}	0.95	0.964
3	6.123×10^6	1.906×10^{-7}	0.86	0.966
4	7.032×10^6	1.753×10^{-7}	0.81	0.968
5	7.841×10^6	1.639×10^{-7}	0.78	0.969
6	8.582×10^6	1.545×10^{-7}	0.75	0.970
7	9.272×10^6	1.468×10^{-7}	0.73	0.971
8	9.917×10^6	1.403×10^{-7}	0.72	0.972
9	1.053×10^7	1.347×10^{-7}	0.71	0.972
10	1.113×10^7	1.296×10^{-7}	0.69	0.973

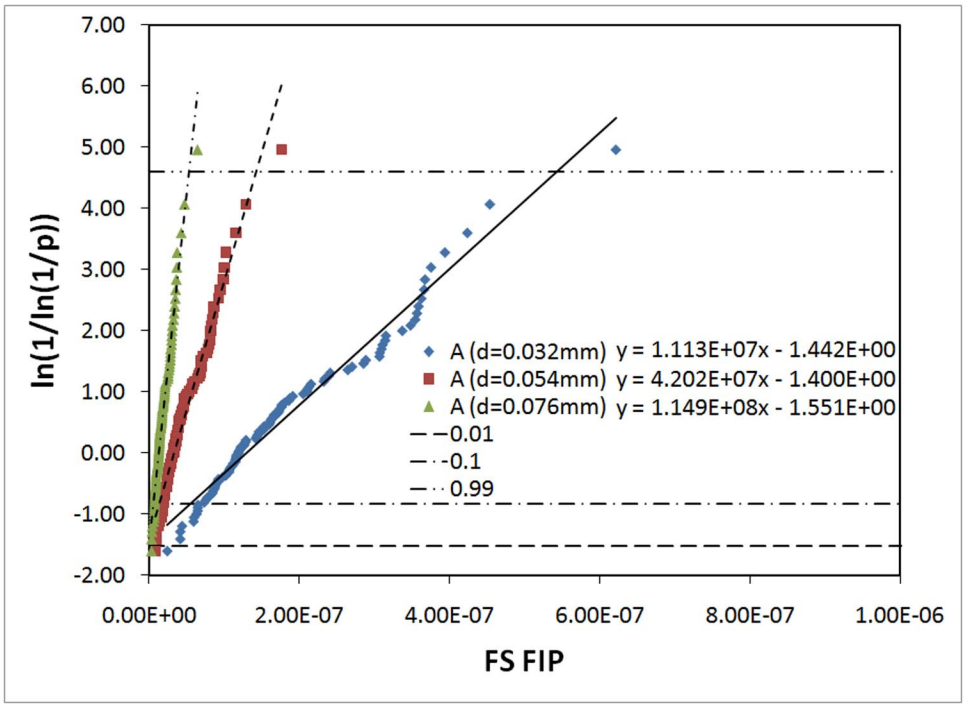

Figure 7.10: The extreme value Fatemi-Socie (FS) FIP calculated over averaging volume with equivalent grain size of 0.032mm, 0.054mm, 0.076mm for microstructure A on a Gumbel probability scale. Note that the equations given for the least squares linear regression are such that $y = \ln(1/\ln(1/p))$ and $x = FIP$.

fatigue crack formation over a larger area. Depending on the local barriers for microstructurally small crack growth, larger averaging volumes (relative to the distance between the dominant microstructural barriers) might better indicate the locations where the critical life limiting cracks form that are large enough to avoid being arrested by these barriers.

Based on the extreme value distributions of the FIPs, Microstructure A is predicted to have the least variability in overall fatigue performance and lower maximum driving forces for fatigue crack formation. Although, the response for Microstructure B was predicted to be very similar, the driving forces for Microstructure A are predicted to be slightly lower according to the fit of the extreme value distribution of FIPs to the Gumbel distribution. Thus, it is likely that microstructures with smaller primary α grain sizes and smaller volume fractions of the primary α grains will have better resistance to fatigue crack formation. This is directly related to the fact that most cyclic slip is occurring in the primary α grains at the

applied peak strain of 0.6%. Lower volume fractions of the primary α grains exhibit less slip activity than the microstructures with higher volume fractions of primary α grains. In addition, the smaller primary α grains have smaller mean free paths for slip.

7.3.2 EVMCF of apparent Schmid factor in random textured Ti-6Al-4V microstructures

The microstructure attributes that are coincident with the grains in which the extreme value FIPs were identified are considered next. Most (*i.e.*, 95%) of the volume averaged extreme value FIPs calculated over a cube shaped averaging volume with equivalent grain size of 0.032mm were identified to be associated with primary α grains. This is expected as slip was modeled to be more limited in the $\alpha + \beta$ colonies. To consider the orientation of the grains predicted to exhibit the estimated extreme value response, Schmid factors were identified for the primary α HCP slip systems including the basal, prismatic, pyramidal $\langle a \rangle$, and pyramidal $\langle a + c \rangle$ slip systems. Figure 7.11 shows cross correlation between the apparent Schmid factor for each type of slip system and the extreme value volume averaged FS FIP for each simulation of Microstructure A. The other microstructures demonstrated similar trends. In most cases, the grains with the maximum grain averaged FIP are oriented for easy basal slip. Additionally, maximum Schmid factors are also observed for prismatic slip and in a few cases for pyramidal $\langle a \rangle$ and pyramidal $\langle a + c \rangle$ slip. However, it is noted that when the magnitude of the Schmid factor for pyramidal $\langle a \rangle$ and pyramidal $\langle a + c \rangle$ slip is high, the magnitude of the Schmid factor for prismatic slip is also fairly high. This is significant because prismatic slip is an easier slip mode than either pyramidal $\langle a \rangle$ and pyramidal $\langle a + c \rangle$ slip; therefore, prismatic slip will likely be favored even when the resolved shear stresses on both the prismatic and pyramidal slip systems is similar.

As noted previously, the primary α grain size has been reported to play a role in the processes of fatigue crack formation. Figure 7.12 shows the cross correlation between the grain volume associated with the center of the volume averaged extreme value FS FIP versus the extreme value FS FIPs for Microstructure A. The volume averaged FIPs in this

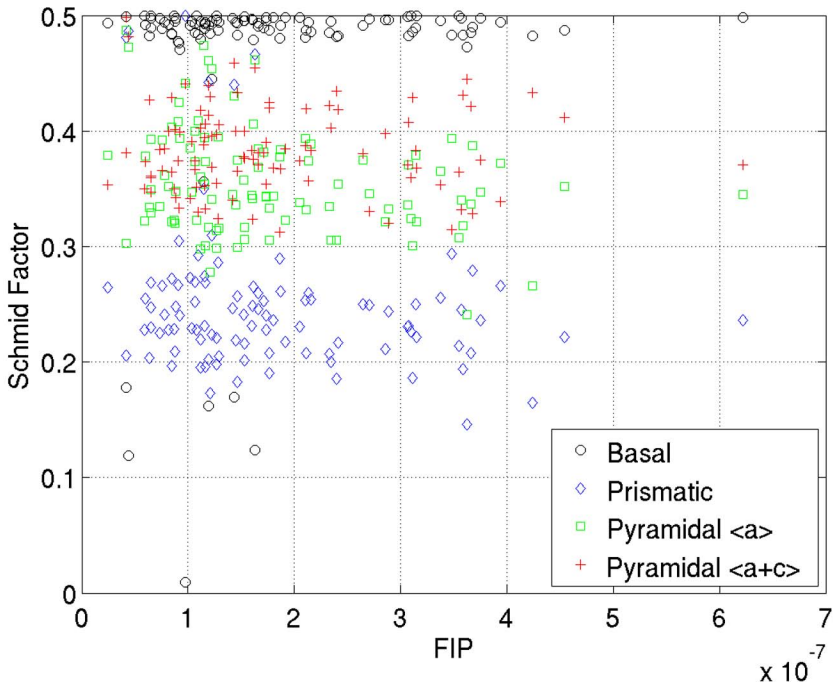

Figure 7.11: The apparent Schmid factors for basal, prismatic, pyramidal $\langle a \rangle$, and pyramidal $\langle a + c \rangle$ for each extreme value Fatemi-Socie FIP calculated over a cube shaped averaging volume with equivalent grain size of 0.032mm estimated from the 100 simulated SVEs for Microstructure A after 10 cycles with 0.6% maximum applied strain.

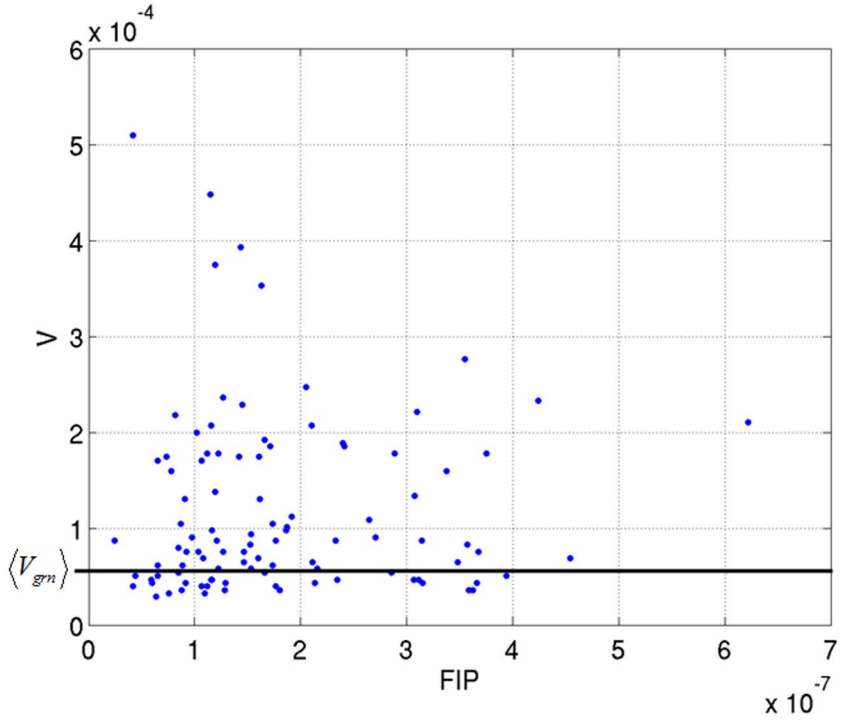

Figure 7.12: The extreme value Fatemi-Socie (FS) FIPs calculated over a cube shaped averaging volume with equivalent grain size of 0.032mm plotted against the grain volume of the grain coincident with the extreme value FIP for the 100 simulated SVEs for Microstructure A after 10 cycles at 0.6% maximum strain. The average grain volume for Microstructure A calculated via Equation 7.3 based on the average grain size of 0.025mm is shown by $\langle V_{grn} \rangle$.

case are calculated over the averaging volume of 9.83×10^{-5} with equivalent grain size of 0.032mm; the mean primary α grain size for Microstructure A is 0.025mm with an approximate volume of 4.56×10^{-5} as calculated via Equation 7.3 (see Table 7.1). The grains with the extreme value FIPs tend to be larger than the average grain size, but the largest observed FIPs do not necessarily occur in the largest grains. This is in agreement with what has been observed experimentally in Ti-6246 [221, 232].

The EVMCF are constructed to quantify the crystallographic attributes that most strongly influence the predicted extreme value response. Similar to the approach demonstrated in Chapter 6, the microstructure dependence of the extreme value FIPs are characterized in terms of the apparent Schmid factor for the different phases of the microstructures considered here. Specifically, Schmid factors are identified that correlate with the extreme

value response using the previously introduced extreme value marked radial correlation function for the Schmid Factor (*i.e.*, $R_{\max(FIP)}\left(m_a^g, m_a^{g'}|r,\Omega\right)$). By considering the extreme value marked correlation functions for apparent Schmid factors, the probabilities of specific grain orientations and misorientations existing coincident with the observed extreme value FIPs are indirectly considered. To construct $R_{\max(FIP)}\left(m_a^g, m_a^{g'}|r,\Omega\right)$, a tessellated scale of the Schmid factor in 0.05 increments was applied. As shown previously in Figure 7.11, grains oriented for easy basal slip were most common at the locations of the estimated extreme value FIPs. Thus, to reduce the dataset to a manageable size, the correlations between the Schmid factors m_a^g were considered for basal slip between 0.45 and 0.5 for the primary α phase, and Schmid factors $m_a^{g'}$ between 0.45 and 0.5 for the same and for the other types of slip and phases, as shown in Figures 7.13 and 7.14 for Microstructure A. The correlations that occurred with the highest significance in Microstructure A are shown in Figure 7.13(a), which plots correlations between the primary α grains oriented for easy basal slip (*i.e.*, with a Schmid factor m_a^g for basal slip between 0.45 and 0.5) and the apparent Schmid factors $m_a^{g'}$ for similarly oriented grains of the same phase. In Figure 7.14(d), the correlations are plotted that occurred with the second highest probability in Microstructure A. These correlations describe the probabilities that primary α grains oriented for easy basal slip exist near $\alpha + \beta$ colonies oriented favorably for bcc slip. Note that the active bcc slip systems considered in the crystal plasticity model are aligned with certain HCP slip systems according to $(0001)_\alpha \,//\, \{101\}_\beta$ and $\left\langle 11\bar{2}0\right\rangle_\alpha \,//\, \langle 111\rangle_\beta$ in order to maintain the BOR. In Figures 7.15-7.17, the correlated Schmid factors are similarly plotted for the different phases that occurred with the highest probability in microstructures B, C, and D, respectively.

In the four random textured microstructure variants of duplex Ti-6Al-4V considered here, it was found that primary α grains oriented with a Schmid factor for basal slip between 0.45 and 0.5 (easy slip) are much more likely to be found at the location of extreme

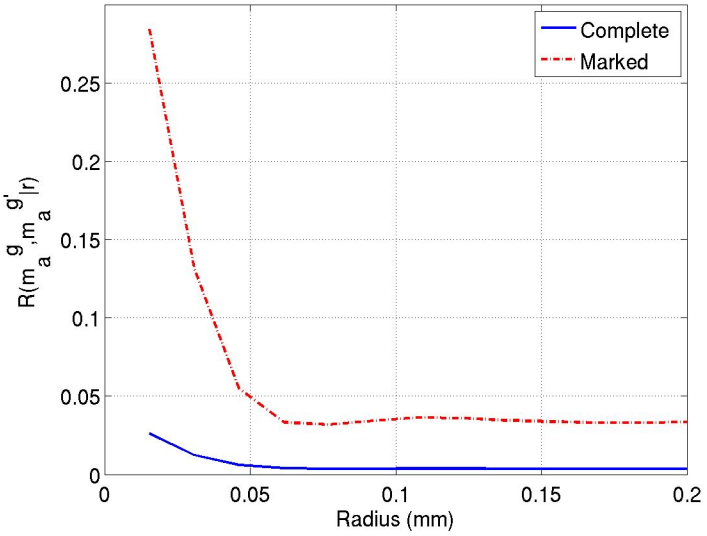

(a)

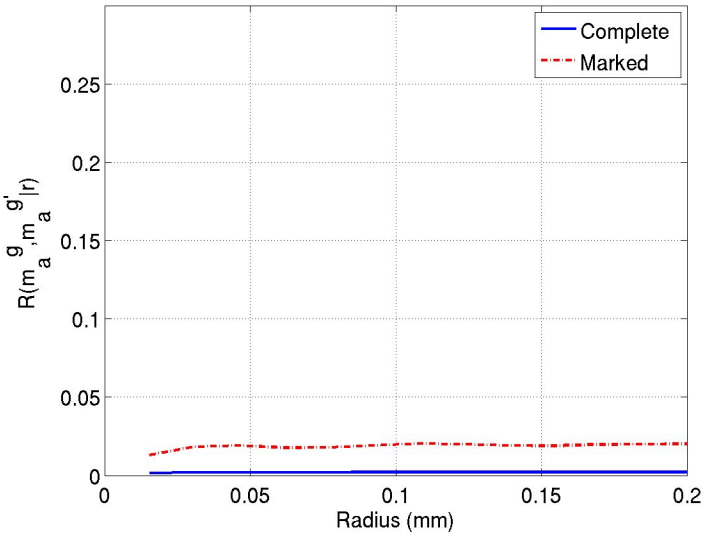

(b)

Figure 7.13: Radial correlation functions for the complete microstructure compared with EVMCF describing the correlation between the apparent Schmid factor m_a^g for basal slip between 0.45 and 0.5 for the primary α phase and the Schmid factor $m_a^{g'}$ for: (a) basal slip between 0.45 and 0.5, (b) prismatic slip between 0.45 and 0.5, (c) pyramidal $\langle a \rangle$ slip between 0.45 and 0.5, and (d) pyramidal $\langle a + c \rangle$ slip between 0.45 and 0.5 for the primary α phase in Microstructure A.

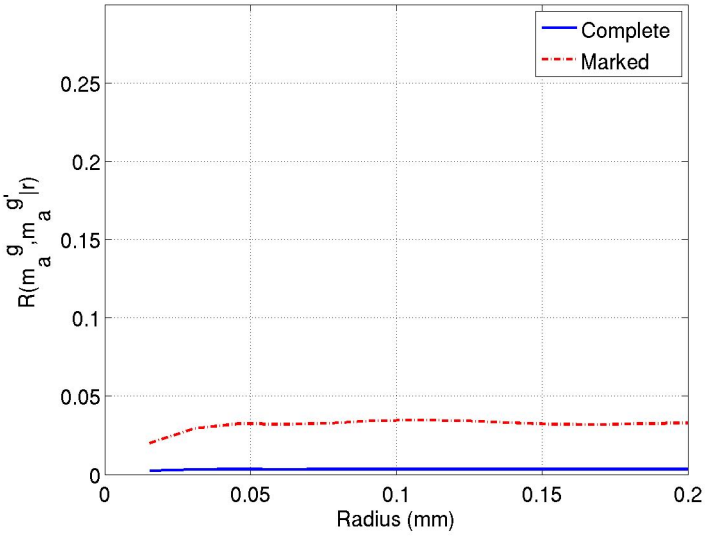

(c)

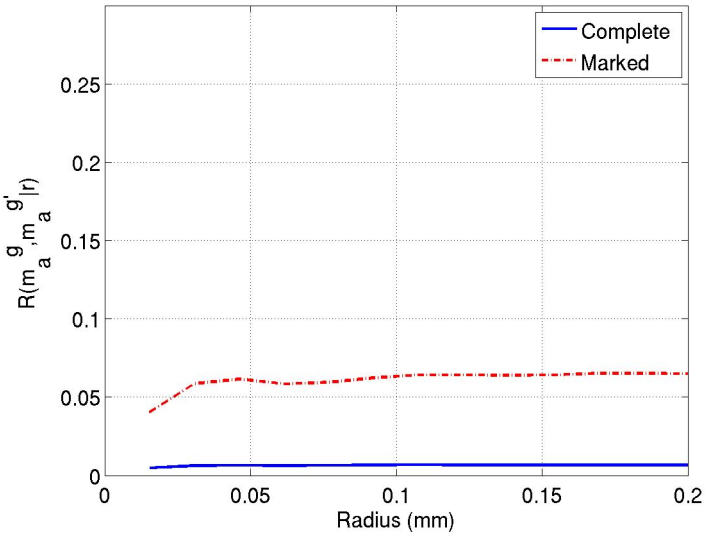

(d)

Figure 7.13: Radial correlation functions for the complete microstructure compared with EVMCF describing the correlation between the apparent Schmid factor m_a^g for basal slip between 0.45 and 0.5 for the primary α phase and the Schmid factor $m_a^{g'}$ for: (a) basal slip between 0.45 and 0.5, (b) prismatic slip between 0.45 and 0.5, (c) pyramidal $\langle a \rangle$ slip between 0.45 and 0.5, and (d) pyramidal $\langle a + c \rangle$ slip between 0.45 and 0.5 for the primary α phase in Microstructure A.

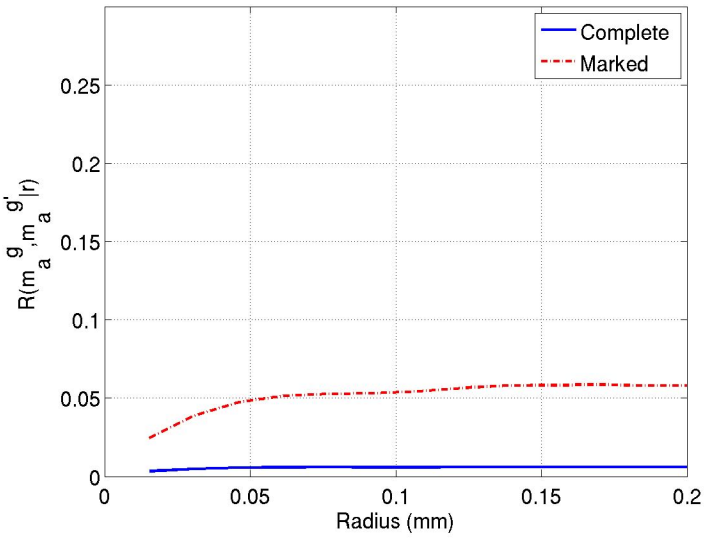

(a)

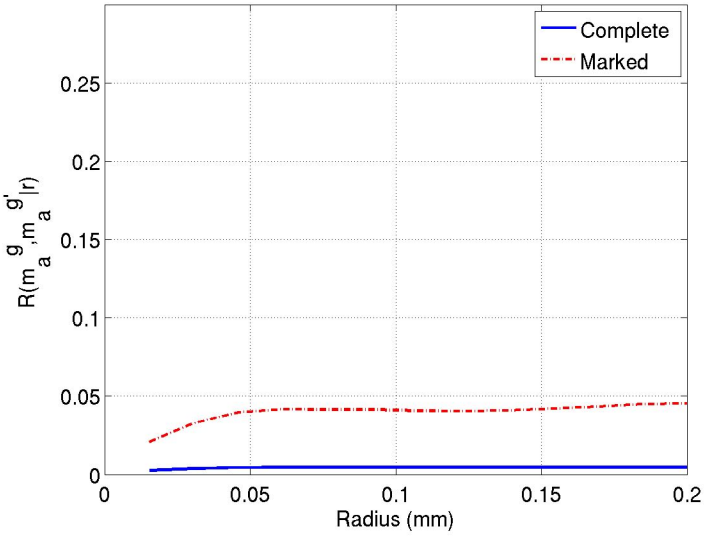

(b)

Figure 7.14: Radial correlation functions for the complete microstructure compared with EVMCF describing the correlation between the apparent Schmid factor m_a^g for basal slip between 0.45 and 0.5 for the primary α phase and the apparent Schmid factor $m_a^{g'}$ for: (a) basal slip between 0.45 and 0.5, (b) prismatic slip between 0.45 and 0.5, (c) pyramidal $\langle a \rangle$ slip between 0.45 and 0.5, and (d) $\langle 111 \rangle \{110\}$ bcc slip (transformed into the hexagonal coordinate system via the BOR) between 0.45 and 0.5 for the $\alpha + \beta$ colony phase in Microstructure A.

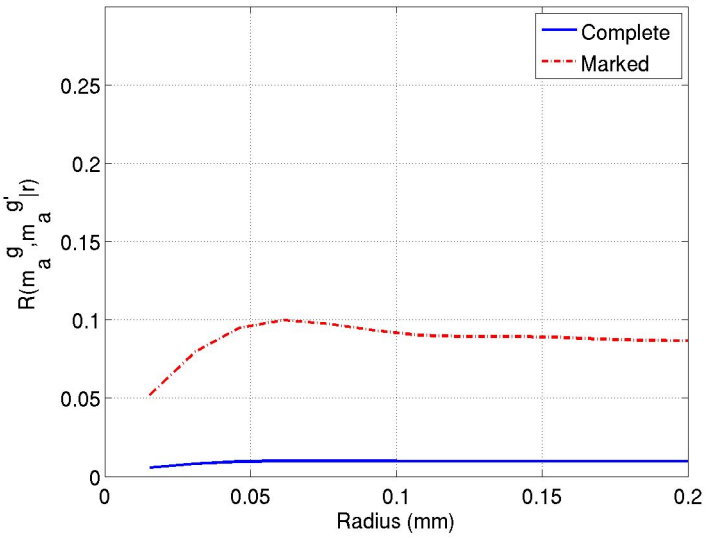

(c)

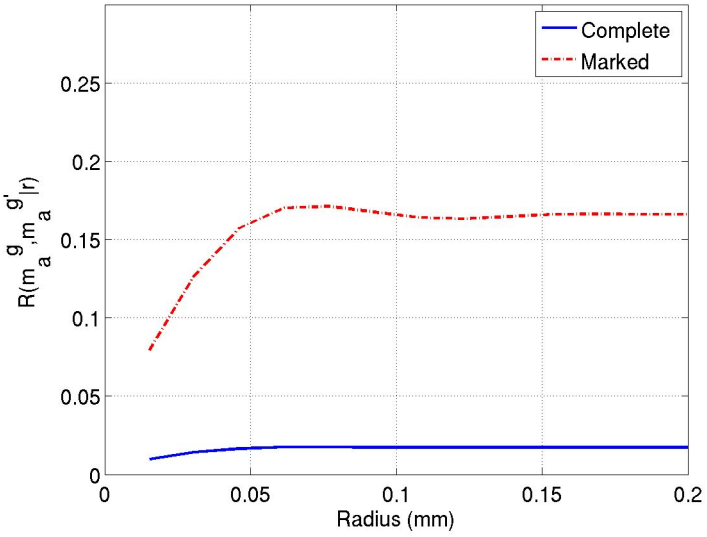

(d)

Figure 7.14: Radial correlation functions for the complete microstructure compared with EVMCF describing the correlation between the apparent Schmid factor m_a^g for basal slip between 0.45 and 0.5 for the primary α phase and the apparent Schmid factor $m_a^{g'}$ for: (a) basal slip between 0.45 and 0.5, (b) prismatic slip between 0.45 and 0.5, (c) pyramidal $\langle a \rangle$ slip between 0.45 and 0.5, and (d) $\langle 111 \rangle \{110\}$ bcc slip (transformed into the hexagonal coordinate system via the BOR) between 0.45 and 0.5 for the $\alpha + \beta$ colony phase in Microstructure A.

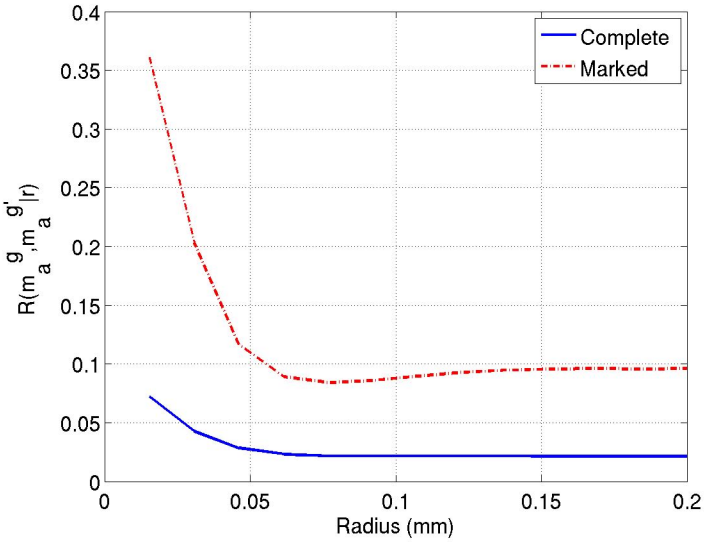

(a)

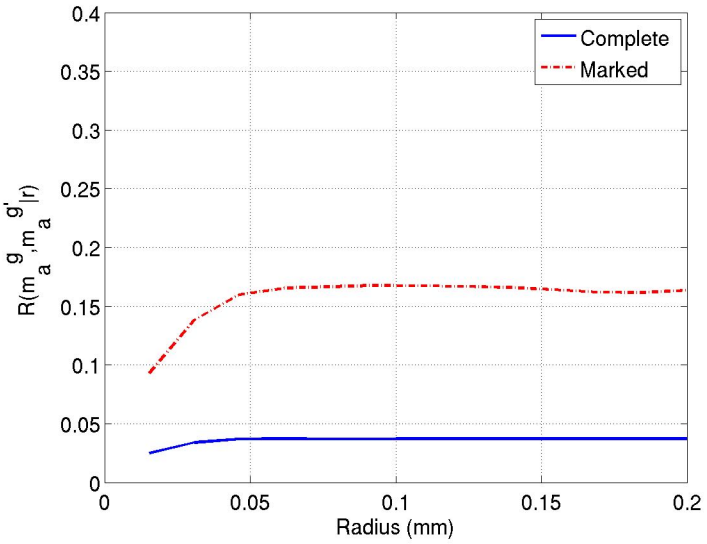

(b)

Figure 7.15: Radial correlation functions for the complete microstructure compared with EVMCF describing the correlation between the apparent Schmid factor m_a^g for basal slip between 0.45 and 0.5 for the primary α phase and the apparent Schmid factor $m_a^{g'}$ or: (a) basal slip between 0.45 and 0.5 and (b) pyramidal $\langle \alpha + \beta \rangle$ slip between 0.45 and 0.5 for the primary α phase in Microstructure B.

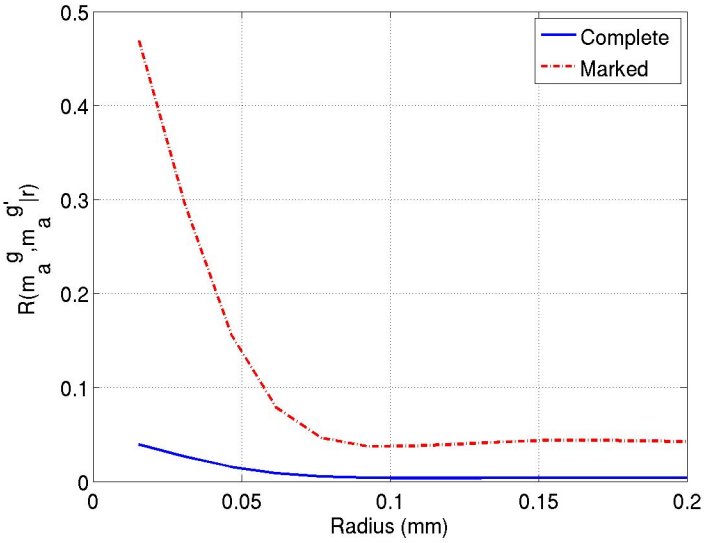

(a)

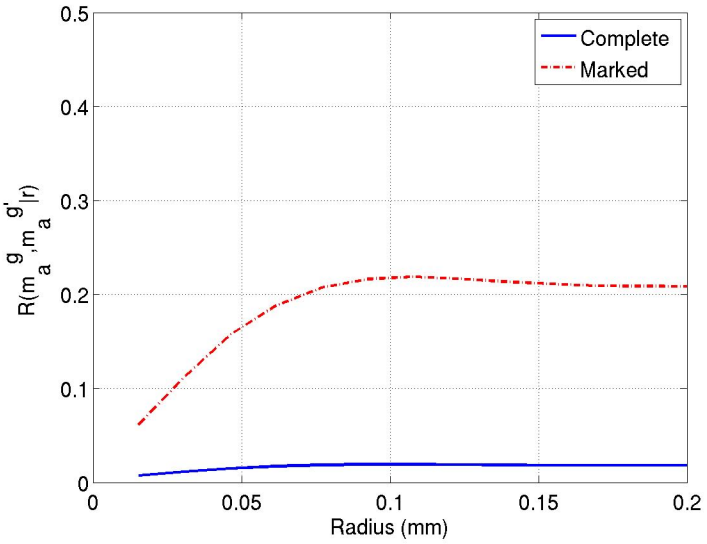

(b)

Figure 7.16: Radial correlation functions for the complete microstructure compared with EVMCF describing the correlation between the apparent Schmid factor m_a^g for basal slip between 0.45 and 0.5 for the primary α phase and the apparent Schmid factor $m_a^{g'}$ for: (a) basal slip between 0.45 and 0.5 for the primary α phase and (b) $\langle 111 \rangle \{110\}$ bcc slip (transformed into the hexagonal coordinate system via the BOR) between 0.45 and 0.5 for the $\alpha + \beta$ colony phase in Microstructure C.

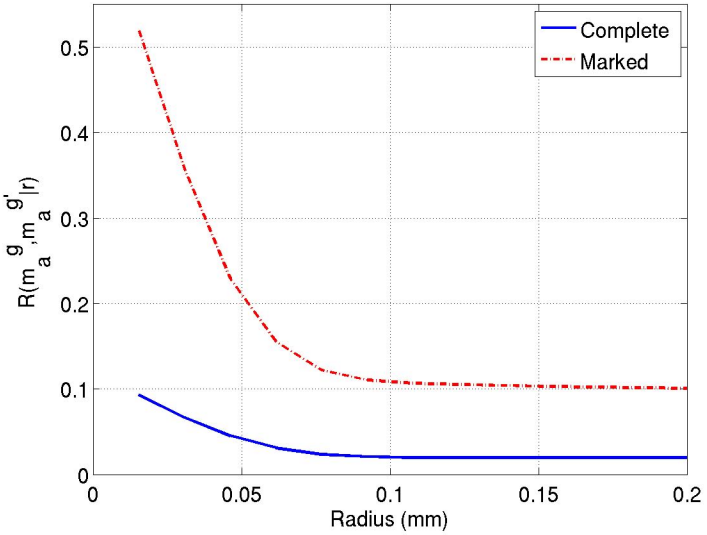

(a)

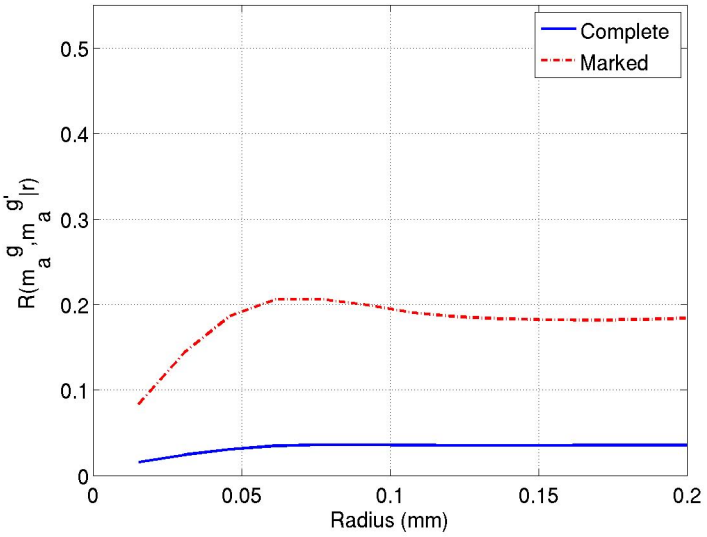

(b)

Figure 7.17: Radial correlation functions for the complete microstructure compared with EVMCF describing the correlation between the apparent Schmid factor m_a^g for basal slip between 0.45 and 0.5 for the primary α phase and the apparent Schmid factor $m_a^{g'}$ for: (a) basal slip between 0.45 and 0.5 and (c) pyramidal $\langle a+c \rangle$ slip between 0.45 and 0.5 for the primary α phase in Microstructure D.

value response than in the overall microstructure. This agrees with what was found by Bridier *et al.* [229,230]. When considering multiple correlated microstructure attributes, it was much more probable to find a primary α grain oriented for easy basal slip near hard oriented $\alpha + \beta$ colonies with high Schmid factors for BOR-modified bcc slip in microstructures A and B or primary α grains with high Schmid factors for pyramidal slip in microstructures B and D. The latter previously mentioned correlated orientation relationships were also identified by Gilbert and Piehler [231] and Bantounas *et al.* [235] in Ti-6Al-4V. Previously cited work [69,218,236–239] demonstrated that these types of hard-soft grain combinations can dramatically increase the local stress state which in turn promotes increased plasticity in these regions. It is not surprising that simulations from microstructures A and C predict these hard-soft grain correlations to occur with highest probability when the primary α grains oriented for easy slip are near the hard oriented $\alpha+\beta$ colonies when the volume fraction of the primary α grains is low. In microstructures B and D, the hard-soft correlations that occurred with the highest probably were observed to be between the primary α grains oriented for slip near the hard oriented primary α grains, which is expected when the volume fraction of the primary α grains is high (*i.e.*, 70%). Other hard-soft grain relationships in the various microstructures are also predicted to occur with significantly higher probabilities at sites of extreme value response than in the overall microstructure. For brevity only those in Microstructure A are shown in Figures 7.13(c) and 7.13(d), which describe correlations between primary α grains oriented for easy basal slip near other primary α grains oriented for harder pyramidal $\langle a \rangle$ or pyramidal $\langle a + c \rangle$ slip modes, respectively. Figure 7.14 shows correlations between primary α grains oriented for easy basal slip and $\alpha+\beta$ colonies that in all cases exhibit harder slip modes. In short, the same key correlated microstructure attributes (grains/phases with a specific Schmid factor) were identified across the range of all the microstructures.

Table 7.8: Fits of the extreme value Fatemi-Socie (FS) FIP distributions to the extreme value Gumbel (Type I) distribution for two different magnitudes of maximum applied strain. The FS FIPs were calculated over averaging volumes with the equivalent grain size of 0.0032mm (see Table 7.2). The relative dispersion is calculated by $(\alpha_n)^{-1}/u_n$.

Max. Strain	α_n	u_n	**Rel. Disp.**	R^2
0.006	1.113×10^{7}	1.296×10^{-7}	0.69	0.973
0.007	1.330×10^{6}	4.524×10^{-6}	0.17	0.985

7.3.3 Influence of peak stress on the extreme value distributions of the FIPs in Ti-6Al-4V

To explore the influence of the peak stress on the extreme value distributions of the driving forces for fatigue damage formation as estimated by the FIPs an additional set of 100 SVEs was instantiated for Microstructure A in the same manner as described previously with the random texture. These volumes were dimensioned 0.400mm along each edge and loaded with a maximum peak strain of 0.7% with a applied strain rate of $0.002s^{-1}$. Periodicity was similarly assumed in all directions.

The extreme value distributions of the FS FIPs for the set of SVEs cycled at 0.6% strain is compared with the SVEs cycled at 0.7% strain for Microstructure A in Figure 7.18. The parameters of the extreme value Gumbel distribution fit to the respective distributions shown in Figure 7.18 are given in Table 7.8. The quality of the fit (*i.e.*, R^2) at the different stain magnitudes is nearly identical. In both cases, the distributions are well fit by the extreme value Gumbel distribution. It can be observed here, as it was observed in Chapter 6 with IN100, that the relative scatter of the distributions as parameterized by $(\alpha_n)^{-1}/u_n$ increases as the magnitude of the maximum applied strain decreases. Similar to that of IN100, plasticity is expected to be more heterogeneous as the maximum applied load drops further below the macroscopic yield stress. This increased heterogeneity increases the overall variability in the extreme value driving forces for fatigue crack formation.

The EVMCF for several different combinations of the apparent Schmid factor are plotted in Figures 7.19 and 7.20. The character of the EVMCF for the set of SVEs cycled at

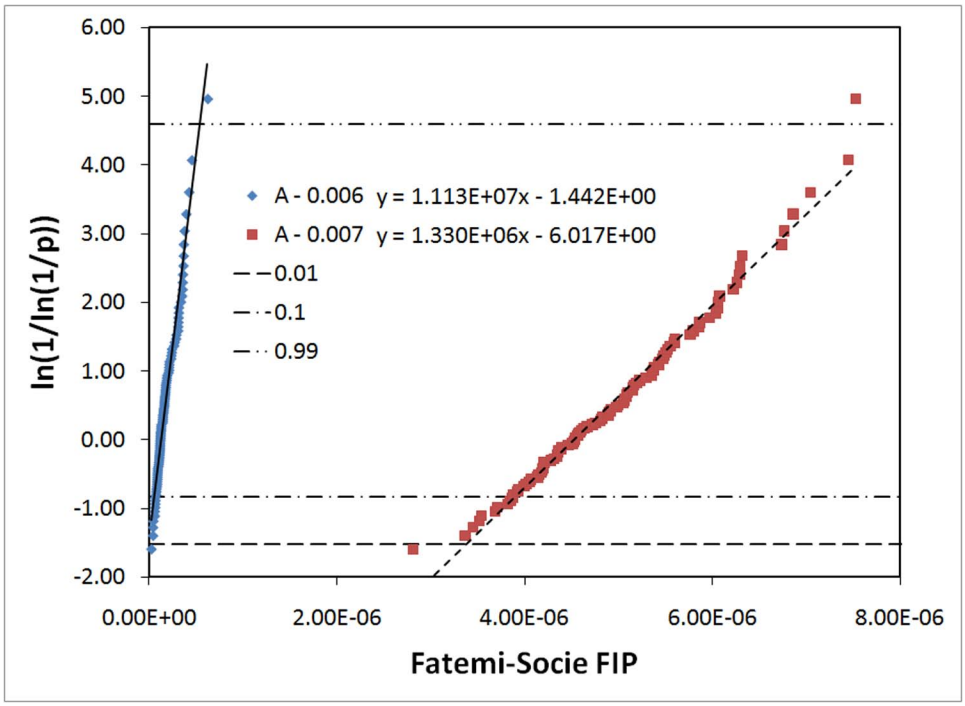

Figure 7.18: The extreme value Fatemi-Socie (FS) FIP calculated over a cube shaped averaging volume with equivalent grain size of 0.032mm for Microstructure A at two different magnitudes of maximum applied strain. Note that the equations given for the least squares linear regression are such that $y = \ln(1/\ln(1/p))$ and $x = FIP$ for the Gumbel probability plot and $x = \ln(FIP)$ for the Fréchet probability plot, respectively.

0.7% strain are very similar to the EVMCFs of the SVEs cycled at 0.6% strain as can be seen by comparing Figures 7.19 and 7.20 with Figures 7.13 and 7.14, respectively. However, there is a noted difference between the EVMCF for the apparent Schmid factor m_a^g for basal slip between 0.45 and 0.5 for the primary α phase and itself such that it was 15% more likely to find primary α grains oriented for easy basal slip for short correlation lengths at the extreme value location of the FIPs in the SVEs cycled at 0.7% strain than in the SVEs cycled at 0.6% strain (*i.e.*, 45% versus 30%). It is predicted by these simulations that at higher magnitudes of applied cyclic load, basal slip is more active at the locations of extreme value response than at lower magnitudes. At higher magnitudes of applied loading, plasticity is more homogeneous and more grains oriented for easy slip are expected to flow regardless of their neighborhood. At lower magnitudes of applied loading, the neighborhood of grains will be more important because stresses sufficient to induce flow will only exist at certain hard/soft combinations where compatibility requirements increase the local stresses sufficient for flow in the softer oriented grains. Therefore, the requirements for flow at lower loading magnitudes are more dependent on the neighborhood than on just whether a grain is oriented for easy slip. Thus, at higher loading magnitudes the extreme value response will be more correlated with clusters of primary α grains oriented for easy slip then at lower magnitudes where slip will be much more dependent on the entire neighborhood. In other words, the extreme value FIPs will be more correlated with grains oriented favorably for slip near other hard oriented grains than single grains or clusters of grains oriented for slip because the hard-soft combination are required to produce stresses sufficient for slip. Whereas this is not the case at higher magnitudes of applied loading.

7.3.4 Influence of grain size distribution on the extreme value distributions of the FIPs in Ti-6Al-4V

In Figure 7.8, it can be observed that the greatest differences between the distributions of the extreme value FIPs for the different microstructures tend to correlate with grain size. For example, Microstructures A and B with similar grain sizes but different volume

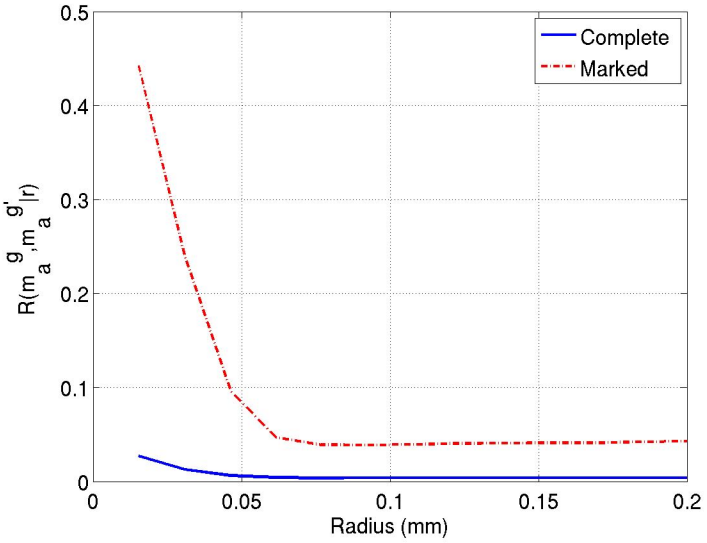

(a)

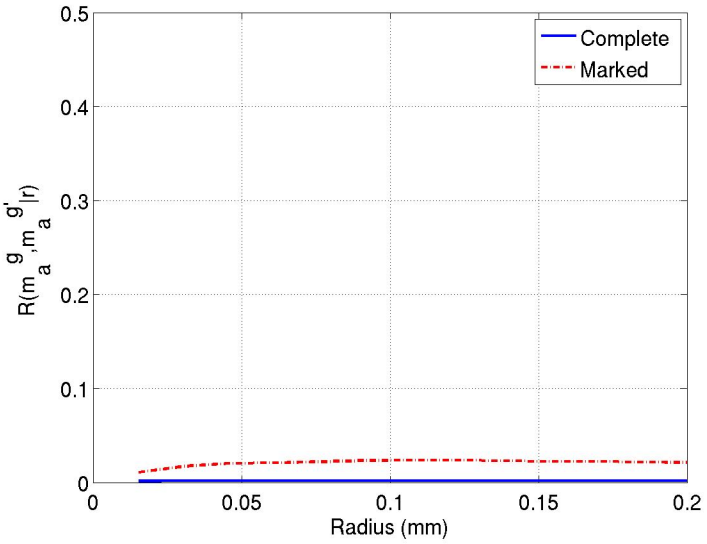

(b)

Figure 7.19: For the set of SVEs cycled at 0.7% strain, the radial correlation functions for the complete microstructure is compared with EVMCF describing the correlation between the apparent Schmid factor m_a^g for basal slip between 0.45 and 0.5 for the primary α phase and the Schmid factor $m_a^{g'}$ for: (a) basal slip between 0.45 and 0.5, (b) prismatic slip between 0.45 and 0.5, (c) pyramidal $\langle a \rangle$ slip between 0.45 and 0.5, and (d) pyramidal $\langle a + c \rangle$ slip between 0.45 and 0.5 for the primary α phase in Microstructure A.

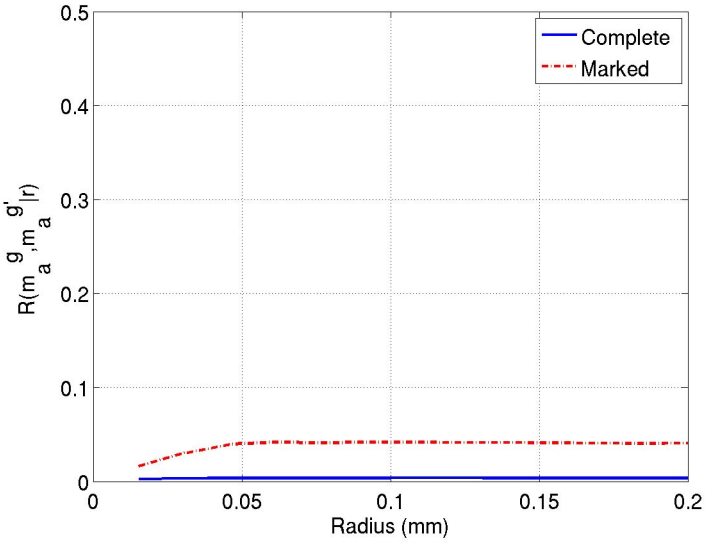

(c)

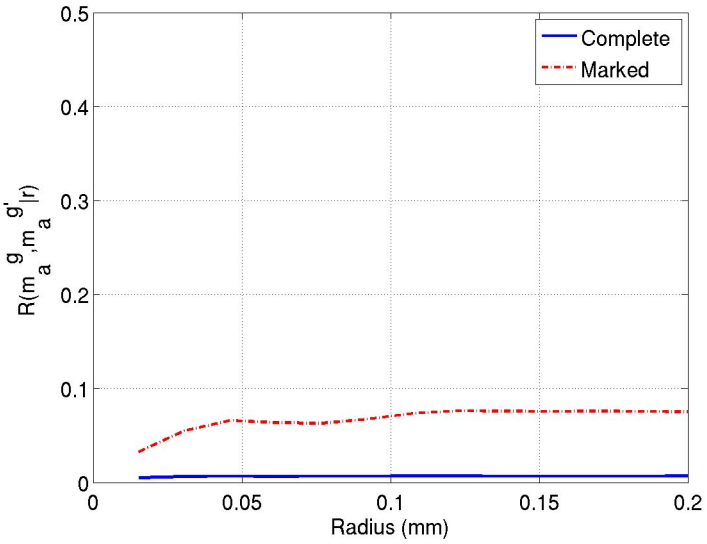

(d)

Figure 7.19: For the set of SVEs cycled at 0.7% strain, the radial correlation functions for the complete microstructure is compared with EVMCF describing the correlation between the apparent Schmid factor m_a^g for basal slip between 0.45 and 0.5 for the primary α phase and the Schmid factor $m_a^{g'}$ for: (a) basal slip between 0.45 and 0.5, (b) prismatic slip between 0.45 and 0.5, (c) pyramidal $\langle a \rangle$ slip between 0.45 and 0.5, and (d) pyramidal $\langle a + c \rangle$ slip between 0.45 and 0.5 for the primary α phase in Microstructure A.

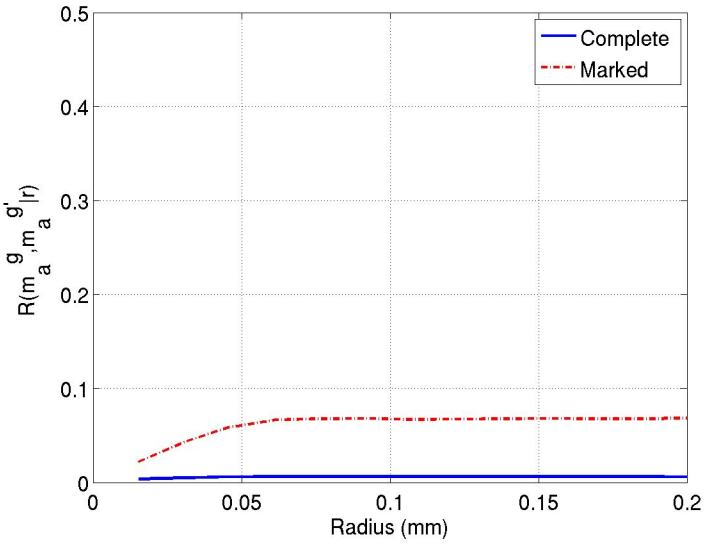

(a)

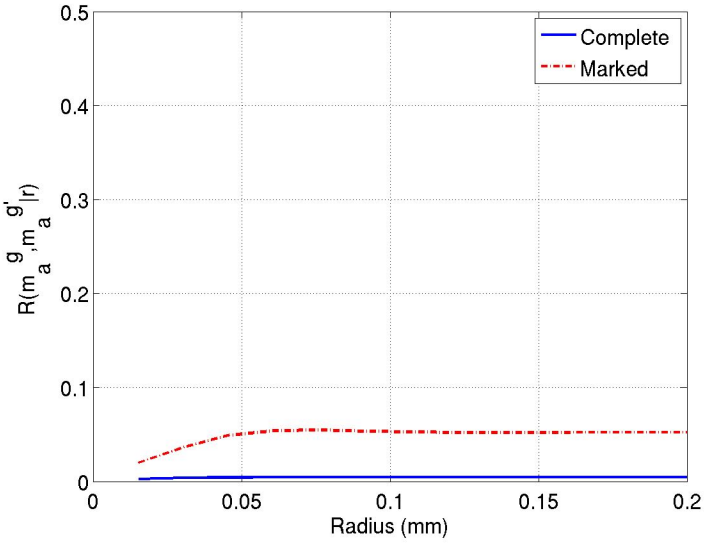

(b)

Figure 7.20: For the set of SVEs cycled at 0.7% strain, the radial correlation functions for the complete microstructure is compared with EVMCF describing the correlation between the apparent Schmid factor m_a^g for basal slip between 0.45 and 0.5 for the primary α phase and the apparent Schmid factor $m_a^{g'}$ for: (a) basal slip between 0.45 and 0.5, (b) prismatic slip between 0.45 and 0.5, (c) pyramidal $\langle a \rangle$ slip between 0.45 and 0.5, and (d) $\langle 111 \rangle \{110\}$ bcc slip (transformed into the hexagonal coordinate system via the BOR) between 0.45 and 0.5 for the $\alpha + \beta$ colony phase in Microstructure A.

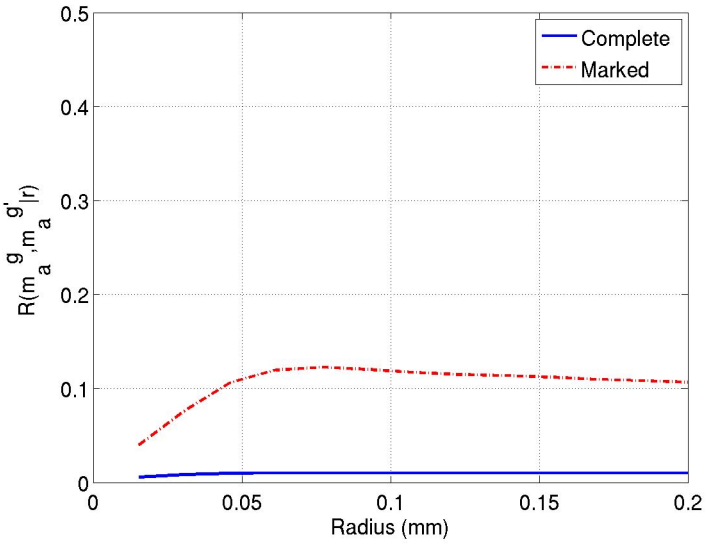

(c)

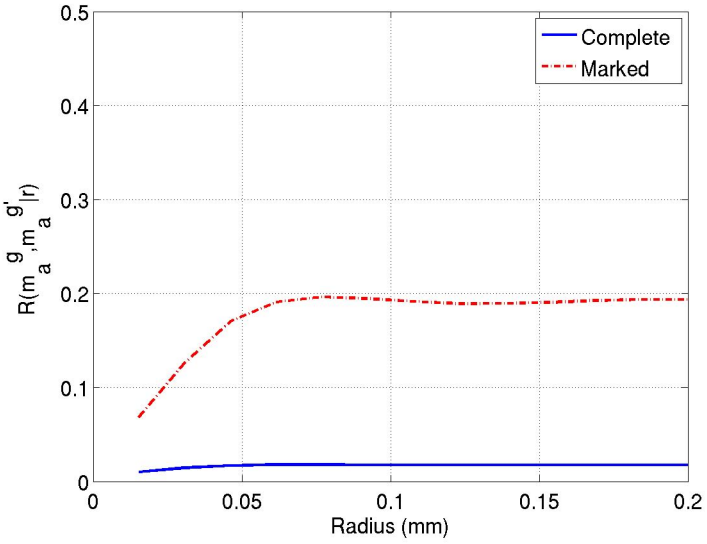

(d)

Figure 7.20: For the set of SVEs cycled at 0.7% strain, the radial correlation functions for the complete microstructure is compared with EVMCF describing the correlation between the apparent Schmid factor m_a^g for basal slip between 0.45 and 0.5 for the primary α phase and the apparent Schmid factor $m_a^{g'}$ for: (a) basal slip between 0.45 and 0.5, (b) prismatic slip between 0.45 and 0.5, (c) pyramidal $\langle a \rangle$ slip between 0.45 and 0.5, and (d) $\langle 111 \rangle \{110\}$ bcc slip (transformed into the hexagonal coordinate system via the BOR) between 0.45 and 0.5 for the $\alpha + \beta$ colony phase in Microstructure A.

fractions of the primary α grains exhibit very similar extreme value behavior. The same can be said of Microstructure C and D. To better understand how the distribution in grain size can affect the driving forces for fatigue crack formation, a set of microstructures with uniform cuboidal grains was constructed. This microstructure with a uniform grain size can then be compared to the previously instantiated microstructures with distributed grain size to quantify the influence of distributed grain size on the extreme value driving forces for fatigue damage formation as indicated by the FIPs.

The SVEs for these microstructures with cuboidal arrays of grains were dimensioned 0.400mm along each edge and cycled with a maximum applied strain of 0.6% with an applied strain rate of $0.002s^{-1}$. The ratio of the minimum to maximum applied strain was zero (*i.e.* R=0). The cuboidal SVE consists of eight cuboidal grains along each edge or 512 grains in all. Each grain was meshed with three brick elements (type C3D8R in ABAQUS [121]) along each edge or 27 elements in all. The volume then was meshed with 24 elements along each edge or 13824 elements in all. The orientation distribution of the lattice of the grains was set to random. A contour plot of the peak Mises stress after ten cycles for the microstructure with the cuboidal array of grains with 30% primary α is shown in Figure 7.21.

The extreme value distributions of the FS FIP for the microstructures with cuboidal grains is compared with the other microstructures in Figure 7.22(a) and 7.22(b) for 30% primary α and 70% primary α, respectively. In both cases, the microstructures with the uniform array of cuboidal grains exhibited distributions of the FS FIPs that were less in magnitude than the other microstructures. The microstructure with the smaller grain size exhibited the next highest magnitudes in the distributions of the extreme value FS FIPs. This demonstrates that grain size variability is predicted to increase the variability and magnitude of the extreme value driving forces for fatigue crack formation. In contrast, it is likely that microstructures with a more uniform grain size distribution will exhibit less scatter in the distributions of the extreme value FIPs. As larger grain sizes also appear to

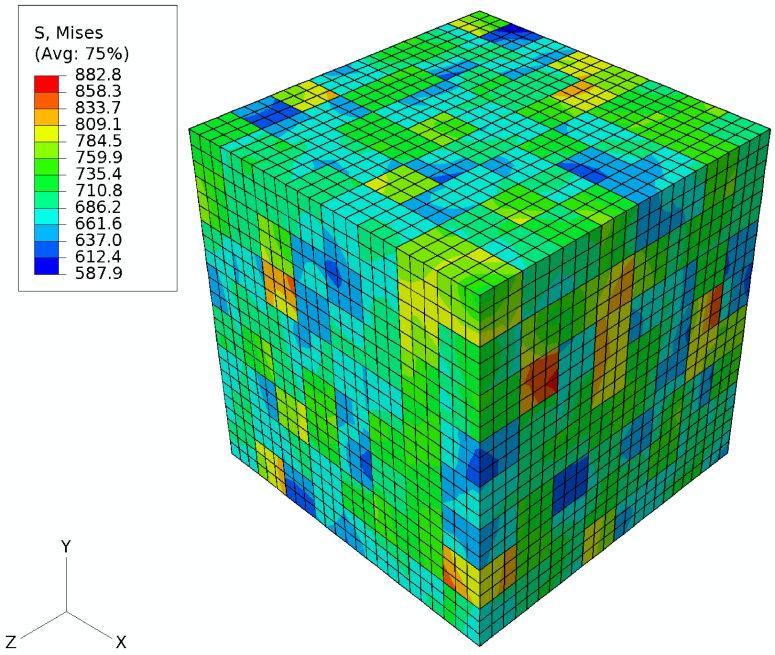

Figure 7.21: Meshed cuboidal SVE with an edge dimension of 0.400mm for the microstructure with an array of cuboidal grains with contours of the Mises stress at the peak strain of 0.6% after 10 cycles.

increase the magnitudes in the distribution of extreme value driving forces for fatigue crack formation, smaller grains are predicted to reduce the magnitudes of the extreme value FIPs.

7.3.5 Change in extreme value distributions of FIPs for surface versus subsurface fatigue crack formation

It is also of interest to consider the driving forces for surface versus subsurface fatigue crack formation. Recall previously that fully periodic boundary conditions were applied to simulated subsurface conditions. Here a set of 100 SVEs was instantiated for Microstructure A with periodic boundary conditions applied as previously described in the y and z directions (see Figure 7.5); however, no constraint was applied in the positive or negative x direction. These boundary conditions simulate a thin sheet with a high surface area to volume ratio where most grains are within a few average grain sizes of the free surface. These 100 SVEs with the free surface boundary conditions in the $\pm$ x-direction were cycled under uniaxial tension in the y-direction (in-plane direction of the thin sheet) with a maximum

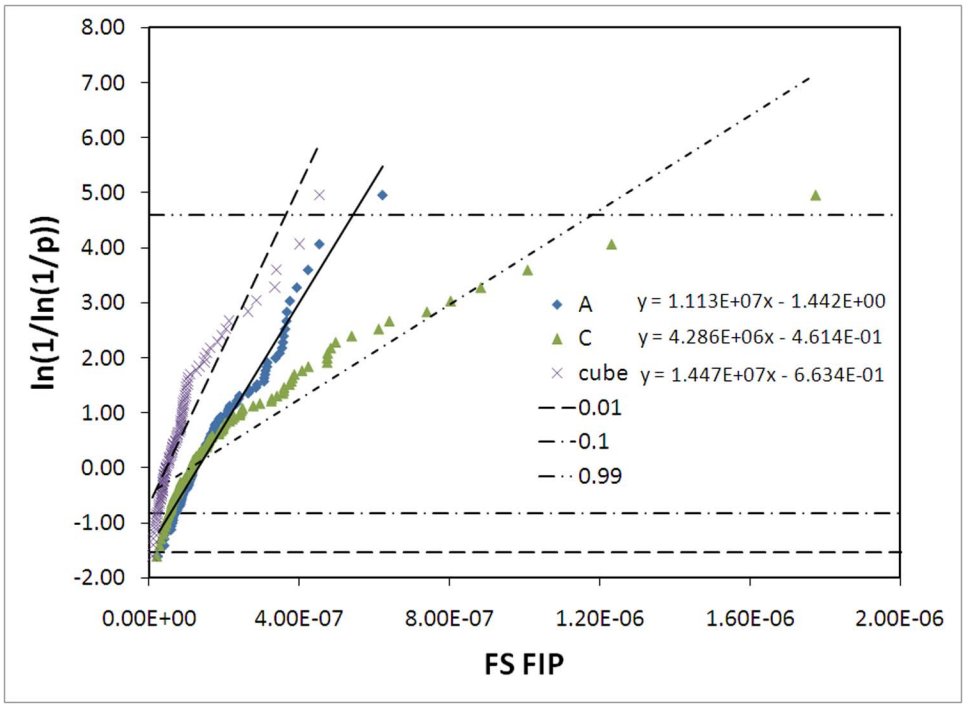

(c)

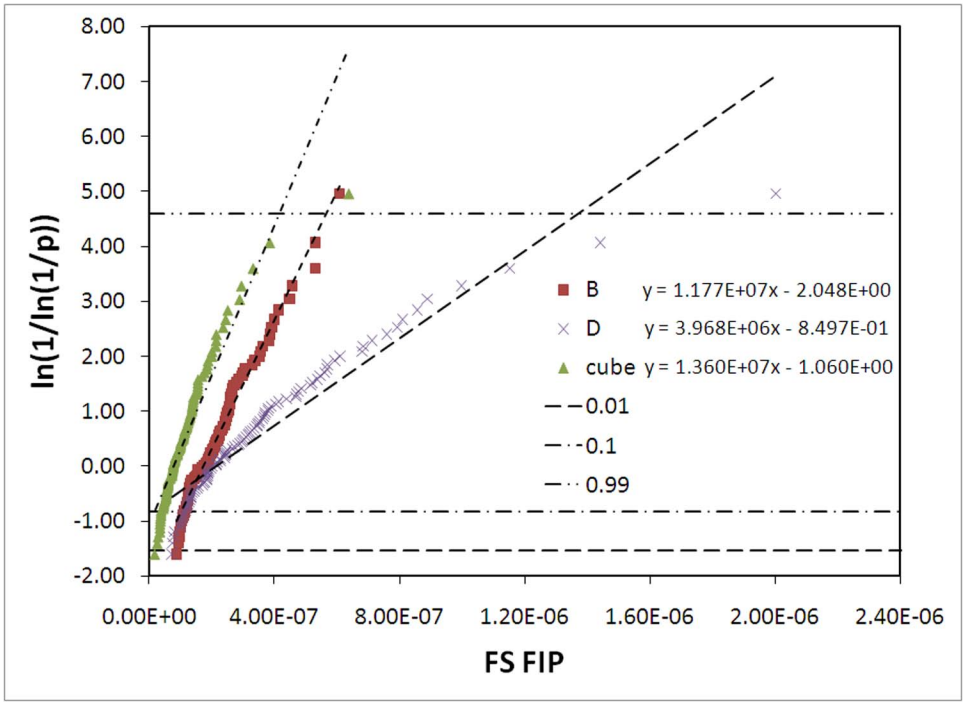

(d)

Figure 7.22: The extreme value distributions of the Fatemi-Socie (FS) FIP plotted on a Gumbel probability scale for Microstructures A and C and for the microstructure with uniform cuboidal grains for (a) 30% primary α and (b) 70% primary α. The FS FIPs were calculated over a cube shaped averaging volume with equivalent grain size of 0.032mm. Note that the equations given for the least squares linear regression are such that $y = \ln(1/\ln(1/p))$ and $x = FIP$.

applied strain of 0.6% applied at a quasi-static rate of $0.002s^{-1}$ at room temperature applied identically to that of the 100 SVEs with fully periodic boundary conditions. The ratio of the maximum to minimum strain was zero (*i.e.*, $R = 0$).

The extreme value distributions of the FS FIPs for the fully periodic simulations is compared to that of the SVEs with parallel free surfaces in Figure 7.23 for both the extreme value Gumbel probability scale and the Fréchet probability scale. The parameters of the fits for the extreme value distributions of the FS FIPs for the extreme value Gumbel distribution and the extreme value Fréchet distribution are given in Tables 7.9 and 7.10, respectively. It is apparent from Figure 7.23 and Tables 7.9 and 7.10, that while the SVEs with fully periodic boundary conditions are well fit by the extreme value Gumbel distribution (*i.e.*, $R^2 = 0.973$), the SVEs with parallel free surfaces are not (*i.e.*, $R^2 = 0.718$). In fact, the extreme value distributions of the FS FIPs for the SVEs with the free surface boundary conditions are much better described by the Fréchet distribution (*i.e.*, $R^2 = 0.989$).

As discussed in Section 3.2, the extreme value Gumbel distribution describes tails that decay exponentially. In contrast, the Fréchet distribution describes tails with polynomial decay. Exponential convergence is faster than that described by a polynomial; therefore, at 0.6% maximum strain, the driving forces are predicted to be higher at the most extreme maxima for the surface driving forces described by the extreme value Fréchet distribution than for subsurface fatigue crack formation described by the extreme value Gumbel distribution. In other words, shorter lives are predicted to be associated with surface crack formation in the high probability regime where the extreme value driving forces for fatigue crack formation are estimated to be higher in magnitude than for subsurface fatigue crack formation. Additionally, there is significant overlap between the two distributions, as can be seen in Figures 7.9 and 7.10, over a large range of the central portion of the extreme value distributions; therefore, there will be competition between surface and subsurface crack formation.

The demarcation between the higher driving forces for fatigue crack formation in the

Table 7.9: Fits of the extreme value Fatemi-Socie (FS) FIP distributions to the extreme value Gumbel (Type I) distribution for SVEs with fully periodic and with partially free boundary conditions. The FS FIPs were calculated over averaging volumes with the equivalent grain size of 0.0032mm (see Table 7.2). The relative dispersion is calculated by $(\alpha_n)^{-1}/u_n$.

BCs	α_n	u_n	**Rel. Disp.**	R^2
1,2,3-dir periodic	1.113×10^7	1.296×10^{-7}	0.69	0.973
1-dir free; 2,3-dir periodic	5.053×10^6	9.972×10^{-8}	1.98	0.718

Table 7.10: Fits of the extreme value Fatemi-Socie (FS) FIP distributions to the extreme value Fréchet (Type II) distribution for SVEs with fully periodic and with partially free boundary conditions. The FS FIPs were calculated over averaging volumes with the equivalent grain size of 0.0032mm (see Table 7.2).

BCs	k	v_n	R^2
1,2,3-dir periodic	1.95	1.130×10^{-7}	0.917
1-dir free; 2,3-dir periodic	1.96	1.256×10^{-7}	0.989

high probability regime for surface crack formation and relative lower driving forces for subsurface crack formation is driven by the free boundary conditions that allow greater slip at the surface than is possible subsurface because of the increased constraint that exists subsurface. In the high probability regime, at the surface there will always be a microstructural arrangement that is associated with greater driving forces for crack formation than any microstructural arrangements of attributes subsurface. However, at moderate to low cumulative probabilities of the distributions of the extreme value FIPs for surface and subsurface boundary conditions there is a significant probability that a more damaging microstructural arrangement can be found subsurface than exists at the surface for a given instantiated SVE. To determine what coupled microstructure attributes have the most influence on the driving forces for surface fatigue crack formation, it is of interest to now consider the EVMCFs for the 100 SVEs with applied free surface boundary conditions.

The EVMCF of the apparent Schmid factors for the different phases are shown for the 100 SVEs of Microstructure A simulated with parallel free surfaces in Figures 7.24 and 7.25. Additionally, the EVMCF between the Schmid factor m_a^s and the free surface s are

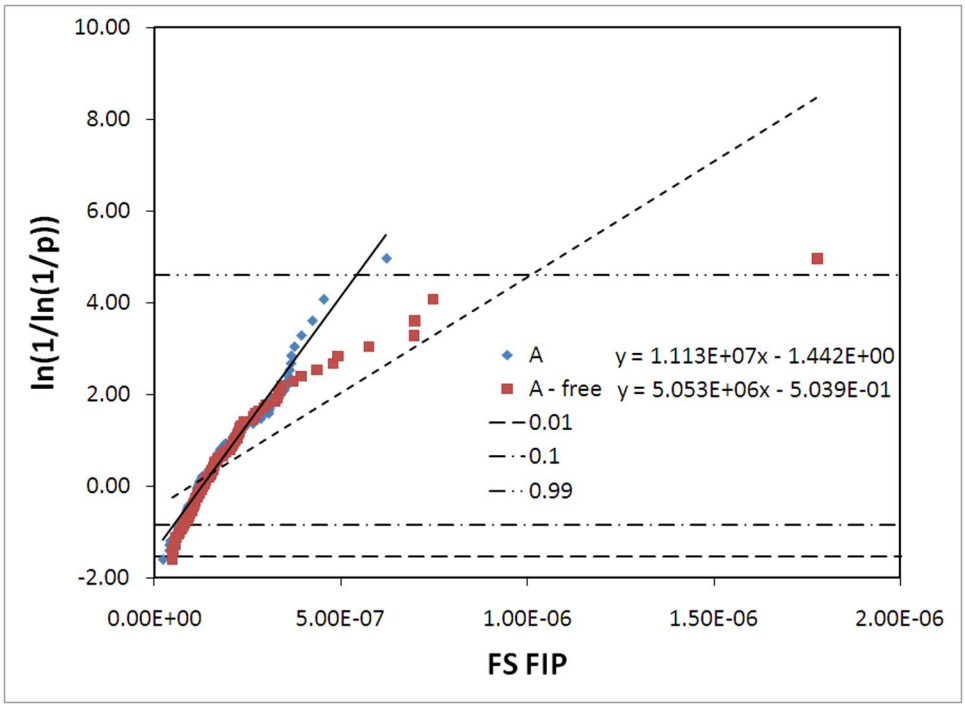

(a)

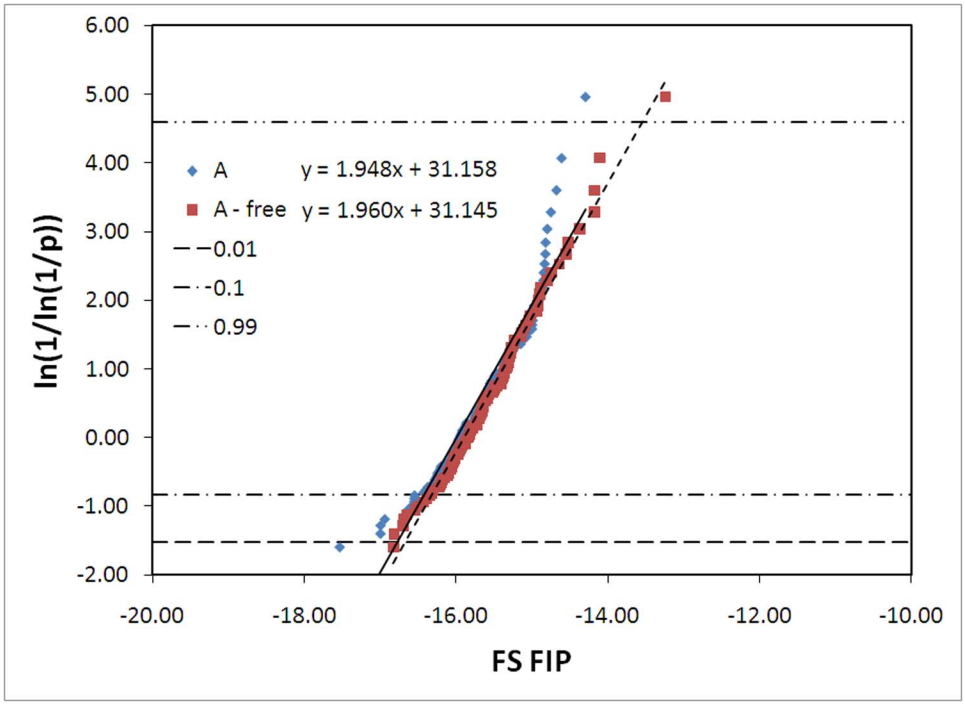

(b)

Figure 7.23: The extreme value Fatemi-Socie (FS) FIP calculated over a cube shaped averaging volume with equivalent grain size of 0.032mm for Microstructure A with periodic BCs and with free BCs plotted on (a) Gumbel (Type I), (b) Fréchet (Type II) probability scales. Note that the equations given for the least squares linear regression are such that $y = \ln(1/\ln(1/p))$ and $x = FIP$ for the Gumbel probability plot and $x = \ln(FIP)$ for the Fréchet probability plot, respectively.

plotted in Figures 7.26 and 7.27. This EVMCF defined between the apparent Schmid factor m_a^g and the free surface s is defined such that, $R_{\max(FIP)}\left(m_a^g, s|\Omega\right) dr$ is the probability that the extreme value FIP for a volume Ω is coincident with a grain whose Schmid factor is m_a^g and that the free surface s can be found within a distance of r to $r + dr$ in any direction. It is noted that these correlation functions are not sampled across the free surface. In essence, they are sampled with equal weight in all possible material directions up to the size of the initial SVE. In this manner they are not artificially biased by the periodic boundary conditions.

There are not any significant differences between the EVMCF for the SVEs with fully periodic boundary conditions and those with the parallel free surfaces as can be seen by comparing Figures 7.13 and 7.14 with Figures 7.24 and 7.25, respectively. In general, the hard soft-grain combinations are slightly less prevalent in the SVEs with the free surfaces than in the SVEs with the fully periodic boundary conditions (see Figures 7.13(c)-(d) and 7.14 versus Figures 7.24(c)-(d) and 7.25). However, when looking at the EVMCF in terms of how the apparent Schmid factors for the different phases are correlated with their proximity to the free surface at the locations of the extreme value FIPs, the only grains more likely to exist at the locations of the extreme value response near the free surface than in the overall microstructure are primary α grains oriented for easy basal or prismatic slip as can be seen in Figure 7.26(a)-(b). Thus, it is predicted that larger grains oriented for easy slip near the free surface have the most influence on the driving forces for fatigue crack formation at the surface. Higher order correlation functions (*e.g.* 3-point correlation functions) need to be applied in future work to determine how/if coupling between grains near the free surface further influence the driving forces for surface fatigue crack formation.

7.4 Summary

The present study illustrates how the introduced microstructure-sensitive extreme value probabilistic framework for damage evolution processes can be applied to evaluate the

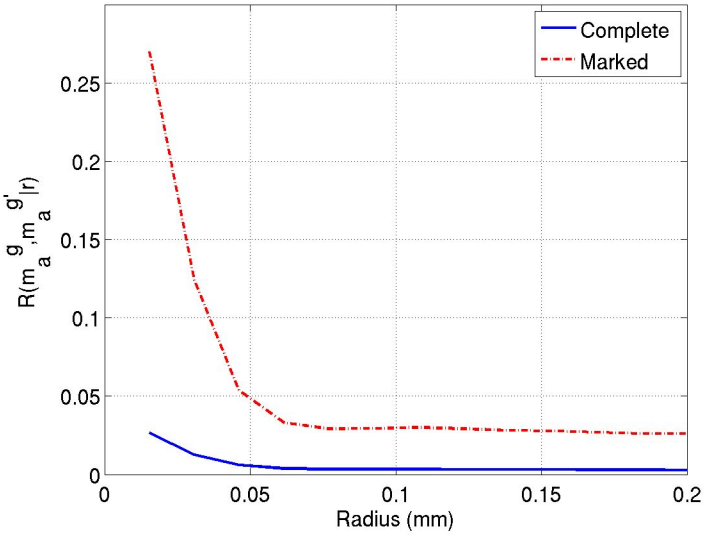

(a)

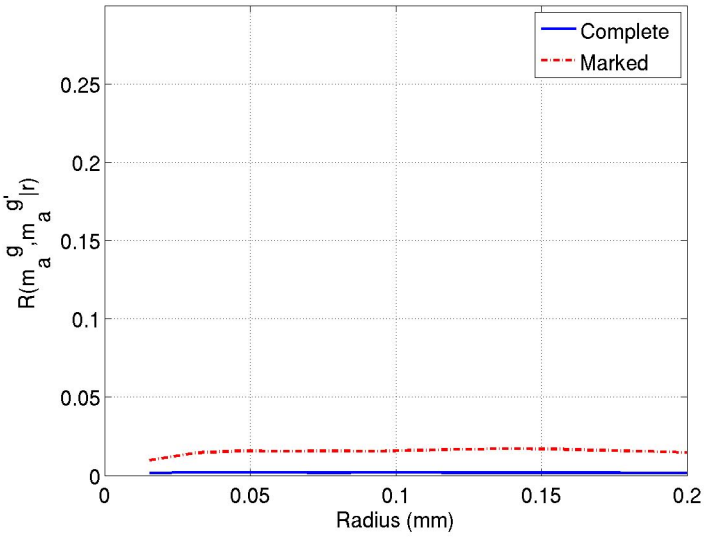

(b)

Figure 7.24: Radial correlation functions for the complete microstructure compared with EVMCF describing the correlation between the apparent Schmid factor m_a^g for basal slip between 0.45 and 0.5 for the primary α phase and the Schmid factor $m_a^{g'}$ for: (a) basal slip between 0.45 and 0.5, (b) prismatic slip between 0.45 and 0.5, (c) pyramidal $\langle a \rangle$ slip between 0.45 and 0.5, and (d) pyramidal $\langle a + c \rangle$ slip between 0.45 and 0.5 for the primary α phase in Microstructure A with free surface BCs.

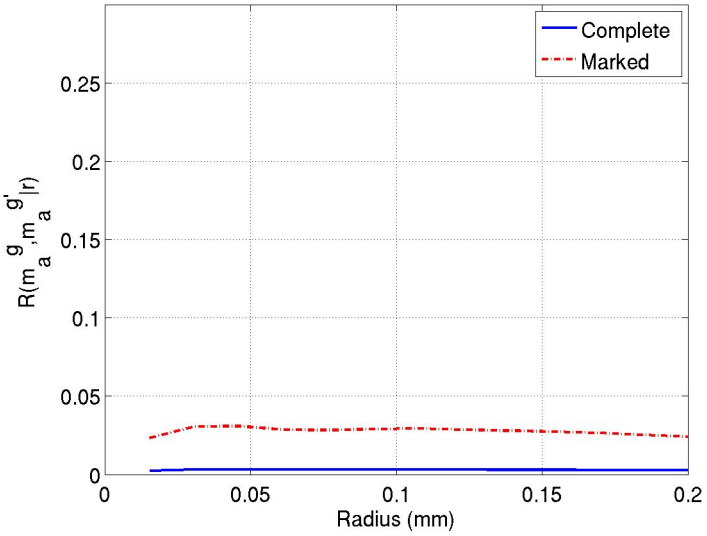

(c)

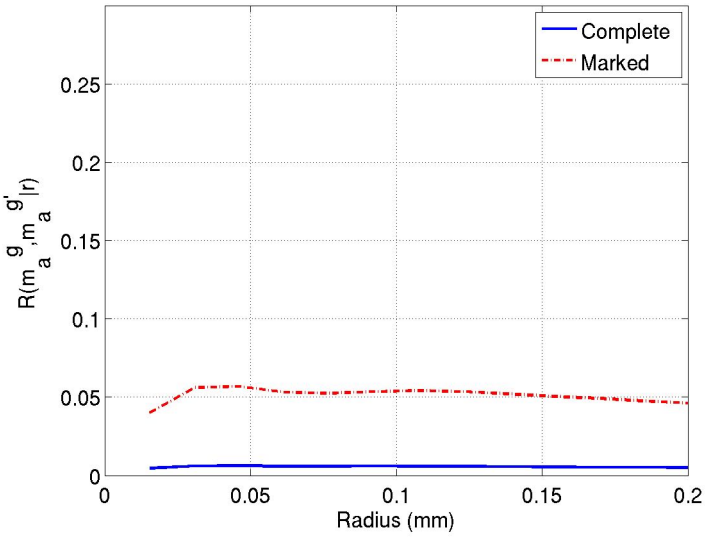

(d)

Figure 7.24: Radial correlation functions for the complete microstructure compared with EVMCF describing the correlation between the apparent Schmid factor m_a^g for basal slip between 0.45 and 0.5 for the primary α phase and the Schmid factor $m_a^{g'}$ for: (a) basal slip between 0.45 and 0.5, (b) prismatic slip between 0.45 and 0.5, (c) pyramidal $\langle a \rangle$ slip between 0.45 and 0.5, and (d) pyramidal $\langle a + c \rangle$ slip between 0.45 and 0.5 for the primary α phase in Microstructure A with free surface BCs.

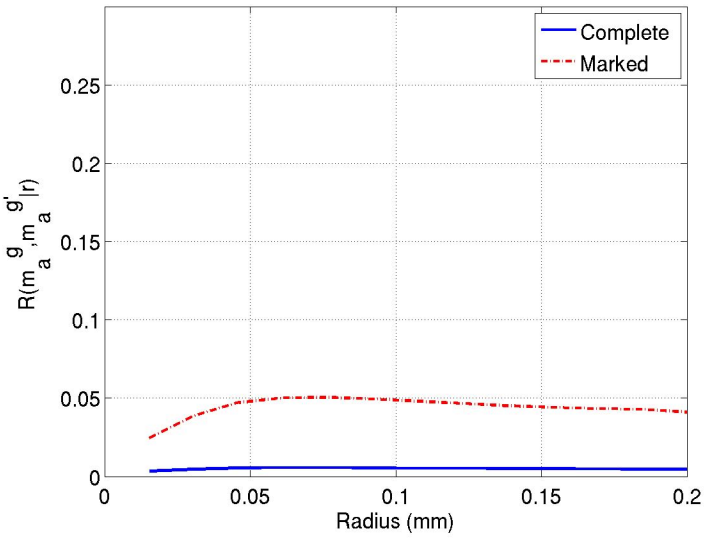

(a)

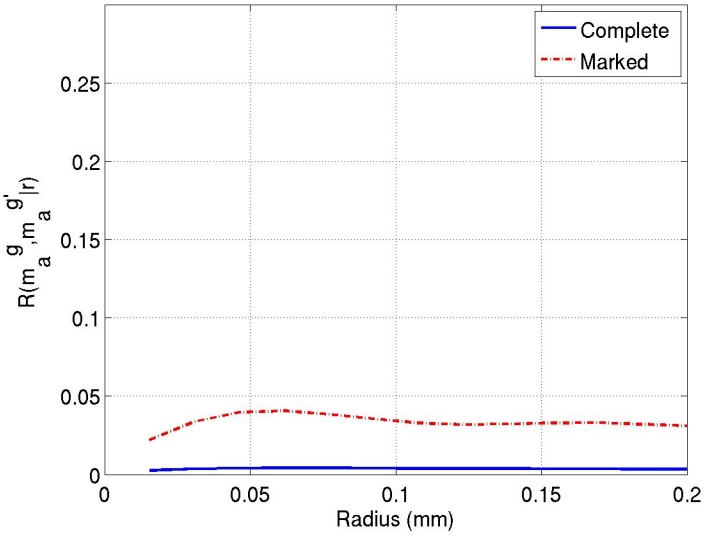

(b)

Figure 7.25: The radial correlation functions for the complete microstructure compared with EVMCF describing the correlation between the apparent Schmid factor m_a^g for basal slip between 0.45 and 0.5 for the primary α phase and the apparent Schmid factor $m_a^{g'}$ for: (a) basal slip between 0.45 and 0.5, (b) prismatic slip between 0.45 and 0.5, (c) pyramidal $\langle a \rangle$ slip between 0.45 and 0.5, and (d) $\langle 111 \rangle \{110\}$ bcc slip (transformed into the hexagonal coordinate system via the BOR) between 0.45 and 0.5 for the $\alpha + \beta$ colony phase in Microstructure A with free surface BCs.

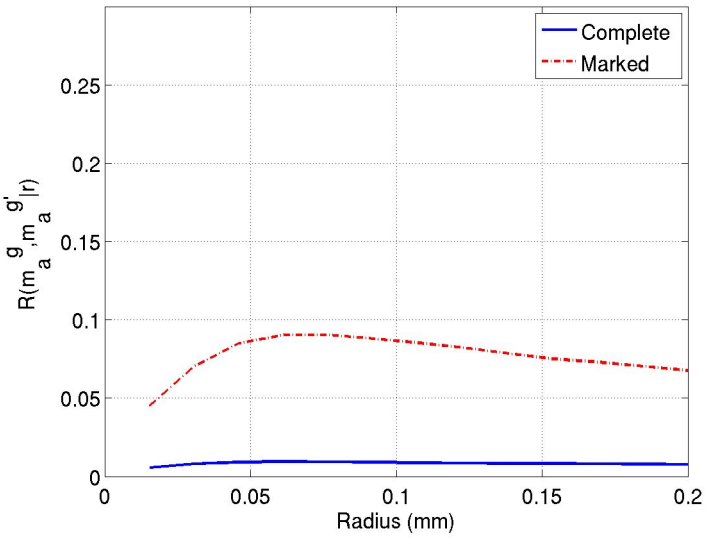

(c)

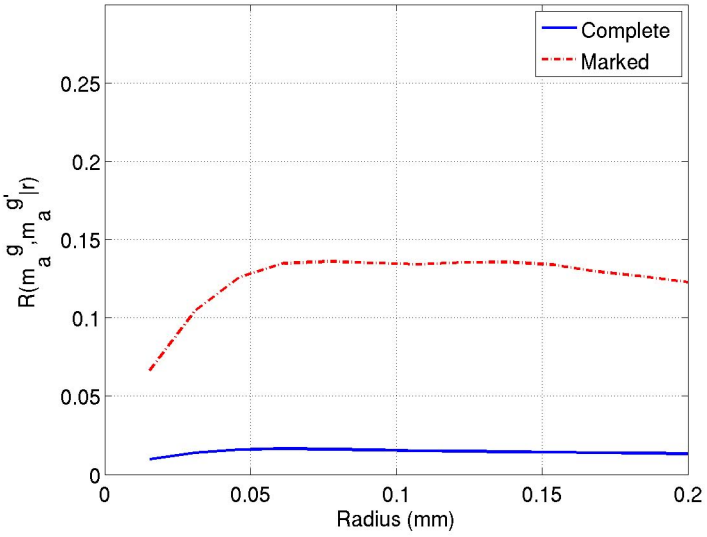

(d)

Figure 7.25: The radial correlation functions for the complete microstructure compared with EVMCF describing the correlation between the apparent Schmid factor m_a^g for basal slip between 0.45 and 0.5 for the primary α phase and the apparent Schmid factor $m_a^{g'}$ for: (a) basal slip between 0.45 and 0.5, (b) prismatic slip between 0.45 and 0.5, (c) pyramidal $\langle a \rangle$ slip between 0.45 and 0.5, and (d) $\langle 111 \rangle \{110\}$ bcc slip (transformed into the hexagonal coordinate system via the BOR) between 0.45 and 0.5 for the $\alpha + \beta$ colony phase in Microstructure A with free surface BCs.

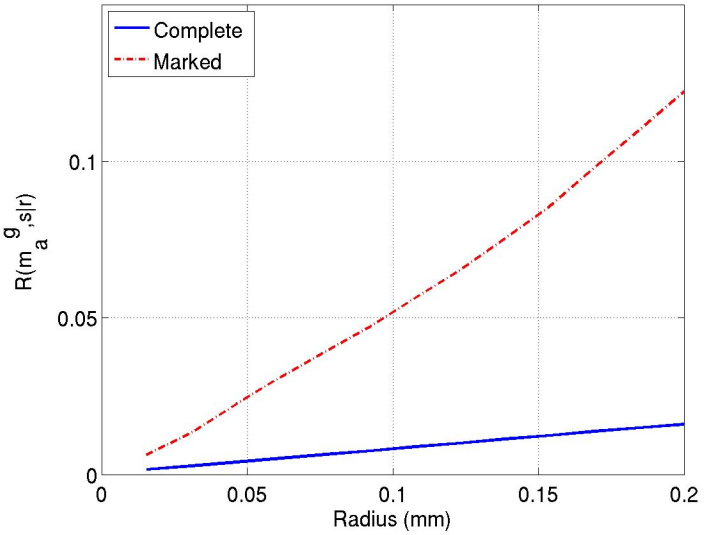

(a)

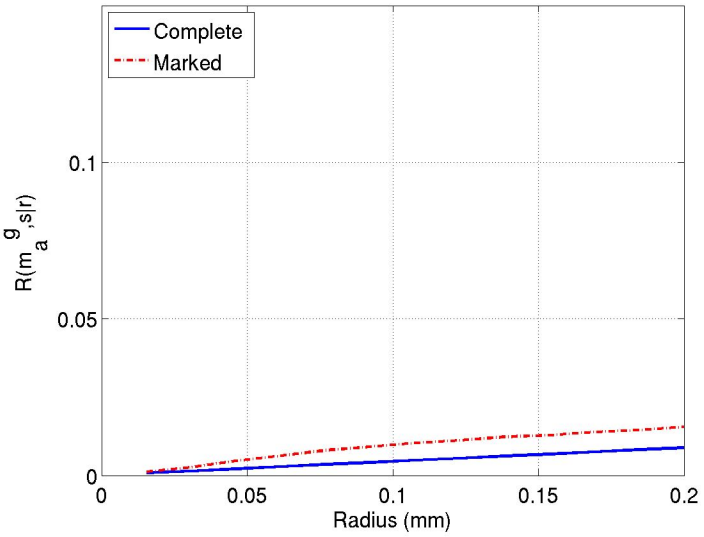

(b)

Figure 7.26: Radial correlation functions for the complete microstructure compared with EVMCF describing the correlation between the apparent Schmid factor m_a^g for (a) basal slip between 0.45 and 0.5, (b) prismatic slip between 0.45 and 0.5, (c) pyramidal $\langle a \rangle$ slip between 0.45 and 0.5, and (d) pyramidal $\langle a + c \rangle$ slip between 0.45 and 0.5 for the primary α phase and the free surface s in Microstructure A with free surface BCs.

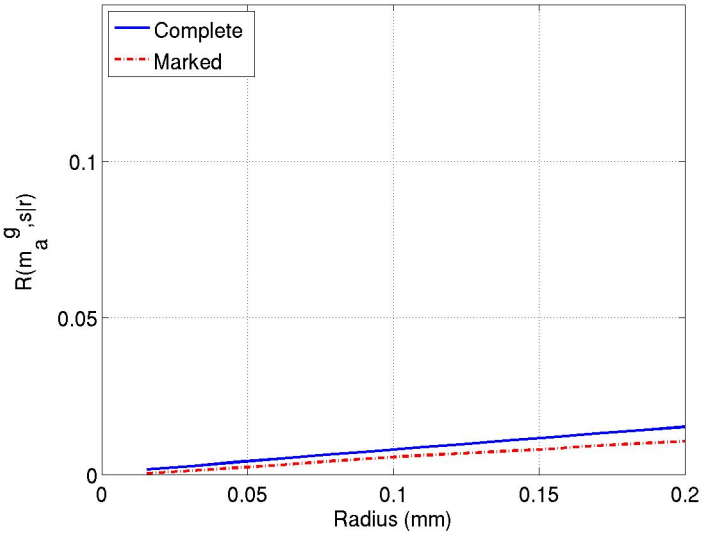

(c)

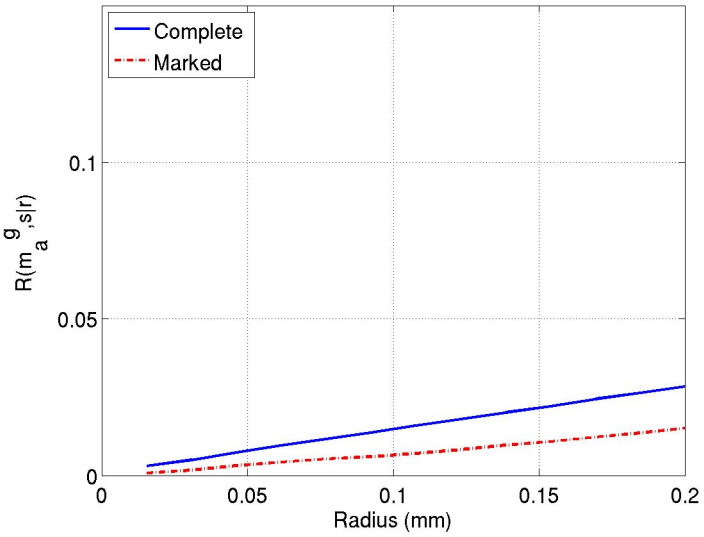

(d)

Figure 7.26: Radial correlation functions for the complete microstructure compared with EVMCF describing the correlation between the apparent Schmid factor m_a^g for (a) basal slip between 0.45 and 0.5, (b) prismatic slip between 0.45 and 0.5, (c) pyramidal $\langle a \rangle$ slip between 0.45 and 0.5, and (d) pyramidal $\langle a + c \rangle$ slip between 0.45 and 0.5 for the primary α phase and the free surface s in Microstructure A with free surface BCs.

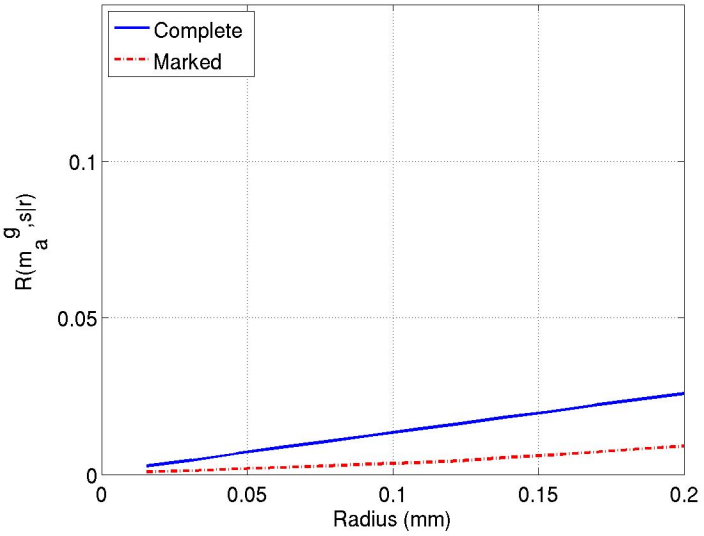

(a)

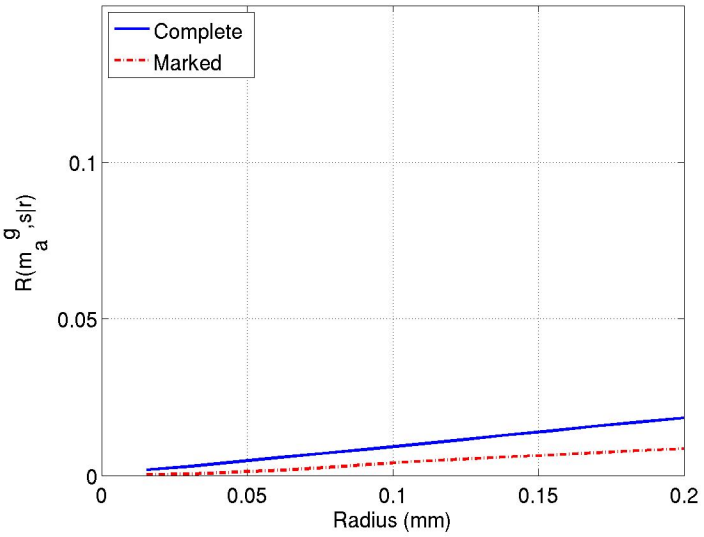

(b)

Figure 7.27: The radial correlation functions for the complete microstructure compared with EVMCF describing the correlation between the apparent Schmid factor m_a^g for (a) basal slip between 0.45 and 0.5, (b) prismatic slip between 0.45 and 0.5, (c) pyramidal $\langle a \rangle$ slip between 0.45 and 0.5, and (d) $\langle 111 \rangle \{110\}$ bcc slip (transformed into the hexagonal coordinate system via the BOR) between 0.45 and 0.5 for the $\alpha + \beta$ colony phase and the free surface s in Microstructure A with free surface BCs.

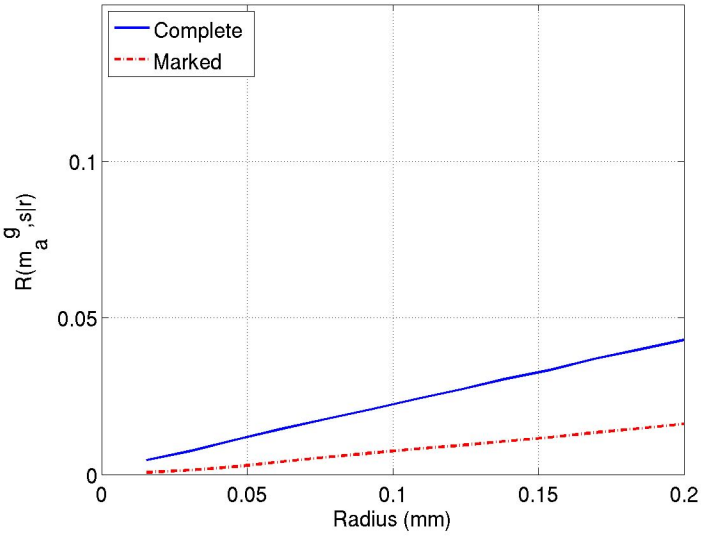

(c)

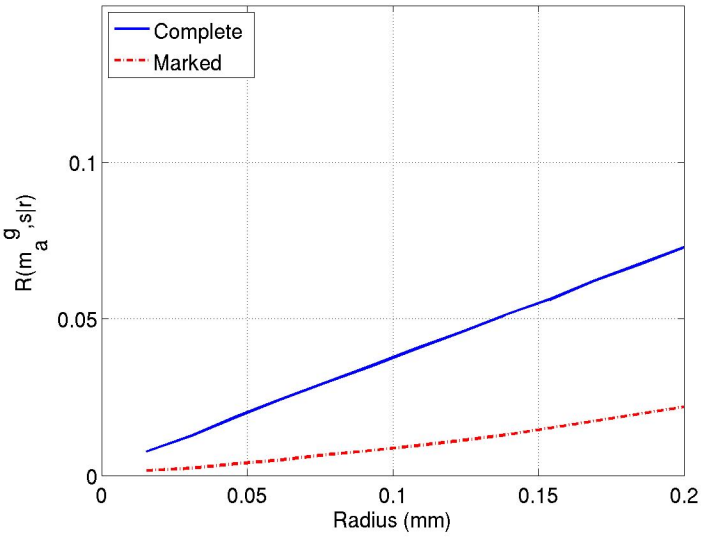

(d)

Figure 7.27: The radial correlation functions for the complete microstructure compared with EVMCF describing the correlation between the apparent Schmid factor m_a^g for (a) basal slip between 0.45 and 0.5, (b) prismatic slip between 0.45 and 0.5, (c) pyramidal $\langle a \rangle$ slip between 0.45 and 0.5, and (d) $\langle 111 \rangle \{110\}$ bcc slip (transformed into the hexagonal coordinate system via the BOR) between 0.45 and 0.5 for the $\alpha + \beta$ colony phase and the free surface s in Microstructure A with free surface BCs.

processes of fatigue crack formation in a complex alloy system. Certain limitations are recognized in terms of applicability to specific $\alpha + \beta$ Ti alloys. In all cases the instantiated SVEs in this study were fit to specific grain size, orientation and disorientation distributions that could be very different from certain material systems examined experimentally. For example, the grain orientation and grain disorientation distributions were assumed to be random; however, this is not very likely in a real material system. Both a random ODF and DDFs were chosen in this study to facilitate sampling of as many different arrangements of grains as possible to better identify the most important correlated attributes related to the processes of fatigue crack formation. In textured $\alpha + \beta$ Ti alloys, some of the arrangements identified here exist with little or no probability. Textured duplex Ti-6Al-4V will be considered in Chapter 8 in the context of computational materials design.

In this chapter, multiple SVEs for each of the four different microstructure were instantiated for duplex Ti-6Al-4V, with varying grain sizes and volume fractions of the primary α grains. It was shown that the grain size appears to be the most important attribute considered relative to the driving forces for fatigue damage formation as estimated by the distributions of the volume averaged extreme value FIPs. Although the volume fraction of primary α grains did influence the extreme value distributions, its influence was less than that of grain size. The EVMCFs demonstrated that grains oriented with high Schmid factors for basal or prismatic slip are most likely to exist coincident with the extreme value response. Additionally the grains oriented for easy slip are predicted with high probability to be near other hard oriented primary α or $\alpha + \beta$ colony grains with high Schmid factors for pyramidal or bcc BOR modified slip, respectively.

When the peak load was increased from 0.6% maximum applied strain to 0.7% maximum applied strain the relative variability was higher for the distribution of FIPs at 0.6% then at 0.7% strain. This was expected as plasticity is more heterogeneously distributed as the maximum load drops further below the macroscopic yield point. The EVMCF did not change significantly between 0.6% maximum applied strain and 0.7% maximum applied

strain; however, there was a noted increase in the probability of finding a grain oriented for easy basal slip coincident with the extreme value response. As the overall loading magnitude increased, it is expected that the easy slip modes will be even more active then they are at lower maximum applied loads where slip is more dictated by the neighborhood.

A set of microstructures with uniformly distributed cuboidal grains was instantiated and compared to the microstructures with distributed grain size. The cuboidal arrays of grains with no variability in the grain size exhibited the least scatter in the overall driving forces for fatigue crack formation. The microstructure with an average primary α grain size of 0.025mm exhibited the next highest scatter of the FIPs followed by the microstructures with an average primary α grain size of 0.050mm. Because most significant plasticity was observed to occur in the primary α grains, the size of the $\alpha+\beta$ colonies is expected to have less influence on the FIPs than than size of the primary α grains. Based on these results it is predicted that microstructures with tighter distributions of grain size will exhibit less variability. Additionally, microstructures with smaller primary α grain sizes are predicted to exhibit lower overall driving forces for fatigue crack formation.

The driving forces for surface fatigue crack formation were compared to those of subsurface fatigue crack formation by simulating 100 SVEs with free boundary conditions on two opposite parallel faces. This is in contrast to all the previously simulated microstructures with periodic boundary conditions on all sides of the cuboidal SVEs. While the distributions in the driving forces for subsurface fatigue crack formation are best characterized by the extreme value Gumbel distribution, the driving forces for surface fatigue crack formation are best characterized by the extreme value Fréchet distribution. As mentioned previously, the extreme value Gumbel distribution describes exponential convergence of the tails of the distribution; the Fréchet distribution describes polynomial tails. As the exponential convergence is faster than polynomial convergence, the extreme maxima of the Fréchet distribution tend to be higher in magnitude than the extreme maxima of the Gumbel distribution. Therefore the driving forces for fatigue crack formation have the potential

to be highest at the surface; however, there is a large range of the extreme value distributions of the FIPs for both surface and subsurface fatigue crack formation that overlap. This explains why there are competing modes of failure in the HCF to VHCF regime between surface and subsurface fatigue crack formation. Additionally, when the driving forces for fatigue crack formation are highest at the surface (*i.e.* when the extreme value response at the surface is associated with the extreme maxima of the extreme value distribution of the FIPs), the overall fatigue lives are predicted to be shorter than when fatigue crack form subsurface where the extreme maxima of the extreme value distributions of the FIPs are of a lower magnitude.

CHAPTER VIII

APPLICATION TO MATERIALS SELECTION

8.1 Introduction

Recently there has been increased emphasis on the role of modeling and simulation in materials design. For example, the National Materials Advisory Board from the National Academies in 2008 advocated for an increased emphasis on Integrated Computational Materials Engineering (ICME) in order to accelerate innovation in the engineering of materials and manufacturing of components [245]. In their published report, the National Materials Board repeatedly emphasized the need for better models and modeling strategies that would allow for better informed design and/or selection of materials. ICME is in contrast to traditional (primarily experimentally driven) empirical materials development which primarily flows from the bottom-up with limited feedback or flexibility from the top (*i.e.*, application). In the framework of ICME, McDowell and Olson [246] have distinguished between a bottom-up approach based on cause and effect, deductive, sequential linkages and the top-down, goals/means, inductive systems engineering approach. Although traditional empirical materials development has historically been driven by the bottom-up approach, they emphasize that simulations based approaches can be incorporated to provide bottom-up feedback to top-down requirements determined by application. Thus, a hierarchical approach is needed that links material models at multiple length and time scales to address the requirements of the specific applications. McDowell [247] recognized the role computational simulation can play in materials design when he stated: "A realistic goal of simulation-assisted, systems-based materials design is to enhance the fraction of design decisions that are supported by simulations." The tools developed in this dissertation offer support to ICME in this context. Specifically, it will be demonstrated that the

microstructure-sensitive extreme value probabilistic framework to evaluate material performance/variability for damage evolution processes that will be outlined in its entirety in this chapter can inform the selection of materials that are more resistant to damage evolution processes like fatigue through computational simulation. It is beyond the scope of this dissertation to consider the developed framework in the context of ICME beyond the application given here; although, there is much that remains to be considered in the application of these types of computational frameworks in ICME.

To this point, the various components of the microstructure-sensitive extreme value probabilistic framework to evaluate material performance/variability for damage evolution processes (*e.g.*, fatigue, fracture, creep) have been introduced and demonstrated, primarily for the processes of fatigue crack formation in the HCF regime. In Chapter 3, the EVMCF was introduced as a means to quantify correlation between multiple interacting microstructure attributes and the extreme value response. In Chapters 4, crystal plasticity models were reviewed as a class of models that can be used to simulate local plastic response on the scale of the grains in polycrystalline metals. These types of models are able to estimate the driving forces for fatigue crack formation in metallic materials where crack nucleation and microstructurally small crack growth is mostly associated with localize plasticity at various microstructural barriers such as grain or phase boundaries (the mechanisms of fatigue crack formation in metals were summarized in Chapter 2). Chapter 5 discussed two methods that have been presented in the literature as a means to instantiate SVEs for polycrystalline materials based on experimentally characterized materials. Particularly, it was considered how to appropriately define a SVE for the heterogeneous plastic response important to fatigue variability in polycrystalline metals. Also, FEA of these instantiated SVEs was addressed including the aspects of meshing and defining appropriate boundary conditions. In Chapters 6 and 7, the strategy of simulating multiple instantiated SVEs to estimate the distribution in the extreme value driving forces for fatigue crack formation via certain FIPs was demonstrated for the P/M Ni-base superalloy IN100 and the duplex

Ti alloy Ti-6Al-4V, respectively. Additionally, the EVMCFs were applied to characterize significant coupling between crystallographic orientation and phase that are important to the extreme value response. In this chapter, Chapter 8, the microstructure-sensitive extreme value framework to evaluate material performance/variability for damage dependent processes is summarized in its entirely and demonstrated in the context of computational materials selection. Specifically, the effect of texture on the distributions of the extreme value driving forces for fatigue damage formation in the four previously introduced microstructural variants of duplex Ti-6Al-4V will be considered.

8.2 Microstructure-sensitive extreme value probabilistic framework for selection of materials with improved damage resistance

The microstructure-sensitive extreme value probabilistic framework for materials selection for improved performance/resistance for damage evolution processes is outlined schematically in Figure 8.1. This framework is carried out is six primary steps, *i.e.*,

1. Instantiate a set of SVEs such that the response of interest in each SVE is a statistical sample of the response for the microstructure ensemble. These volumes can be instantiated by fitting distributions of microstructure attributes important to the response to those from experimentally characterized microstructures (see Chapter 5). Additionally, contrived target distributions of the materials attributes can be used for iterative materials design/selection. Determination of the appropriate size of these SVEs was discussed previously in Section 5.2.

2. The response for given loading and boundary conditions are estimated via computational simulation (see Chapters 4 and 5). To estimate microstructure-sensitive extreme value response, phenomenological and/or physics based models are required that account for the influence of the microstructure on the overall response (*e.g.*, crystal plasticity models for grain scale cyclic plastic response). It is essential that these microstructure-sensitive models be experimentally calibrated or that the results be

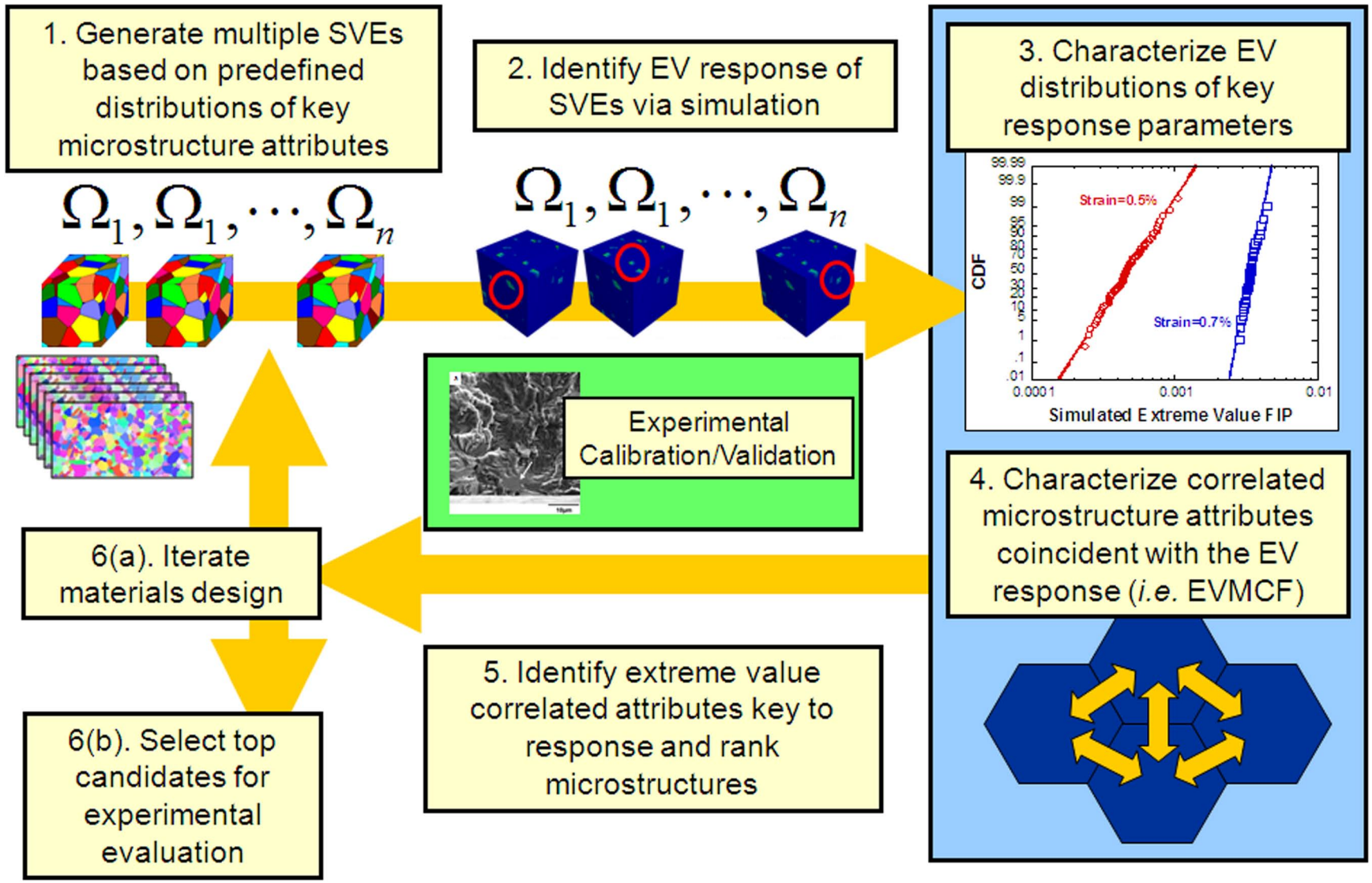

Figure 8.1: Schematic of the microstructure-sensitive extreme value probabilistic framework for materials selection of materials for improved performance/variability for damage evolution processes.

validated with experiments.

3. The extreme value distribution of response of interest can be characterized for the set of simulated SVEs. It is desired to determine if the extreme value distribution of response can be described by any of the three known extreme value distributions so the mathematical properties of those known distributions can be used to describe the data (see Chapter 3).

4. The EVMCF is characterized for the microstructure attributes that have the most influence on the extreme value response (see Chapter 3). In this manner, the driving forces for damage formation are statistically characterized in terms of the coupled microstructure attributes that have the most influence the extreme value response.

5. Based on the extreme value distributions of response, multiple microstructural variants for the same material system can be ranked in terms of their maximum minimum response or for minimum variability (see Chapter 7).

6. Based on the distribution of coupled microstructure attributes as characterized by the EVMCF, new microstructure variants can be proposed and then evaluated for performance by iteration through the previously presented steps. Additionally, the best candidate microstructures for a given application can be selected and then validated experimentally. Computational down selection of possible microstructural variants can be very beneficial both economically and in terms of overall development time.

In this manner, one can evaluate the effect of material microstructure on extreme value response, identify coupled attributes important to the extreme value response, and evaluate new microstructural variants that could potentially exhibit better performance for a given application. To this point in the dissertation, all the steps in this framework have been demonstrated except iteration on a candidate microstructure (see Step 6). In particular, in Chapter 6 the Steps 1 through 4 for the were demonstrated for the Ni-base superalloy

IN100. In Chapter 7, Steps 1 through 5 were demonstrated for several microstructural variants of duplex $\alpha + \beta$ Ti-6Al-4V. To demonstrate how this framework can be iterated to evaluated newly derived microstructures based on the conclusions of previous iterations, in the following section, Section 8.3, several textured microstructures for duplex Ti-6Al-4V are proposed that are hypothesized to be more resistant to subsurface fatigue crack formation than the random variants studied in Chapter 7.

8.2.1 Limitations of the framework

It is important to point out the limitations of the proposed framework. This framework was developed to evaluate materials for their microstructure-sensitive performance/variability with respect to damage evolution processes. Additionally, application of the framework can provide understanding that could be used to design microstructures to achieve the desired performance for a specific damage evolution process. Better informed materials selection is possible via this framework because of the new capability of being able to quantify the coupling of microstructure attributes that are the most significant to the extreme value response. As presented here, this approach is model-based. Experimental calibration/-validation of the computational model is essential. Model calibration can be added as a sub-step to the design loop to ensure that modifications in the developed microstructures are properly accounted for in the models. Additionally, regardless of the results that come from any application of this framework to a material system, the most promising material variants should be tested/evaluated experimentally. Accordingly, in Chapters 6 and 7 the results for IN100 and Ti-6Al-4V were evaluated in the context of previous experiments.

Even with calibration, specific models limit the possible results of the computational simulations. For example, the crystal plasticity models used in this work which were described in Chapter 4 do not consider grain boundary interactions beyond the requirement of compatibility throughout the imposed deformation. As the processes of dislocation transmission and/or blockage across grain boundaries can play an important role in the processes

of fatigue damage formation across multiple grains, than using models that neglect dislocation transmission across grain boundaries can neglect the true operant damage mechanisms on the scale larger than a single grain.

In addition to being limited by the requirement of experimental validation, microstructure-sensitive model can be computationally intensive. Some of the obstacles to computational simulation have been overcome with the advent of faster computers. However, much work remains in developing models and modeling strategies that are more computationally efficient. The proposed strategy of simulating multiple SVEs in place of a single RVEs is one such approach [198, 242]. Often simulating multiple SVEs can be much faster and just as informative as simulating one very large RVE for a given problem. Much more work, however, is required in this area.

The approach outlined here is not necessarily invertible. In other words, given a set of coupled microstructure attributes it is not readily apparent what the response associated with those attributes would be without experiementation or simulation. Therefore, the coupled microstructure attributes associated with the extreme value distributions cannot be identified without appropriate simuations or experiements.

8.3 Case study: Texture effects on the extreme value driving forces for fatigue damage formation in duplex Ti-6Al-4V

In this section, it is hypothesized that a duplex Ti-6Al-4V microstructure loaded perpendicular to a strong basal texture will reduced the overall distribution of extreme value driving forces for subsurface fatigue crack formation. This hypothesis is based on the fact that combinations of primary α grains oriented for easy basal slip are so prevalent near hard oriented primary α or $\alpha + \beta$ colony grains at the locations of the extreme value FIPs as characterized by the EVMCFs of the apparent Schmid factors as was shown in Chapter 7. By loading a duplex Ti-6Al-4V microstructure perpendicular to a strong basal texture, the majority of the grains will be oriented for easy prismatic slip and the primary α grains oriented for easy basal slip or hard orientated primary α or $\alpha + \beta$ colony grains should be

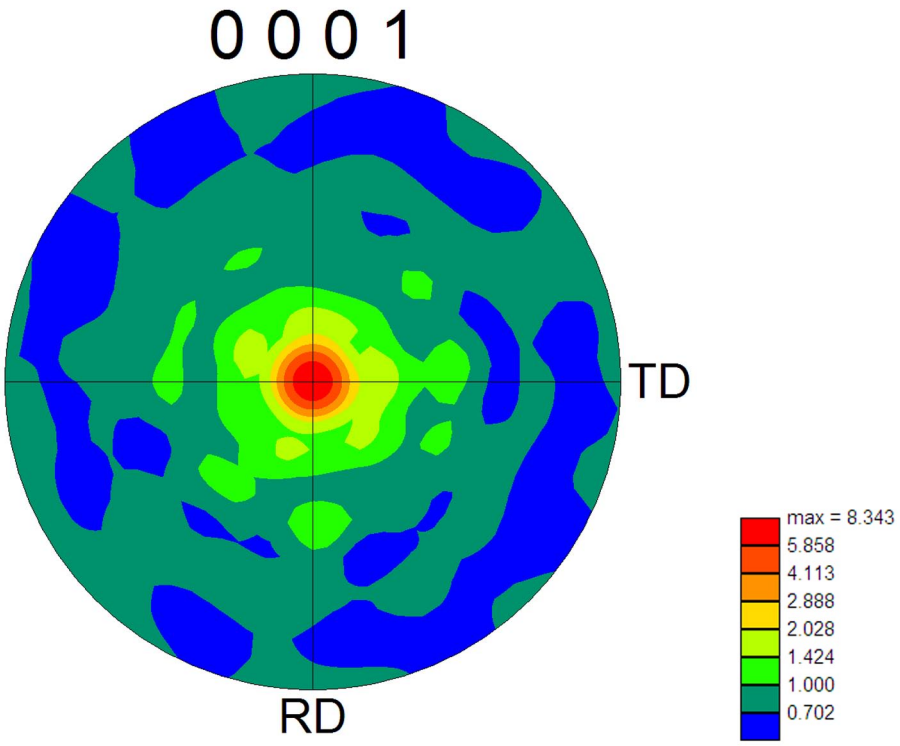

Figure 8.2: Pole figure representing strong basal textures for optimized set of SVEs instantiated for several different duplex Ti-6Al-4V microstructures.

much less prevalent.

To evaluate this hypothesis, 100 SVEs were instantiated for each of the four microstructural variants of duplex Ti-6Al-4V described in Table 7.1 with a strong basal texture as shown in Figure 8.2 instead of the random texture generated previously (see Figure 7.4). The target grain size distribution, random disorientation distribution and phase volume fraction for the basal textured microstructures were the same as the microstructures instantiated with the random texture. These microstructure were loaded cyclically with a maximum applied strain of 0.6% in the direction perpendicular to the strong basal texture (*i.e.*, in the TD-RD plane as shown in Figure 8.2). As can be seen in Figure 8.3, loading the microstructure in this manner favors prismatic slip. The load was applied with a quasistatic strain rate of 0.002^{-1}s with a ratio of the maximum to minimum applied cyclic strain of zero (*i.e.*, $R = 0$).

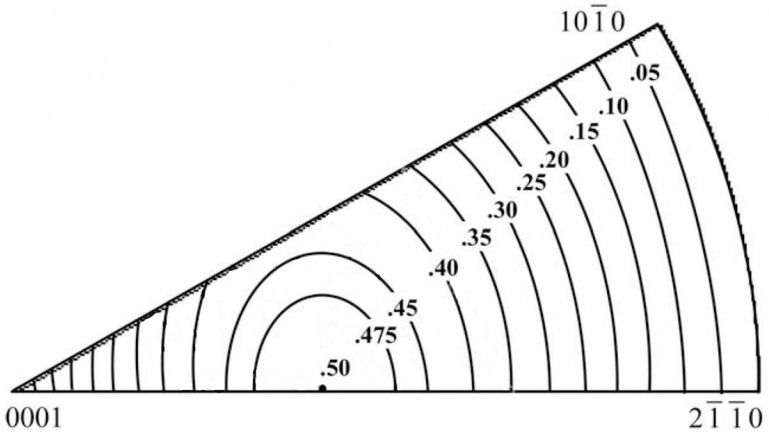

(a)

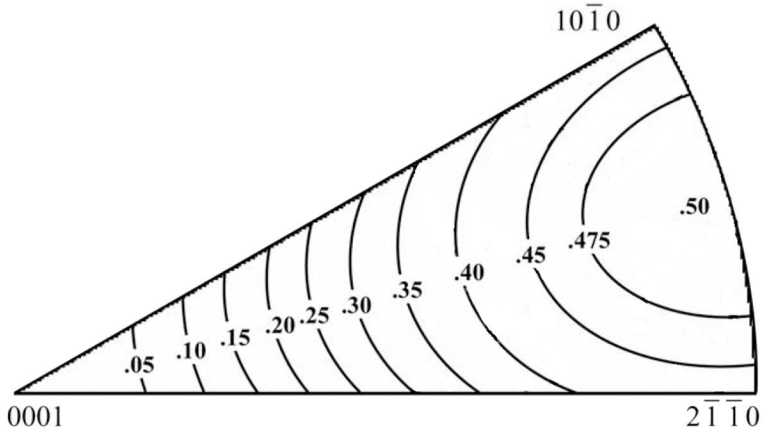

(c)

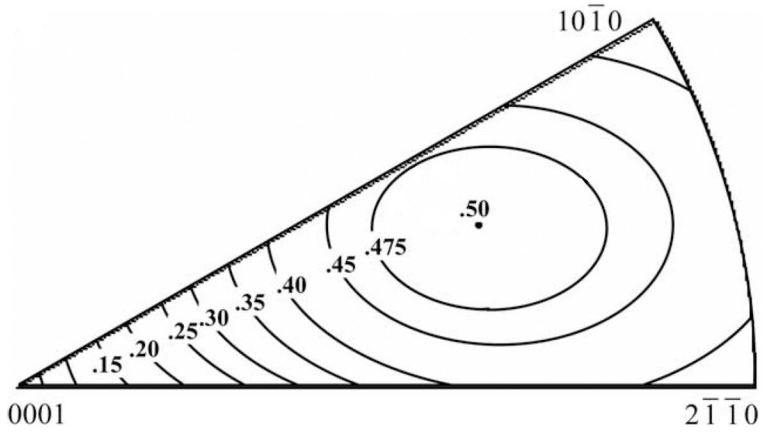

(c)

Figure 8.3: Inverse pole figure with contours of Schmid factors for (a) basal, (b) prismatic, and (c) first order pyramidal $\langle a \rangle$ slip systems (Figures adapted from similar Figures in [248]

The extreme value distributions for the FS FIPs plotted on a Gumbel probability scale (see Appendix B) for the three different averaging volumes defined in Table 7.2 for the duplex Ti-6Al-4V microstructures with a strong basal texture and random texture are shown in Figure 8.4. The fits of the extreme value FS FIPs calculated over an averaging volume with equivalent grain size of 0.032mm to the extreme value Gumbel distribution for the microstructures with the strong basal texture are shown in Figure 8.5 and given in Table 8.1. As can be seen in Figures 8.4 and 8.5, the extreme value driving forces for fatigue damage formation as estimated by the FIPs in most cases are less for the SVEs loaded perpendicular to the strong basal textures than for the random textures as hypothesized. The differences between the textures are more muted when calculated over larger sized averaging volumes as is shown in Figure 8.4. It is likely that the local lattice orientation has less of an influence on the local driving forces for fatigue damage formation over larger length scales (*i.e.*, over several grain sizes versus the first few nearest neighbors).

The noted exception to the trend of the basal texture microstructures exhibiting lower extreme value FIPs was Microstructure B. In microstructure B, while the extreme value FIPs for the basal texture microstructures were less than the random texture SVEs in the lower probability region, the extreme value FIPs of the basal textured Microstructure B was higher than that of the random textured microstructure in the high probability region ($p > 0.99$ or $\ln(1/\ln(1/p)) > 4.6$). It appears that the increased volume fraction of the primary α grains that is exhibited in Microstructure B versus Microstructure A can counteract the influence of the texture. It is interesting, however, that Microstructure D that also has a higher volume fraction of the primary α grains showed a similar trend for FIPs calculated over larger averaging volumes as can be seen in Figure 8.4(d). It is also possible that because each instantiation of Microstructure B sampled many more grains then SVE for the other microstructures that a rare severe combination of primary α grains was instantiated that was not observed in the other microstructures. This can be further examined by considering the coupled microstructure attributes coincident with the extreme value FIPs.

Table 8.1: Fits of the extreme value Fatemi-Socie (FS) FIP distributions to the extreme value Gumbel (Type I) distribution for the duplex Ti-6Al-4V microstructures with a strong basal texture. The FS FIPs were calculated over averaging volumes with the equivalent grain size of 0.0032mm (see Table 7.2). The relative dispersion is calculated by $(\alpha_n)^{-1}/u_n$.

Micro.	α_n	u_n	**Rel. Disp.**	R^2
A	1.257×10^7	9.387×10^{-8}	0.85	0.978
B	6.562×10^6	1.117×10^{-7}	1.36	0.787
C	5.032×10^6	1.008×10^{-7}	1.97	0.927
D	4.968×10^6	1.485×10^{-7}	1.36	0.879

The bi-modal extreme value distributions of the FIPs observed for the simulated SVEs of Microstructures C and D for the random textured microstructure was also observed for the basal textured microstructures. The number of grains was similar for both cases; therefore, the previous argument given in Chapter 7 that there are not enough grains in each simulated SVE to produce a asymptotic extreme value distribution of the considered response also applies to the simulated SVEs with the basal textured microstructures.

To understand how the texture of the microstructure influences the extreme value distributions of the FS FIPs, it is of interest to consider the EVMCFs. Here the EVMCF are constructed in terms of the radial distribution function for the apparent Schmid factor m_a^g for the two different phases, the primary α grains and the $\alpha + \beta$ colonies, as describe previously in Chapters 6 and 7. The EVMCF for Microstructure A for the SVEs simulated with the strong basal texture for select Schmid factor combinations for the two phases are given in Figures 8.6 and 8.7. Even though the microstructures with the strong basal texture were oriented to minimize basal slip and promote prismatic slip, significant basal slip was observed at the locations of extreme value response. This can be seen by comparing Figures 8.6(a) and 7.13(a). The EVMCF for high Schmid factors for basal slip in the basal textured microstructure is about 6% less than in the random textured microstructures, but is still as high as 22% at shorter correlation lengths. Additionally, the same soft-hard grain relationships characterized to be significant by the EVMCF for the random textured microstructures are also observed to be significant in the basal textured microstructures.

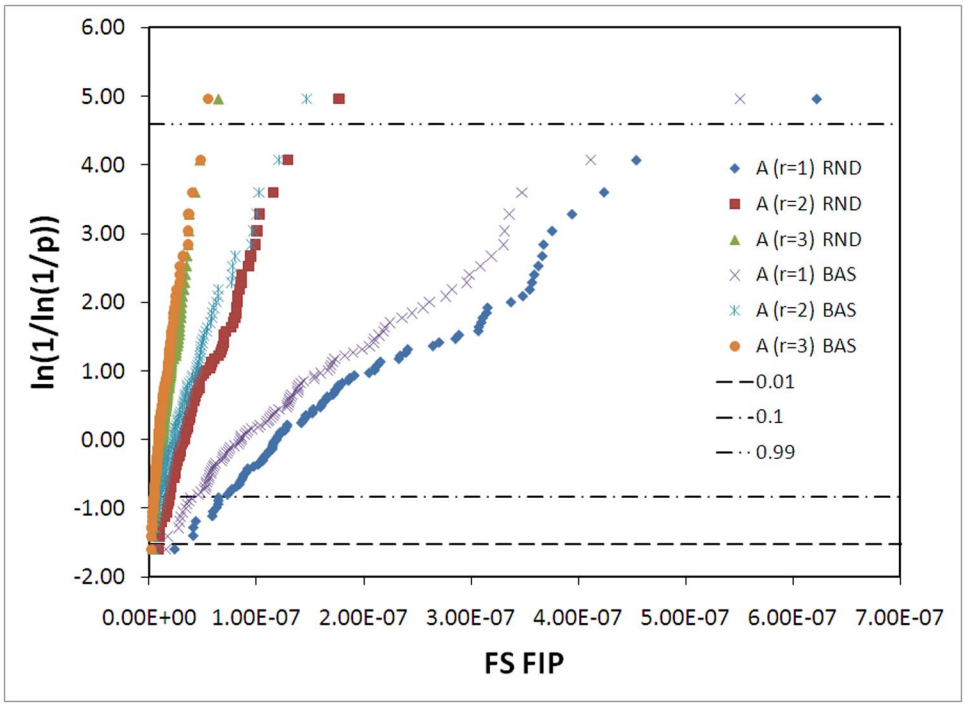

(a)

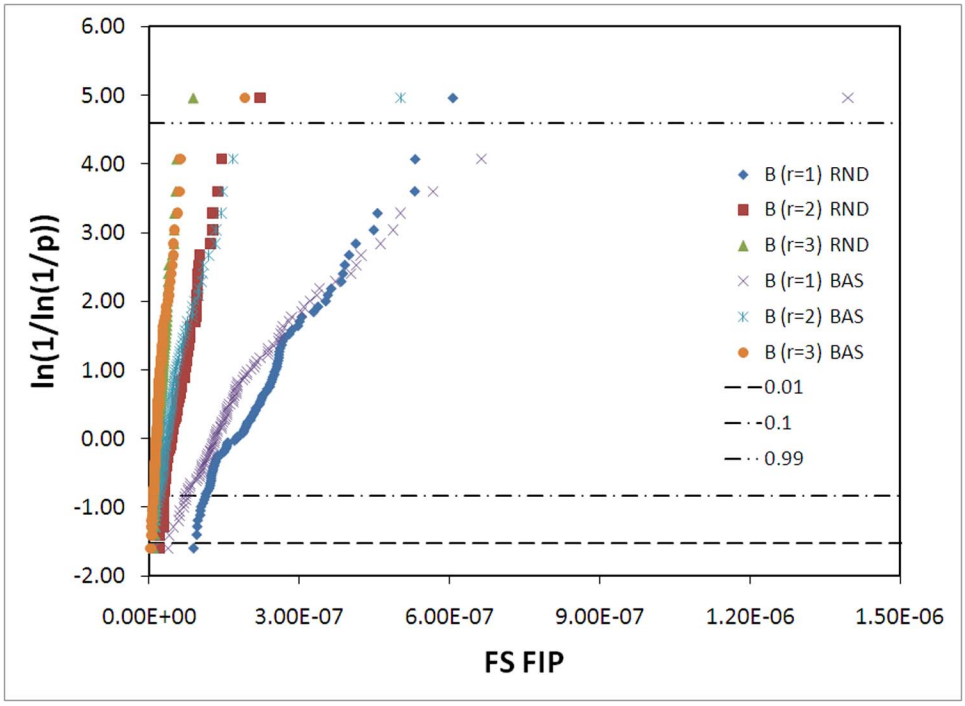

(b)

Figure 8.4: The extreme value Fatemi-Socie (FS) FIP calculated over three different cube shaped averaging volumes as described in Table 7.2 for Microstructures (a) A, (b) B, (c) C and (d) D for both the random (RND) and basal (BAS) textures. The 0.01, 0.1 and 0.99 probability levels are indicated.

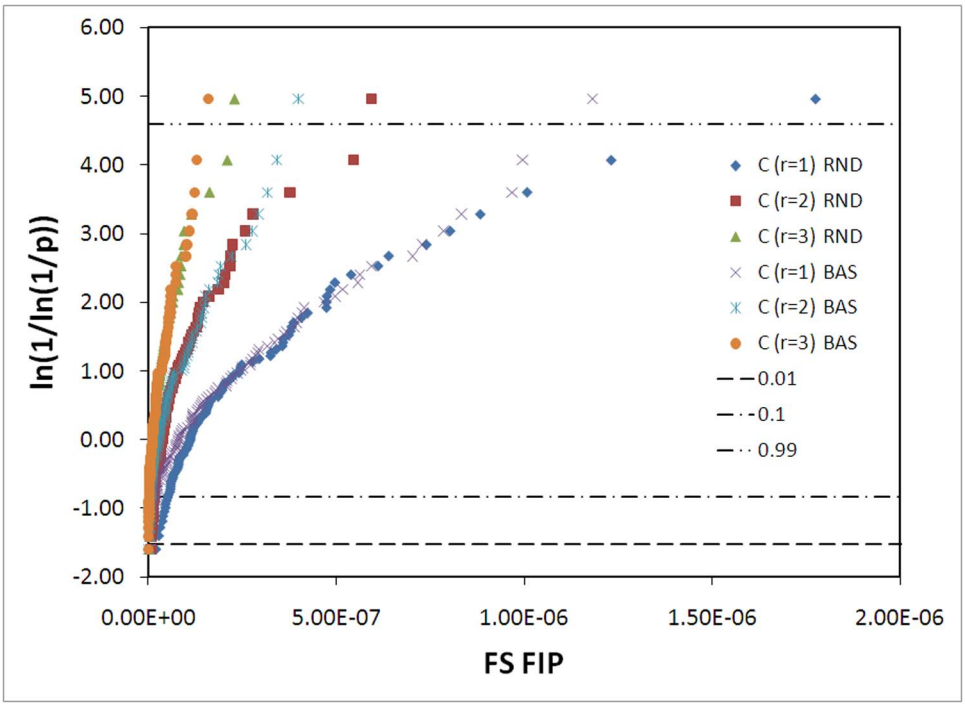

(c)

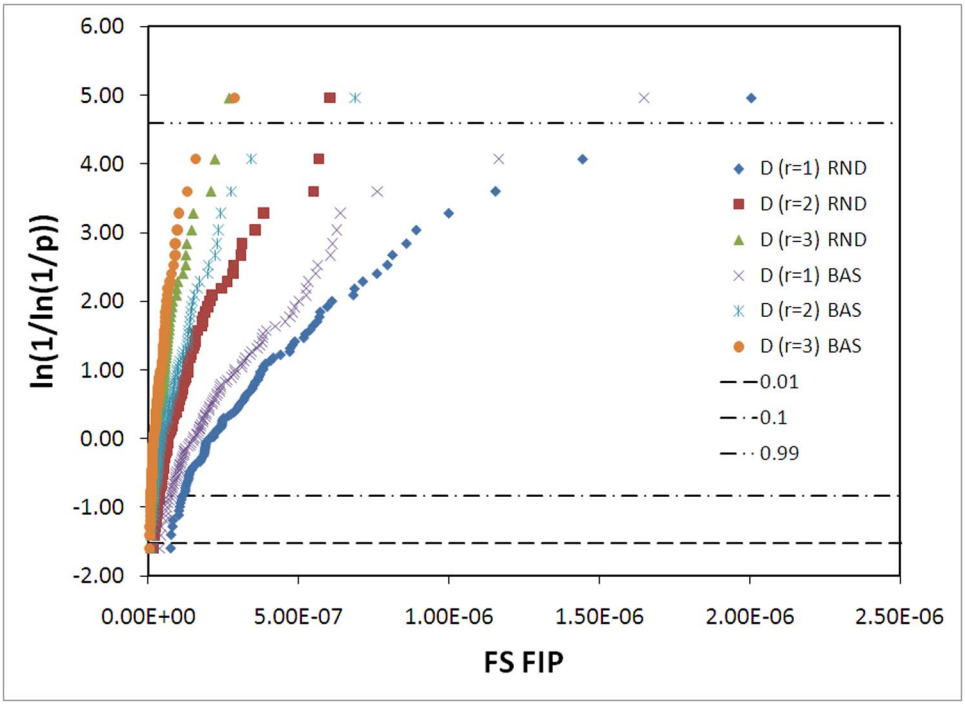

(d)

Figure 8.4: The extreme value Fatemi-Socie (FS) FIP calculated over three different cube shaped averaging volumes as described in Table 7.2 for Microstructures (a) A, (b) B, (c) C and (d) D for both the random (RND) and basal (BAS) textures. The 0.01, 0.1 and 0.99 probability levels are indicated.

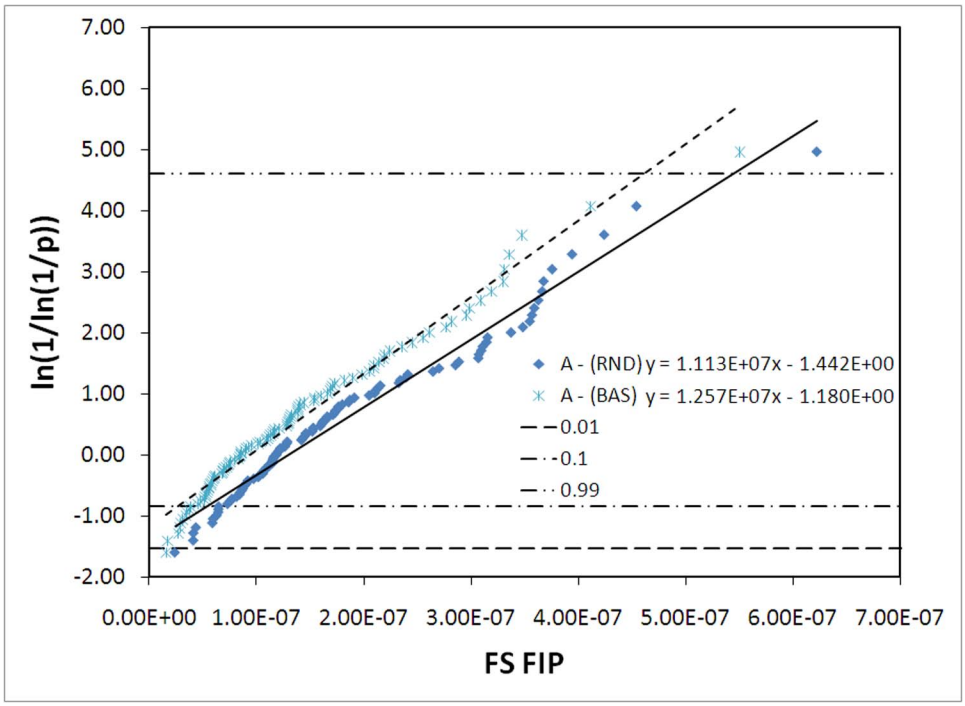

(a)

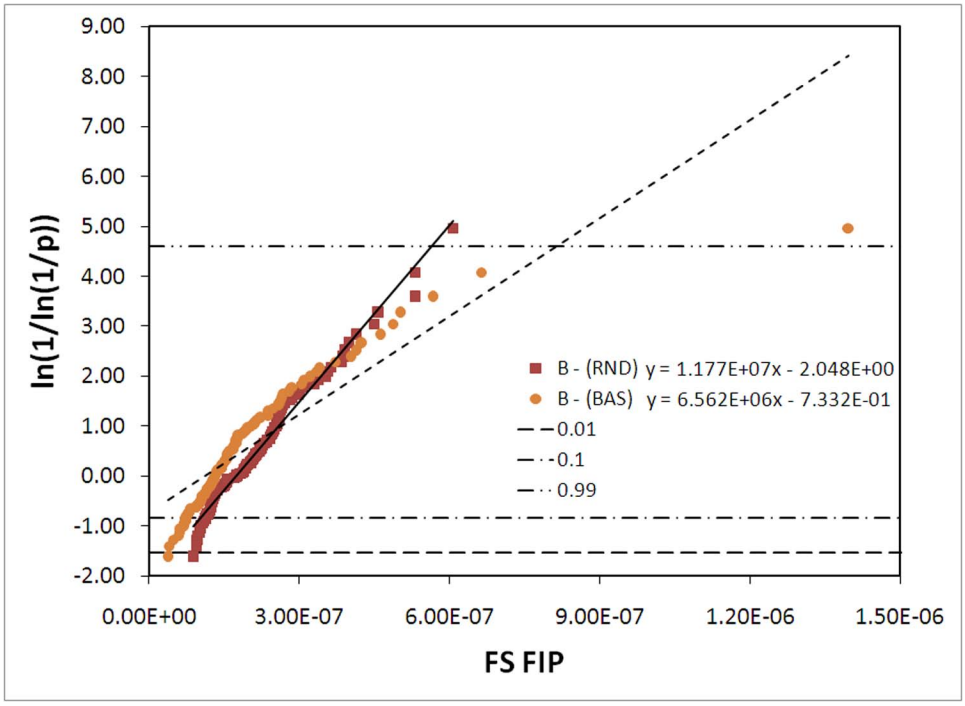

(b)

Figure 8.5: The extreme value Fatemi-Socie (FS) FIP calculated over a cube shaped averaging volume with equivalent grain size of 0.032mm for Microstructures (a) A, (b) B, (c) C and (d) D for both the random (RND) and basal (BAS) textures. Note that the equations given for the least squares linear regression are such that $y = \ln(1/\ln(1/p))$ and $x = FIP$ for the Gumbel probability plot. The 0.01, 0.1 and 0.99 probability levels are indicated.

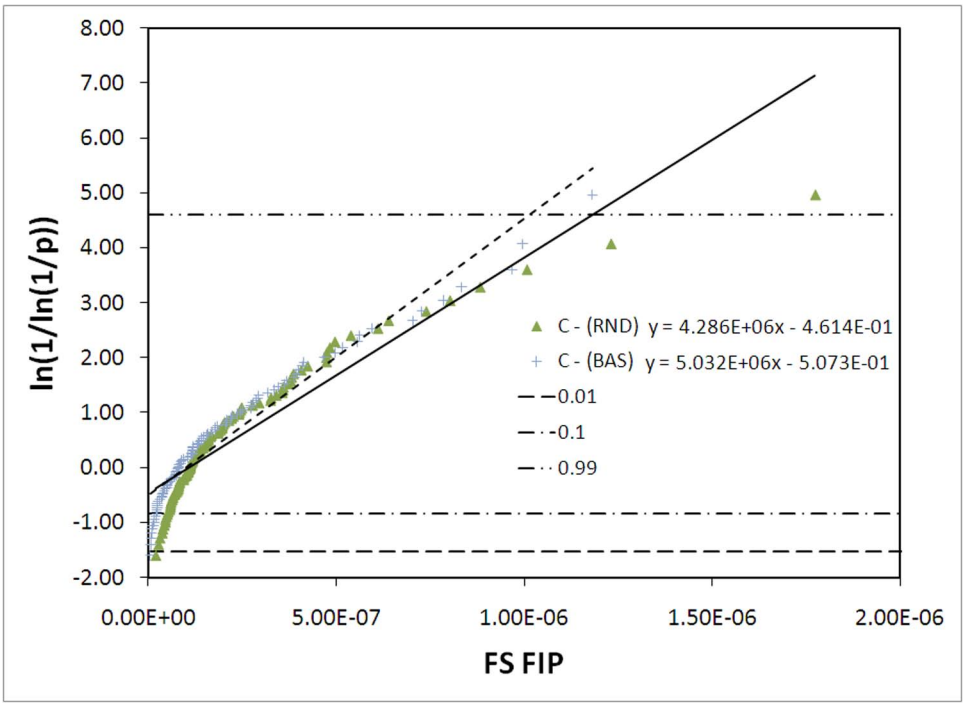

(c)

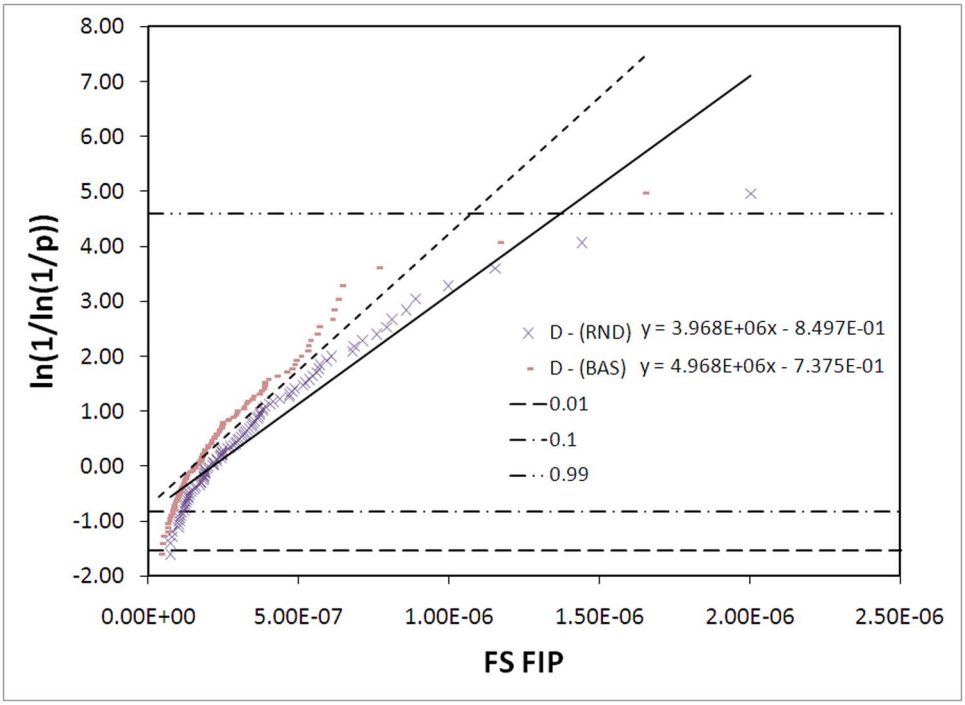

(d)

Figure 8.5: The extreme value Fatemi-Socie (FS) FIP calculated over a cube shaped averaging volume with equivalent grain size of 0.032mm for Microstructures (a) A, (b) B, (c) C and (d) D for both the random (RND) and basal (BAS) textures. Note that the equations given for the least squares linear regression are such that $y = \ln(1/\ln(1/p))$ and $x = FIP$ for the Gumbel probability plot. The 0.01, 0.1 and 0.99 probability levels are indicated.

For example, Figure 8.6(c)-(d) describes a 2.5% and 5% probability of finding a primary α grain oriented for easy basal slip near a primary α grain oriented for hard basal or easy pyramidal $\langle a \rangle$ or pyramidal $\langle a + c \rangle$ slip, respectively, in the basal textured microstructures. The same coupled grains in the random textured microstructures as seen in Figure 7.13(c)-(d) occurred at the locations of extreme value response with just the slightly higher probability of 3.5% and 6.5%, respectively. Similar trends can be observed by comparing easy basal slip in the primary α grains to harder pyramidal $\langle a \rangle$ or bcc BOR modified slip in the $\alpha + \beta$ colonies as can be seen in Figures 8.7(c)-(d) and 7.14(c)-(d) in the basal and random textured microstructures, respectively.

It is also of particular interest to consider how prismatic slip correlated with the extreme value response because prismatic slip was hypothesized to be much more prevalent in the basal textured microstructures. The EVMCF for prismatic slip for the random textured microstructures were negatively correlated with the extreme value response as can be seen in Figures 8.8 and 8.9. Here negative correlation means that the high Schmid factors for prismatic slip in the primary α grains near grains with high Schmid factors for the same and other types of slip for both phases was less likely to be observed at the locations of extreme value response than in the overall microstructure. In contrast, in the microstructures loaded perpendicular to the strong basal texture where prismatic slip was expected to be much more prevalent, positive correlation was observed between grains oriented for prismatic slip and the extreme value response as can be seen in Figures 8.10 and 8.11. However, in most cases the probability of finding grains oriented for prismatic slip at the extreme value locations was less than a percent higher than finding the same correlated Schmid factors in the overall microstructure in the basal textured microstructures. Therefore, although basal slip was more limited and prismatic slip more prevalent at the locations of extreme value response in the basal textured microstructures than in the random textured microstructures, basal slip remained the most important slip mode.

It is also of interest to consider the EVMCF for the random and basal textured variants

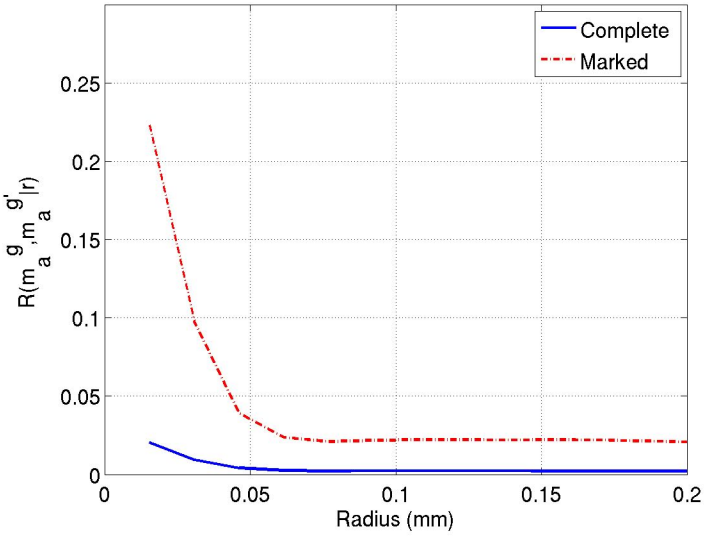

(a)

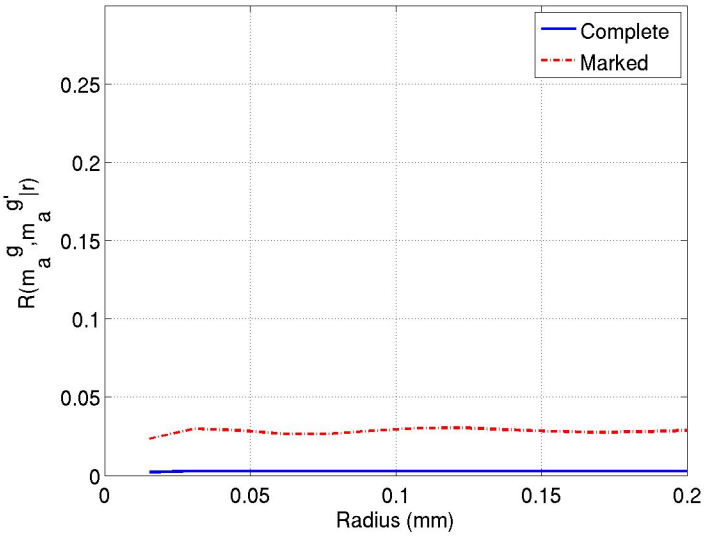

(b)

Figure 8.6: Radial correlation functions for the complete microstructure compared with EVMCF describing the correlation between the apparent Schmid factor m_a for basal slip between 0.45 and 0.5 for the primary α phase and the Schmid factor m'_a for: (a) basal slip between 0.45 and 0.5, (b) prismatic slip between 0.45 and 0.5, (c) pyramidal $\langle a \rangle$ slip between 0.45 and 0.5, and (d) pyramidal $\langle a + c \rangle$ slip between 0.45 and 0.5 for the primary α phase in Microstructure A with a strong basal texture.

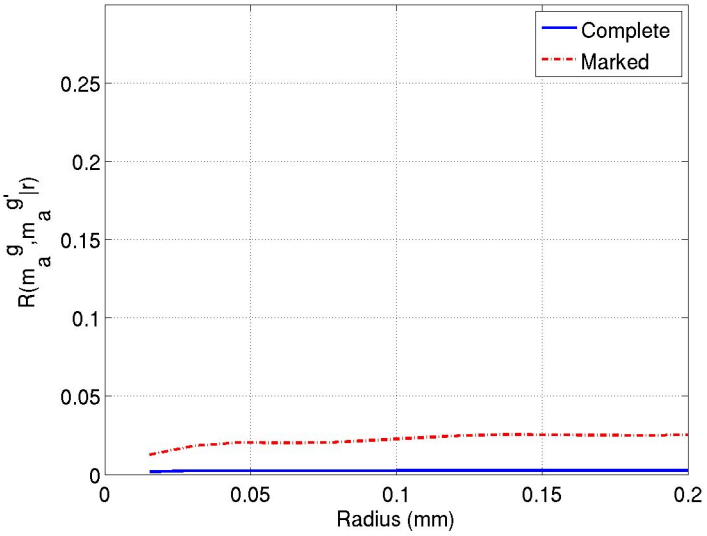

(c)

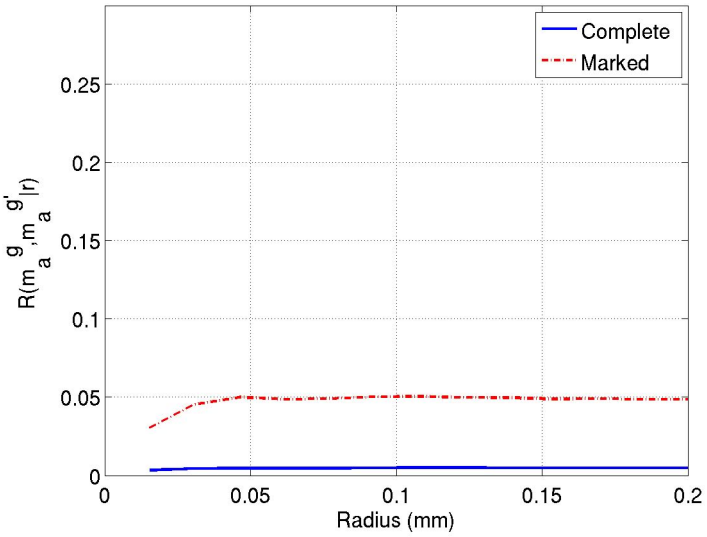

(d)

Figure 8.6: Radial correlation functions for the complete microstructure compared with EVMCF describing the correlation between the apparent Schmid factor m_a for basal slip between 0.45 and 0.5 for the primary α phase and the Schmid factor m'_a for: (a) basal slip between 0.45 and 0.5, (b) prismatic slip between 0.45 and 0.5, (c) pyramidal $\langle a \rangle$ slip between 0.45 and 0.5, and (d) pyramidal $\langle a + c \rangle$ slip between 0.45 and 0.5 for the primary α phase in Microstructure A with a strong basal texture.

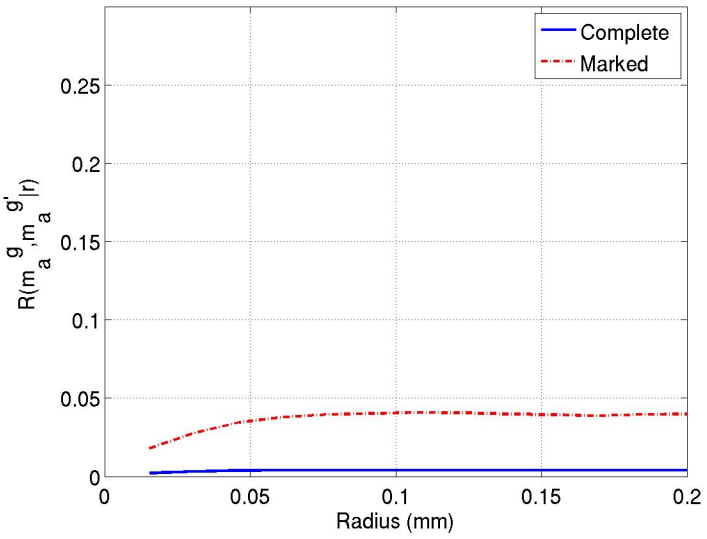

(a)

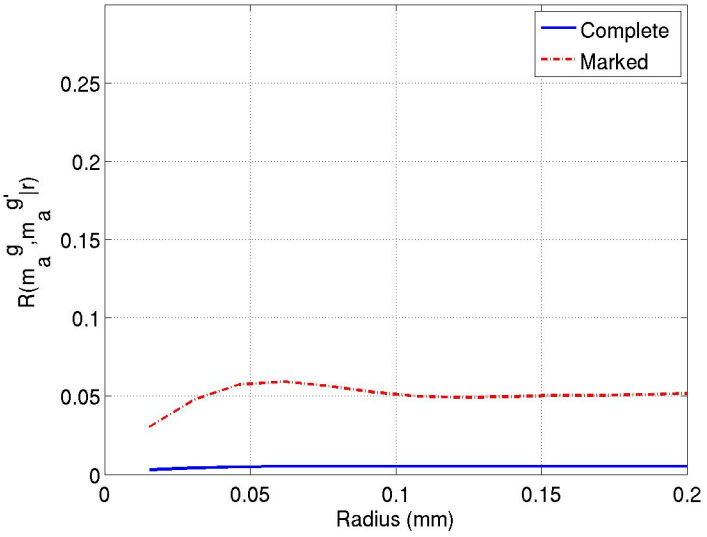

(b)

Figure 8.7: Radial correlation functions for the complete microstructure compared with EVMCF describing the correlation between the apparent Schmid factor m_a for basal slip between 0.45 and 0.5 for the primary α phase and the apparent Schmid factor m'_a for: (a) basal slip between 0.45 and 0.5, (b) prismatic slip between 0.45 and 0.5, (c) pyramidal $\langle a \rangle$ slip between 0.45 and 0.5, and (d) $\langle 111 \rangle \{110\}$ bcc slip (transformed into the hexagonal coordinate system via the BOR) between 0.45 and 0.5 for the $\alpha + \beta$ colony phase in Microstructure A with a strong basal texture.

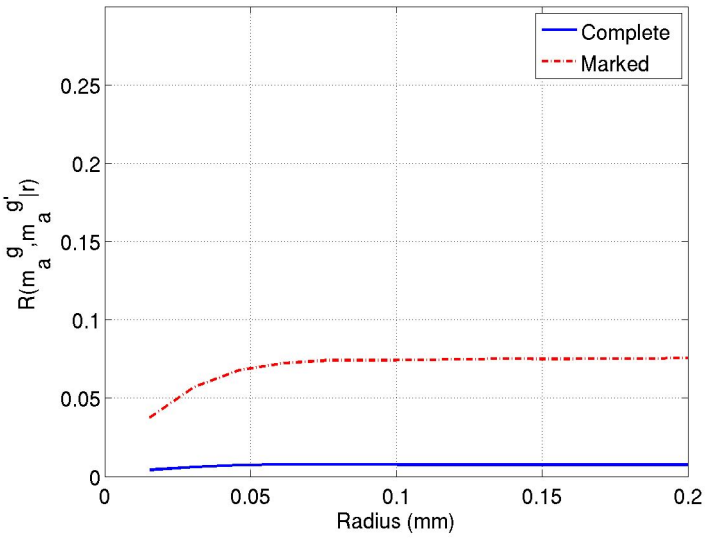

(c)

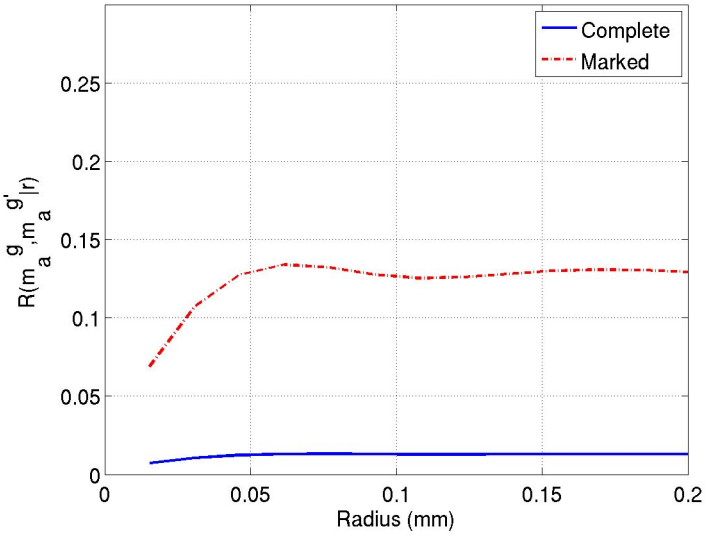

(d)

Figure 8.7: Radial correlation functions for the complete microstructure compared with EVMCF describing the correlation between the apparent Schmid factor m_a for basal slip between 0.45 and 0.5 for the primary α phase and the apparent Schmid factor m'_a for: (a) basal slip between 0.45 and 0.5, (b) prismatic slip between 0.45 and 0.5, (c) pyramidal $\langle a \rangle$ slip between 0.45 and 0.5, and (d) $\langle 111 \rangle \{110\}$ bcc slip (transformed into the hexagonal coordinate system via the BOR) between 0.45 and 0.5 for the $\alpha + \beta$ colony phase in Microstructure A with a strong basal texture.

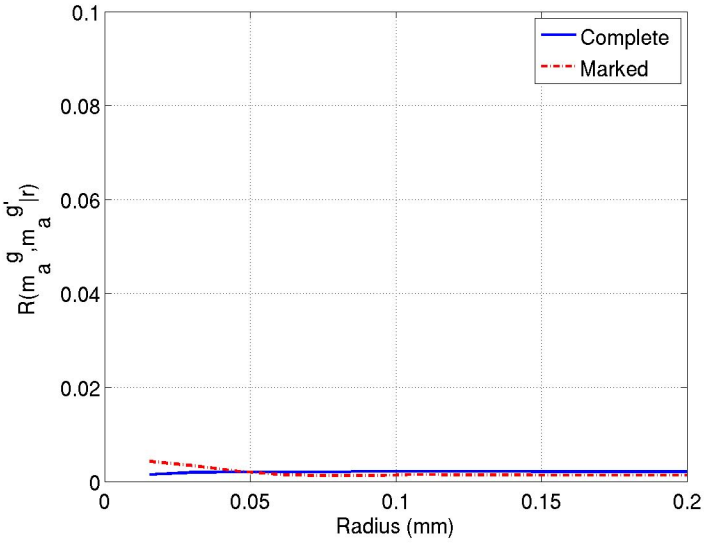

(a)

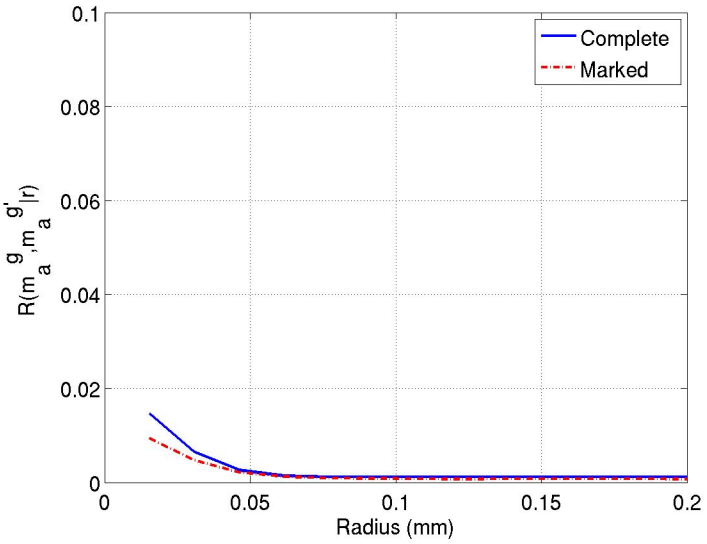

(b)

Figure 8.8: Radial correlation functions for the complete microstructure compared with EVMCF describing the correlation between the apparent Schmid factor m_a for prismatic slip between 0.45 and 0.5 for the primary α phase and the Schmid factor m'_a for: (a) basal slip between 0.45 and 0.5, (b) prismatic slip between 0.45 and 0.5, (c) pyramidal $\langle a \rangle$ slip between 0.45 and 0.5, and (d) pyramidal $\langle a + c \rangle$ slip between 0.45 and 0.5 for the primary α phase in Microstructure A with a random texture.

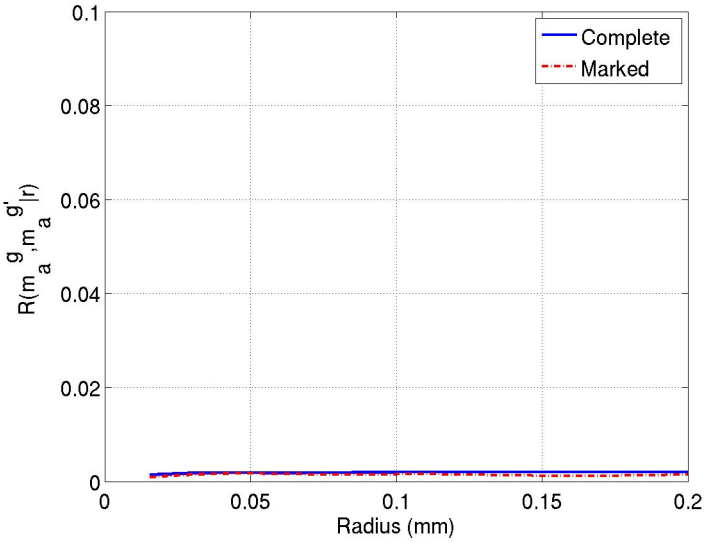

(c)

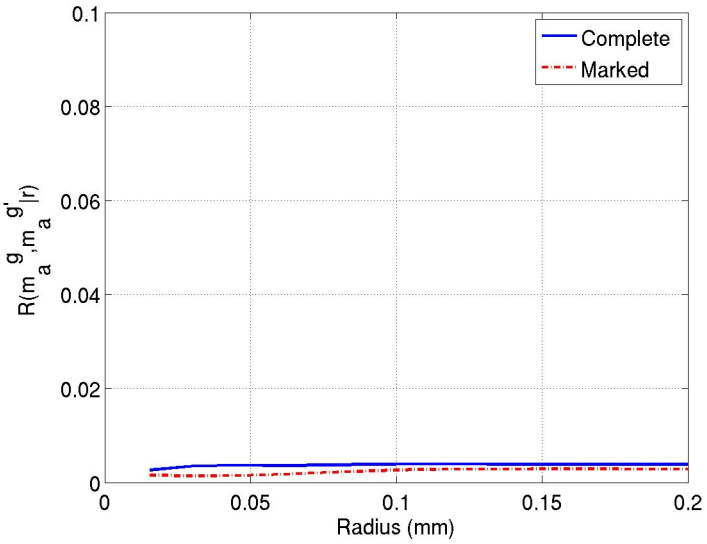

(d)

Figure 8.8: Radial correlation functions for the complete microstructure compared with EVMCF describing the correlation between the apparent Schmid factor m_a for prismatic slip between 0.45 and 0.5 for the primary α phase and the Schmid factor m'_a for: (a) basal slip between 0.45 and 0.5, (b) prismatic slip between 0.45 and 0.5, (c) pyramidal $\langle a \rangle$ slip between 0.45 and 0.5, and (d) pyramidal $\langle a + c \rangle$ slip between 0.45 and 0.5 for the primary α phase in Microstructure A with a random texture.

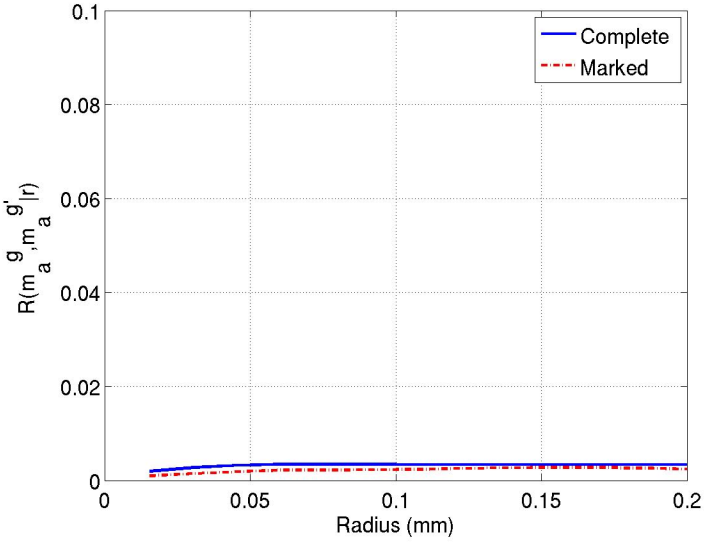

(a)

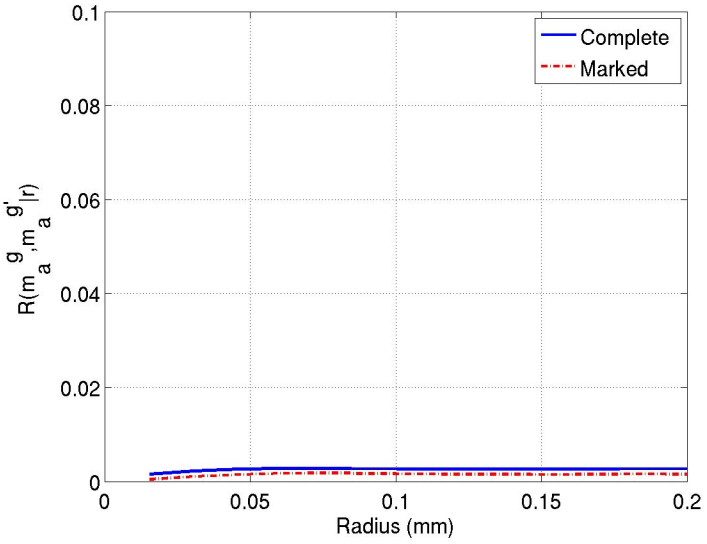

(b)

Figure 8.9: Radial correlation functions for the complete microstructure compared with EVMCF describing the correlation between the apparent Schmid factor m_a for prismatic slip between 0.45 and 0.5 for the primary α phase and the apparent Schmid factor m'_a for: (a) basal slip between 0.45 and 0.5, (b) prismatic slip between 0.45 and 0.5, (c) pyramidal $\langle a \rangle$ slip between 0.45 and 0.5, and (d) $\langle 111 \rangle \{110\}$ bcc slip (transformed into the hexagonal coordinate system via the BOR) between 0.45 and 0.5 for the $\alpha + \beta$ colony phase in Microstructure A with a random texture.

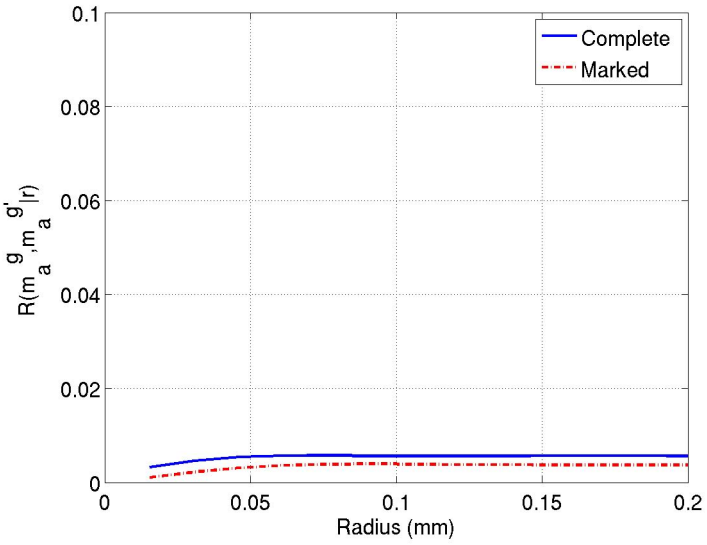

(c)

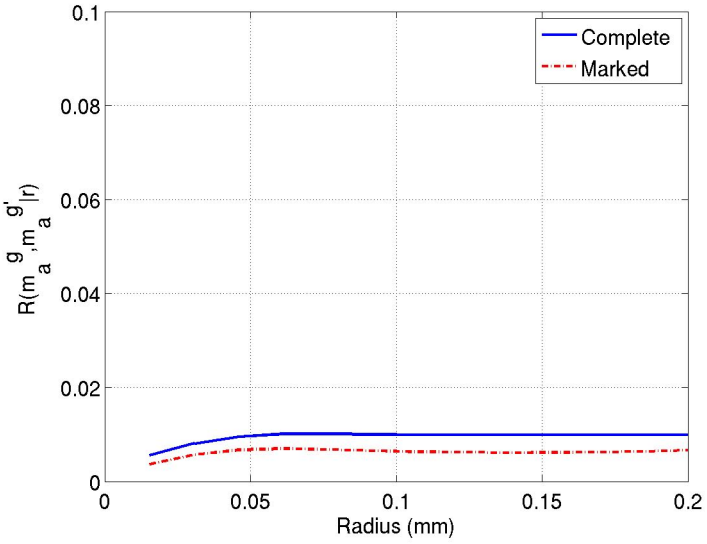

(d)

Figure 8.9: Radial correlation functions for the complete microstructure compared with EVMCF describing the correlation between the apparent Schmid factor m_a for prismatic slip between 0.45 and 0.5 for the primary α phase and the apparent Schmid factor m'_a for: (a) basal slip between 0.45 and 0.5, (b) prismatic slip between 0.45 and 0.5, (c) pyramidal $\langle a \rangle$ slip between 0.45 and 0.5, and (d) $\langle 111 \rangle \{110\}$ bcc slip (transformed into the hexagonal coordinate system via the BOR) between 0.45 and 0.5 for the $\alpha + \beta$ colony phase in Microstructure A with a random texture.

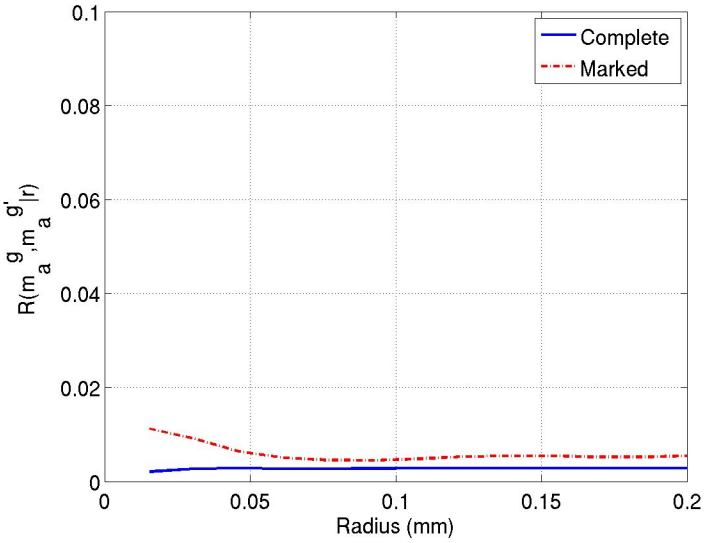

(a)

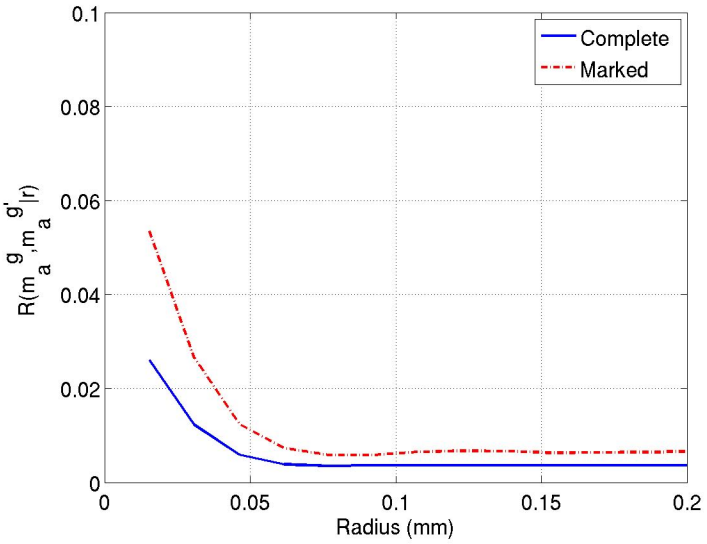

(b)

Figure 8.10: Radial correlation functions for the complete microstructure compared with EVMCF describing the correlation between the apparent Schmid factor m_a for prismatic slip between 0.45 and 0.5 for the primary α phase and the Schmid factor m'_a for: (a) basal slip between 0.45 and 0.5, (b) prismatic slip between 0.45 and 0.5, (c) pyramidal $\langle a \rangle$ slip between 0.45 and 0.5, and (d) pyramidal $\langle a + c \rangle$ slip between 0.45 and 0.5 for the primary α phase in Microstructure A with a strong basal texture.

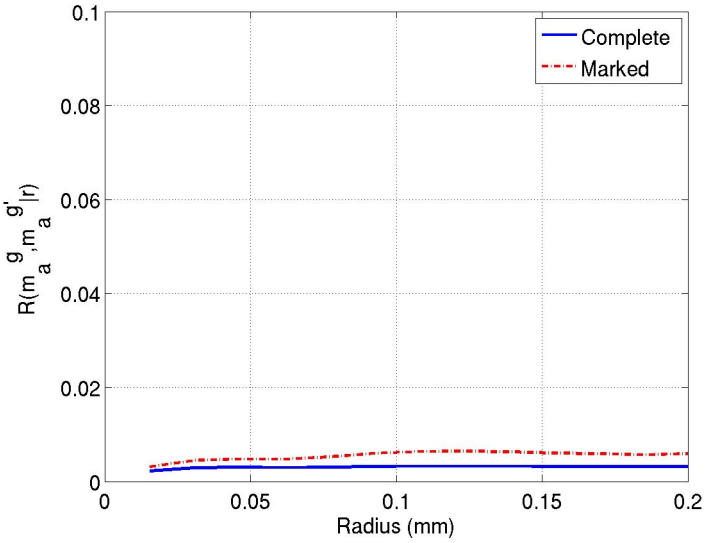

(c)

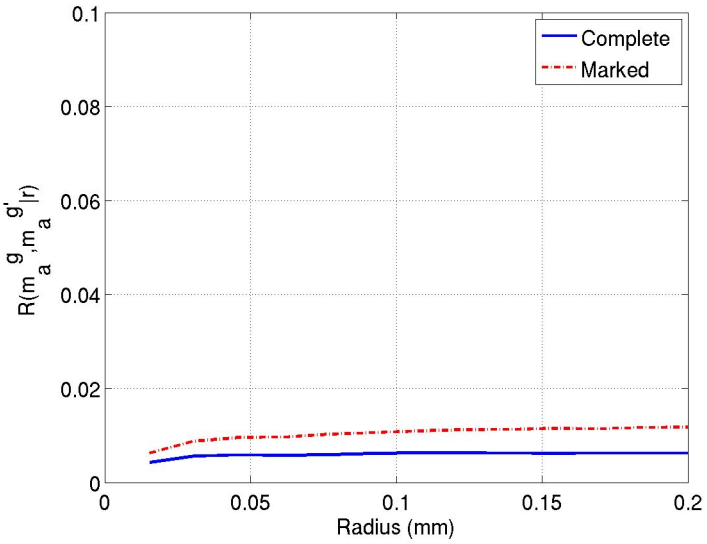

(d)

Figure 8.10: Radial correlation functions for the complete microstructure compared with EVMCF describing the correlation between the apparent Schmid factor m_a for prismatic slip between 0.45 and 0.5 for the primary α phase and the Schmid factor m'_a for: (a) basal slip between 0.45 and 0.5, (b) prismatic slip between 0.45 and 0.5, (c) pyramidal $\langle a \rangle$ slip between 0.45 and 0.5, and (d) pyramidal $\langle a + c \rangle$ slip between 0.45 and 0.5 for the primary α phase in Microstructure A with a strong basal texture.

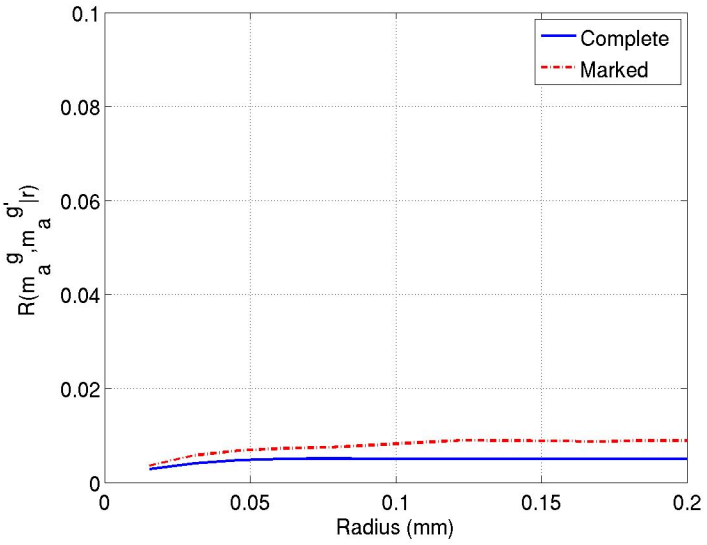

(a)

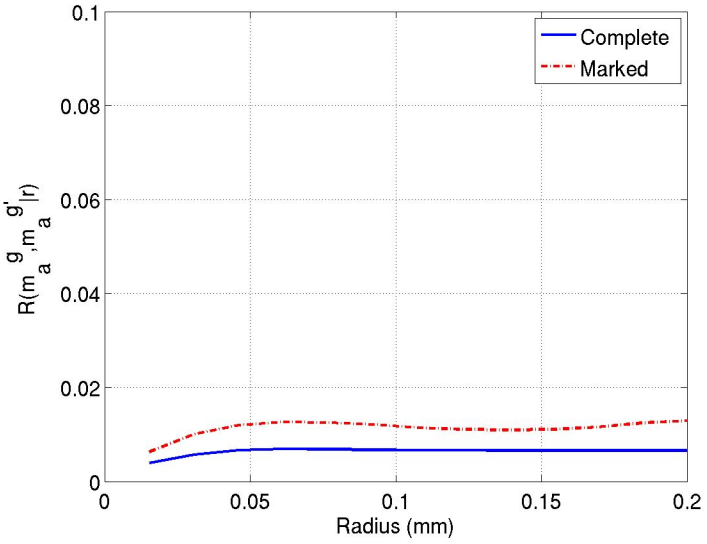

(b)

Figure 8.11: Radial correlation functions for the complete microstructure compared with EVMCF describing the correlation between the apparent Schmid factor m_a for prismatic slip between 0.45 and 0.5 for the primary α phase and the apparent Schmid factor m'_a for: (a) basal slip between 0.45 and 0.5, (b) prismatic slip between 0.45 and 0.5, (c) pyramidal $\langle a \rangle$ slip between 0.45 and 0.5, and (d) $\langle 111 \rangle \{110\}$ bcc slip (transformed into the hexagonal coordinate system via the BOR) between 0.45 and 0.5 for the $\alpha + \beta$ colony phase in Microstructure A with a strong basal texture.

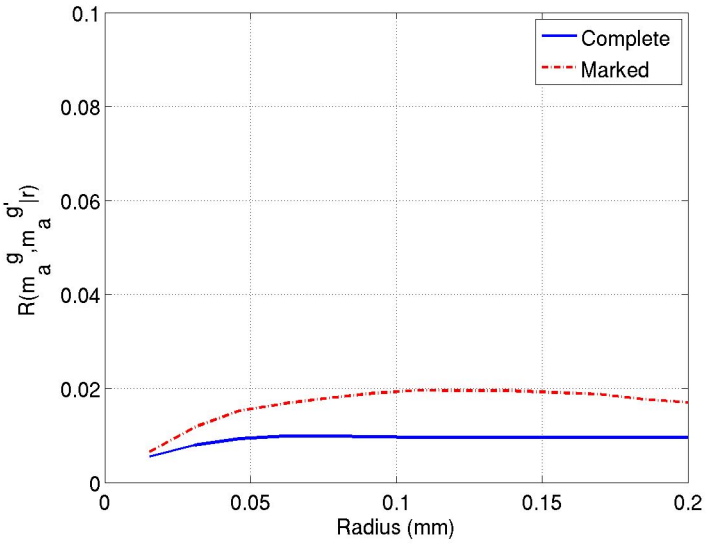

(c)

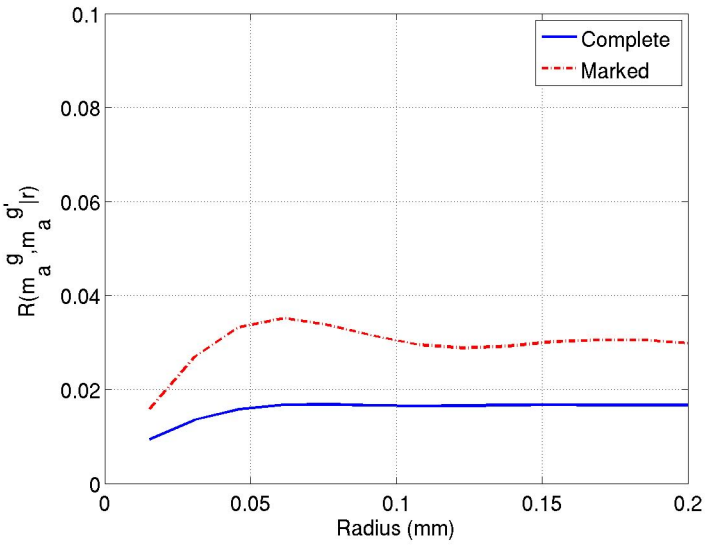

(d)

Figure 8.11: Radial correlation functions for the complete microstructure compared with EVMCF describing the correlation between the apparent Schmid factor m_a for prismatic slip between 0.45 and 0.5 for the primary α phase and the apparent Schmid factor m'_a for: (a) basal slip between 0.45 and 0.5, (b) prismatic slip between 0.45 and 0.5, (c) pyramidal $\langle a \rangle$ slip between 0.45 and 0.5, and (d) $\langle 111 \rangle \{110\}$ bcc slip (transformed into the hexagonal coordinate system via the BOR) between 0.45 and 0.5 for the $\alpha + \beta$ colony phase in Microstructure A with a strong basal texture.

of Microstructure B to better understand why this particular microstructure showed less of an reduction in the extreme value FIPs than the other microstructures. The EVMCF are plotted for the radial distribution function for the random and strong basal textures for high apparent Schmid factors for basal slip in the primary α grains versus high apparent Schmid factors basal, prismatic, pyramidal $\langle a \rangle$ and pyramidal $\langle a + c \rangle$ also in the primary α grains in Figures 8.12 and 8.13, respectively. Although basal slip is slightly less probable in the basal textured microstructures than the random texture microstructures (32% versus 37% at short correlation lengths), the differences between the two cases are not large. The EVMCF are also similarly plotted for the two textures for high apparent Schmid factors for prismatic slip in the primary α grains versus high apparent Schmid factors basal, prismatic, pyramidal $\langle a \rangle$ and pyramidal $\langle a + c \rangle$ also in the primary α grains in Figures 8.14 and 8.15, respectively. In both cases, there is no positive correlation between high apparent Schmid factors for prismatic slip and the extreme value FIPs in the basal textured microstructures. This is in contrast to what was observed with Microstructure A, where there was positive correlation between high apparent Schmid factors for prismatic slip and the extreme value FIPs. Microstructure B has a much higher volume fraction of the primary α grains than Microstructure A. It is likely that in order to observe the same improvement in Microstructure B that was observed in Microstructure A an even stronger basal texture is required. The increased density of the primary α grains in Microstructure B relative to Microstructure A increases the chance that the grain combinations that most increase the local driving forces for fatigue crack formation can exist. Thus, an even stronger texture is required to counteract the higher volume fraction in order to get a similar improvement in Microstructure B that was observed in Microstructure A for the extreme value distribution of the FIPs.

These results highlight the importance of understanding the distributions of extreme value microstructure attributes when studying extreme value response. Here the texture was designed to promote prismatic slip to reduce the probability of occurrence of the primary α grains oriented for each basal slip near hard oriented primary α and $\alpha + \beta$ colonies

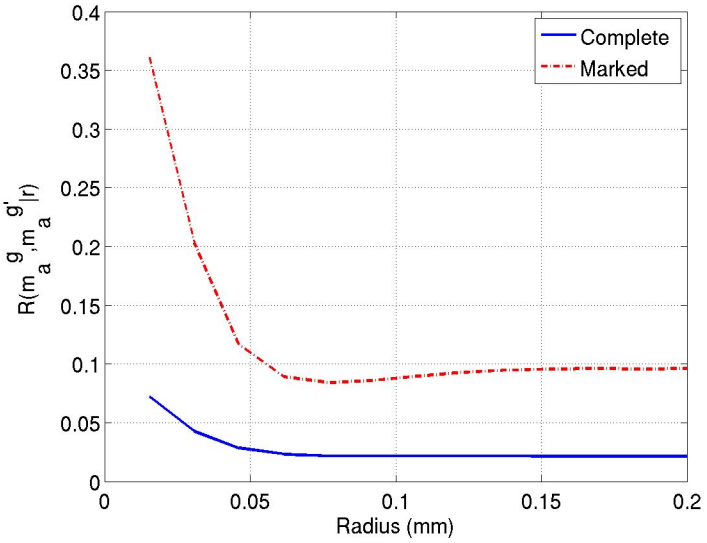

(a)

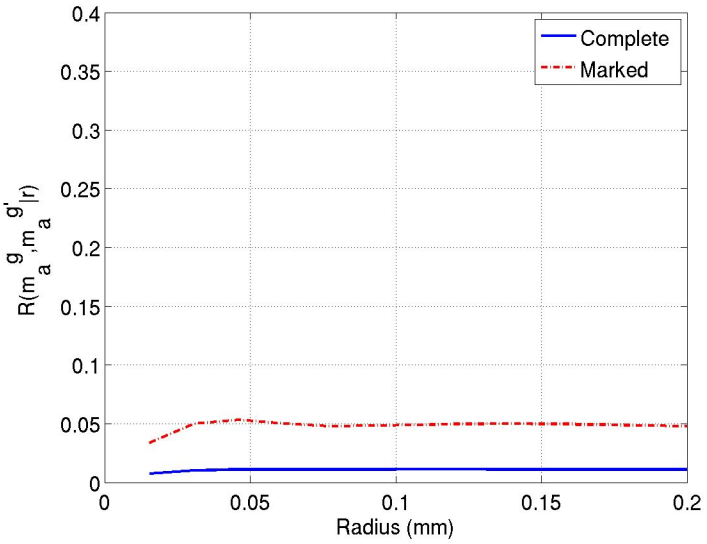

(b)

Figure 8.12: Radial correlation functions for the complete microstructure compared with EVMCF describing the correlation between the apparent Schmid factor m_a for basal slip between 0.45 and 0.5 for the primary α phase and the Schmid factor m'_a for: (a) basal slip between 0.45 and 0.5, (b) prismatic slip between 0.45 and 0.5, (c) pyramidal $\langle a \rangle$ slip between 0.45 and 0.5, and (d) pyramidal $\langle a + c \rangle$ slip between 0.45 and 0.5 for the primary α phase in Microstructure B with a random texture.

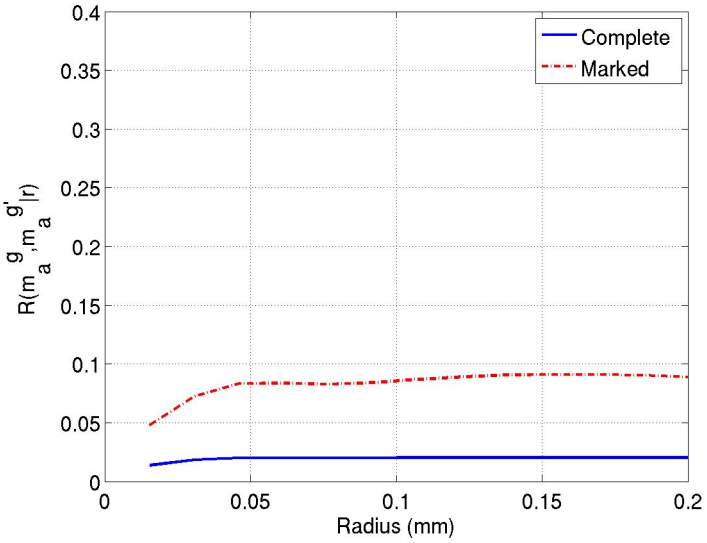

(c)

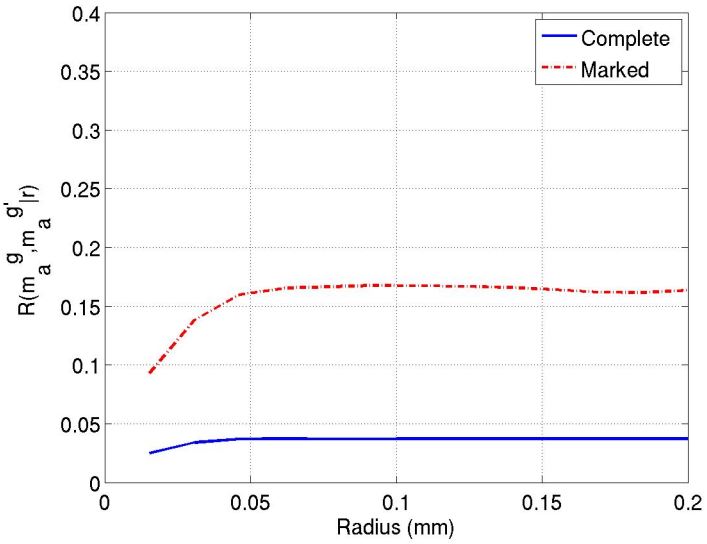

(d)

Figure 8.12: Radial correlation functions for the complete microstructure compared with EVMCF describing the correlation between the apparent Schmid factor m_a for basal slip between 0.45 and 0.5 for the primary α phase and the Schmid factor m'_a for: (a) basal slip between 0.45 and 0.5, (b) prismatic slip between 0.45 and 0.5, (c) pyramidal $\langle a \rangle$ slip between 0.45 and 0.5, and (d) pyramidal $\langle a + c \rangle$ slip between 0.45 and 0.5 for the primary α phase in Microstructure B with a random texture.

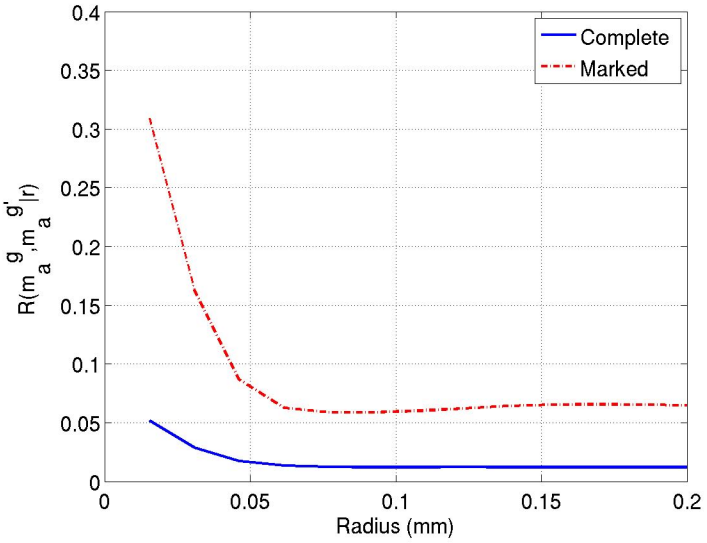

(a)

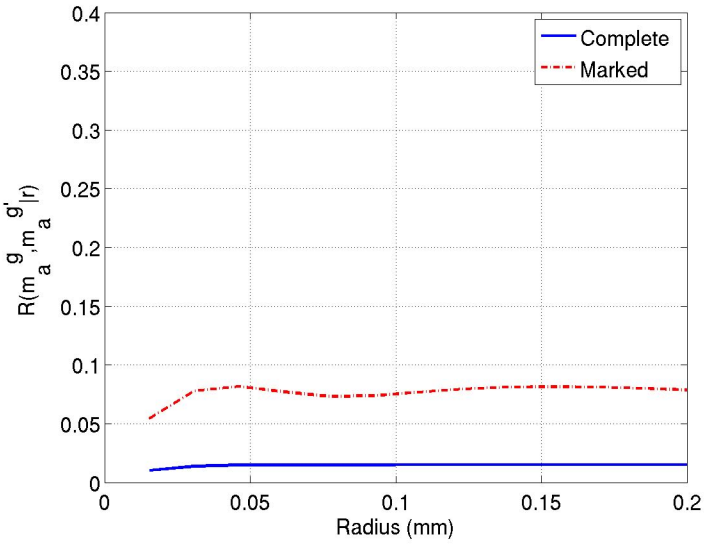

(b)

Figure 8.13: Radial correlation functions for the complete microstructure compared with EVMCF describing the correlation between the apparent Schmid factor m_a for basal slip between 0.45 and 0.5 for the primary α phase and the Schmid factor m'_a for: (a) basal slip between 0.45 and 0.5, (b) prismatic slip between 0.45 and 0.5, (c) pyramidal $\langle a \rangle$ slip between 0.45 and 0.5, and (d) pyramidal $\langle a + c \rangle$ slip between 0.45 and 0.5 for the primary α phase in Microstructure B with a strong basal texture.

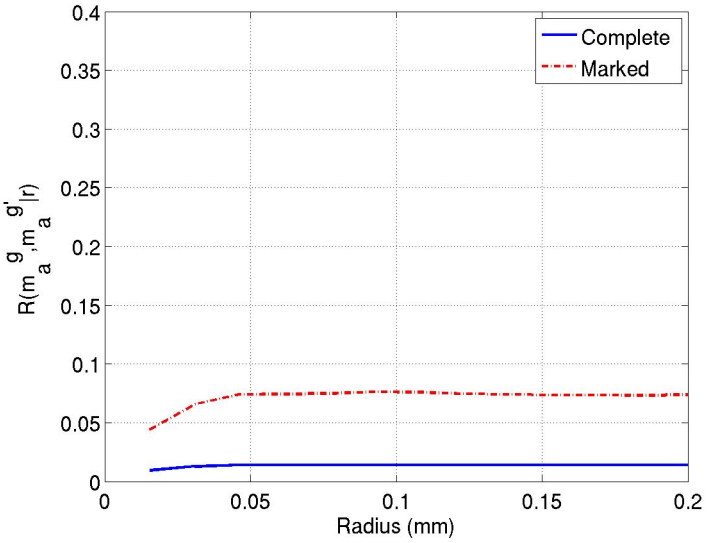

(c)

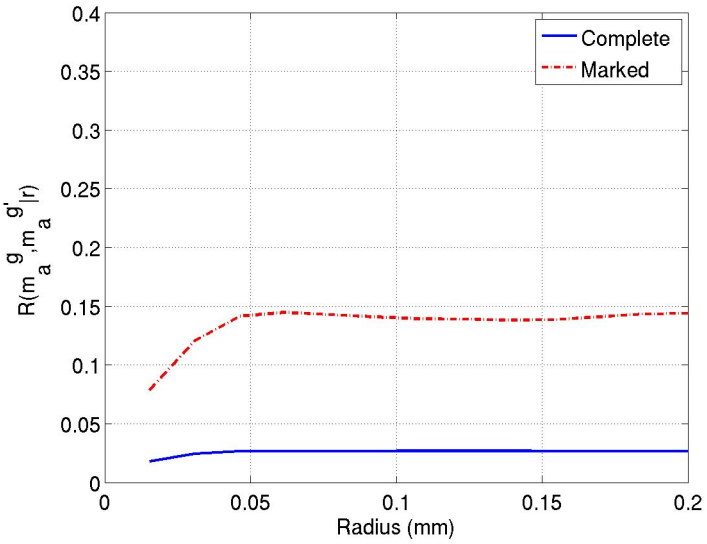

(d)

Figure 8.13: Radial correlation functions for the complete microstructure compared with EVMCF describing the correlation between the apparent Schmid factor m_a for basal slip between 0.45 and 0.5 for the primary α phase and the Schmid factor m'_a for: (a) basal slip between 0.45 and 0.5, (b) prismatic slip between 0.45 and 0.5, (c) pyramidal $\langle a \rangle$ slip between 0.45 and 0.5, and (d) pyramidal $\langle a + c \rangle$ slip between 0.45 and 0.5 for the primary α phase in Microstructure B with a strong basal texture.

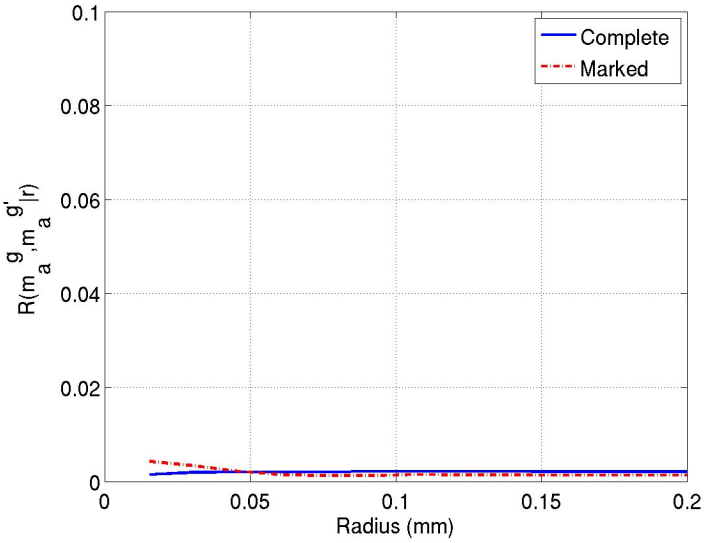

(a)

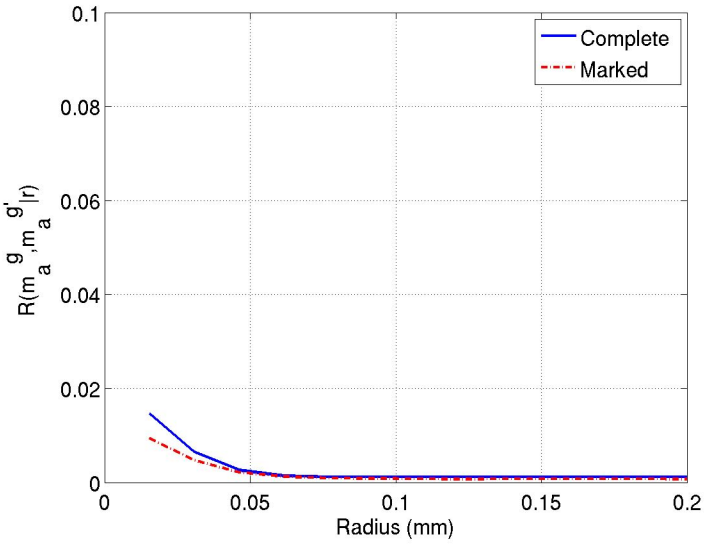

(b)

Figure 8.14: Radial correlation functions for the complete microstructure compared with EVMCF describing the correlation between the apparent Schmid factor m_a for prismatic slip between 0.45 and 0.5 for the primary α phase and the Schmid factor m'_a for: (a) basal slip between 0.45 and 0.5, (b) prismatic slip between 0.45 and 0.5, (c) pyramidal $\langle a \rangle$ slip between 0.45 and 0.5, and (d) pyramidal $\langle a + c \rangle$ slip between 0.45 and 0.5 for the primary α phase in Microstructure B with a random texture.

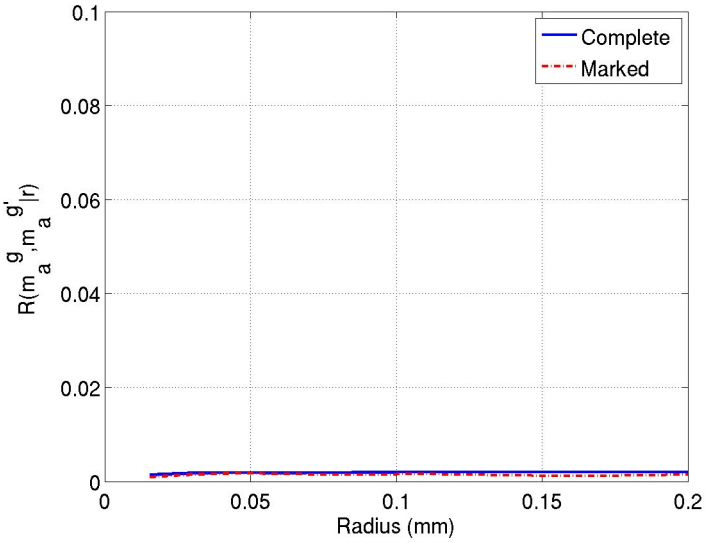

(c)

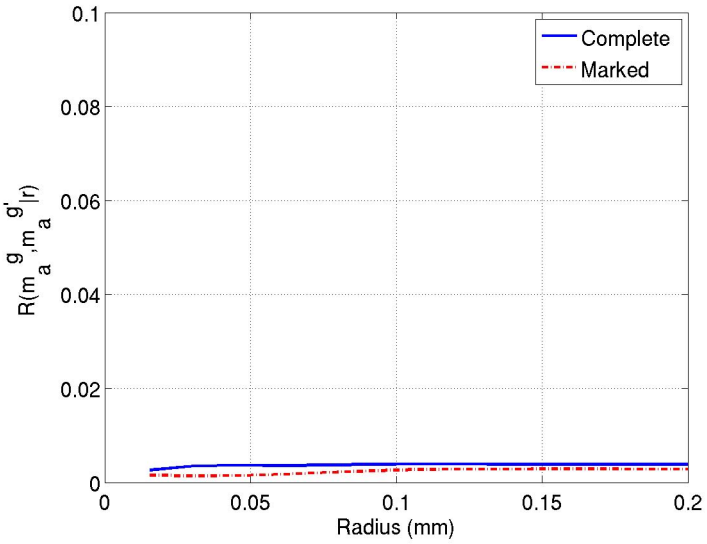

(d)

Figure 8.14: Radial correlation functions for the complete microstructure compared with EVMCF describing the correlation between the apparent Schmid factor m_a for prismatic slip between 0.45 and 0.5 for the primary α phase and the Schmid factor m'_a for: (a) basal slip between 0.45 and 0.5, (b) prismatic slip between 0.45 and 0.5, (c) pyramidal $\langle a \rangle$ slip between 0.45 and 0.5, and (d) pyramidal $\langle a + c \rangle$ slip between 0.45 and 0.5 for the primary α phase in Microstructure B with a random texture.

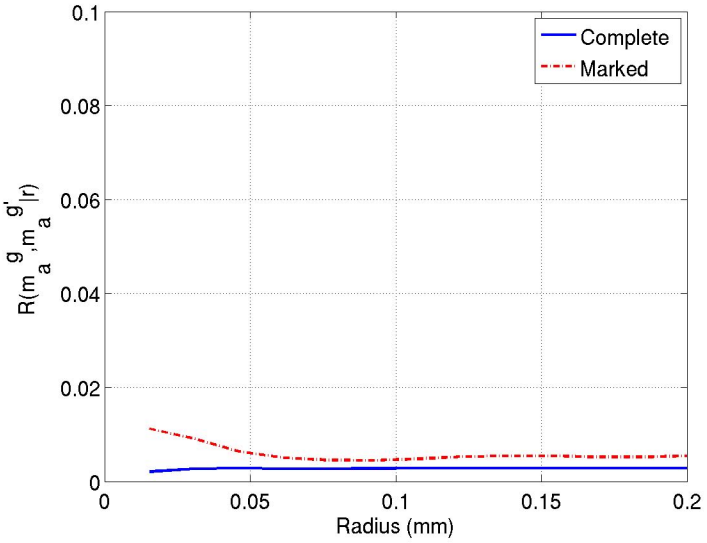

(a)

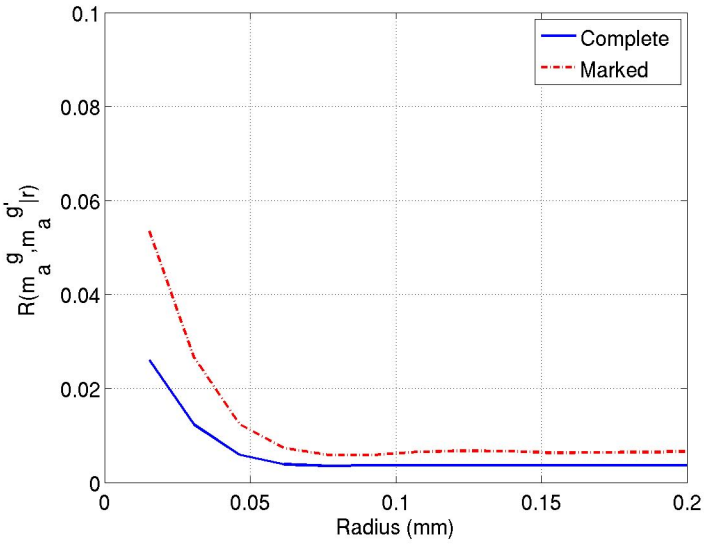

(b)

Figure 8.15: Radial correlation functions for the complete microstructure compared with EVMCF describing the correlation between the apparent Schmid factor m_a for prismatic slip between 0.45 and 0.5 for the primary α phase and the Schmid factor m'_a for: (a) basal slip between 0.45 and 0.5, (b) prismatic slip between 0.45 and 0.5, (c) pyramidal $\langle a \rangle$ slip between 0.45 and 0.5, and (d) pyramidal $\langle a + c \rangle$ slip between 0.45 and 0.5 for the primary α phase in Microstructure B with a strong basal texture.

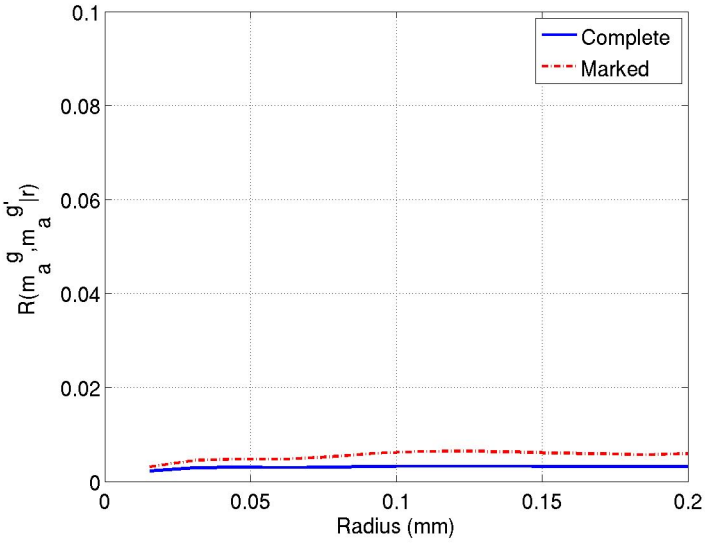

(c)

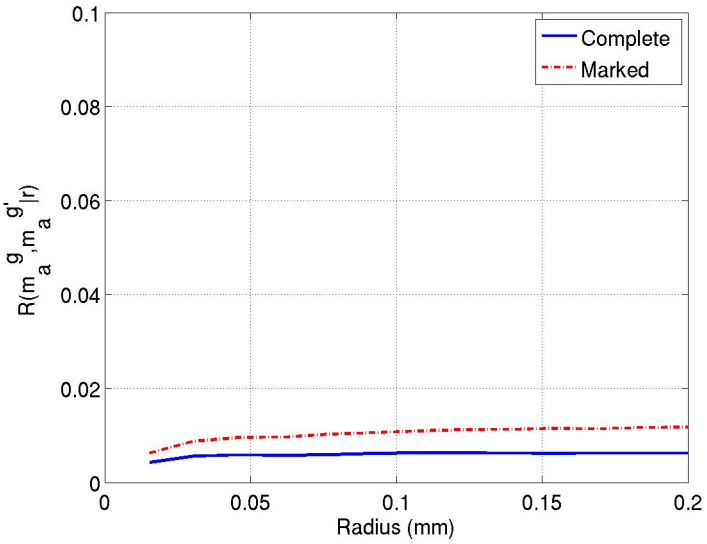

(d)

Figure 8.15: Radial correlation functions for the complete microstructure compared with EVMCF describing the correlation between the apparent Schmid factor m_a for prismatic slip between 0.45 and 0.5 for the primary α phase and the Schmid factor m'_a for: (a) basal slip between 0.45 and 0.5, (b) prismatic slip between 0.45 and 0.5, (c) pyramidal $\langle a \rangle$ slip between 0.45 and 0.5, and (d) pyramidal $\langle a + c \rangle$ slip between 0.45 and 0.5 for the primary α phase in Microstructure B with a strong basal texture.

that appeared to be most important to the processes of subsurface fatigue crack formation in the random textured microstructures. However, there was still a significant probability of finding basal oriented primary α grains near harder oriented primary α or $\alpha + \beta$ colony grains. This was unexpected as the basal texture was about nine times random (see Figure 8.2). It was shown, however, that even though basal slip did occur more than expected in the microstructures loaded perpendicular to the strong basal texture that designing microstructures with certain textures can produce materials that exhibit improved resistance to the damage evolution processes of interest or fatigue in this case. The microstructures with the strong basal texture did exhibited a clear reduction in the distribution in the extreme value FIPs. This supports the original hypothesis.

However, some microstructural variants performed better than others. For example, while Microstructure B did exhibit lower extreme value FIPs in the lower probability region, it had an opposite effect in the high probability region where the FIPs for the basal texture microstructure was greater than that of the random textured microstructure. This further indicates the importance of considering the interactions of multiple microstructure attributes relative to their influence on the extreme value driving forces for fatigue damage formation. While Microstructure A with the basal texture with small primary α grains and lower volume fractions of the primary α grains exhibited lower extreme value FIP distributions than the random textured case, Microstructure B with the same grain size as Microstructure A but with a higher volume fraction of primary α grains did not in the high probability region. It is likely a even stronger basal texture is required in the case of Microstructure B with the higher density of primary α grains to significantly decrease the likelihood of the existence of the grain combinations that have the greatest influence on the extreme value driving forces for fatigue crack formation.

8.4 Summary

Here the microstructure-sensitive extreme value probabilistic framework to evaluate material performance/variability for damage evolution processes was summarized in six steps in the context of materials design. Multiple SVEs for a given material system can be instantiated to evaluate the influence of the stochastic microstructure on the variability of the damage response. Physics based phenomenological models can then be used to predict how these SVEs would respond for given loading and boundary conditions. The distribution of the extreme value response can then be characterized for a given set of SVEs for a particular microstructure. Additionally, the EVMCF can be constructed to evaluate the significance of various coupled microstructure attributes relative to the extreme value response. With this information, multiple microstructures can be rank ordered in terms of maximum minimum response or minimum variability. Moreover, new candidate microstructure can be proposed based on the findings of previous iterations.

By using this type of computational framework in place of extensive experimentation multiple microstructural variants can be evaluated and down selected to a limited set of the most promising candidates for a given application. It is emphasized, however, that this framework does not eliminate the need for experimentation. To ensure a good solution, limited experimental calibration/validation is required for the utilized computational models. Moreover, the most promising microstructures should be thoroughly tested and validated experimentally before they are placed in service. The framework, however, does provide a powerful tool were many more microstructures can be evaluated than could ever be done experimentally. Additionally, simulation provides much more information in terms of the local stress/strain fields than can at this time be captured experimentally in three dimensional opaque materials except in limited rare cases (*e.g.*, with a synchrotron light source). This additional information can provide insight that is not always available experimentally, which can be used to direct the design of new microstructures that will exhibit better performance/variability for a given application.

To demonstrate the materials design of new material microstructures for a given material system based on the findings of applying the aforementioned framework to previously characterized microstructure, it was hypothesized that duplex Ti-6Al-4V microstructures would exhibit lower driving forces for fatigue crack formation when loaded perpendicular to a strong basal texture than was demonstrated with the random textured microstructures evaluated in Chapter 7. It was shown that the microstructures loaded perpendicular to a strong basal texture did tend to exhibit lower driving forces for fatigue damage formation. This was particularly true when the primary α grain size was small and the relative volume fraction of the primary α grains was relatively less that the other microstructures for the SVE size considered here. The noted exception was Microstructure B with the strong basal texture which did exhibit lower extreme value FIPs at lower probabilities than the random textured microstructures; however, at extremely high probabilities the extreme value FIPs were higher for the basal textured microstructures than the random texture microstructures. It is likely that with the increased volume fraction of the primary α grains an even stronger texture is necessary in the case of Microstructure B to significantly reduce the probabilities of the grain combinations that have the greatest influence on the extreme value driving forces for fatigue crack formation. This further supports the approach presented here that characterizes how coupled microstructure attributes affect the extreme value driving forces for fatigue crack formation. Although the basal textured microstructures exhibited less basal slip as expected, there still was a significant population of grains oriented for easy basal slip. Better performance can likely be achieved then shown here if a new set of microstructures can be designed such that the grains oriented for easy basal slip are even less prevalent than that of the microstructures demonstrated here.

CHAPTER IX

SUMMARY AND CONCLUSIONS

9.1 Overview

This dissertation has introduced a novel microstructure-sensitive extreme value probabilistic framework to evaluate material performance/variability for damage evolution processes (*e.g.*, fatigue, fracture, creep). Current methods that consider the microstructure-dependence of extreme value behavior for processes involving damage evolution within microstructure primarily only account for the extreme value distributions of single microstructure attributes (*e.g.*, grain/phase size, grain orientation, grain misorientation). However, in many damage evolution processes like fatigue of polycrystalline metals (see Chapter 2), the mechanisms of crack formation and propagation are not just dependent on a single attribute, but are a function of the complex interactions between multiple neighboring microstructure attributes. For example, the process of crystallographic fatigue crack formation in typical polycrystalline metals is dependent on phase/grain size, phase volume fraction, grain orientation, grain misorientation, *etc*.

As reviewed in Chapter 3, extreme value statistical theory has been developed extensively since the middle of the twentieth century. Gumbel [72] described many of the important results in his seminal work. In relation to variability in fatigue life, extreme value statistics has been applied to characterized how extreme value distributions of extreme value microstructure attributes influence the scatter of fatigue response [3]. However, as mentioned previously, little regard has been give as to how interacting microstructure attributes influence the extreme value response. As correlation functions have been used successfully for many years to characterize interrelationships between microstructure attributes, it

has been desired to use correlation functions to similarly characterize the coupled microstructure attributes that have the most influence on the extreme value response. Based on previous work that introduced marked correlation functions to describe how coupled microstructure attributes influences mean value response, here new extreme value marked correlation functions (EVMCFs) were introduced to describe how coupled microstructure attributes correlate with extreme value response. Specifically, these EVMCFs are designed to quantify the coupled microstructure attributes that have the greatest statistical relevance to the key extreme value response variables (*e.g.*, stress, elastic/plastic strain) that correlate with the damage evolution processes of interest.

As the application in this work was to characterize the microstructure-dependence of the variability in high cycle fatigue (HCF) in polycrystalline metals, crystal plasticity models were utilized to estimate local plasticity on the scale of the grains (the primary driving force for fatigue crack formation in most metals). In Chapter 4, the well defined kinematical relations for crystal plasticity constitutive models were reviewed. Additionally, various internal state variable models were considered that have been derived to model polycrystalline plasticity under cyclic loading conditions. In particular, constitutive models were considered for cyclic plasticity of pure copper, P/M Ni-base superalloy IN100, and duplex $\alpha + \beta$ Ti alloy Ti-6Al-4V.

In Chapter 5, simulation of multiple statistical volume elements (SVEs) was considered as a means to computationally estimate the microstructure-sensitive extreme value distributions of the driving forces for fatigue crack formation. Each SVE for a given response was instantiated to be a statistical sample of the entire ensemble; therefore, the response of interest in each SVE is not expected to be the same. This is in contrast to computational simulation of a single representative volume element (RVE), which often is untenably large for rare event (extreme value) phenomena. To instantiate SVEs for a given material system, two previously published methods for instantiation of microstructure volume elements of

polycrystalline materials were considered. The first method is based on the Voronoi tessellation. By randomly inserting grain centers and then optimizing their position via a simulated annealing algorithm, the Voronoi tessellation can be used to construct a set of space filling convex grains whose grain size/volume distribution can be fit to some prespecified distribution. Additionally, a similar simulated annealing algorithm can be used to fit distributions of grain orientation and grain disorientation to prespecified targets. The second algorithm considered here to instantiate microstructure volume elements, is based on packing grain equivalent ellipsoids into a volume and then filling the remaining space through a uniform grain growth technique. A grain equivalent ellipsoid is generated by fitting an ellipsoid to an experimentally characterized grain (in three dimensions) by using the zeroth, first and second order moments of the grain. The distribution of the ratios of the major axis of the grain equivalent ellipsoids fit to the set of experimentally characterized grains can then be used to describe the distribution in grain shape. The microstructure volume elements can be instantiated by packing ellipsoids whose major axes are randomly sampled from the pre-characterized/defined distributions of the ratios of the major axes of grain equivalent ellipsoids.

Additionally, in Chapter 5, various aspects of the FE simulation of SVEs were considered, including the application of appropriate meshes and boundary conditions to estimate the extreme value response on the scale of the dominant microstructural features (*e.g.* grains). The relations for the periodic boundary conditions were defined to simulate subsurface material conditions. The minimum SVE size was also evaluated for the periodic boundary conditions to ensure that the lower order moments of plasticity changed minimally with increasing SVE size. Specifically, the minimum number of grain neighbors required across the periodic boundary conditions to minimize further changes in the cyclic plastic response aveaged over a single grain was determined. Also the sensitivity of the extreme value response to the density of the voxellated mesh and averaging volume of response was considered.

In Chapters 6 and 7, the microstructure-sensitive extreme value framework was exercised to characterize the variability in fatigue crack formation in IN100 and duplex Ti-6Al-4V. Specifically, the framework was exercised to estimate the local driving forces for fatigue damage formation, to validate these with limited existing experiments, and to explore how the extreme value probabilities of certain fatigue indicator parameters (FIPs) affect overall variability in fatigue life in the HCF regime. Various FIPs have been introduced and used previously as a means to quantify the potential for fatigue crack formation based on experimentally observed mechanisms. In this manner, the distributions in the driving forces for different microstructural variants, loading conditions, and boundary conditions were considered. Via the EVMCF, important crystallographic relationships are shown to be statistically prevalent at the locations of extreme value response.

The framework is then described in terms of computational materials design in Chapter 8. Information gathered from previous application of the framework can be used to propose microstructural variants that are predicted to exhibit improved performance for a given application. In this manner, the design of microstructures more resistant to subsurface fatigue crack formation is considered for duplex Ti-6Al-4V by introducing textured microstructures that were designed to exhibit a special texture. These textured microstructures are then compared to the random textured microstructures considered previously for Ti-6Al-4V in Chapter 7.

9.2 Original and foundational concepts and methods introduced

This dissertation has introduced several original concepts and methods to aid in understanding microstructure-dependent extreme value damage evolution processes such as fatigue crack formation. Additionally, methods and strategies have been introduced to aid in the computational simulation of SVEs with distributed microstructure. Specifically, the original concepts and methods introduced here include:

- **Extreme-value marked correlation functions** - In Chapter 2, the novel concept

of extreme value marked correlation functions (EVMCF) was introduced. In contrast to the marked correlation functions introduced previously by Pyrz [119, 120] that characterizes how coupled attributes correlate with mean value response, these EVMCF describe correlation between coupled microstructure attributes and the extreme value response. These EVMCF are constructed by selectively sampling the correlation statistics of microstructure attributes at the locations of extreme value response. Coupling between various microstructure attributes with the EVMCFs can be described with any typical correlation function including, n-point correlation functions, nearest neighbor correlation functions, lineal path correlation functions, radial distribution functions, *etc.* The applicability of most types of correlation functions, allows flexibility in constructing the EVMCF depending on the material system and application of interest. Different types of correlation functions will provide different information for the considered application. EVMCFs offer a method to quantify the coupling between multiple microstructure attributes relative to their influence on the extreme value response of interest. Heretofore, such a direct method to quantify the influence of multiple interacting microstructure attributes on the extreme value response was not available.

- **Ellipsoid packing based polycrystal SVE instantiation** - Based on the concept of packing ellipsoids into a fixed volume, the software EllipPolycrystalGen was developed to instantiate polycrystalline microstructure volume elements with more realistic grain morphology. This algorithm generates ellipsoids by randomly sampling the distribution of aspect ratios of grain equivalent ellipsoids measured from experimentally characterized microstructures. In this manner, grains with more realistic geometry can be generated, including elongated grains such as those that would be observed in rolled materials. The initial ellipsoids packed in the volume are set to be some fraction of the actual size of the grain equivalent ellipsoids of the experimentally characterized microstructures. In this way, when no more non-overlapping

ellipsoids can be placed into the volume, an annealing algorithm is used to fill in the remaining empty space. Although, packing grain equivalent ellipsoids into a volume has been used previously as a method to generate volumes of polycrystalline microstructure, the application of an annealing algorithm to fill the remaining space is a concept unique to this work. Previous methods to generate polycrystalline microstructure with ellipsoid packing allowed for overlap between the ellipsoids placed into the volumes. The ellipsoids placed into the volume are set to be some fraction in size of the experimentally characterized grain equivalent ellipsoids so that after the ellipsoids are allowed to grow during the annealing step to fill the remaining empty space, the final grain volume distribution of these instantiated microstructures is close to that of the experimentally characterized microstructures. Similar to the algorithm developed to instantiate polycrystalline microstructure based on the Voronoi tessellation, VorPolycrystalGen, once the grain structure is instantiated, the grain orientation and disorientation is assigned and optimized to fit prespecified target distributions.

- **Use of multiple SVEs to estimate extreme value distribution of a response variable** - In Chapters 6-8, it was demonstrated that multiple SVEs could be instantiated and simulated to estimate the extreme value distributions of a response variable of interest. In this case, consideration was given for the extreme value driving forces for fatigue crack formation as estimated by the FIPs. Extreme value statistical theory recognizes that the asymptotic extreme value distributions can only be estimated if the sample size n is sufficient. The sample size for the extreme value distributions constructed in this work is related to the number of microstructure attributes in each SVE that most influence the microstructure-dependent response. It is assumed that if enough SVEs of sufficient size are simulated then the asymptotic extreme value distribution of the considered response can be estimated. In other words, to estimate the asymptotic extreme value distribution for the response of interest, the instantiated SVEs must contain a sufficiently large sample n of the microstructure attributes that

most influence that response. It was recognized that if the SVE size was not sufficient then the asymptotic form of the extreme value distribution of response could not be obtained. It is noted that depending on the application it is not always desirable to only consider volumes sufficient to estimate the asymptotic extreme value distributions. Such would be the case if one were considering the extreme value distributions of response at a notch root even if the critically stress volume at the notch root was insufficient to sample enough microstructure to estimate the asymptotic extreme value distribution of the response variable. The minimum size of the SVEs used in this work was argued to depend on the boundary and loading conditions. Essentially, the lower order moments of the extreme value response of interest averaged over a volume on the scale of the dominant microstructure attributes (*e.g.*, grains) should not very significantly if the size of the SVE is increased. Otherwise the volume does not constitute a SVE. This criteria used to set the minimum SVE size here, might not be sufficient to estimate the asymptotic extreme value distributions of the response as previously discussed. Determination of the minimum size required to estimate the asymptotic extreme value distribution is left for future work.

- **Microstructure-sensitive extreme value probabilistic framework for materials selection of microstructures with improved HCF resistance** - A general framework has been introduced for the design and selection of microstructures for improved microstructure-dependent extreme value response for applications dependent on damage evolution processes (*e.g.* fatigue, fracture, creep). This framework is based on application of the EVMCFs which characterize the coupled microstructure attributes that have the most statistical relevance to the extreme value response and helps to inform the design process for a given application. In contrast to traditional empirically based design strategies, this framework has the potential to reduce expensive experimentation and provide better information regarding the mechanisms of and microstructure attributes that most influence the damage evolution processes

of interest.

9.3 Instantiation of microstructure volume elements to simulate microstructure-sensitive extreme value fatigue response

In Chapter 5, the various aspect important to the simulation of instantiated microstructure volume elements have been considered. Specifically, it was shown that:

- Distributions of grain size/volume for microstructure volume elements instantiated via the Voronoi tessellation can be optimized to fit experimentally determined grain size distributions by randomly perturbing the grain centers using a simulated annealing algorithm. The Voronoi tessellation, however, offers limited control over the morphology of the grains. Additionally, the upper and lower of tails of the distribution of grain size/volume for the microstructure volume elements instantiated via the Voronoi tessellation tend to be truncated.

- Microstructure volume elements can be instantiated by packing ellipsoids into a volume. These ellipsoids are generated from distributions of aspect ratios of grain equivalent ellipsoids that have been fit to experimentally characterized grains. Using grain equivalent ellipsoids to instantiate polycrystalline microstructure allows much more control over grain shape than the previous considered Voronoi tessellation. For example, rolling textures with elongated grain can be generated, which was not the case with the microstructures instantiated based on the Voronoi tessellation. Additionally, multi-modal grain/phase size distributions can be generated.

- Grain orientation and grain disorientation can be fit to the respective target distribution prespecified by the user using a simulated annealing technique for both the Voronoi tessellation and ellipsoidal based microstructure instantiation techniques.

- For various mesh densities, the response calculated over nonlocal averaging volumes converges when the averaging volumes are on the scale of the grains. If the averaging

volumes are on the scale of the individual elements no convergence was achieved.

- The lower order moments of the grain scale plastic response are stable when SVEs are sufficiently large to incorporate at a minimum the 2nd nearest neighbor interactions before periodicity.

9.4 Microstructure-sensitive extreme value probabilities of fatigue in the Ni-base superalloy IN100

In Chapter 6, the developed microstructure-sensitive extreme value probabilistic framework was applied to evaluate HCF in the P/M Ni-base superalloy, IN100. Specifically, it was observed that:

- Multiple statistical volume elements (SVEs) can be instantiated and simulated using appropriate constitutive models to estimate extreme value distributions of key response parameters.

- Cyclic plastic strain based fatigue indicator parameters computed over nonlocal averaging volumes on the scale of the microstructure attributes relevant to the mechanisms of fatigue crack formation can be used to identify key microstructure attributes that correlate with extreme value response.

- The simulated extreme value distributions of the Fatemi-Socie fatigue indicator parameter (FIP) that estimate the driving forces for fatigue crack formation are fit with high confidence (*i.e.*, $R^2 > 0.97$) by the Gumbel distribution.

- The shape of the extreme value distributions of the Fatemi-Socie FIPs appears to be well defined with as few as 25 SVEs as demonstrated by the similarity in the parameters of the fits of the observations to the Gumbel distributions for sample sizes of 25, 50, 75 and 100 SVEs. A procedure was introduce to determine the minimum number of simulated SVEs required to adequately characterize the extreme value distribution of response. The number of data points is gradually increased

until the character of the extreme value distribution is relatively unchanged when further data points are added. If the extreme value distribution is described by one of the well known asymptotic extreme value distribution, the goodness of fit for a particular number of SVEs can easily be quantified by comparing the differences in the parameters of the fit asymptotic extreme value distribution for different sample sizes.

- Relative scatter in the distribution of the extreme value FIPs increases with reduced maximum applied cyclic loads. This is in agreement with what has been observed experimentally. It is likely that variability in the relative distribution of the driving forces for fatigue crack formation as estimated by the FIPs increases as the maximum applied load falls further below the macroscopic yield because the local plasticity becomes more heterogeneous.

- These simulations predict that cube slip may play an important role in fatigue crack formation, particularly when there are multiple grains oriented for cube slip clustered in the same region or clusters of grains oriented for cube slip surrounded by other grains oriented favorable for octahedral slip. These observations support the results of previous experiments of fatigue in this material system [210]. Thus, as fatigue crack formation is dominated by the presence of non-metallic inclusions or voids for this particular material system, it is expected that given two inclusions of similar character that fatigue cracks will form preferentially near the inclusion that is surrounded by grains or grain clusters unfavorably oriented for octahedral slip.

- There are many different grain combinations that do not increase the driving forces for fatigue crack formation as significantly as those with grains oriented with high magnitudes of the apparent Schmid factor (*i.e.* between 0.45-0.5) for cube slip. This understanding can inform the materials design of special textured materials for specific applications with well defined loading conditions.

9.5 Microstructure-sensitive extreme value probabilities of fatigue in duplex Ti-6Al-4V

In Chapter 7, the developed microstructure-sensitive extreme value probabilistic framework was applied to characterize fatigue crack formation in HCF of several microstructure variants of randomly textured duplex Ti-6Al-4V. Specifically, it was demonstrated that:

- The extreme value FIPs for the microstructures with lower volume fractions of the primary α phase and smaller grain sizes tended to be the lowest in magnitude.
- The grain size distribution appeared to have the most influence on the extreme value distributions of the FIPs followed by the volume fraction of the primary α grains.
- In agreement with experiments, primary α grains oriented favorably for basal slip (with a Schmid factor for basal slip between 0.45 and 0.5) have a much higher probability of being associated with the regions of extreme value FIPs than in the overall microstructure.
- In agreement with experiments, hard-soft grain interactions between primary α grains oriented favorably for basal slip and primary α grains oriented favorably for pyramidal or $\alpha+\beta$ colonies oriented favorably for BOR modified bcc slip correlate with increased driving forces for fatigue crack formation over a relatively wide range of $\alpha+\beta$ Ti alloy systems.
- Similar to that of IN100, increasing the peak cyclic load also decreased the relative scatter in the distribution of the extreme value FIPs.
- Grains oriented for easy basal slip (with Schmid factors between 0.45 and 0.5 for basal slip) are more prevalent at the locations of extreme value response at higher cyclic loads then at lower applied cyclic loads. It is likely that as the maximum applied load approaches yield, the neighborhood is less important than whether a grain is oriented for easy basal slip relative to the magnitude of the FIPs because

plasticity is more homogeneous. Whereas when the maximum applied load falls further below the macroscopic applied yield point, plasticity is more heterogeneous and only occurs at locations where the stress is concentrated due to soft-hard grain interactions, harder second phases, etc.

- If the scatter in the distribution in grain size can be reduced, the associated scatter in the distributions of the extreme value FIPs will also be less as demonstrated by the simulated microstructures with uniform cuboidal grains.

- It was shown that while the distributions for subsurface fatigue crack formation tend to be best described by the extreme value Gumbel distribution, the distribution in the driving forces for surface fatigue crack formation is better described by the extreme value Fréchet distribution. This is significant because as the extreme value Gumbel distribution describes tails that decay exponentially, the extreme value Fréchet distribution describes tails with polynomial decay. As exponential decay is faster, the distribution of the extreme value driving forces for surface crack formation will tend to be greater at higher probabilities than for subsurface crack formation.

- At low to moderate probabilities of the extreme value distributions for subsurface and surface fatigue crack formation there is significant overlap between the two distributions. This supports the observations of competing modes of failure between surface and subsurface fatigue crack formation which has been observed experimentally in these types of duplex Ti alloys (*e.g.*, [221, 232]).

9.6 Applicability of the proposed microstructure sensitive extreme value probabilistic framework to materials design

In Chapter 8, the microstructure-sensitive extreme value probabilistic framework for damage evolution processes was framed in the context of computational materials design. To demonstrate materials design via this framework, it was hypothesized that duplex Ti-6Al-4V microstructures would exhibit lower driving forces for fatigue crack formation when

loaded perpendicular to a strong basal texture than was demonstrated with the random textured microstructures evaluated in Chapter 7. It was concluded that:

- This type of computational framework can be used in place of extensive experimentation to evaluate multiple microstructural variants and down select to a limited set of the most promising candidates for a given application.
- To ensure a good solution, limited experimental calibration/validation is required because of the current limits in the capabilities of current computational models.
- The microstructure for duplex Ti-6Al-4V loaded perpendicular to a strong basal texture did exhibit an improvement in the extreme value driving forces for fatigue crack formation over the random textured microstructure in most cases. This was particularly the case for the microstructures with smaller primary α grain and smaller volume fractions of the primary α grains.
- In some cases, particularly for Microstructure B, the basal texture microstructures exhibited more variability and higher driving forces for fatigue damage formation than the random textured microstructures. It was shown that in these cases where the volume fraction of the primary α grains was high it is likely that an even stronger basal texture would be required to reduce the driving forces of fatigue crack formation.
- As shown by the EVMCFs, although the basal texture microstructures exhibited less basal slip, there still was a significant population of grains oriented for easy basal slip. A stronger basal texture would likely remove even more of the undesirable grain combinations that tend to increase the local driving forces for fatigue crack formation.

9.7 Recommendations for future work

A new framework has been introduced in this dissertation that can be used to evaluate the microstructure-sensitive extreme value response for damage evolution processes driven by

coupled interacting microstructure attributes. Additionally, this framework can be used in the context of computational materials designs to iterate through multiple microstructural variants for a given material system to identify the microstructures predicted to exhibit the best performance for a given application. This framework, however, has only been demonstrated for a few simple cases. Moreover, the application of this framework to computational materials design was only carried out for one iteration of a specific material system, duplex Ti-6Al-4V. A diverse field of importance is emerging relative to understanding how coupled microstructure attributes influence the extreme value response for various damage processes. This dissertation has only provided a general framework and more refinement likely is required. Several specific areas for immediate future work are suggested. Specifically, such areas include:

- **Microstructure representation for computational simulation**. Methods to simulate complex material microstructure such as that found in polycrystalline metals are lacking. For example, FE simulation of polycrystalline metals was demonstrated here with relatively coarse voxellated meshes that were limited to grain scale estimations of response. The grain boundaries are poorly resolved by these types of voxellated meshes and sub-grain scale understanding of response is limited. It currently is not clear how refined the grain boundaries and meshes have to be to capture the effects of grain boundaries. Various modeling strategies should be evaluated and considered in terms of their ability to estimate the extreme value response on the scale of the microstructure attributes of interest. For example, typically Lagrangian FE modeling approaches have been used to simulated deformation of solid materials. Are there other modeling approaches that might be better for some applications (*e.g.*, Eulerian based FE codes)? More efficient and robust algorithms also need to be developed to instantiate microstructure volume elements for simulation that are representative of real material systems. The first order methods considered here based on the Voronoi tessellation and on the placement of grain equivalent ellipsoids into a fixed volume

are likely not sufficient for high order estimation of the response at even the grain scale. Additionally, better algorithms must be developed to mesh complex microstructure; this is a very active area of on going research.

- **Development of improved constituitive models for polycrystals**. For the types of polycrystalline metallic material systems considered here, improved constituitive models that account for the role of grain boundaries in slip blockage and transmission, as well as models for slip heterogeneity (*e.g.*, banding in grains) should also be considered. Such processes are not considered in the current crystal plasticity models described in Chapter 4, but as reviewed in Chapter 2 are likely important for the processes of fatigue crack formation in these types of material systems. There are more recient nonlocal (gradient) plasticity models linked to GNDs and that purport to address dislocation pileups, but they do not expressly address slip blockage/transmission or slip heterogeniety (*e.g.*, [249–252]).

- **Application of the developed framework to other damage dependant processes such as creep and fracture**. In this work the microstructure-sensitive extreme value probabilistic framework was applied to consider the processes of fatigue crack formation in polycrystals. How can this framework be applied to consider the variability of other damage evolution processes? What models would be able to capture the extreme value response of interest for other damage evolution processes? There is much promise in the application of the developed framework to answer some of these questions.

- **Expanding EVMCFs to consider higher order microstructure coupling**. In this work, the EVMCFs were only constructed in terms of the radial distribution function. Algorithms need to be developed to characterize in EVMCFs in terms of other correlation functions. This will be particularly useful in the evaluation of anisotropic microstructures such as those that result from rolling processes. Consideration can also

be given to how can the EVMCF be constructed in terms of higher order correlation functions (*e.g.*. 3-point correlation function). There are also important unanswered questions concerning how to deal with the associated computational and data management challenges associated with higher-order EVMCFs. Particularly, how would one appropriately interrogate the plethora of information contained in even higher order correlation function to determine the most significant relationships between the microstructure attributes relative to the extreme value response?

- **Minimum SVE size required to characterize asymptotic extreme value distributions for a given response variable**. In this work, the SVE size was set to minimize changes in the lower order moments of the cyclic plastic response such that the local response on the scale of the dominant microstructure attributes would change little with increasingly larger volumes. Can a minimum SVE size be defined to characterize a converged asymptotic extreme value distribution for a response parameter of interest? How dependent is the asymptotic extreme value distributions for larger SVEs on SVE size? Do the asymptotic extreme value distributions for a given response converge to a single distribution for the largest SVEs indicating an upper bound on the response variable of interest? In contrast, do the asymptotic distributions continue to shift for increasingly larger volumes indicating that the response variables are unbounded? Is there a more systematic way to select SVEs for simulations to enhance efficiency of the estimation of the extreme value distributions of response such as what has been done for constructing RVE sets to estimate mean value response parameters (*cf.* [178])?

- **Determination of appropriate conditions by which to define the minimum SVE size to capture the interactions of the microstructure attributes on the appropriate length scale**. The procedure demonstrated here to determine the appropriate SVE size to ensure that the lower order moments of the cyclic plastic response on the scale

of the individual grains was described in Section 5.7. This method slowly increased the size of the periodic SVE by adding layers of grains until the response on the scale of the individual grains changed less then a certain percentage from one a SVE of one size to the next largest SVE considered. This approach was implemented for computational convenience as the crystal plasticity models employed here struggled with convergence for larger sized models (in terms of the number of integration points). It was shown that at a minimum, the periodic SVEs should be at least as large as necessary to capture second nearest neighbor interactions. In many cases the SVEs simulated in this work considered longer range interactions than the second nearest neighbor interaction. However, a more rigorous method to determine the minimum SVE size would require starting with very large periodic microstructure volume elements and then comparing the response averaged over individual grains for that large volume to that of the grain averaged response in smaller sized periodic microstructure volume elements. Many assumptions are made by starting with the smaller microstructures and going up in size versus the latter proposed method. For example, it is assumed that once the grain average response stabilizes from one size SVE to the next, this will hold for even larger SVEs. Additionally, it was assumed that the periodic boundary conditions minimally influenced the cyclic plastic response on the scale of the individual grains once that response converged to a relatively fixed value for increasingly larger SVEs. It is possible that longer range interactions can be neglected (or missed) by such an approach. Additionally, it is possible that the periodic boundary conditions could be biasing the response averaged on the scale of the individual grains. Therefore, it is suggested as future work to better clarify a more rigorous approach to define a minimum SVE size for a given length scale of interaction. Specifically, the approach of working from larger volumes to smaller ones should be compared to the approach used here to determine if longer range interactions are important for the cyclic plastic response on the scale of the individual grains.

How important are such longer range interactions on the lower order moments of the cyclic plastic response on the scale of the grains? How important are they on the higher order moments of the cyclic plastic response on the scale of the grains? Can the longer range interactions be neglected and still allow one to accurately compare and rank the extreme value response for a set of candidate microstructures? How do differing boundary conditions (*e.g.* periodic, traction free, fixed) affect the minimum SVE size?

- **Materials selection and design for extreme value distributions of microstructure attributes**. Materials selection and design has primarily been developed in terms of mean value response. Little work has been done to determine a framework for improving material response on the basis of tailoring extreme value attributes and associated responses such as minimum fatigue life. There are many potential processing challenges that need to be considered in developing materials that have been tailored to eliminate/introduce specific extreme value attributes. Specifically, how does one process a material to influence the extreme value attributes?

APPENDIX A

SEMI-IMPLICIT INTEGRATION OF CRYSTAL PLASTICITY CONSTITUTIVE RELATIONS

A.1 Semi-implicit integration scheme for constitutive relations for duplex Ti-6Al-4V crystal plasticity model

McGinty [166] proposed a integration scheme for large strain based crystal plasticity relations with fully implicit integration of the slip rates, but with explicit update of the hardening variables. The slip rates in power-law type rate-dependent crystal plasticity models such as those given in Equations 4.45 and 4.60 are the very difficult to integrate numerically. This difficulty of numerical integration is due to the fact that when terms in these power-law type flow rules are raised to a very large power (which is typically the case) instability results unless the term being raised to the large power is near unity. Numerical integration of the evolution of the hardening variables is typically much less stiff. Thus, for these power-law rate-dependent type models with fairly simple evolution of the hardening variables, the semi-implicit approach proposed by McGinty can be effective because fully implicit update of all the independent variables does not necessarily improve the result and is much more expensive computationally. Here this semi-implicit integration scheme will be demonstrated for the duplex Ti-6Al-4V crystal plasticity model introduced in Chapter 4.

Let $\Delta t = t_{n+1} - t_n$ be a generic time increment where t_n and t_{n+1} are the time at the beginning and end of the increment, respectively. To solve the global equilibrium equations over the time increment Δt, the values of the Cauchy stress, the internal state variables, and the material Jacobian matrix are required for each iteration. Hereafter the subscript $n + 1$ is assumed in the absence of any subscript unless otherwise specified. In this case the

independent variables are the slip rates $\dot{\gamma}^\alpha$ and the internal state variables χ^α and κ^α. It is assumed that t_n, $\mathbf{T}_n$, $\dot{\gamma}_n^\alpha$, χ_n^α, κ_n^α, $\mathbf{F}_n$ and the material constants are known and that an estimate $\mathbf{F}$ of is available at time $n+1$.

The objective is to determine the values of the independent variables at the end of the time step. A Newton-Raphson iterative technique is used to estimate the current value of the slip rates (*cf.* [253]). The other independent variables are estimated explicitly for each iteration of the Newton-Raphson loop. If the flow rule given in Equation 4.60 is set to zero, this results in the function f^α such that

$$f^\alpha = \dot{\gamma}^\alpha - \dot{\gamma}_o \left\langle \frac{|\tau^\alpha - \chi^\alpha| - \kappa^\alpha}{D^\alpha} \right\rangle^M \operatorname{sgn}(\tau^\alpha - \chi^\alpha) = 0 \tag{A.1}$$

The value of the function in Equation A.1 at $\dot{\gamma}^\beta$ can be approximated using a Taylor series expansion about $\dot{\gamma}_n^\beta$, *i.e.*,

$$f^\alpha\left(\dot{\gamma}^\beta\right) = f^\alpha\left(\dot{\gamma}_n^\beta\right) + \sum_\beta^N \frac{\partial f^\alpha\left(\dot{\gamma}_n^\beta\right)}{\partial \dot{\gamma}^\beta} \Delta\dot{\gamma}^\beta + O\left[\left(\dot{\gamma}^\beta\right)^2\right] + \ldots \tag{A.2}$$

Neglecting the higher order terms (*i.e.*, $O\left[\left(\dot{\gamma}^\beta\right)^2\right]$) and recognizing that $f^\alpha\left(\dot{\gamma}^\beta\right) = 0$ (see Equation A.1), the result is

$$f^\alpha\left(\dot{\gamma}_n^\beta\right) \cong -\sum_\beta^N \frac{\partial f^\alpha\left(\dot{\gamma}_n^\beta\right)}{\partial \dot{\gamma}^\beta} \Delta\dot{\gamma}^\beta \tag{A.3}$$

Solving the set of simultaneous equations given in Equation A.3 for $\Delta\dot{\gamma}^\beta$ results in a new estimate of $\dot{\gamma}^\beta$. Even though the higher order terms were neglected, a highly accurate estimate of $\dot{\gamma}^\beta$ can be obtained by solving Equation A.3 repeatedly, each time starting with the new estimate of $\dot{\gamma}^\beta$ determined from the previous iteration. This iteration is repeated until a error threshold is satisfied between the values of the slip rates from the previous iteration and their values from the current.

The Jacobian of the Newton-Raphson iteration, $\partial\left(\dot{\gamma}^\alpha\right)/\partial\dot{\gamma}^\beta$, is determined by differentiating Equation A.1.

To calculate the derivatives of the absolute value, consider that for an arbitrary real number u (*i.e.* $u \in \Re$), $|u| = \sqrt{u^2}$ such that $|u|$ denotes the absolute value of u. If u is a real valued function of x such that $f(x) = |u(x)| = \sqrt{u(x)^2}$, then by the chain rule it can be shown that

$$f'(x) = \frac{df}{du}\frac{du}{dx} = \frac{1}{2}\left(u^2\right)^{-\frac{1}{2}} \cdot 2u \cdot \frac{du}{dx} \tag{A.4}$$

Simplifying Equation A.4 yields

$$f'(x) = \frac{u(x)\,u'(x)}{|u(x)|} = u'(x)\,\mathrm{sgn}(u(x)) \tag{A.5}$$

By Equation A.5, the derivative of Equation A.1 is given as

$$\frac{\partial f^\alpha}{\partial \dot{\gamma}^\beta} = \frac{\partial \dot{\gamma}^\alpha}{\partial \dot{\gamma}^\beta} - \dot{\gamma}_o M \left\langle \frac{|\tau^\alpha - \chi^\alpha| - \kappa^\alpha}{D^\alpha} \right\rangle^{M-1} \left[\frac{\left(\frac{\partial \tau^\alpha}{\partial \dot{\gamma}^\beta} - \frac{\partial \chi^\alpha}{\partial \dot{\gamma}^\beta}\right)\mathrm{sgn}(\tau^\alpha - \chi^\alpha) - \left(\frac{\partial \kappa^\alpha}{\partial \dot{\gamma}^\beta}\right)}{D^\alpha} - \frac{|\tau^\alpha - \chi^\alpha| - \kappa^\alpha}{(D^\alpha)^2}\left(\frac{\partial D^\alpha}{\partial \dot{\gamma}^\beta}\right) \right] \tag{A.6}$$

To determine $\partial \tau^\alpha / \partial \dot{\gamma}^\beta$, the chain rule can be applied such that

$$\frac{\partial \tau^\alpha}{\partial \dot{\gamma}^\beta} = \left[\left(\frac{\partial \tau^\alpha}{\partial \mathbf{T}}\right) : \left(\frac{\partial \mathbf{T}}{\partial \mathbf{E}^e}\right) : \left(\frac{\partial \mathbf{E}^e}{\partial \mathbf{F}^e}\right) : \left(\frac{\partial \mathbf{F}^e}{\partial \mathbf{F}^p}\right) : \left(\frac{\partial \mathbf{F}^p}{\partial \mathbf{L}_o^p}\right) : \left(\frac{\partial \mathbf{L}_o^p}{\partial \dot{\gamma}^\beta}\right) \right] \tag{A.7}$$

The first four term on the right hand side of Equation A.7 can be derived from Equations 4.23, 4.14, 4.15, 4.4, respectively. Note that all the parameters are based on their values at the end of the time step. The last two terms on the right hand side of Equation A.7 is determined by integrating Equations 4.7 and 4.8, respectively. Integrating the rate of change of the plastic deformation gradient given in Equation 4.7 *i.e.*, $\dot{\mathbf{F}}^p = \mathbf{L}_o^p \cdot \mathbf{F}^p$ yields

$$\mathbf{F}^p = \exp\left(\mathbf{L}_o^p \Delta t\right) \cdot \mathbf{F}_n^p \tag{A.8}$$

The exponential in Equation A.8 can be estimated by the Cayley-Hamilton theorem of linear algebra as done by McGinty [166], *i.e.*,

$$\exp\left(\mathbf{L}_o^p \Delta t\right) = \mathbf{I} + \frac{\sin\phi}{\phi}\left(\mathbf{L}_o^p \Delta t\right) + \frac{1-\cos\phi}{\phi^2}\left(\mathbf{L}_o^p \cdot \mathbf{L}_o^p\right)(\Delta t)^2 \tag{A.9}$$

where

$$\phi = \sqrt{\frac{1}{2}\left(\mathbf{L}_o^p : \mathbf{L}_o^p\right)}\Delta t \tag{A.10}$$

Equation A.7 can be simplified by neglecting the higher order terms (see [166]), *i.e.*,

$$\frac{\partial \tau^\alpha}{\partial \dot{\gamma}^\beta} = \cong -\mathbf{P}^\alpha : \mathbb{C} : \mathbf{P}^\beta \tag{A.11}$$

As the Jacobian only affects the convergence of the solution and not the accuracy of the final answer, the approximation given by Equation A.11 does not affect the final result.

Update of the hardening variables is done explicitly at each stage of the Newton-Raphson iterative loop. The current backstress can been estimated via a backward Euler scheme such that

$$\chi^\alpha = \chi_n^\alpha + \dot{\chi}^\alpha \Delta t \tag{A.12}$$

Recalling the evolution of the backstress defined in Equation 4.61, Equation A.12 becomes

$$\chi^\alpha = \chi_n^\alpha + \left[h\dot{\gamma}^\alpha - h_D \chi^\alpha \left|\dot{\gamma}^\alpha\right|\right]\Delta t \tag{A.13}$$

The derivative of the backstress with respect to the slip rates (*i.e.*, $\frac{\partial \chi^\alpha}{\partial \dot{\gamma}^\beta}$) required in Equation A.6, can be determined via the chain rule, *i.e.*,

$$\frac{\partial \chi^\alpha}{\partial \dot{\gamma}^\beta} = \frac{\partial \chi^\alpha}{\partial \dot{\gamma}^\alpha}\frac{\partial \dot{\gamma}^\alpha}{\partial \dot{\gamma}^\beta} \tag{A.14}$$

Taking the derivative of Equation A.13 with respect to $\dot{\gamma}^\beta$ yields

$$\frac{\partial \chi^\alpha}{\partial \dot{\gamma}^\alpha} = \frac{\partial \chi_n^\alpha}{\partial \dot{\gamma}^\alpha} + \left[h - h_D \chi^\alpha \mathrm{sgn}\left(\dot{\gamma}^\alpha\right) - h_D \left|\dot{\gamma}^\alpha\right| \frac{\partial \chi^\alpha}{\partial \dot{\gamma}^\alpha}\right]\Delta t \tag{A.15}$$

Because χ_n^α is assumed constant over the time step, $\partial\chi_n^\alpha/\partial\dot{\gamma}^\alpha = 0$. Solving Equation A.15 for $\partial\chi^\alpha/\partial\dot{\gamma}^\alpha = 0$ yields

$$\frac{\partial\chi^\alpha}{\partial\dot{\gamma}^\alpha} = \frac{\left[h - h_D\chi^\alpha \mathrm{sgn}\left(\dot{\gamma}^\alpha\right)\right]\Delta t}{1 + h_D\left|\dot{\gamma}^\alpha\right|\Delta t} \tag{A.16}$$

Inserting Equation A.16 into Equation A.14 yields

$$\frac{\partial\chi^\alpha}{\partial\dot{\gamma}^\beta} = \left\{\frac{\left[h - h_D\chi^\alpha \mathrm{sgn}\left(\dot{\gamma}^\alpha\right)\right]\Delta t}{1 + h_D\left|\dot{\gamma}^\alpha\right|\Delta t}\right\}\delta_{\alpha\beta} \tag{A.17}$$

because $\delta_{\alpha\beta} = \partial\dot{\gamma}^\alpha/\partial\dot{\gamma}^\beta$ such that $\delta_{\alpha\beta}$ is the Dirac delta function and $\delta_{\alpha\beta} = 0$ if $\alpha \neq \beta$. Thus, Equation A.17 simplifies to

$$\frac{\partial\chi^\alpha}{\partial\dot{\gamma}^\alpha} = \left\{\frac{\left[h - h_D\chi^\alpha \mathrm{sgn}\left(\dot{\gamma}^\alpha\right)\right]\Delta t}{1 + h_D\left|\dot{\gamma}^\alpha\right|\Delta t}\right\} \tag{A.18}$$

The update of the threshold stress is calculated in the same manner as that of the back-stress using a backward Euler scheme, *i.e.*

$$\kappa^\alpha = \kappa_n^\alpha + \left[-\mu\kappa_s^\alpha\left|\dot{\gamma}^\alpha\right|\right]\Delta t \tag{A.19}$$

were the evolution of the threshold stress was defined previously in Equation 4.63. The derivative of the threshold stress with respect to the slip rate which is required to compute Equation A.6 is derived in a similar manner to that of Equation A.18, *i.e.*,

$$\frac{\partial\kappa^\alpha}{\partial\dot{\gamma}^\alpha} = \frac{\left[-\mu\left(\kappa^\alpha - \frac{\kappa_y}{\sqrt{d^\alpha}}\right)\mathrm{sgn}\left(\dot{\gamma}^\alpha\right)\right]\Delta t}{1 + \mu\left|\dot{\gamma}^\alpha\right|\Delta t} \tag{A.20}$$

There is no evolution of the drag stress (*i.e.* $\dot{D}^\alpha = 0$); therefore, the terms with the derivatives of the drag stress in Equation A.6 drops out. Thus, all the terms necessary to calculate the local Jacobian in Equation A.6 required to calculate the slip rates have now been defined, *i.e.*,

$$\frac{\partial f^\alpha}{\partial\dot{\gamma}^\beta} = \delta_{\alpha\beta} - \dot{\gamma}_o M\left\langle\frac{\left|\tau^\alpha - \chi^\alpha\right| - \kappa^\alpha}{D^\alpha}\right\rangle^{M-1}\left(\frac{1}{D^\alpha}\right) \tag{A.21}$$

A line search algorithm is also applied at the end of each iteration of the Newton-Raphson loop to aid in convergence.

A weighted convergence criteria applied to the Newton-Raphson loop is applied to calculated the error, *i.e.*,

$$ERROR \equiv \frac{1}{N}\sqrt{\sum_{\alpha=1}^{N}\left(\frac{\dot{\gamma}^{\alpha}}{\dot{\gamma}_{\max}}f^{\alpha}\right)^{2}} \leq TOL \tag{A.22}$$

where $\dot{\gamma}_{\max} \equiv |\dot{\gamma}^{\alpha}|$ for $\alpha = 1, \ldots, N$. By using this weighted convergence criterion, the solution does not waist time trying to solve for relatively insignificant slip rates.

A.2 Estimation of the material Jacobian

ABAQUS [121] standard requires the UMAT to send back an estimation of the material Jacobian for the constitutive model at each integration point. The form of the Jacobian required by ABAQUS is

$$\frac{\partial\left(\Delta\boldsymbol{\sigma}\right)}{\partial\left(\Delta\boldsymbol{\epsilon}\right)} \tag{A.23}$$

where $\Delta\boldsymbol{\sigma}$ is the increment in the Cauchy stress and $\Delta\boldsymbol{\epsilon}$ is the increment in the total (integrated) strain over the time increment dt, *i.e.*,

$$\Delta\boldsymbol{\epsilon} = \int_{t_n}^{t_{n+1}} \mathbf{D}dt \tag{A.24}$$

The rate of deformation $\mathbf{D}$ was previously defined in Equation 4.12. The material Jacobian can be approximated in rate form as

$$\frac{\partial\left(\Delta\boldsymbol{\sigma}/\Delta t\right)}{\partial\left(\Delta\boldsymbol{\epsilon}/\Delta t\right)} \approx \frac{\partial\dot{\boldsymbol{\sigma}}}{\partial\mathbf{D}} \tag{A.25}$$

Hill and Rice [127] suggested that the elastic law of single crystals under large deformation can be expressed as

$$\overset{\triangledown}{\boldsymbol{\sigma}} + \boldsymbol{\sigma}\mathrm{tr}\left(\mathbf{D}^{e}\right) = \mathbb{C} : \mathbf{D}^{e} \tag{A.26}$$

The elastic part of the rate of deformation tensor $\mathbf{D}^e$ is defined such that $\mathbf{D} = \mathbf{D}^e + \mathbf{D}^p$ where $\mathbf{D}^p$ is the inelastic rate of deformation tensor. The Jaumann rate of the Cauchy stress $\overset{\triangledown}{\boldsymbol{\sigma}}$ is defined as

$$\overset{\triangledown}{\boldsymbol{\sigma}} = \dot{\boldsymbol{\sigma}} - \mathbf{W}^e \cdot \boldsymbol{\sigma} + \boldsymbol{\sigma} \cdot \mathbf{W}^e \tag{A.27}$$

where $\dot{\boldsymbol{\sigma}}$ is the material time rate of $\boldsymbol{\sigma}$ and $\mathbf{W}^e$ is the elastic spin tensor. Neglecting the spin terms on assuming tr $(\mathbf{D}^e)$ to be small, results in the expression

$$\dot{\boldsymbol{\sigma}} = \mathbb{C} : \mathbf{D}^e = \mathbf{C} : (\mathbf{D} - \mathbf{D}^p) \tag{A.28}$$

Differentiating Equation A.28 with respect to the rate of deformation tensor results in

$$\frac{\partial \dot{\boldsymbol{\sigma}}}{\partial \mathbf{D}} = \mathbb{C} - \mathbb{C} : \left(\frac{\partial \mathbf{D}^p}{\partial \boldsymbol{\sigma}}\right) : \left(\frac{\partial \boldsymbol{\sigma}}{\partial \dot{\boldsymbol{\sigma}}}\right) : \left(\frac{\partial \dot{\boldsymbol{\sigma}}}{\partial \mathbf{D}}\right) \tag{A.29}$$

Assuming that $\boldsymbol{\sigma} = \boldsymbol{\sigma}_n + \dot{\boldsymbol{\sigma}}\Delta t$ and recognizing that

$$\left.\frac{\partial \boldsymbol{\sigma}}{\partial \dot{\boldsymbol{\sigma}}}\right|_{\text{fixed orientation}} = (\mathbf{I} \otimes \mathbf{I})\, \Delta t \tag{A.30}$$

Equation A.29 can be simplified such that

$$\frac{\partial \dot{\boldsymbol{\sigma}}}{\partial \mathbf{D}} = \left[\mathfrak{I} + \mathbb{C} : \left(\frac{\partial \mathbf{D}^p}{\partial \boldsymbol{\sigma}}\right) \Delta t\right]^{-1} : \mathbb{C} \tag{A.31}$$

where $\mathfrak{I}$ is the fourth rank identity tensor.

The derivative of the plastic rate of deformation tensor with respect to the Cauchy stress $\partial \mathbf{D}^P / \partial \boldsymbol{\sigma}$ can be estimate via the chain rule, *i.e.*,

$$\frac{\partial \mathbf{D}^P}{\partial \boldsymbol{\sigma}} = \frac{\partial \mathbf{D}^P}{\partial \dot{\gamma}^\alpha} \frac{\partial \dot{\gamma}^\alpha}{\partial \tau^\alpha} \frac{\partial \tau^\alpha}{\partial \boldsymbol{\sigma}} \tag{A.32}$$

To calculate $\partial \mathbf{D}^P / \partial \dot{\gamma}^\alpha$, it is recognized that the plastic part of the rate of deformation tensor is calculated as shown by Equation 4.12, *i.e.*,

$$\mathbf{D}^p = \frac{1}{2}\left[\mathbf{L}^p + (\mathbf{L}^p)^T\right] \tag{A.33}$$

Note that these tensors are all calculated in the current reference frame. Recalling that the plastic velocity gradient in the current reference frame is given by Equation 4.9 which can be expressed as

$$\mathbf{D}^p = \frac{1}{2}\mathbf{F}^e \cdot \left\{\sum_{\alpha=1}^{N_\alpha}\left[\dot{\gamma}^\alpha \mathbf{P}^\alpha + \dot{\gamma}^\alpha (\mathbf{P}^\alpha)^T\right]\right\} \cdot (\mathbf{F}^e)^{-1} \tag{A.34}$$

Taking the derivative of Equation A.34 with respect to the slip rates yields

$$\frac{\partial \mathbf{D}^p}{\partial \dot{\gamma}^\alpha} = \frac{1}{2}\mathbf{F}^e \cdot \left\{\sum_{\alpha=1}^{N_\alpha}\left[\mathbf{P}^\alpha + (\mathbf{P}^\alpha)^T\right]\right\} \cdot (\mathbf{F}^e)^{-1} \tag{A.35}$$

The derivative of the slip rates with respect to the resolved shear stress can be calculated directly from the flow rule in Equation 4.60 and the previously defined derivatives for the hardening variables in Equations A.18 and A.20 , respectively, *i.e.*,

$$\frac{\partial \dot{\gamma}^\alpha}{\partial \tau^\alpha} = \dot{\gamma}_o M \left\langle \frac{|\tau^\alpha - \chi^\alpha| - \kappa^\alpha}{D^\alpha} \right\rangle^{M-1} \left(\frac{1}{D^\alpha}\right) \tag{A.36}$$

The derivative of the resolved shear stress with respect to the Cauchy stress $\partial\tau^\alpha/\partial\boldsymbol{\sigma}$ can be determined directly from Equations 4.16 and 4.22, *i.e.*,

$$\frac{\partial \tau^\alpha}{\partial \boldsymbol{\sigma}} = \mathbf{P}^\alpha \tag{A.37}$$

Thus, all necessary derivatives have been defined for Equation A.29.

APPENDIX B

LINEARIZATION AND FIT OF THE GUMBEL DISTRIBUTION

From Section 3.2, it is recalled that the cumulative distribution function (CDF) of the Gumbel extreme value distribution for the largest values can be expressed as

$$F^I_{Y_n}(y) = \exp\left[-e^{-\alpha_n(y-u_n)}\right] \tag{B.1}$$

where u_n is the characteristic largest value of the initial variate X, and α_n is an inverse measure of dispersion of the largest value of X. Here n refers to the size of the samples of the initial variate X in the set of distributions of X from which Y_n is sampled. The expression in Equation B.1 is the asymptotic form of the Type I extreme value distribution of the largest values and therefore is valid as the sample size approaches infinity [75]. To linearize the Gumbel distribution, Equation B.1 can be solved for the extreme value parameter y given a probability p, *i.e.*,

$$\ln\left[\ln\left(\frac{1}{p}\right)\right]^{-1} = \alpha_n y - \alpha_n u_n \tag{B.2}$$

Thus, an expression is obtained in the form $y = mx + b$ of where $y = \ln\left[\ln\left(1/p\right)\right]^{-1}$, $m = \alpha_n$, $x = y$, and $b = -\alpha_n u_n$. Ranking the data from a sample of the extreme value distribution Y_n in the order of smallest to largest (*i.e.*, $y^1, y^2, \ldots, y^n$), one can determine estimators $F_{Y_n}\left(y^1\right)$, $F_{Y_n}\left(y^2\right)$, $F_{Y_n}\left(y^n\right)$, *etc.* using the median rank statistic defined as

$$\tilde{y} = \frac{j - 0.3}{n + 0.4} \tag{B.3}$$

for the j^{th} ranked observation in a sample of size n [254]. Here the superscripts on y refer to their rank for a particular sample of Y_n. The procedure then to plot a given dataset on a linearized scale for the Gumbel distribution is:

1. Using Equation B.1, the probability for each observation in the dataset is estimated.

2. Determine $\ln\left[\ln\left(1/p\right)\right]^{-1}$ for each observation and plot it against the original observation.

3. Using a least squares (or similar) fit, a line of the form $y = mx + b$ is fit to the data.

4. The estimated parameters for the distribution is determined according to $m = \alpha_n$, $x = y$, and $b = -\alpha_n u_n$.

This general procedure is outlined and explained in detail by Kapur and Lamerson [254] for similar distributions.

REFERENCES

[1] (2008) Document # ENG06IA018. National Transportation Safety Board (NTSB). [Online]. Available: http://ntsb.gov/ntsb/brief.asp?ev_id=20060809X01126&key=1 1.1

[2] J. Escobar. (2008) American airlines 767 engine failure. Aircraft Maintenance Technology (AMT) Society. [Online]. Available: "http://www.amtonline.com/web/online/Top-News/American-Airlines-767-Engine-Failure/1$2404" 1.1

[3] H. V. Atkinson and G. Shi, "Characterization of inclusions in clean steels: a review including the statistics of extremes methods," *Progress in Materials Science*, vol. 48, no. 5, pp. 457–520, 2003. 1.2, 1.2, 3.3.2, 3.5, 3.3.2, 7.1.1, 9.1

[4] W. Weibull, "A statistical theory of the strength of materials," in *Proceedings 151*. Stockholm: Royal Swedish Academy of Engineering Sciences, 1939. 1.2, 3.3.1

[5] S. Suresh, *Fatigue of Materials*, 2nd ed. Cambridge: Cambridge University Press, 1998. 1.2, 2.2.1, 2.2.2, 4.1, 4.2, 7.1.1

[6] D. L. McDowell, "Basic issues in the mechanics of high cycle metal fatigue," *International Journal of Fracture*, vol. 80, no. 2-3, pp. 103–45, 1996. 1.2, 2.2.1, 2.3.1, 2.3.1, 6.2.4, 7.1.1

[7] S. Torquato, *Random heterogeneous materials : microstructure and macroscopic properties*, ser. Interdisciplinary applied mathematics ; v. 16. New York: Springer, 2002. 1.3.1, 3.4, 3.4.1

[8] M. Groeber, S. Ghosh, M. D. Uchic, and D. M. Dimiduk, "A framework for automated analysis and simulation of 3d polycrystalline micro structures. part 1: Statistical characterization," *Acta Materialia*, vol. 56, no. 6, pp. 1257–1273, 2008. 1.3.2, 5.3, 5.3.2, 7.2.3

[9] M. Groeber, S. Ghosh, M. D. Uchic, and D. M. Dimiduk, "A framework for automated analysis and simulation of 3d polycrystalline micro structures. part 2: Synthetic structure generation," *Acta Materialia*, vol. 56, no. 6, pp. 1274–1287, 2008. 1.3.2, 5.3, 5.3.2, 7.2.3

[10] P. Forsyth, "A two-stage process of fatigue crack growth," in *Symposium on Crack Propagation*, Cranfield, 1971, pp. 76–94. 2.2

[11] K. J. Miller, "Metal fatigue. past, current and future," *Proceedings of the Institution of Mechanical Engineers C*, vol. 205, no. 5, pp. 291–304, 1991. 2.2, 2.2.1

[12] K. J. Miller, "Materials science perspective of metal fatigue resistance," *Materials Science and Technology*, vol. 9, no. 6, pp. 453–62, 1993. 2.2, 2.2.1

[13] D. L. McDowell, "Multiaxial fatigue strength," in *ASM Handbook*. Materials Park, OH: ASM International, 1996, vol. 19, pp. 263–273. 2.2, 2.3.1

[14] D. F. Socie, "Critical plane approaches for multiaxial fatigue damage assessment," in *Advances in Multiaxial Fatigue, ASTM STP 1191*, D. L. McDowell and R. Ellis, Eds. Philadelphia: American Society of Testing and Materials, 1993, pp. 7–36. 2.2, 2.3.1, 2.3.1, 2.3.1, 6.2.4

[15] D. L. McDowell, "Multiaxial small fatigue crack growth in metals," *International Journal of Fatigue*, vol. 19, no. Suppl 1, pp. 127–135, 1997. 2.2

[16] D. L. McDowell, "Damage mechanics and metal fatigue: a discriminating perspective," *International Journal of Damage Mechanics*, vol. 8, no. 4, pp. 376–403, 1999. 2.2, 2.3.1

[17] B.-T. Ma and C. Laird, "Overview of fatigue behavior in copper single crystals. I. Surface morphology and stage I crack initiation sites for tests at constant strain amplitude," *Acta Metallurgica*, vol. 37, no. 2, pp. 235–336, 1989. 2.1

[18] J. C. Figueroa and C. Laird, "Crack initiation mechanisms in copper polycrystals cycled under constant strain amplitudes and in step tests," *Materials Science and Engineering*, vol. 60, no. 1, pp. 45–58, 1983. 2.2

[19] P. Neumann and A. Tönnessen, "Crack initiation at grain boundaries in f.c.c. materials," in *Strength of Metals and Alloys*, P. Kettunen, T. Lepistö, and M. Lehtonen, Eds. Oxford: Pergamon, 1988, vol. 2, pp. 743–748. 2.3

[20] J. Lankford and F. N. Kusenberger, "Initiation of fatigue cracks in 4340 steel," *Metallurgical Transactions*, vol. 4, no. 2, pp. 553–559, 1973. 2.4

[21] D. L. McDowell, "An engineering model for propagation of small cracks in fatigue," *Engineering Fracture Mechanics*, vol. 56, no. 3, pp. 357–77, 1997. 2.2.1, 2.2.2

[22] K. Dang Van, "Macro-micro approach in high-cycle multiaxial fatigue," in *Advances in Multiaxial Fatigue, ASTM STP 1191*, D. L. McDowell and R. Ellis, Eds. Philidelphia: ASTM, 1993, pp. 120–130. 2.2.1, 2.3.1

[23] K. Tanaka, "Short-crack fracture mechanics in fatigue conditions," in *Current Research on Fatigue Cracks, Current Japanese Materials Research*, T. Tanaka, M. Jono, and K. Komai, Eds. Amsterdam: Elsevier, 1987, vol. 1, pp. 93–117. 2.2.1

[24] K. Tanaka and Y. Akiniwa, "Propagation and non-propagation of small fatigue cracks," in *ICF7*, Houston, TX, 1989, pp. 869–887. 2.2.1

[25] K. Tanaka, Y. Akiniwa, Y. Nakai, and R. P. Wei, "Modelling of small fatigue crack growth interacting with grain boundary," *Engineering Fracture Mechanics*, vol. 24, no. 6, pp. 803–819, 1986. 2.2.1

[26] K. Tokaji, T. Ogawa, Y. Harada, and Z. Ando, "Limitations of linear elastic fracture mechanics in respect of small fatigue cracks and microstructure," *Fatigue and Fracture of Engineering Materials and Structures*, vol. 9, no. 1, pp. 1–14, 1986. 2.2.1

[27] K. S. Chan, J. Lankford, and D. L. Davidson, "Comparison of crack-tip field parameters for large and small fatigue cracks," *Journal of Engineering Materials and Technology*, vol. 108, no. 3, pp. 206–213, 1986. 2.2.1

[28] C. Li, "Vector CTD analysis for crystallographic crack growth," *Acta Metallurgica et Materialia*, vol. 38, no. 11, pp. 2129–2134, 1990. 2.2.1

[29] B. A. Bilby, A. H. Cottrell, and K. H. Swinden, "Spread of plastic yield from a notch," *Proceedings of the Royal Society of London A*, vol. 272, no. 135, pp. 304–&, 1963. 2.2.1

[30] J. R. Weertman, *Dislocation based fracture mechanics*. Singapore: World Scientific, 1996. 2.2.1

[31] A. N. Stroh, "Dislocations and cracks in anisotropic elasticity," *Philosophical Magazine*, vol. 3, no. 30, pp. 625–&, 1958. 2.2.1

[32] X. Wu, W. Deng, A. Koul, and J. P. Immarigeon, "A continuously distributed dislocation model for fatigue cracks in anisotropic crystalline materials," *International Journal of Fatigue*, vol. 23, pp. S201–S206, 2001. 2.2.1

[33] X. J. Wu, "A continuously distributed dislocation model of Zener-Stroh-Koehler cracks in anisotropic materials," *International Journal of Solids and Structures*, vol. 42, no. 7, pp. 1909–1921, 2005. 2.2.1

[34] A. Navarro and E. R. de los Rios, "A model for short fatigue crack propagation with an interpretation of the short-long crack transition," *Fatigue and Fracture of Engineering Materials and Structures*, vol. 10, pp. 169–186, 1987. 2.2.1

[35] T. Mura and Y. Nakasone, "Theory of fatigue crack initiation in solids," *Journal of Applied Mechanics*, vol. 57, no. 1, pp. 1–6, 1990. 2.2.1

[36] T. Mura, "A theory of fatigue crack initiation," *Materials Science and Engineering A*, vol. 176, no. 1-2, pp. 61–70, 1994. 2.2.1

[37] G. Venkataraman, Y. W. Chung, and T. Mura, "Application of minimum energy formalism in a multiple slip band model for fatigue. I. calculation of slip band spacings," *Acta Metallurgica et Materialia*, vol. 39, no. 11, pp. 2621–9, 1991. 2.2.1

[38] G. Venkataraman, Y. W. Chung, Y. Nakasone, and T. Mura, "Free energy formulation of fatigue crack initation along persistent slip bands. calculation of S-N curves and crack depths," *Acta Metallurgica*, vol. 38, no. 1, pp. 31–40, 1990. 2.2.1

[39] E. A. Repetto and M. Ortiz, "A micromechanical model of cyclic deformation and fatigue-crack nucleation in f.c.c. single crystals," *Acta Materialia*, vol. 45, no. 6, pp. 2577–95, 1997. 2.2.1

[40] S. Serebrinsky and M. Ortiz, "A hysteretic cohesive-law model of fatigue-crack nucleation," *Scripta Materialia*, vol. 53, no. 10, pp. 1193–1196, 2005. 2.2.1

[41] S. Brinckmann and E. Van der Giessen, "A fatigue crack initiation model incorporating discrete dislocation plasticity and surface roughness," *International Journal of Fracture*, vol. 148, pp. 155–167, 2007. 2.2.1

[42] P. Paris, M. Gomez, and W. Anderson, "A rational analytic theory of fatigue," *The Trend in Engineering*, vol. 13, pp. 9–14, 1961. 2.2.2

[43] H. Lamba, "J-integral applied to cyclic loading," *Engineering Fracture Mechanics*, vol. 7, no. 4, pp. 693–703, 1975. 2.2.2

[44] J. A. Bannantine, J. J. Comer, and J. L. Handrock, *Fundamentals of Metal Fatigue Analysis*. Englewood Cliffs, New Jersey: Prentice Hall, 1990. 2.2.2

[45] ENSIP, *Engine Structural Integrity Program Handbook*. United States Air Force, 2002. 2.2.3

[46] C. Bathias and J. Ni, "Determination of fatigue limit between 10^5 and 10^9 cycles using an ultrasonic fatigue device," in *Second Symposium on Adbances in Fatigue Lifetime Predictive Techniques*, ser. ASTM Special Technical Publication, ASTM. Philadelphia, PA: American Society for Testing and Materials, 1993, pp. 141–152. 2.2.3

[47] C. Bathias, "There is no infinite fatigue life in metallic materials," *Fatigue and Fracture of Engineering Materials and Structures*, vol. 22, pp. 559–5565, 1999. 2.2.3

[48] K. J. Miller, "The fatigue limit and its elimination," *Fatigue and Fracture of Engineering Materials and Structures*, vol. 22, no. 7, pp. 545–557, 1999. 2.2.3

[49] I. Marines, X. Bin, and C. Bathias, "An understanding of very high cycle fatigue of metals," *International Journal of Fatigue*, vol. 25, no. 9-11, pp. 1101–1107, 2003. 2.5, 3.2, 3.3

[50] D. Eylon and C. M. Pierce, "Effect of microstructure on notch fatigue properties of Ti-6Al-4V," *Metallurgical and Materials Transactions A*, vol. 7A, no. 1, pp. 111–121, 1976. 2.2.3

[51] A. T. Winter, O. B. Pedersen, and K. V. Rasmussen, "Dislocation microstructure in fatigue copper polycrystals," *Acta Metallurgica*, vol. 29, no. 5, pp. 735–748, 1981. 2.2.4, 6.1

[52] V. P. Bennett and D. L. McDowell, "Polycrystal orientation distribution effects on microslip in high cycle fatigue," *International Journal of Fatigue*, vol. 25, no. 1, pp. 27–39, 2003. 2.2.4, 2.3.1, 5.7, 6.1, 6.2.4

[53] M. Sauzay and T. Jourdan, "Polycrystalline microstructure, cubic elasticity, and nucleation of high-cycle fatigue cracks," *International Journal of Fracture*, vol. 141, no. 3-4, pp. 431–446, 2006. 2.2.4, 5.7, 6.1

[54] W. N. Findley, "Theory for effect of mean stress on fatigue of metals under combined torsion and axial load or bending," in *American Society of Mechanical Engineers – Papers*. American Society of Mechanical Engineers (ASME), New York, NY, United States, 1958, p. 5. 2.3.1

[55] I. V. Papadopoulos, "A new criterion of fatigue-strenght for out-of-phase bending and torsion of hard metals," *International Journal of Fatigue*, vol. 16, no. 6, pp. 377–384, 1994. 2.3.1

[56] I. V. Papadopoulos, "A high-cycle fatigue criterion applied in biaxial and triaxial out-of-phase stress conditions," *Fatigue and Fracture of Engineering Materials and Structures*, vol. 18, no. 1, pp. 79–91, 1995. 2.3.1

[57] I. V. Papadopoulos and V. P. Panoskaltsis, "Invariant formulation of a gradient dependent multiaxial high-cycle fatigue criterion," *Engineering Fracture Mechanics*, vol. 55, no. 4, pp. 513–528, 1996. 2.3.1

[58] M. A. Crisfield, "Plasticity computions using the Mohr-Coulomb yield criterion," *Engineering Computations*, vol. 4, pp. 300–308, 1987. 2.3.1

[59] I. V. Papadopoulos, P. Davoli, C. Gorla, M. Filippini, and A. Bernassconi, "A comparative study of multiaxial high-cycle fatigue criteria for metals," *International Journal of Fatigue*, vol. 19, no. 3, pp. 219–235, 1997. 2.3.1

[60] J. Coffin, L. F., "A study of the effects of cyclic thermal stresses on a ductile metal," *Transactions of the American Society of Mechanical Engineers*, vol. 76, pp. 931–950, 1954. 2.3.1

[61] S. S. Manson, "Behavior of materials under conditions of thermal stress," National Advisory Commission on Aeronautics: Report 1170. Lewis Flight Propulsion Laboratory, Tech. Rep., 1954. 2.3.1

[62] "ASTM Standard E606-00, Standard test method for strain-controlled fatigue testing," in *Annual Book of ASTM Standards*. Philadelphia, PA: American Society for Testing and Materials, 2000, vol. 03.01, pp. 525–539. 2.3.1

[63] A. Fatemi and D. F. Socie, "A critical plane approach to multiaxial fatigue damage including out-of-phase loading," *Fatigue and Fracture of Engineering Materials and Structures*, vol. 11, no. 3, pp. 149–65, 1988. 2.3.1, 6.2.4, 7.1.3

[64] A. Fatemi and P. Kurath, "Multiaxial fatigue life predictions under the influence of mean-stresses," *Journal of Engineering Materials and Technology*, vol. 110, no. 4, pp. 380–388, 1988. 2.3.1

[65] D. L. McDowell and J. Y. Berard, "A ΔJ-based approach to biaxial fatigue," *Fatigue and Fracture of Engineering Materials and Structures*, vol. 15, no. 8, pp. 719–41, 1992. 2.3.1, 6.2.4, 6.5, 7.7

[66] V. P. Bennett and D. L. McDowell, "Polycrystal orientation effects on microslip and mixed-mode behavior of microstructurally small cracks," in *Mixed-Mode Crack Behavior*, K. J. Miller and D. L. McDowell, Eds. West Conshohocken, PA: American Society for Testing and Materials, 1999, pp. 203–228. 2.3.1, 6.2.4

[67] R. Döring, J. Hoffmeyer, T. Seeger, and M. Vormwald, "Short fatigue crack growth under nonproportional multiaxial elastic-plastic strains," *International Journal of Fatigue*, vol. 28, pp. 972–982, 2006. 2.3.1, 6.2.4, 7.1.3

[68] J. Hoffmeyer, R. Döring, T. Seeger, and M. Vormwald, "Deformation behaviour, short crack growth and fatigue lives under multiaxial nonproportional loading," *International Journal of Fatigue*, vol. 28, pp. 508–520, 2006. 2.3.1, 6.2.4, 7.1.3

[69] F. P. E. Dunne, A. J. Wilkinson, and R. Allen, "Experimental and computational studies of low cycle fatigue crack nucleation in a polycrystal," *International Journal of Plasticity*, vol. 23, no. 2, pp. 273–295, 2007. 2.3.1, 6.2.4, 7.1.2, 7.1.3, 7.7, 7.14

[70] K. O. Findley and A. Saxena, "Low cycle fatigue in René 88DT at 650 degrees C: Crack nucleation mechanisms and modeling," *Metallurgical and Materials Transactions A*, vol. 37A, no. 5, pp. 1469–1475, 2006. 2.3.1, 6.2.4, 7.1.3

[71] T. Hoshide and D. F. Socie, "Mechanics of mixed mode small fatigue crack growth," *Engineering Fracture Mechanics*, vol. 26, no. 6, pp. 841–850, 1987. 2.3.1, 6.2.4, 6.5

[72] E. J. Gumbel, *Statistics of Extremes*. New York: Columbia University Press, 1958. 3.2, 3.2, 3.2, 3.5, 9.1

[73] A. Haldar and S. Mahadevan, *Probability, Reliability and Statistical Methods in Engineering Design*. New York: John Wiley and Sons, Inc., 2000. 3.2

[74] A. H.-S. Ang and W. H. Tang, *Probability Concepts in Engineering Planning and Design: Volume II Decision, Risk, and Reliability*, 1990, vol. 2. 3.2, 3.2, 3.2

[75] E. Castillo, *Extreme value theory in engineering*. Boston: Academic, 1988. 3.2, 3.2, 3.2, 3.2, 3.5, B

[76] S. Wilks, "Order statistics," *Bulletin American of the American Mathematical Society*, vol. 54, 1948. 3.2

[77] H. Cramer, *Mathematical Methods of Statistics*. Princeton Univeristy Press, 1946. 3.2, 3.2

[78] J. Galambos, *The Asymptotic Theory of Extreme Order Statistics*. New York: John Wiley and Sons, 1978. 3.2

[79] S. Kotz and S. Nadarajah, *Extreme value distributions*. London: Imperial Collage Press, 2000. 3.2

[80] J. H. Zuo, Z. G. Wang, and E. H. Han, "Effect of microstructure on ultra-high cycle fatigue behavior of Ti-6Al-4V," *Materials Science and Engineering A*, vol. 473, pp. 147–152, 2008. 3.3

[81] K. S. Revi Chandran and S. K. Jha, "Duality of the S-N fatigue curve caused by competing failure modes in a titanium alloy and the role of poisson defect statistics," *Acta Materialia*, vol. 53, pp. 1867–1881, 2005. 3.3

[82] S. K. Jha, M. J. Caton, and J. M. Larsen, "A new paradigm of fatigue variability behavior and implications for life prediction," *Materials Science and Engineering A*, vol. 468, pp. 23–32, 2007. 3.3, 3.3, 3.4, 6.1, 7.1.2

[83] S. K. Jha, M. J. Caton, and J. M. Larsen, "Mean vs. life-limiting fatigue behavior of a nickel-based superalloy," in *Superalloys 2008*, R. C. Reed, K. A. Green, P. Caron, T. P. Gabb, M. G. Fahrmann, E. S. Huron, and S. A. Woodard, Eds. TMS (The Minerals, Metals and Materials Society), 2008, pp. 565–572. 3.3, 6.1, 6.2

[84] Y. Murakami, S. Kodama, and S. Konuma, "Quantitative evaluation of defects of non-metallic inclusions on fatigue strength of high strength steels. I: Basic fatigue mechanism and evaluation of correlation between the fatigue fracture stress and the size and location of non-metallic inclusions." *International Journal of Fatigue*, vol. 11, no. 5, pp. 291–298, 1989. 3.3.2

[85] Y. Murakami, T. Toriyama, and E. M. Coudert, "Instructions for a new method of inclusion rating and correlations with the fatigue limit," *Journal of Testing and Evaluation*, vol. 22, no. 4, pp. 318–326, 1994. 3.3.2

[86] S. Beretta and Y. Murakami, "Statistical analysis of defects for fatigue strength prediction and quality control of materials," *Fatigue and Fracture of Engineering Materials and Structures*, vol. 21, no. 9, pp. 1049–1065, 1998. 3.3.2

[87] B. H. Choi and S. H. Song, "Prediction of fatigue limit of induction surface hardened 1.05Cr-0.23Mo steel alloy using extreme value statistics," *Journal of Materials Science*, vol. 40, no. 20, pp. 5427–5433, 2005. 3.3.2

[88] M. A. Przystupa, R. J. Bucci, P. E. Magnusen, and A. J. Hinkle, "Microstructure based fatigue life predictions for thick plate 7050-T7451 airframe alloys," *International Journal of Fatigue*, vol. 19, no. Suppl 1, pp. 285–288, 1997. 3.3.2

[89] B. L. Adams, M. Lyon, and B. Henrie, "Microstructures by design: Linear problems in elastic-plastic design," *International Journal of Plasticity*, vol. 20, no. 8-9, pp. 1577–1602, 2004. 3.4

[90] C. P. Przybyla, B. L. Adams, and M. P. Miles, "Methodology for determining the variance of the taylor factor: Application in Fe-3%Si," *Journal of Engineering Materials and Technology*, vol. 129, no. 1, pp. 82–93, 2007. 3.4

[91] B. L. Adams, S. R. Kalidindi, and D. Fullwood, *Microstructure Design for Materials Performance*, 2nd ed. Provo, UT: Brigham Young Univeristy, 2008. 3.4, 3.4

[92] A. Morawiec, *Orientations and Rotations: Computations in Crystallographic Textures*. New York: Springer, 2004. 3.4

[93] H.-J. Bunge, *Texture Analysis in Materials Science*. Gottingen: Cuvillier Verlag, 1993. 3.4, 4.2

[94] S. Torquato and G. Stell, "Microstructure of two-phase random media. V. The n-point matrix probability functions for impenetrable spheres," *Journal of Chemical Physics*, vol. 82, no. 2, pp. 980–987, 1985. 3.4.1

[95] M. J. Huang, "The n-point orientation correlation function and its application," *International Journal of Solids and Structures*, vol. 42, no. 5-6, pp. 1425–1441, 2005. 3.4.1

[96] A. M. Gokhale, A. Tewari, and H. Garmestani, "Constraints on microstructural two-point correlation functions," *Scripta Materialia*, vol. 53, no. 8, pp. 989–993, 2005. 3.4.1

[97] A. Tewari, A. M. Gokhale, J. E. Spowart, and D. B. Miracle, "Quantitative characterization of spatial clustering in three-dimensional microstructures using two-point correlation functions," *Acta Materialia*, vol. 52, no. 2, pp. 307–319, 2004. 3.4.1

[98] J. Quintanilla and S. Torquato, "Lineal measure of clustering in overlapping particle systems," *Physical Review E*, vol. 54, no. 4, pp. 4027–4036, 1996. 3.4.1

[99] H. Singh, A. M. Gokhale, A. Sreeranganathan, Y. Mao, S. I. Lieberman, and S. Tamirisakandala, "Computer simulations of "realistic" partially anisotropic microstructures statistically similar to real microstructures," *Computational Materials Science*, vol. 44, pp. 1050–1055, 2009. 3.4.1, 5.3

[100] A. Tewari and A. M. Gokhale, "Nearest neighbor distances in uniform-random polydispersed microstructures," *Materials Science and Engineering A*, vol. 396, no. 1-2, pp. 22–27, 2005. 3.4.1

[101] A. Tewari and A. M. Gokhale, "Nearest neighbor distances in uniaxial fiber composites," *Computational Materials Science*, vol. 31, no. 1-2, pp. 13–23, 2004. 3.4.1

[102] A. Tewari and A. M. Gokhale, "Nearest-neighbor distances between particles of finite size in three-dimensional uniform random microstructures," *Materials Science and Engineering A*, vol. 385, no. 1-2, pp. 332–341, 2004. 3.4.1

[103] M. A. Groeber, B. K. Haley, M. D. Uchic, D. M. Dimiduk, and S. Ghosh, "3D reconstruction and characterization of polycrystalline microstructures using a fib-sem system," *Materials Characterization*, vol. 57, no. 4-5, pp. 259–273, 2006. 3.4.1, 5.3

[104] A. J. Henrie, B. L. Adams, and R. J. Larsen, "Creating a model for percolation of grain boundaries in polycrystalline materials," in *Mater. Sci. Forum (Switzerland)*, vol. 408-412. Seoul, South Korea: Trans Tech Publications, 2002, pp. 419–24. 3.4.1

[105] G. Q. Liu, H. B. Yu, and X. G. Qin, "Three-dimensional grain topology-size relationships in a real metallic polycrystal compared with theoretical models," *Materials Science and Engineering A*, vol. 326, no. 2, pp. 276–281, 2002. 3.4.1

[106] M. A. Wall, A. J. Schwartz, and L. Nguyen, "A high-resolution serial sectioning specimen preparation technique for application to electron backscatter diffraction," *Ultramicroscopy*, vol. 88, no. 2, pp. 73–83, 2001. 3.4.1

[107] C. T. Wu, B. L. Adams, C. L. Bauer, D. Casasent, A. Morawiec, S. Ozdemir, and A. Talukder, "Mapping the mesoscale interface structure in polycrystalline materials," *Ultramicroscopy*, vol. 93, no. 2, pp. 99–109, 2002. 3.4.1

[108] C. Zhang, A. Suzuki, T. Ishimaru, and M. Enomoto, "Characterization of three-dimensional grain structure in polycrystalline iron by serial sectioning," *Metallurgical and Materials Transactions A*, vol. 35A, no. 7, pp. 1927–1933, 2004. 3.4.1

[109] J. D. Budai, W. Yang, B. C. Larson, J. Z. Tischler, W. Liu, and G. E. Ice, "2D and 3D x-ray structural microscopy using submicron-resolution laue microdiffraction," in *Materials Research Society Symposium Proceedings*, vol. 840, 2005, pp. 175 – 180. 3.4.1

[110] J. Budai, W. Liu, J. Tischler, Z. Pan, D. Norton, B. Larson, W. Yang, and G. Ice, "Polychromatic x-ray micro- and nanodiffraction for spatially-resolved structural studies," *Thin Solid Films*, vol. 516, no. 22, pp. 8013 – 8021, 2008. 3.4.1

[111] A. King, G. Johnson, and W. Ludwig, "Diffraction contrast tomography - A synchrotron radiation technique for mapping polycrystalline microstructures in 3D," *Materials Science Forum*, vol. 571-572, pp. 207 – 212, 2008. 3.4.1

[112] L. Wcislak, H. Bunge, H. Klein, U. Garbe, and J. Schneider, "High-resolution texture imaging with hard synchrotron radiation in the moving area detector technique," *Nuclear Instruments and Methods in Physics Research, Section B: Beam Interactions with Materials and Atoms*, vol. 199, no. SUPPL., pp. 38 – 43, 2003. 3.4.1

[113] M. P. Miller, J. V. Bernier, J.-S. Park, and A. Kazimirov, "Experimental measurement of lattice strain pole figures using synchrotron x rays," *Review of Scientific Instruments*, vol. 76, no. 113903, pp. 1–11, 2005. 3.4.1

[114] J.-S. Park, P. Revesz, A. Kazimirov, and M. P. Miller, "A methodology for measuring in situ lattice strain of bulk polycrystalline material under cyclic load," *Review of Scientific Instruments*, vol. 78, no. 023910, pp. 1–11, 2007. 3.4.1

[115] X. Gao, C. P. Przybyla, and B. L. Adams, "Methodology for recovering and analyzing two-point pair correlation functions in polycrystalline materials," *Metallurgical and Materials Transactions A*, vol. 37A, no. 8, pp. 2379–2387, 2006. 3.4.1

[116] B. L. Adams, "Orientation imaging microscopy: application to the measurement of grain boundary structure," *Materials Science and Engineering A*, vol. A166, no. 1-2, pp. 59–66, 1993. 3.4.1

[117] B. L. Adams, S. I. Wright, and K. Kunze, "Orientation imaging: the emergence of a new microscopy," *Metallurgical Transactions A*, vol. 24A, no. 4, pp. 819–31, 1993. 3.4.1

[118] V. Randle, *Microtecture Determination and its Applications*. London: Maney for the Institute of Materials, 2003. 3.4.1, 5.3.1

[119] R. Pyrz, "Correlation of microstructure variability and local stress-field in two-phase materials," *Materials Science and Engineering A*, vol. 177, no. 1-2, pp. 253–259, 1994. 3.4.2, 3.10, 3.11, 3.12, 3.5, 9.2

[120] R. Pyrz, "Quantitative description of the microstructure of composites .1. Morphology of unidirectional composite systems," *Composites Science and Technology*, vol. 50, no. 2, pp. 197–208, 1994. 3.4.2, 3.5, 9.2

[121] ABAQUS, Simulia. Providence, RI, 2008, 6.8-EF1 ed. 4.1, 5.4, 5.7, 6.2.2, 7.2.3, 7.3, 7.3.4, A.2

[122] T. Hasegawa, T. Yakou, and U. F. Kocks, "Forward and reverse rearrangements of dislocations in tangled walls," *Materials Science and Engineering*, vol. 81, no. 1-2, pp. 189–199, 1986. 4.1

[123] E. Orowan, "Causes and effects of internal stresses," in *Internal Stresses and Fatigue in Metals*, G. M. Rassweiler and W. L. Grube, Eds. New York: Elsevier, 1959, pp. 59–80. 4.1

[124] R. Hill, "Generalized constitutive relations for incremental deformation of metal crystals by multislip," *Journal of the Mechanics and Physics of Solids*, vol. 14, no. 2, pp. 95–&, 1966. 4.2

[125] E. H. Lee, "Elastic-plastic deformation at finite strains," *Journal of Applied Mechanics*, vol. 36, no. 1, pp. 1–&, 1969. 4.2, 4.2

[126] J. R. Rice, "Inelastic constitutive relations for solids: An internal-variable theory and its application to metal plasticity," *Journal of the Mechanics and Physics of Solids*, vol. 19, no. 6, pp. 433–&, 1971. 4.2

[127] R. Hill and J. R. Rice, "Constitutive analysis of elastic-plastic crystals at arbitrary strain," *Journal of the Mechanics and Physics of Solids*, vol. 20, no. 6, pp. 401–&, 1972. 4.2, A.2

[128] R. J. Asaro and J. R. Rice, "Strain localization in ductile single-crystals," *Journal of the Mechanics and Physics of Solids*, vol. 25, no. 5, pp. 309–338, 1977. 4.2

[129] R. Hill and K. S. Havner, "Perspectives in the mechanics of elastoplastic crystals," *Journal of the Mechanics and Physics of Solids*, vol. 30, no. 1-2, pp. 5–22, 1982. 4.2

[130] D. Peirce, R. J. Asaro, and A. Needleman, "Material rate dependence and localized deformation in crystalline solids," *Acta Metallurgica*, vol. 31, no. 12, pp. 1951–1976, 1983. 4.2

[131] R. J. Asaro, "Large strain plasticity in crystalline materials," *Journal of Metals*, vol. 35, no. 8, pp. A28–A28, 1983. 4.2

[132] R. J. Asaro, "Micromechanics of crystals and polycrystals," *Advances in Applied Mechanics*, vol. 23, pp. 1–115, 1983. 4.2

[133] A. Needleman, R. J. Asaro, J. Lemonds, and D. Peirce, "Finite-element analysis of crystalline solids," *Computer Methods in Applied Mechanics and Engineering*, vol. 52, no. 1-3, pp. 689–708, 1985. 4.2

[134] S. R. Kalidindi, C. A. Bronkhorst, and L. Anand, "Crystallographic texture evolution in bulk deformation processing of fcc metals," *Journal of the Mechanics and Physics of Solids*, vol. 40, no. 3, pp. 537–569, 1992. 4.2, 4.4

[135] J. Lemaitre and J. L. Chaboche, *Mechanics of Solid Materials*. Cambridge University Press, 1990. 4.2.1

[136] D. L. McDowell, "Internal state variable theory," in *Handbook of Materials Modeling, Part A: Methods*, S. Yip and M. F. Horstemeyer, Eds. the Netherlands: Springer, 2005, vol. 03.01, pp. 1151–1170. 4.2.1

[137] C. Miehe, J. Schröder, and J. Schotte, "Computational homogenization analysis in finite plasticity simulation of texture development in polycrystalline materials," *Computer methods in applied mechanics and engineering*, vol. 171, pp. 387–418, 1999. 4.2.1

[138] M. Ortiz and L. Stainier, "The variational formulation of viscoplastic constitutive updates," *Computer methods in applied mechanics and engineering*, vol. 171, pp. 419–444, 1999. 4.2.1

[139] N. Thompson, N. Wadsworth, and N. Louat, "Origin of fatigue fracture in copper," *Philosophical Magazine*, vol. 1, no. 2, pp. 113–126, 1956. 4.3.1

[140] B. Gong, Z. Wang, and Z. Wang, "Cyclic hardening mechanisms in [001] copper single crystals," *Materials Science and Engineering A*, vol. 245, pp. 55–63, 1998. 4.3.1

[141] B. Gong, Z. Wang, and Z. Wang, "Cyclic deformation behavior and dislocation structures of [001] copper single crystals - I. cyclic stress-strain response and surface feature," *Acta Materialia*, vol. 45, no. 4, pp. 1365–1377, 1997. 4.3.1

[142] Z. Wang, B. Gong, and Z. Wang, "Cyclic deformation behavior and dislocation structures of [001] copper single crystals - II. characteristics of dislocation structures," *Acta Materialia*, vol. 45, no. 4, pp. 1379–1391, 1997. 4.3.1, 4.2

[143] H. Mughrabi, F. Ackermann, and K. Hertz, "Persistent slip bands in fatigued face-centered and body-centered cubic metals." in *Fatigue Mechanisms, Special Technical Publication*, J. T. Fong, Ed. Philadelphia: American Society for Testing and Materials, 1979, vol. 675, pp. 69–105. 4.2

[144] B. Xu and Y. Jiang, "A cyclic plasticity model for single crystals," *International Journal of Plasticity*, vol. 20, no. 12, pp. 2161–2178, 2004. 4.3.1, 4.3.1, 4.3, 4.4

[145] J. L. Bassani and T. Y. Wu, "Latent hardening in single-crystals. 2. Analytical characterization and predictions," *Proceedings of the Royal Society of London Series A*, vol. 435, pp. 21–41, 1991. 4.3.1

[146] M. M. Shenoy, "Constitutive modeling and life prediction in Ni-base superalloys," Ph.D. dissertation, Georgia Institute of Technology, 2006. 4.3.2, 4.3.2, 4.3.2

[147] M. Shenoy, J. Zhang, and D. L. McDowell, "Estimating fatigue sensitivity to polycrystalline Ni-base superalloy microstructures using a computational approach," *Fatigue and Fracture of Engineering Materials and Structures*, vol. 30, no. 10, pp. 889–904, 2007. 4.3.2, 4.3.2, 4.3.2, 5.3.1, 6.2.2, 7.1.3

[148] M. Shenoy, Y. Tjiptowidjojo, and D. McDowell, "Microstructure-sensitive modeling of polycrystalline IN100," *International Journal of Plasticity*, vol. 24, no. 10, pp. 1694–1730, 2008. 4.3.2, 4.3.2, 4.3.2, 6.2.2

[149] C. P. Przybyla and D. McDowell, "Microstructure-sensitive extreme value probabilities for high cycle fatigue of Ni-base superalloy IN100," *International Journal of Plasticity*, vol. 26, pp. 372–394, 2010. 4.3.2, 6.1, 7.1.3, 7.1.3, 7.2.1

[150] J. L. Chaboche, "Constitutive equations for cyclic plasticity and cyclic viscoplasticity," *International Journal of Plasticity*, vol. 5, pp. 247–302, 1989. 4.3.2, 4.3.2

[151] D. Bettge and W. Österle, ""cube slip" in near-[111] oriented specimens of a single-crystal nickel-base superalloy," *Scripta Materialia*, vol. 40, no. 4, pp. 389–395, 1999. 4.3.2, 6.1, 6.1, 6.1

[152] P. J. Phillips, R. R. Unocic, L. Kovarik, D. Mourer, D. Wei, and M. J. Mills, "Low cycle fatigue of a Ni-based superalloy: Non-planar deformation," *Scripta Materialia*, vol. 62, pp. 790–793, 2010. 4.3.2, 6.1, 6.1, 6.2, 6.2.2

[153] J. R. Mayeur and D. L. McDowell, "A three-dimensional crystal plasticity model for duplex Ti-6Al-4V," *International Journal of Plasticity*, vol. 23, no. 9, pp. 1457–1485, 2007. 4.3.3, 7.2.2

[154] M. Zhang, J. Zhang, and D. L. McDowell, "Microstructure-based crystal plasticity modeling of cyclic deformation of Ti-6Al-4V," *International Journal of Plasticity*, vol. 23, no. 8, pp. 1328–1348, 2007. 4.3.3, 5.3.1, 7.2.2

[155] F. Bridier, D. L. McDowell, P. Villechaise, and J. Mendez, "Crystal plasticity modeling of slip activity in Ti-6Al-4V under high cycle fatigue loading," *International Journal of Plasticity*, vol. 25, no. 6, pp. 1066–1082, 2009. 4.3.3, 4.3.3, 7.2.2, 7.7

[156] R. Courant, K. Friedrichs, and H. Lewy, "Über die partiellen differenzengleichungen der mathematischen physik," *Mathematische Annalen*, vol. 100, no. 1, pp. 32–74, 1928. 4.4

[157] X. W. Ling, M. F. Horstemeyer, and G. P. Potirniche, "On the numerical implementation of 3D rate-dependent single crystal plasticity formulations," *International Journal for Numerical Methods in Engineering*, vol. 63, no. 4, pp. 548–568, 2005. 4.4

[158] S. N. Kuchnicki, A. M. Cuitiño, and R. A. Radovitzky, "Efficient and robust constitutive integrators for single-crystal plasticity modeling," *International Journal of Plasticity*, vol. 22, pp. 1988–2011, 2006. 4.4

[159] A. V. Amirkhizi and S. Nemat-Nasser, "A framework for numerical integration of crystal elasto-plastic constitutive equations compatible with explicit finite element codes," *International Journal of Plasticity*, vol. 23, pp. 1918–1937, 2007. 4.4

[160] S. N. Kuchnicki, R. A. Radovitzky, and A. M. Cuitiño, "An explicit formulation for multiscale modeling of bcc metals," *International Journal of Plasticity*, vol. 24, pp. 2173–2191, 2008. 4.4

[161] H. W. Li, H. Yang, and Z. C. Sun, "A robust integration algorithm for implementing rate dependent crystal plasticity into explicit finite element method," *International Journal of Plasticity*, vol. 24, pp. 267–288, 2008. 4.4

[162] A. M. Maniatty, P. R. Dawson, and Y. S. Lee, "A time integration algorithm for elastoviscoplastic cubic-crystals applied to modeling polycrystalline deformation," *International Journal for Numerical Methods in Engineering*, vol. 35, no. 8, pp. 1565–1588, 1992. 4.4

[163] A. M. Cuitiño and M. Ortiz, "Computational modeling of single-crystals," *Modelling and Simulation in Materials Science and Engineering*, vol. 1, no. 3, pp. 225–263, 1993. 4.4

[164] G. Sarma and T. Zacharia, "Integration algorithm for modeling the elasto-viscoplastic response of polycrystalline materials," *Journal of the Mechanics and Physics of Solids*, vol. 47, pp. 1219–1238, 1999. 4.4

[165] F. T. Meissonnier, E. P. Busso, and N. P. O'Dowd, "Finite element implementation of a generalised non-local rate-dependent crystallographic formulation for finite strains," *International Journal of Plasticity*, pp. 601–640, 2001. 4.4

[166] R. D. McGinty, "Multiscale representation of polycrystalline inelasticity," Ph.D. dissertation, Georgia Institute of Technology, 2001. 4.4, A.1, A.1, A.1

[167] R. Hill, "Elastic properties of reinforced solids: Some theoretical principles," *Journal of Mechanics of Physics of Solids*, vol. 11, no. 5, pp. 357–372, 1963. 5.2

[168] Z. Hashin and S. Shtrikman, "A variational approach to the theory of the elastic behaviour of multiphase materials," *Journal of the Mechanics and Physics of Solids*, vol. 11, no. 2, pp. 127–140, 1963. 5.2

[169] Z. Hashin and S. Shtrikman, "On some variational principles in anisotropic and nonhomogeneous elasticity," *Journal of the Mechanics and Physics of Solids*, vol. 10, no. 4, pp. 335–342, 1962. 5.2

[170] M. Li, S. Ghosh, O. Richmond, H. Weiland, and T. N. Rouns, "Three dimensional characterization and modeling of particle reinforced metal matrix composites part II: Damage characterization," *Materials Science and Engineering A*, vol. 266, no. 1-2, pp. 221–240, 1999. 5.2

[171] Z. Shan and A. M. Gokhale, "Representiative volume element for non-uniform microstructure," *Computational Materials Science*, vol. 24, no. 3, pp. 361–379, 2002. 5.2

[172] T. Kanit, S. Forest, I. Galliet, V. Mounoury, and D. Jeulin, "Determination of the size of the representative volume element for random composites: statistical and numberical approach," *International Journal of Solids and Structures*, vol. 40, pp. 3347–3679, 2003. 5.2, 6.3.1

[173] M. Ostoja-Starzewski, "Material spatial randomness: from statistical to representative volume element," *Probabilistic Engineering Mechanics*, vol. 21, pp. 112–132, 2004. 5.2

[174] J. R. Willis, "Elasticity theory of composites," in *Mechanics of Solids, The Rodney Hill 60th Anniversary Volume*, H. G. Hopkins and M. J. Sewell, Eds. Oxford: Pergamon Press, 1982, pp. 653–686. 5.2

[175] S. Swaminathan, S. Ghosh, and N. J. Pagano, "Statistically equivalent representative volume elements for unidirectional composite microstructures: Part I - Without damage," *Journal of Composite Materials*, vol. 40, no. 7, pp. 583–604, 2006. 5.2

[176] S. Swaminathan and S. Ghosh, "Statistically equivalent representative volume elements for unidirectional composite microstructures: Part II - With interfacial debonding," *Journal of Composite Materials*, vol. 40, pp. 605–621, 2006. 5.2

[177] M. A. Tschopp, G. B. Wilks, and J. E. Spoward, "Multi-scale characterization of orthotropic microstructures," *Moelling and Simulation in Materials Science and Engineering*, vol. 16, pp. 1–14, 2008. 5.2

[178] S. R. Niezgoda, D. M. Turner, D. T. Fullwood, and S. R. Kalidindi, "Optimized structure based representative volume element sets reflecting the ensemble-average 2-point statistics," *Acta Materialia*, vol. 58, pp. 4432–4445, 2010. 5.2, 6.3.1, 9.7

[179] M. Groeber, S. Ghosh, M. D. Uchic, and D. M. Dimiduk, "Developing a robust 3-d characterization representation framework for modeling polycrystalline materials," *JOM*, vol. 59, no. 9, pp. 32–36, 2007. 5.3

[180] A. Brahme, M. H. Alvi, D. Saylor, J. Fridy, and A. D. Rollett, "3D reconstruction of microstructure in a commercial purity aluminum," *Scripta Materialia*, vol. 55, no. 1, pp. 75–80, 2006. 5.3, 5.3.2, 7.2.3

[181] C. L. Y. Yeong and S. Torquato, "Reconstructing random media," *Physical Review E*, vol. 57, no. 1, pp. 495–506, 1998. 5.3

[182] C. L. Y. Yeong and S. Torquato, "Reconstructing random media. II. Three-dimensional media from two-dimensiomal cuts," *Physical Review E*, vol. 58, no. 1, pp. 224–233, 1998. 5.3

[183] M. G. Rozman and M. Utz, "Efficient reconstruction of multiphase morphologies from correlation functions," *Physical Review E*, vol. 6306, no. 6, 2001. 5.3

[184] B. L. Hansen, B. L. Adams, M. E. Lyon, and A. Henrie, "On the reconstruction of polycrystalline microstructures from two-point correlation statistics," *Journal of Computer-Aided Materials Design*, vol. 10, no. 3, pp. 163–173, 2003. 5.3

[185] D. M. Saylor, J. Fridy, B. S. El-Dasher, K. Y. Jung, and A. D. Rollett, "Statistically representative three-dimensional microstructures based on orthogonal observation sections," *Metallurgical and Materials Transactions A*, vol. 35A, no. 7, pp. 1969–1979, 2004. 5.3, 5.3.2

[186] H. Singh, A. M. Gokhale, Y. Mao, and J. E. Spowart, "Computer simulations of realistic microstructures of discontinuously reinforced aluminum alloy (dra) composites," *Acta Materialia*, vol. 54, no. 8, pp. 2131–2143, 2006. 5.3

[187] F. Aurenhammer, "Voronoi diagrams - A survey of a fundamental geometric date structure," *Computing Surveys*, vol. 23, no. 3, pp. 345–405, 1991. 5.3.1

[188] C. B. Barber and H. Huhdanpaa, "Qhull," 2003. 5.3.1, 5.3.1

[189] D. Gross and M. Li, "Constructing microstructures of poly- and nanocrystalline materials for numerical modeling and simulation," *Applied Physics Letters*, vol. 80, no. 5, pp. 746–748, 2002. 5.3.1

[190] F. Barbe, S. Forest, and G. Cailletaud, "Intergranular and intragranular behavior of polycrystalline aggregates. part 2: Results," *International Journal of Plasticity*, vol. 17, no. 4, pp. 537–563, 2001. 5.3.1

[191] F. Barbe, L. Decker, D. Jeulin, and G. Cailletaud, "Intergranular and intragranular behavior of polycrystalline aggregates. part 1: F.e. model," *International Journal of Plasticity*, vol. 17, no. 4, pp. 513–536, 2001. 5.3.1

[192] V. Randle, *The measurement of grain boundary geometry*, ser. Electron microscopy in materials science series. Bristol: Institute of Physics Pub., 1993. 5.3.1

[193] J. C. Russ, *The image processing handbook*, 3rd ed. CRC Press, 2008. 5.3.2

[194] J. P. MacSleyne, J. P. Simmons, and M. De Graef, "On the use of moment invariants for the automated analysis of 3d particle shapes," *Modelling and Simulation in Materials Science and Engineering*, vol. 16, no. 4, pp. 1–17, 2008. 5.3.2

[195] MATLAB, The MathWorks, Inc., 2009, r2009a ed. 5.3.2

[196] M. Sauzay, "Cubic elasticity and stress distribution at the free surface of polycyrstals," *Acta Materialia*, vol. 55, pp. 1193–1202, 2007. 5.7

[197] M. Sauzay, "Influence of crystalline elasticity anisotropy on schmid factor distribution at the free surface of polycrystals," *Comptes Rendus de l'Academie des Sciences Serie II b/Mecanique*, vol. 334, no. 6, pp. 353–61, 2006. 5.7

[198] C. Przybyla, R. Prasannavenkatesan, N. Salajegheh, and D. L. McDowell, "Microstructure-sensitive modeling of high cycle fatigue," *International Journal of Fatigue*, vol. 32, no. 3, pp. 512–525, 2009. 6.1, 7.1.3, 7.1.3, 8.2.1

[199] J. M. Hyzak and I. M. Bernstein, "The effect of defects on the fatigue crack initiation process in 2 p/m super-alloys. 1. Fatigue origins," *Metallurgical Transactions A*, vol. 13, no. 1, pp. 33–43, 1982. 6.1

[200] M. Goto and D. M. Knowles, "Initiation and propagation behaviour of microcracks in Ni-base superalloy Udimet 720 Li," *Engineering Fracture Mechanics*, vol. 60, no. 1, pp. 1–18, 1998. 6.1

[201] H. T. Pang and P. A. S. Reed, "Fatigue crack initiation and short crack growth in nickel-base turbine disc alloys-the effects of microstructure and operating parameters," *International Journal of Fatigue*, vol. 25, no. 9-11, pp. 1089–1099, 2003. 6.1

[202] S. K. Jha, M. J. Caton, J. M. Larsen, A. H. Rosenberger, K. Li, and W. J. Porter, "Superimposing mechanisms and their effect on the variability in fatigue lives of a nickel-based superalloy," in *Materials Damage Prognosis*, J. M. Larsen, L. Christodoulou, J. R. Calcaterra, M. L. Dent, M. M. Derriso, W. J. Hardman, J. W. Jones, and S. M. Russ, Eds. TMS (The Minerals, Metals and Materials Society), 2005. 6.1, 6.1

[203] A. Shyam, C. J. Torbet, S. K. Jha, J. M. Larsen, M. J. Caton, C. J. Szczepanski, T. M. Pollock, and J. W. Jones, "Development of ultrasonic fatigue for rapid, high temperature fatigue studies in turbine engine materials," in *Superalloys 2004*. Minerals, Metals and Materials Society, 2004, pp. 259–268. 6.1

[204] J. Miao, T. M. Pollock, and J. W. Jones, "Very high cycle fatigue behavior of nickel-based superalloy René 88DT at 593 °C." in *Forth International Conterence on Very High Cycle Fatigue (VHCF-4)*, J. E. Allison, J. W. Jones, J. M. Larsen, and R. O. Ritchie, Eds. Ann Arbor, Michigan, USA: The Minerals, Metals and Materials Society (TMS), 2007. 6.1

[205] S. D. Antolovich and N. Jayaraman, "Metallurgical instabilities during the high-temperature low-cycle fatigue of nickel-base super-alloys," *Materials Science and Engineering A*, vol. 57, no. 1, pp. L9–L12, 1983. 6.1

[206] B. A. Lerch, N. Jayaraman, and S. D. Antolovich, "A study of fatigue damage mechanisms in waspoloy from 25-degrees-C to 800-degrees-C," *Materials Science and Engineering*, vol. 66, no. 2, pp. 151–166, 1984. 6.1

[207] R. V. Miner, T. P. Gabb, J. Gayda, and K. J. Hemker, "Orientation and temperature-dependence of some mechanical-properties of the single-crystal nickel-base superalloy René-N4 .3. Tension-compression anisotropy," *Metallurgical Transactions A*, vol. 17, no. 3, pp. 507–512, 1986. 6.1, 6.1

[208] E. F. Westbrooke, L. E. Forero, and F. Ebrahimi, "Slip analysis in a Ni-base superalloy," *Acta Materialia*, vol. 53, no. 7, pp. 2137–2147, 2005. 6.1, 6.1

[209] A. Nitz, U. Lagerpusch, and E. Nembach, "CRSS anisotropy and tension/compression asymmetry of a commercial superalloy," *Acta Materialia*, vol. 46, no. 13, pp. 4769–4779, 1998. 6.1, 6.1

[210] K. Li, N. E. Ashbaugh, and A. Rosenberger, "Crystallographic initiation of nickel-base superalloy IN100 at RT and 538 degrees C under low cycle fatigue conditions," in *Superalloys 2004*. The Minerals, Metals and Materials Society (TMS), 2004. 6.1, 6.2, 6.11, 6.4, 7.1.3, 9.4

[211] J. S. Miao, T. M. Pollock, and J. W. Jones, "Crystallographic fatigue crack initiation in nickel-based superalloy René 88DT at elevated temperature," *Acta Materialia*, vol. 57, no. 20, pp. 5964–5974, 2009. 6.1, 6.2, 6.2.2

[212] J. N. Vincent and L. Remy, "Temperature dependence of the pseudo-cleavage mechanism in the threshold regime of a super-alloy," in *Fatigue thresholds: fundamentals and engineering applications*, J. Blacklund, A. F. Blom, and C. J. Beevers, Eds., Stockholm, 1981, pp. 441–454. 6.2

[213] J. E. King, "Crystallographic fatigue crack-growth in NIMONIC APl," *Fatigue of Engineering Materials and Structures*, vol. 4, no. 4, pp. 311–320, 1981. 6.2

[214] D. P. Mourer and J. L. Williams, "Dual heat treat process development for advanced disk applications," in *Superalloys 2004*, K. A. Green, T. M. Pollock, H. Harada, T. E. Howson, R. C. Reed, J. J. Schirra, and S. Walston, Eds. Champion, Pennsylvania: TMS (The Minerals, Metals and Materials Society), 2004, pp. 401–407. 6.2, 6.2.2

[215] K. Sadananda and P. Shahinian, "Analysis of crystallographic high temperature fatigue crack growth in a nickel base alloy," *Metallurgical and Materials Transactions A*, vol. 12A, pp. 343–351, 1981. 6.2

[216] J. K. Mackenzie and M. J. Thompson, "Some statistics associated with the random disorientation of cubes," *Biometrika*, vol. 44, pp. 205–210, 1957. 6.2.3

[217] J. K. Mackenzie, "Second paper on statistics associated with the random disorientation of cubes," *Biometrika*, vol. 45, pp. 229–240, 1958. 6.2.3

[218] F. P. E. Dunne, D. Rugg, and A. Walker, "Lengthscale-dependent, elastically anisotropic, physically-based hcp crystal plasticity: Application to cold-dwell fatigue in Ti alloys," *International Journal of Plasticity*, vol. 23, no. 6, pp. 1061–1083, 2007. 6.2.4, 7.1.2, 7.7, 7.14

[219] J. X. Zhang, R. Prasannavenkatesan, M. M. Shenoy, and D. L. McDowell, "Modeling fatigue crack nucleation at primary inclusions in carburized and shot-peened martensitic steel," *Engineering Fracture Mechanics*, vol. 76, no. 3, pp. 315–334, 2009. 6.2.4

[220] R. Prasannavenkatesan, J. X. Zhang, D. L. McDowell, G. B. Olson, and H. J. Jou, "3D modeling of subsurface fatigue crack nucleation potency of primary inclusions in heat treated and shot peened martensitic gear steels," *International Journal of Fatigue*, vol. 31, no. 7, pp. 1176–1189, 2009. 6.2.4, 7.1.3

[221] C. J. Szczepanski, S. K. Jha, J. M. Larsen, and J. W. Jones, "Microstructural influences on very-high-cycle fatigue-crack initiation in Ti-6246," *Metallurgical and Materials Transactions A*, vol. 39A, no. 12, pp. 2841–2851, 2008. 7.1, 7.1.1, 7.1.2, 7.3.2, 9.5

[222] M. Liao, "Probabilistic modeling of fatigue related microstructural parameters in aluminum alloys," *Engineering Fracture Mechanics*, vol. 76, no. 5, pp. 668–680, 2009. 7.1.1

[223] C. H. Wells and C. P. Sullivan, "Low-cycle fatigue crack initiation in Ti-6Al-4V," *Asm Transactions Quarterly*, vol. 62, no. 1, pp. 263–&, 1969. 7.1.2

[224] M. R. Bache and W. J. Evans, "Impact of texture on mechanical properties in an advanced titanium alloy," in *12th International Conference on the Strength of Materials ICSMA-12*, vol. 319-321, 2001, pp. 409–414. 7.1.2

[225] M. R. Bache, W. J. Evans, B. Suddell, and F. R. M. Herrouin, "The effects of texture in titanium alloys for engineering components under fatigue," *International Journal of Fatigue*, vol. 23, no. SUPPL. 1, pp. S153–S159, 2001. 7.1.2

[226] M. R. Bache, "A review of dwell sensitive fatigue in titanium alloys: the role of microstructure, texture and operating conditions," *International Journal of Fatigue*, vol. 25, no. 9-11, pp. 1079–1087, 2003. 7.1.2

[227] A. N. Stroh, "The formation of cracks as a result of plastic flow," *Proceedings of the Royal Society of London A*, vol. 223, no. 1154, pp. 404–414, 1954. 7.1.2

[228] G. J. Baxter, W. M. Rainforth, and L. Grabowski, "Tem observations of fatigue damage accumulation at the surface of the near-alpha titanium alloy imi 834," *Acta Materialia*, vol. 44, no. 9, pp. 3453–3463, 1996. 7.1.2

[229] F. Bridier, P. Villechaise, and J. Mendez, "Analyis of slip and crack initiation processes activated by fatigue in a α/β titanium alloy in relation with local crystallographic orientation," in *9th International Fatigue Congress*. Atlanta, GA: Elsevier, 2006. 7.1.2, 7.14

[230] F. Bridier, P. Villechaise, and J. Mendez, "Slip and fatigue crack formation processes in an α/β titanium alloy in relation to crystallographic texture on different scales," *Acta Materialia*, vol. 56, no. 15, pp. 3951–3962, 2008. 7.1.2, 7.14

[231] J. L. Gilbert and H. R. Piehler, "On the nature and crystallographic orientation of subsurgace cracks in high cycle fatigue of Ti-6Al-4V," *Metallurgical Transactions A*, vol. 24, no. 3, pp. 669–680, 1993. 7.1.2, 7.14

[232] S. K. Jha and J. M. Larsen, "Random heterogeneity scales and probabilistic description of the long-lifetime regime of fatigue," in *Fourth International Conference on Very High Cycle Fatigue (VHCF-4)*, J. E. Allison, J. W. Jones, J. M. Larsen, and R. O. Ritchie, Eds. Ann Arbor, Michigan, USA: The Minerals, Metals and Materials Society (TMS), 2007, pp. 385–96. 7.1.2, 7.3.2, 9.5

[233] Y. Mahajan and H. Margolin, "Low-cycle fatigue behavior of Ti-6Al-2Sn-4Zr-6Mo .1. The role of microstructure in low-cycle crack nucleation and early crack-growth," *Metallurgical Transactions A*, vol. 13, no. 2, pp. 257–268, 1982. 7.1.2

[234] K. Le Biavant, S. Pommier, and C. Prioul, "Local texturing and fatigue crack initiation in Ti-6Al-4V titanium alloy," *Fatigue and Fracture of Engineering Materials and Structures*, vol. 25, pp. 527–545, 2002. 7.1.2

[235] I. Bantounas, D. Dye, and T. C. Lindley, "The effect of grain orientation on fracture morphology during high-cycle fatigue of Ti-6Al-4V," *Acta Materialia*, vol. 57, no. 12, pp. 3584–3595, 2009. 7.1.2, 7.14

[236] V. Hasija, M. J. Mills, D. S. Joseph, and S. Ghosh, "Deformation and creep modeling in polycrystalline Ti-6Al alloys," *Acta Materialia*, vol. 51, no. 15, pp. 4533–4549, 2003. 7.1.2, 7.14

[237] G. Venkataramani, D. Deka, and S. Ghosh, "Crystal plasticity based FE model for understanding microstructural effects on creep and dwell fatigue in Ti-6242," *Journal of Engineering Materials and Technology, Transactions of the ASME*, vol. 128, no. 3, pp. 356–365, 2006. 7.1.2, 7.14

[238] G. Venkataramani, S. Ghosh, and M. Mills, "A size-dependent crystal plasticity finite-element model for creep and load shedding in polycrystalline titanium alloys," *Acta Materialia*, vol. 55, no. 11, pp. 3971–3986, 2007. 7.1.2, 7.14

[239] F. P. E. Dunne and D. Rugg, "On the mechanisms of fatigue facet nucleation in titanium alloys," *Fatigue and Fracture of Engineering Materials and Structures*, vol. 31, no. 11, pp. 949–958, 2008. 7.1.2, 7.7, 7.14

[240] S. K. Jha, J. M. Larsen, A. H. Rosenberger, and G. A. Hartman, "Dual fatigue failure modes in Ti-6Al-2Sn-4Zr-Wo and consequences on probabilistic life prediction," *Scripta Materialia*, vol. 48, no. 12, pp. 1637–1642, 2003. 7.1.2

[241] S. K. Jha, J. M. Larsen, and A. H. Rosenberger, "Towards a physics-based description of fatigue variability behavior in probabilistic life-prediction," *Engineering Fracture Mechanics*, vol. 76, no. 5, pp. 681–694, 2009. 7.1.2

[242] D. L. McDowell, "Simulation-based strategies for microstructure-sensitive fatigue modeling," *Materials Science and Engineering A*, vol. 468-470, pp. 4–14, 2007. 7.1.3, 8.2.1

[243] V. Horalek, "ASTM grain-size model and related random tessellation models," *Materials Characterization*, vol. 25, no. 3, pp. 263–284, 1990. 7.2.4

[244] A. Morawiec, "Misorientation-angle distribution of randomly oriented symmetric objects," *Journal of Applied Crystallography*, vol. 28, pp. 289–293, 1995. 7.2.4

[245] T. M. Pollock, J. E. Allison, D. G. Backman, M. C. Boyce, M. Gersh, E. A. Holm, R. LeSar, M. Long, A. C. Powell IV, J. Schirra, John, D. D. Whitis, and C. Woodward, Eds., *Integrated Computational Materials Engineering: A Transformational Discipline for Improved Competitiveness and National Security*. Washington, D.C.: The National Academies Press, 2008. 8.1

[246] D. L. McDowell and B. Olson, Greg, "Concurrent design of hierarchical materials and structures," *Science of Modelling and Simulation*, vol. 15, pp. 207–240, 2008. 8.1

[247] D. L. McDowell, "Simulation-assisted materials design for the concurrent design of materials and products," *Mechanics and Modeling Issues in Materials Design*, pp. 21–25, September 2007. 8.1

[248] F. Bridier, P. Villechaise, and J. Mendez, "Analysis of the different slip systems activated by tension in a α/β titanium alloy in relation with local crystallographic orientation," *Acta Materialia*, vol. 53, no. 3, pp. 555–567, 2005. 8.3

[249] H. Liang and F. P. E. Dunne, "GND accumulation in bi-crystal deformation: Crystal plasticity analysis and comparison with experiements," *International Journal of Mechanical Sciences*, vol. 51, pp. 326–333, 2009. 9.7

[250] M. Kuroda and V. Tvergaard, "A finite deformation theory of higher-order gradient crystal plasticity," *Journal of the Mechanics and Physics of Solids*, vol. 56, pp. 2573–2584, 2008. 9.7

[251] V. Levkovitch and B. Svendsen, "On the large-deformation- and continuum-based formation of models for extended crystal plasticity," *International Journal of Solids ans Structures*, vol. 43, pp. 7246–7267, 2006. 9.7

[252] L. P. Evers, D. M. Parks, W. A. M. Brekelmans, and M. G. D. Geers, "Crystal plasticity model with enhanced hardening by geometrically necessary dislocation accumulation," *Journal of the Mechanics and Physics of Solids*, vol. 50, pp. 2403–2424, 2002. 9.7

[253] W. H. Press, S. A. Teukolsky, W. T. Vetterling, and B. P. Flannery, *Numerical Recipes in Fortran 77*, 2nd ed. Cambridge University Press, 2001. A.1

[254] K. C. Kapur and L. R. Lamberson, *Reliability in Engineering Design*. New York: John Wiley and Sons, 1977. B, B